
Feasibility of Vibration-based Damage Detection for Pinned Turbine Blades

Leon Brits
12020282

Submitted in Partial Fulfilment of the Requirements for the Degree

Master of Engineering (Mechanical Engineering)

in the

Department of Mechanical and Aeronautical Engineering

Faculty of Engineering, Built-environment and Information
Technology

University of Pretoria



UNIVERSITEIT VAN PRETORIA
UNIVERSITY OF PRETORIA
YUNIBESITHI YA PRETORIA

November, 2018

Executive Summary

Feasibility of Vibration-based Damage Detection for Pinned Turbine Blades

Author	: Leon Brits
Student Number	: 12020282
Supervisors	: Prof. P.S. Heyns and Dr. H.M. Inglis
University	: University of Pretoria
Department	: Mechanical and Aeronautical Engineering
Degree	: Master of Engineering, MEng (Mechanical Engineering)

Turbine blades are subjected to various damage mechanisms with fatigue as the primary contributor. During operation, damage accumulates in the form of crack initiation and propagation. This may lead to catastrophic failure, which is cause for concern in terms of availability and safety of the turbine. To optimize the maintenance schedule and to provide operational flexibility of the turbine, the state of health of the blades is monitored. This is usually accomplished through non-destructive testing (NDT) during outages. Conventional NDT techniques for in-situ inspection of turbine blade and disk assemblies is difficult and often ineffective, due to limited access to areas of concern, as well as the complex geometries of blade roots. Off-site inspection can be costly if the blades are still assembled in the turbine disk since the process of removing and reinstalling these blades is critical and labour-intensive, increasing the turbine downtime and overall costs.

These problems could potentially be overcome by employing inspection techniques that offer the prospect of assessing obstructed areas through monitoring the global dynamic characteristics of the structure, which provide relatively easily interpretable data. With global inspection methods, a degree of measurement sensitivity is forfeited but the potential to detect more severe damage, without prior knowledge of the precise damage area location, exists.

In this dissertation, the feasibility of a vibration-based structural damage identification technique that could be usable in support of conventional NDT to detect cracks in pinned turbine blades during off-line in-situ inspection, is evaluated. The investigation was limited to considering uninstalled single blades only, and thus off-site inspection of this component is regarded above the turbine disk assembly. This is clearly a simplified case and does not address the critical case from a practical perspective of having a large number of blades mounted onto a disk with pins, which is really the circumstance under which the technique could become useful. This study must thus be considered as a first step towards addressing the real practical problem. In this simplified problem, the following questions are answered: Is it possible to detect damage in an unconstrained and isolated blade using vibration response, and if so, can different damage scenarios be identified? The proposed vibration-based damage detection method entails a multi-class support vector machine classification procedure in which the natural frequencies are employed as the discriminatory feature for damage detection and identification of different single-location damage scenarios.

The natural frequencies were acquired from accurate experimental modal analysis of freely supported individual pinned turbine blades through impact testing. To confirm and predict the expected behaviour of the blades, a healthy numerical model was built and validated whereafter defects and damage were introduced. This includes geometrical variability at the root, observed in the procured blades, and the anticipated worst-case single-location damage at the most probable locations near or on the root, obtained from literature and discussions with experts in the industry. Artificial damage, i.e. a uniform 1mm notch, was introduced in the root at the upper pinhole on the leading edge pressure side; and just above the root at the aerofoil base on the trailing- and the leading edge. To establish the discriminative quality of the modal property natural frequency, it was necessary to determine its sensitivity to geometrical variability and damage. It was also required to establish the damage-specific behaviour or damage trend in the experimental data of

these damage scenarios to conclude their distinctiveness. This analysis was extended to outlining the feature quality by exploring the separability of class clusters for the healthy and damage scenario(s).

The feasibility of the proposed method is assessed using experimental data through simple hypothesis testing regarding the detection and identification of both geometrical variability in healthy blades, and damage. It was found that healthy blades are very similar, as geometrical variability cannot be detected. This is because the distributions of natural frequencies fall within a range about a mean value in an ambiguous cluster. In contrast to this, the damage scenarios were found to be distinct, and thus discernible from the healthy blades. These classes formed discrete clusters, each with a similar distribution than the healthy blades. The conclusion of the feasibility study serves as proof of concept.

Keywords: Modal analysis; Impact testing; Frequency response functions; Natural frequencies; Damage detection; Damage identification; Support vector machines; Classification; Finite element analysis

Acknowledgements

I would like to thank my Almighty Father for giving me the strength, knowledge, ability, and opportunity to undertake this research and to persevere and complete it satisfactorily. Without his blessings, this achievement would not have been possible. All glory to God!

”But those who trust in the LORD will find new strength. They will soar high on wings like eagles. They will run and not grow weary. They will walk and not faint.”

Isaiah 40:31

I would like to thank and acknowledge the following people for their continued support, guidance, patience, and contribution in the completion of this work:

- Prof. P.S. Heyns, my academic supervisor, for his abundant insight into various topics of vibration-based condition monitoring and the vision for the Centre for Asset Integrity Management (C-AIM). He is an inspiring global leader with a contagious passion, not just for the field but also for the participating people, especially students that attempt to discover the uncharted territory within. In his busy schedule, time to consult him is always available. I would also like to thank him for granting me the great opportunity to pursue my post-graduate studies at the C-AIM research group, the privilege of working alongside him, his valuable inputs, and allowing me to develop and apply engineering judgement.
- Dr. H.M. Inglis, my academic co-supervisor, for her pursuit to understanding an idea, her enthusiasm to question, and her patience to explain and teach. I would also like to thank her for the privilege of collaborating with her, and for investing her time to convey her valuable inputs and unmatched research domain insight into this dissertation.
- Mr. R. Scheepers, my industrial mentor and corporate specialist for structural integrity at Eskom, for his involvement in this project, and procurement of the healthy test blades. Without his specialised knowledge and these blades, this project would have been difficult to realize.
- Mr. G. Breytenbach, instructor and mechanical technician at C-AIM, for his assistance in setting up the experiment in the C-AIM SASOL labs, and his valuable input during the testing phase of the project.
- Dr. M. Johannes, post-graduate lecturer for Non-destructive testing (NDT) and NDT specialist at the Council for Scientific and Industrial Research (CSIR), for his assistance during the initial stages of the project and providing valuable background on NDT methods pertaining to these blades.
- Mr. R. Hefti, Mr. A. de Klerk, Mr. P. Seis, and Mr. S. Ramaphoko from MAN Diesel & Turbo South Africa (MDT-ZA) Primeserv, for their assistance in attaining valuable background on the installation of pinned turbine blades, and the non-destructive testing of all the test blades.
- Eskom Research, Testing, and Development (RT&D), and Eskom Power Plant Engineering Institute (EPPEI), for the discarded blades used in this study and the financial support of this research, respectively.
- Ms. B. Mokoka, C-AIM EPPEI programme manager, for her kindness, her diligence, and her willingness to assist and ensure that plans go accordingly regarding any administration pertaining to C-AIM.
- Mr. S. Schmidt, C-AIM Ph.D. student, for his insight into statistics and machine learning, and being a sounding board.

I would also like to extend my appreciations on a more personal note to the following people:

- My loving parents, Dr. Leon and Mrs. Benette Brits, for their unreserved interest, support, and encouragement throughout this journey for my academic and personal goals. Their attempts to understand this work were admirable even though they knew that I would repeat myself, they never gave up. Their willingness to listen allowed me to gather my thoughts and pen them down on paper. I would also like to thank them for always having faith in me, for always having my best interests at heart, and for giving me perspective and advice when I needed it the most. Their emotional support outdid their financial support, but I would like to thank them equally for both, although words cannot express this notion. Thank you for the opportunity to further my education. I never took it for granted. They taught me that hard work pays off, and this inspired me to persevere and not to limit myself to the current state of my abilities but to always strive to improve them. Thank you for setting such a great example.
- My brothers and sister, for putting up with me, challenging me, and believing in me.
- Friends, and academic colleagues, that became friends.

Table of Contents

1	Introduction	1
1.1	Background and Problem Statement	1
1.2	Literature Survey	3
1.2.1	Definition of Damage and Relevant Concepts	3
1.2.2	Pinned Turbine Blades	6
1.2.3	Modal Analysis	9
1.2.4	Structural Damage Identification Strategy	14
1.2.5	Vibration-based Structural Damage Identification	15
1.2.6	Machine Learning-based Damage Detection	21
1.3	Scope of Research	25
1.4	Document Overview	29
2	Design of Experimental Procedure and Finite Element Model	30
2.1	Basic Information on Test Blades	30
2.2	Experimental Modal Analysis - Design and Set-up	31
2.2.1	Experimental Protocol	32
2.2.2	Repeatability of Test	34
2.2.3	Definition of Benchmark Result	37
2.3	Numerical Modal Analysis - Development and Validation	38
2.3.1	FE Model Set-up	38
2.3.2	Modal Analysis and Harmonic Response Analysis	39
2.3.3	FE Model Validation	40
2.3.4	Conclusion	42
3	Feature Sensitivity Study	43
3.1	Sensitivity to Small Geometrical Variability in Healthy Blades	44
3.1.1	3D FEA Modelling of Small Geometrical Variability	46
3.1.2	Comparison of Results: Experiment vs. FEM	46
3.1.3	Conclusions	49
3.2	Sensitivity to Damage in Blades	50
3.2.1	3D FEA Modelling to Identify Most Probable Damage Location in the Blade Root during Turbine Operation	50
3.2.2	Introduction of Damage	53
3.2.3	Results	54
3.3	Damage Trend in Blades	59
3.3.1	Effect of Geometrical Variability on Damage Classes	59
3.3.2	Shift in Frequency due to Damage	61
3.3.3	Numerical Damage Propagation	61
3.3.4	Spatial Relation of Natural Frequencies for Damage Classes	66
3.4	Conclusion	69
4	Damage Detection and Identification	70
4.1	Data Characterization of Healthy and Damaged Cases	71
4.1.1	Healthy Blades	72
4.1.2	Damaged Blades	76
4.2	Classification Procedure	80
4.2.1	Classifier Structure	81
4.2.2	Approach to Address Degree of Over-fitting and Uncertain Regions	82
4.3	Classification Results	83

- 4.3.1 Hypothesis Test I - Geometrical Variability Identification 83
- 4.3.2 Hypothesis Tests II and III - Damage Detection and Identification 86
- 4.3.3 Damage Classification using FEM as Training Data (Low-cost Model) 89
- 4.4 Conclusion 91
- 5 Conclusion and Recommendations 93**
- 5.1 Conclusion 93
- 5.2 Recommendations 95
- References 97**
- A Notes on EMA Design and Set-up A-1**
- A.1 Modal Analysis Equipment Configuration A-1
- A.2 Design and Set-up A-2
- A.3 EMA Protocol/Methodology A-3
- B Geometrical Variability in Test Blades and Class Allocations B-1**
- C Drawings of Damage Scenarios C-1**
- C.1 Damage Class 1: Blade Root Upper Pinhole Radial Notch C-1
- C.2 Damage Class 2: Aerofoil Base Trailing Edge Notch C-2
- C.3 Damage Class 3: Aerofoil Base Leading Edge Notch C-3
- D Experimental Data and Additional Results and Details D-1**

List of Abbreviations

ART	Acoustic resonant testing
CAD	Computer-aided design
EMA	Experimental modal analysis
EPPEI	Eskom Power Plant Engineering Institute
EPRI	Electric Power Research Institute
FE	Finite element
FEA	Finite element analysis
FEM	Finite element modelling
FFT	Fast-Fourier transform
FRF	Frequency response function
IP	Intermediate pressure
HCF	High cycle fatigue
LCF	Low cycle fatigue
LDV	Laser Doppler vibrometry
LP	Low pressure
MDOF	Multi-degree-of-freedom
MDT-ZA	MAN Diesel & Turbo South Africa
MPI	Magnetic-particle inspection
NDT	Non-destructive testing
OEM	Original equipment manufacturer
OvA	One-versus-All
OvO	One-versus-One
RBF	Radial basis function
RBM	Rigid-body-motion
SDOF	Single-degree-of-freedom
SISO	Single-input-single-output
SHM	Structural health monitoring
SML	Supervised machine learning
SV	Support vector
SVDD	Support vector domain description
SVM	Support vector machine

Nomenclature

General

$[C]$	Damping matrix
$[D]$	Dynamic stiffness matrix
$[H]$	Transfer function matrix
$[K]$	Stiffness matrix
$[M]$	Mass matrix
$\{f\}$	Force vector
$\{X\}$	Eigenvector or mode shape
$\{x\}$	Response vectors
A	Amplitude
a	Crack length
a_{max}	Critical crack length
C	Misclassification tolerance parameter
dB	Decibel
E	Elastic modulus
e_{μ}	Total percentage error
e_i	Percentage error
f_n	Natural frequency
i	Imaginary number
k	Stiffness
m	Mass
N	Number of cycles
n	Total number of items
R	Radius
s	Laplace transform of time
T	Temperature
t	Time

Greek Symbols

α	Radial basis kernel width
Δ	Change/shift in particular value
μ	Mean
μ_s	Static friction coefficient
ν	Poisson's ratio
ω_n	Eigenvalue or natural frequency
ρ	Density
σ	Standard deviation
σ_{ts}	Tensile strength
σ_y	Yield strength

Subscripts

0	Reference
μ	Average
abs	Absolute value
i	Specific item
max	Maximum value

Chapter 1: Introduction

1.1 Background and Problem Statement

Steam turbines need to be highly reliable with high mean times between failures since the cost and downtime that are consequences of failures can be considerable. Turbine blades are exposed to various damage mechanisms such as stress corrosion cracking, cyclic fatigue, and creep. During operation of the blades, damage accumulates and results in crack initiation and propagation. Failures can be catastrophic and may result in significant unavailability of the turbine. They also hold severe implications for personnel and plant safety. To ensure safe operation, reliability, and high availability of the turbine in a capacity-constrained environment, excellent oversight of these deteriorating components is required. To optimize the maintenance schedule and provide operational flexibility, a failure prevention policy is therefore employed, which requires periodic in-situ inspection of these components using qualified non-destructive testing (NDT) techniques for detection and monitoring of damage evolution. The damage in the component is monitored until the end of the component life or until refurbishment or replacement. Where an active damage mechanism has been identified, a specifically developed strategy based on in-situ inspections is normally used. Where no known active damage mechanism has been identified, damage monitoring is done proactively. Therefore, as the blades' condition deteriorates, the influence of the damage mechanism on blade dynamic response and life must be assessed (Dewey and Lam, 2008; Scheepers and Booyesen, 2012; Hattingh et al., 2016).

Damage identification methods, which include NDT, can be either local or global, depending on the method's ability to cover the volume of the component, relative to the overall dimensions of the structure (Bray and Stanley, 1997; Mix, 2005; Ooijevaar, 2014). With local methods, the focus is directed to a part of the structure and since it is generally the more sensitive method, small damage can be detected. However, the location of the damage must be known. With global methods, a relatively large volume can be analysed at once, albeit with limited sensitivity and only relatively severe damage cases can usually be identified. This method employs indirect measurements to assess structural state (Barthorpe, 2011). For effective testing, it is required that the scanning surface of the component must be visible or accessible, depending on the NDT method applied (Mix, 2005). NDT can also be used as a health-monitoring tool, and thus NDT can be used to characterize the damage as well as determine the damage severity (Worden and Dulieu-Barton, 2004).

With in-situ- or off-site inspection, the structure is taken off-line so that inspection of the structure or its individual components can be conducted, respectively. Off-site inspection can be costly if the blades are installed in the turbine disk, i.e. the blade root attachments are secured to the disk head since the assembly process of removing and reinstalling these blades is critical and labour-intensive, increasing the turbine downtime and overall costs. With in-situ or in-service inspection, the turbine assembly can obstruct the area of damage, further limiting the accessibility and reliability of local techniques. This is more likely to happen in cases where the blades are installed and the roots are not accessible with equipment, e.g. probes, due to limited scanning area on the blade root platform. Additionally, the geometric features of the turbine blade, i.e. complex blade root and twisting and tapering of the blade aerofoil contribute to this. Under such circumstances, global techniques might become sensible for damage localization. This suggests the development and application of global damage identification techniques to overcome these problems since it has the ability to access the obstructed area in some manner through the global dynamic characteristics (Bray and Stanley, 1997; Fan and Qiao, 2011; Kong et al., 2017). For example, in-situ inspection of a turbine blade aerofoil is simple compared to the in-situ inspection of its blade root. This is due to better accessibility and visibility, for when the blade root is attached to the turbine disk, the desired scanning surface/area is obstructed (Charlesworth, 2011). In-situ inspection may also hold the potential to increasing inspection intervals and thus turbine availability.

Structural damage identification is often regarded in a hierarchy of four levels. Level 1 is the qualitative damage detection (presence of damage) in a structure and does not require prior knowledge of system

behaviour from damage. Level 2–4 entails damage diagnosis in which the probable structural damage location is determined, the extent of structural damage is quantified, and the remaining useful life of the structure is estimated. It is implied that each level requires that details on all lower levels are available (Ngwangwa et al., 2006; Fan and Qiao, 2011). Farrar and Doebling (1997) express the necessity for research on structural damage identification to be more dedicated to specific applications in industries that would benefit from this knowledge, i.e. health monitoring of long design life structures to quantify and extend the life of these structures through specially developed techniques. They also insist that this research should emphasise the testing of real structures in their operating environment above laboratory tests of representative structures. This, however, would require more collaboration between academia, industry, and government organizations due to the magnitude of such projects.

Physical objects vibrate at a distinct set of natural frequencies and thus have a unique signature defined by their system dynamics. Changes in the measured response or system dynamics due to damage can be observed in vibration analysis. Various structural damage identification techniques, based on global vibration response monitoring or vibration analysis, have been developed to diagnose the health of structures. These techniques, which mainly identify damage at Levels 1 and 2, monitor variation of modal properties such as the natural frequencies, damping loss factors, and mode shapes. When a structural model is used, Level 3 may be attained (Ngwangwa et al., 2006; Fan and Qiao, 2011). Worden and Dulieu-Barton (2004) extended the hierarchical strategy by introducing Level 2.5, which is the classification or description of the structural damage. Machine learning is employed, and class labels are assigned to a sample of measured data (in this study, natural frequencies) from a finite set. The specific damage properties or behaviour of each class is encoded to a model to categorize new data accordingly. This enables effective identification at Level 3 and 4 since understanding the physics of damage, i.e. characterisation, is a prerequisite for these levels.

In solving the problem of structural damage identification using natural frequency-based methods, two formulations to acquire structural modal parameters are available. The forward problem is used to determine the change in natural frequency of a given structure based on damage properties (Ngwangwa et al., 2006). This serves as a theoretical foundation for natural frequency-based methods and employs the information from Levels 1–3. The inverse problem is used to determine damage properties of a given structure based on natural frequency measurements (Fan and Qiao, 2011). The inverse approach uses the product of the forward problem to obtain the information for Levels 1–3. Hence, in developing the technique as a diagnostic procedure, investigation of the forward problem precedes that of the inverse problem. This is for the reason that before the possibility of applying the technique on a structure, its natural frequencies due to specific damage must first be known to allow detection and identification of that damage by natural frequencies. Level 2.5 is trained on the product of the forward problem to calculate the product of the inverse problem.

During the installation of blades to the turbine disk, modal analysis with hammer impact excitation and accelerometers are usually employed in which success is confirmed by ensuring that the first five natural frequencies of the blade fall within a desired range. This requires only prior specialist instruction to teach the procedure and interpretation of its results. During scheduled maintenance, the bladed disks are removed from the turbine to a controlled environment, with constant conditions, for off-line NDT inspection (i.e. generally by ultrasonic testing). Since modal analysis is already a part of the installation procedure, and hence the skills and equipment are available, it is proposed in this study that modal analysis is also applied during the scheduled maintenance as part of an off-line in-situ damage identification method. This will only be promoted if found feasible, which this dissertation starts to prove.

To ensure minimal external influence from additional mass added by accelerometer(s) on the blade dynamics and to allow more freedom on the measuring locations, a scanning laser vibrometer is used. This also removes any difficulties regarding multiple accelerometers and cabling, if not wireless. To acquire the natural frequencies of a structure, only a single measurement point is required. However, in context of the real-world problem, the predefined single measurement point for each blade can be tracked with the software from a central position. Thus, the set-up will be more convenient and probably be less labour-intensive. The

predefined points for measurement and excitation, established from thorough research, can be labelled prior to testing along with the software configuration. Hence, it will be simple to perform and to interpret the results since it very closely resembles the installation procedure. It is also financially more sensible to use the existing practical technique as specialist training and additional equipment would not be required, except for the laser vibrometer.

In this work, the introduction to a global vibration-based structural damage identification technique, usable in support of conventional NDT to detect cracks in blades during off-line in-situ inspection of stationary blades, is presented. This methodology could increase the capability and reliability of crack detection in turbine blades, especially in their roots. If this approach is successful, it could be further developed for implementation in prevention of in-service failures with consequential damage and extended outage durations. This type of analysis may also allow improvement of the maintenance schedule and inspection intervals with the purpose of deciding whether immediate repair or replacement of the blades is necessary as well as to schedule repair work and set inspection intervals if the rotor blades can still continue in operation (Hattingh et al., 2016). However, the feasibility of the proposed method must first be assessed to establish the potential for further development. Therefore, a simplified problem of a freely supported removed blade is presented above the real practical problem in which the off-site conditions of the real-world problem, i.e. a controlled environment with constant conditions, are considered.

1.2 Literature Survey

The definition of damage is established for this study. Next, a brief review on fatigue cracks in turbomachinery is presented, which includes the most probable damage mechanisms and locations. Pinned turbine blades are then introduced with focus on their installation and on cracks observed at pinholes. This is followed by a brief overview of modal analysis. This includes frequency response functions, motivation for using non-contact measurements methods, impact vibration testing, and model validation. The structural damage identification problem is presented in which the use of response-based methods is promoted. Then, vibration analysis as a damage identification method is discussed, with emphasis on natural frequency-based methods. This includes the effect of damage on the dynamic behaviour and stiffness of a structure. Finally, an overview of the principles of machine learning applied to damage identification, specifically supervised machine learning with support vector machines, is provided. This includes the basics of dimensional reduction, feature extraction and -selection. The proposed method in this study comprises support vector machines using natural frequency-based vibration analysis for damage classification.

1.2.1 Definition of Damage and Relevant Concepts

From a perspective of structural integrity, the definition of damage is very broad. Damage is traditionally defined as changes in either or both the material or geometric properties of the structure (Dewey and Lam, 2008). This includes failure of structural materials (e.g. cracking, buckling, breaking, or delamination); loosening of assembled parts (e.g. loose bolts, rivets, or glued joints); loss of any assembled part; and flaws, voids, cracks, thin spots, etc., caused during manufacturing and operation (Wang et al., 1997). Hence, it is essential that an explicit definition of damage is established to ensure that any confusion regarding what 'damage' is to be detected and identified by a specific method, can be removed. The following ranked terminologies are used in this study as defined by Worden and Dulieu-Barton (2004) and Dewey and Lam (2008):

- A defect is defined as inherent in the material and statistically an unknown quantity exists in all materials. This does not hinder the structure's operational capacity as it operates at design conditions. Thus, it also includes any uncertainty in the material or introduced in the component that does not affect the functionality. This does not refer to change in the geometry brought on by alleviating or removing stress concentrations, which also affects the structural integrity, as this will enhance the remaining useful life of the blade (Dowling, 2012). Thus, any geometrical variability falls within this category.

- Damage does not hinder the structure's operational capacity; however, it is no longer operating in its ideal condition and may affect the performance slightly. For example, during the operational extent of a turbine, it experiences various mechanisms (wear, degradation, or fatigue) which grow to a physical consequence or damage. A fault hinders the structure's operational capacity since it can no longer operate sufficiently or safely. In this study, damage and fault will be integrated into the former single term and are considered as minor and critical or worst-case stages of damage.
- With failure, the structural integrity of the healthy structure is severely compromised by a progressive damage mechanism and it can and should no longer operate at all. This causes serious concern in terms of availability and safety of the structure. It is crucial that corrective action is mediated to prevent the incident from repeating.

These terms are derived from describing the quality of a system as its ability to meet user requirements. Thus, critical damage is an undesirable decrease in quality due to a change in the system to some degree. Hence, it can be concluded that failures arise from damage, which arose from some defects caused by various mechanisms that accumulated over time. The structure still functions satisfactorily in the damage level; however, the failure level is in total contrast to this. Thus, it is essential that a rigid interpretation for this margin be established to allow its detection. Therefore, the worst-case damage or damage on the edge of this margin must be detected and identified since it will lead to failure if uncorrected. This will contribute to the remedial decision process to ensure safe operation and restore operational capacity. In this dissertation, defects will always refer to geometrical variability, whereas damage will always refer to the worst-case scenario.

1.2.1.1 Fatigue Cracks

Fatigue cracks are characterized by three phases (Anderson, 2005; Totten, 2008; Plesiutchnig et al., 2016): crack initiation, in which cyclic loading leads to a small crack forming at a stress concentration; stable crack propagation, in which incremental crack growth occurs per cycle; and structural failure or final fracture, in which rapid crack growth occurs after reaching a critical size. The total number of cycles to failure are the combined number of cycles required for initiation and propagation, respectively (Lackner, 2005; Dowling, 2012).

The mechanism of crack initiation is slip accumulation during cyclic loading, in which plastic deformation leads into eventual strain localization and ultimately into crack initiation (Dowling, 2012; Sangid, 2013). When the number of cycles accumulates, the number of defects increases with the rise in dislocations in the micro-structure of the material. With the increase of the density of dislocations, the total system energy is minimized through the formation of unique structures. Forward and reverse loading occurs per cycle, creating irreversible slip lines from slip moving in distinct paths. This leads to localized strain in the material, which is a sign of crack initiation, and takes the form of slip bands inside the material crystals. A small crack can be the result of an increase of the slip band width due to more crystals showing signs of slip bands from cycle build-up (Sangid, 2013). As soon as a crack initiated in the material, any escalation in size or length of that crack is considered as propagation (Anderson, 2005; Totten, 2008). The rate and progression of cracks are primarily controlled by the material structure at the crack and the localized stresses (Budynas and Nisbett, 2011; Dowling, 2012). With the final fracture stage, crack growth is primarily controlled by the material's fracture toughness, which is related to rapid crack growth acceleration and will cause abrupt failure in tension overload (Budynas and Nisbett, 2011; Dowling, 2012). Thus, the highest stress region will result in the highest stress-intensity factor, which will lead to crack initiation with an accelerated growth rate when compared to the other regions. A larger initial crack size also contributes to this (Anderson, 2005; Dowling, 2012).

1.2.1.2 Fatigue Cracks in Turbomachinery Blades

The blades and attachment grooves in a steam turbine are some of the most-highly stressed components in a turbine (Rauschenbach et al., 2010; Scheepers and Booyesen, 2012). This is due to the high turbine

speed and the dead weight of the blades, resulting in exposure to massive centrifugal forces and stresses in the blades during operation, causing both high and low cycle fatigue (Dewey and Lam, 2008). These high stresses cause fatigue crack propagation.

High cycle fatigue (HCF) is the fatigue of rotating components, brought on mainly by centrifugal and dynamic forces. This leads to high mean stress levels caused by vibration and resonance of blades at critical speeds during transient loading conditions, that can occur anywhere along the length of the blade and accumulates over time (Witek, 2009; Bhagi et al., 2013; Booyesen et al., 2015). HCF is also caused by passing of blades by non-uniform stream of air produced by a blade cascade (Witek, 2009). Low cycle fatigue (LCF) is primarily a consequence of start-stop cycling and centrifugal force, resulting in centrifugal stresses with a steady magnitude and stress distribution during full speed, with the maximum steady-state stresses occurring at stress concentrations, i.e. in the root attachments and transition of the base to the aerofoil (Dewey and Lam, 2008). Crack initiation is more likely to occur with LCF, which is associated with significant amounts of plastic deformation, whereas HCF is associated with relatively small elastic deformations (Dowling, 2012). HCF damage is identified as a main source of LP turbine blade failures (Witek, 2009; Mazur et al., 2009; Bhagi et al., 2013; Booyesen et al., 2015). Booyesen et al. (2015) state that these dynamic stresses are influenced by the source and magnitude of the excitation, and the damping in the blade. In the case of a free-standing turbine blade, the damping is naturally low, thus resulting in high dynamic stresses at resonance conditions.

Shlyannikov et al. (2014) and Citarella et al. (2015) considered a steam turbine blade and found through finite element analysis (FEA) that the bending stresses represent only 0.15% of the stress caused by the inertia loading, concluding that the bending moment induced by steam pressure can be ignored. This is supported by Poursaeidi and Salavatian (2009), who calculated that during steady-state condition the centrifugal stress acting on a generator fan blade is much greater than the bending stress, using FEA.

Bhagi et al. (2013) conducted a brief review on common failures of turbine blades, including the failure mechanisms and locations. They found that high stress areas are more likely to occur near the blade root (i.e. the root and aerofoil base), leading-, and trailing edges. Additionally, areas near the root platform (aerofoil base) experience the highest centrifugal forces, producing a steady-state stress level that contributes to fatigue crack propagation. The blade root attachments experience the highest steady state stresses due to geometric stress concentrations. Stress concentrations have significantly higher localized stress than the mean stress outside the vicinity of the sharp edge. This can cause cracking in the sharp section changes of the root (Lackner, 2005; Dowling, 2012; Booyesen et al., 2015). The dominant and severe crack locations are usually found at the root (Lackner, 2005; Mazur et al., 2009). Fatigue cracks are transgranular with no branching with relatively smooth fracture surfaces (Anderson, 2005; Mazur et al., 2009; Scheepers and Booyesen, 2012). Blade crack locations, specific to these areas, reported by various authors in previous investigations are illustrated in Figure 1.1, and summarized in Table 1.1.

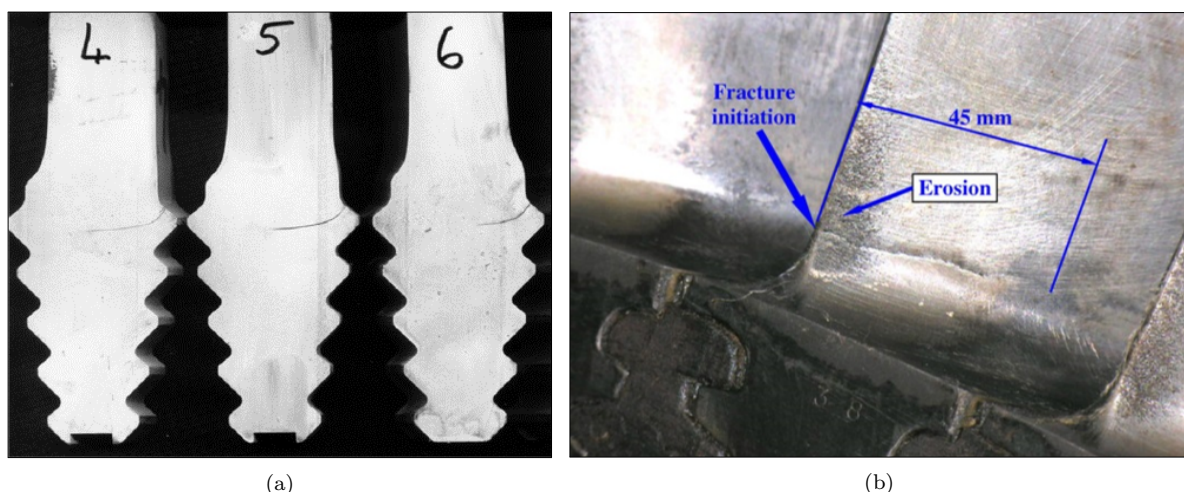


Figure 1.1: Turbine blade crack locations near or at the root from previous investigations, a) Blade root (Booyesen et al., 2015); b) Aerofoil base (Mazur et al., 2009)

Table 1.1: Brief summary of turbine blade crack locations in or near the root as reported by various authors

Crack Location	Blade Type	Author
Blade root (overall)	LP steam turbine blade	Plesiutchnig et al. (2016) Booyesen et al. (2015) Nurbanasari and Abdurrachim (2014) Bhagi et al. (2013) Vaishaly and Ramarao (2013) Oberholster (2010) Kubiak Sz et al. (2009) Dewey and Lam (2008) Rauschenbach et al. (2008) Xu et al. (2007) Clossen et al. (2006)
	IP steam turbine blade Gas turbine blade	Charlesworth (2011) Bhagi et al. (2013)
Aerofoil base (trailing edge)	LP steam turbine blade	Plesiutchnig et al. (2016) Shukla and Harsha (2015) Kim (2011) Mazur et al. (2009) Dewey and Lam (2008)
	Aircraft gas turbine blade Gas engine compressor blade	Bhagi et al. (2013) Lackner (2005)
Aerofoil base (leading edge)	LP steam turbine blade	Citarella et al. (2015) Shlyannikov et al. (2014) Mazur et al. (2009) Dewey and Lam (2008) Kubiak Sz et al. (2004)
	Compressor blade	Poursaeidi and Bakhtiari (2014) Witek (2011) Lackner (2005)

To ensure that resonance and resultant fatigue cracking does not occur at running speed, the vibration response of turbine blades are often controlled through lacing wires, arc bands, integral shrouds or friction damping pins (Bhat et al., 1996; Drozdowski et al., 2015); unless it is not necessary, in which the blades are referred to as free-standing. Various root attachment designs, used to attach blades to rotors and rotor discs, are commonly used depending on which design the original equipment manufacturer (OEM) favours. This is shown in Figure 1.2 and includes axial entry fir tree-, pinned fork-, inverted T-, and straddle root (Dewey and Lam, 2008; Scheepers and Booyesen, 2012). Free-standing pinned fork or pinned turbine blades are considered in this study.

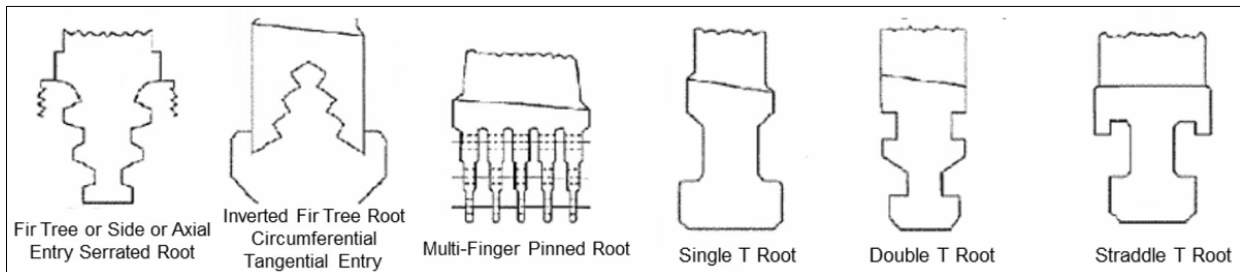


Figure 1.2: Some examples of root attachment designs commonly used by OEMs (Rowbotham et al., 2015)

1.2.2 Pinned Turbine Blades

The radial entry pinned root is a common attachment configuration for different sizes of steam turbine rotor blades, such as smaller stages of IP turbines to the largest stages on LP turbines (Rauschenbach et al., 2010). The key feature of this connection is a series of circumferential slots machined into the disk head, with corresponding fingers machined into the blade root. This is shown in Figure 1.3a, in which the blade fingers

are inserted into the disk head slots and then secured into place with tapered axial pins. During installation or assembly, the individual pinned roots are properly aligned with the disk head to allow individual reaming of holes for pin insertion as shown in Figure 1.3b, courtesy of MAN Diesel & Turbo South Africa (MDT-ZA). A close fit or press-fit between the pin and the disk minimizes the bending stress and ensures equally distributed centrifugal and steam bending loads between multiple pins. In addition, the multiple fingers guard against catastrophic root failure prior to crack discovery in the attachments (Dewey and Lam, 2008). The assembly process is therefore critical to successful pinned root designs (Singh and Lucas, 2011). The pins are either hot or cold riveted through holes in both the disk and blade fingers (Charlesworth, 2011). During operation, a blade can experience resonance at other higher natural frequencies. These resonant oscillations are avoided through tuning the structural frequencies away from the excitation frequencies by changing the blade geometry at specified areas through correctional grinding (material removal). This aims to adjust the desired frequency of the desired blade with minimal effect on the others and with minimal impact on the blade aerodynamic performance (Duong et al., 2013).

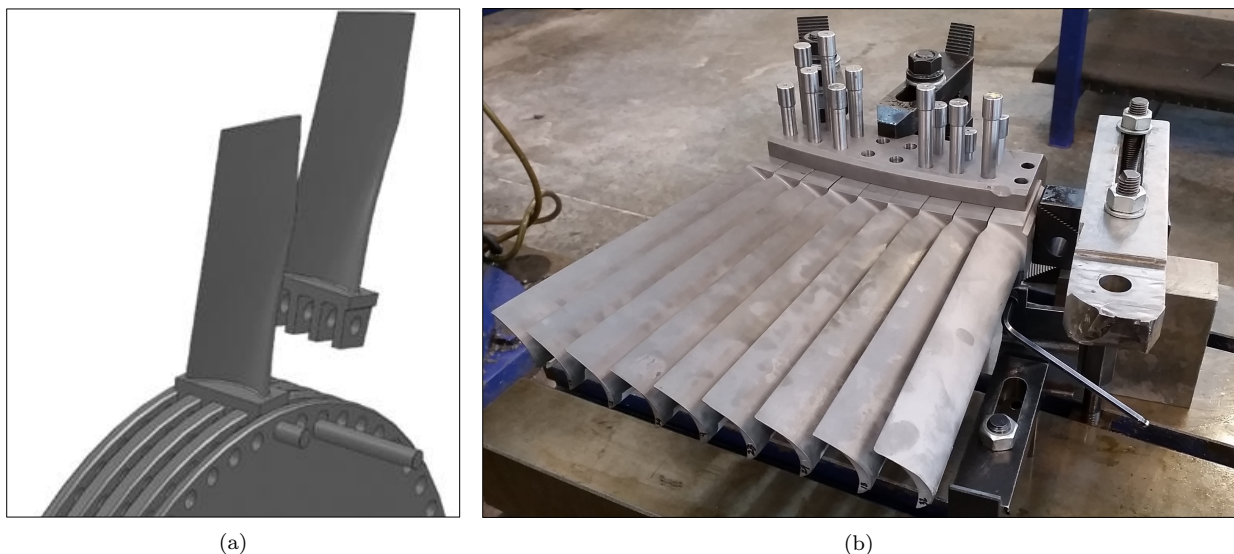


Figure 1.3: a) CAD model of pinned root turbine blade installation (Singh and Lucas, 2011), b) Installation procedure of discarded stage 2 pinned turbine blades in a disk section (courtesy of MDT-ZA)

The removal of blades from the disk presents an associated risk of damage to the disk pinholes, which may then require repair since the pins must be forcibly removed, and pinhole reaming is required for blade reinstallation. This enlarges the pinhole diameter and can only be done a limited number of times before the pinhole size limit is reached on both the blade and the disk, which will then result in an improper fit. This is reasoned by Hattingh et al. (2016) who presented a case study pertaining to the damage assessment and refurbishment of steam turbine blade/rotor attachment holes. This was verified by industry (including MDT-ZA). Additionally, the pins yield or are distorted due to the stresses produced from larger finger root blades. This adds to the difficulty and cost in removing these blades for inspection (Dewey and Lam, 2008).

During turbine operation, the area around the pinholes experience very high stresses, resulting in cracks arising at various orientations at the upper pinhole due to compression and tension stress from the axial pins (Clossen et al., 2006; Rauschenbach et al., 2008). Figure 1.4 shows the crack orientations in the anticipated defect area along with examples of pinhole cracks. This is explored in a later section of the study. Dewey and Lam (2008) and Hattingh et al. (2016) found that for a pinned stage 1 LP turbine blade disk, the critical location is at the 2–3 o'clock and 9–10 o'clock positions on the bottom pinhole on the central prong. This implies, from reaction forces, that for the blade this is found at the upper pinhole at these locations. Xu et al. (2007) confirmed this in their failure analysis of a stage 1 LP pinned turbine blade. The crack initiation and propagation in the blade finger were caused by HCF and a surface defect due to rough machining. This is shown in Figure 1.5.

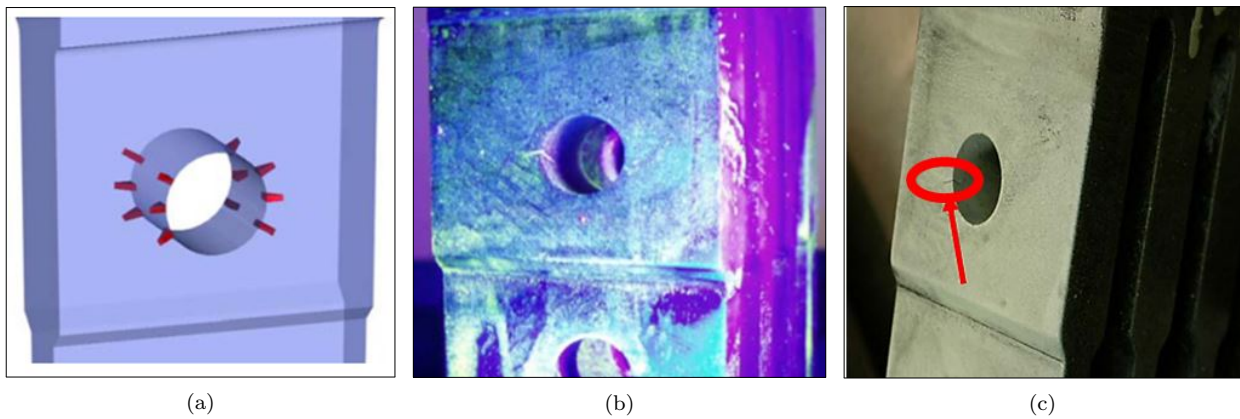


Figure 1.4: a) Anticipated defect area in a radial-entry pinned turbine blade root (Rauschenbach et al., 2008); Examples of root pinhole cracks in a last-stage LP turbine rotor blade, b) (Rauschenbach et al., 2008) and c) (Clossen et al., 2006)

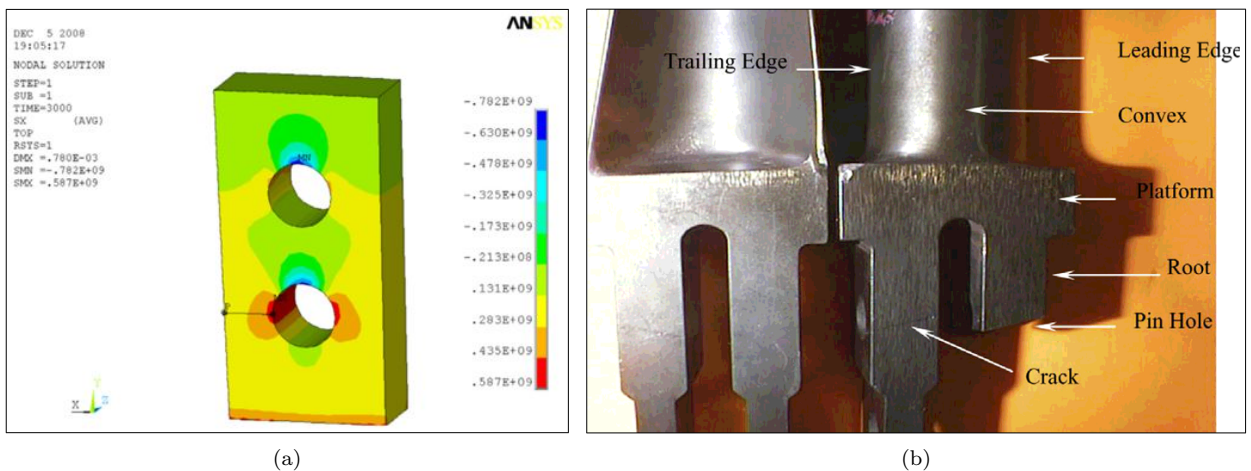


Figure 1.5: a) Radial stress distribution for the centre prong of a stage 1 LP steam turbine disk showing peak stress at the bottom pinhole (Hattingh et al., 2016); b) Stage 1 LP steam turbine blade geometry and failure location reported by Xu et al. (2007)

Charlesworth (2011) noted that, considering a stage 2 intermediate pressure (IP) turbine blade, common issues present with pinned blade turbine rotor designs include radial cracking from the pinholes in the blade fingers and in the disk head rims (Hattingh et al., 2016). Figure 1.6 shows an IP blade with a fully cracked or detached finger that was removed from a customer rotor. This blade root was no longer able to withstand the forces in full load operation and could have led to catastrophic failure of the rotor if it failed prematurely to inspection. The challenge for in-situ inspection of pinned blade roots is the volumetric inspection to find the crack initiation sites, with severely limited access from blade root platforms (Charlesworth, 2011).

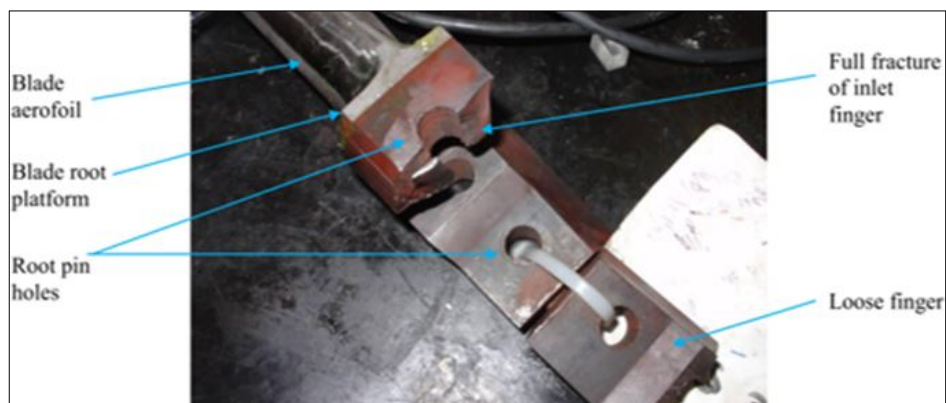


Figure 1.6: Pinned root cracking and failure to stage 2 IP turbine blade reported by Charlesworth (2011)

1.2.3 Modal Analysis

Classical modal analysis determines the dynamic characteristics of a structure, which include natural frequencies, damping values, and patterns of structural deformation or mode shapes. This procedure is illustrated in Figure 1.7 and consists of an acquisition phase and an analysis phase. With the first phase, experiments are performed on a test object by exciting the structure with a known source, e.g. an impact hammer or electrodynamic shaker, causing it to vibrate. Responses to the input force are then measured in the X-, Y-, and Z-directions with sensors, i.e. load cells, accelerometers or optical devices. The measured response is usually in the form of a transfer function or a frequency response function (FRF). The transfer function is the complex Laplace domain relationship of the response output of a structure to the input force applied on that structure, and the FRF may be viewed as the transfer function evaluated along the imaginary axis (Mix, 2005; Heyns, 2008; Song et al., 2014). Thus, the FRF is related to the transfer function through the Fourier transform. With the final phase, the modal parameters are extracted from the object's measured FRFs and considered for processing, depending on the analysis objective. These FRFs are often curve-fitted to estimate the modal parameters (Heyns, 2008; Song et al., 2014).

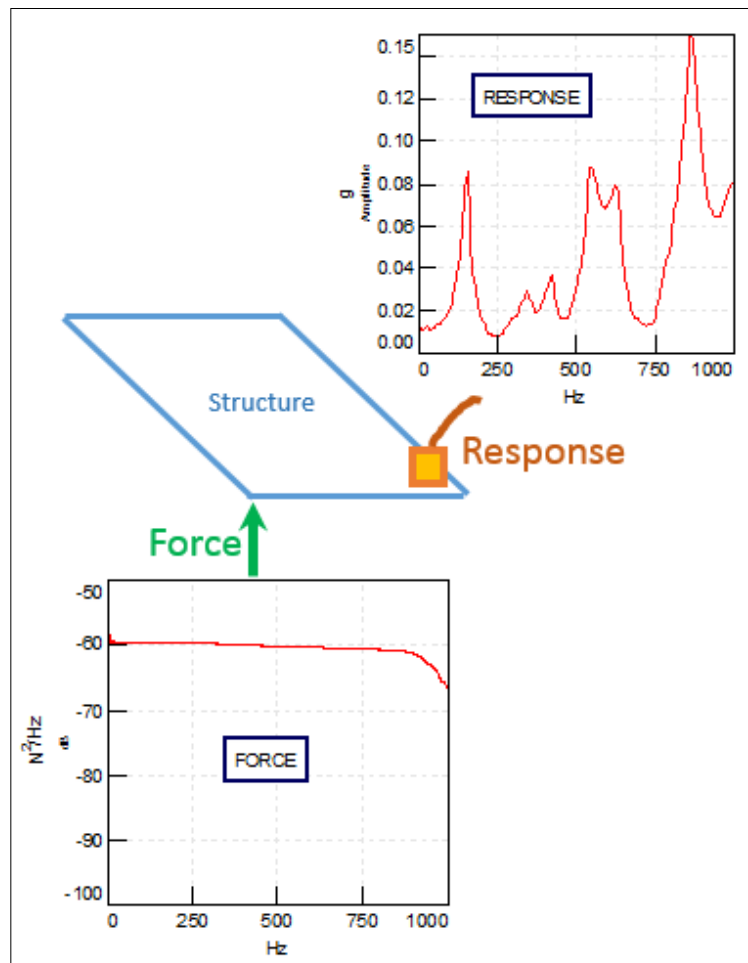


Figure 1.7: The acquisition phase of the modal analysis procedure (Siemens, 2016a)

With theoretical modal analysis, the workings behind the scenes within the signal processing software as well as the FEA software when performing modal analysis can be explained. The dynamic behaviour of some simpler systems can adequately be described by single-degree-of-freedom (SDOF) models; however, most systems are more complex and generally require multiple-degree-of-freedom (MDOF) models to describe their dynamics effectively (Heyns, 2008; Inman, 2014). The dynamics of a discrete MDOF mechanical system can be used to solve blade vibrations (Xu et al., 2007; Shukla and Harsha, 2016), and can be expressed as a linear and time invariant second-order differential equation (Ngwangwa et al., 2006; Heyns, 2008; Inman, 2014):

$$[M]\{\ddot{x}\}(t) + [C]\{\dot{x}\}(t) + [K]\{x\}(t) = \{f\}(t). \quad (1.1)$$

With:

$[M]$ = Mass matrix $[N \times N]$

$[C]$ = Damping matrix $[N \times N]$

$[K]$ = Stiffness matrix $[N \times N]$

$\{f\}(t)$ = Force vector $[N \times 1]$

$\{x\}(t)$ = Response vectors $[N \times 1]$

In the case of harmonic oscillations in which no external force is applied ($\{f\}(t) = \{0\}$), the structure may be assumed to vibrate in free harmonic form, in which $\{x\}(t) = \{X\}e^{i\omega t}$. To solve the dynamic characteristic, modal analysis should be carried out for the structure. Without regard to the influence of environment load and damping, the non-damping ($[C] = [0]$) free vibration equation of the numerical model can be written as (Heyns, 2008; Inman, 2014; Shukla and Harsha, 2016):

$$\begin{aligned} [M]\{\ddot{x}\}(t) + [K]\{x\}(t) &= \{0\}, \\ -\omega^2[M]\{X\}e^{i\omega t} + [K]\{X\}e^{i\omega t} &= \{0\}. \end{aligned} \quad (1.2)$$

Solving Equation 1.2 yields the eigenvalue equation:

$$([K] - \omega^2[M])\{X\} = \{0\}, \quad (1.3)$$

in which ω [rad/s] is the eigenvalue or the natural frequency, and $\{X\}$ is the corresponding eigenvector and mode shape of the structure. By solving the eigenvalue problem, the natural frequencies and mode shapes of the object with light damping or no damping can be obtained (Heyns, 2008; Inman, 2014; Shukla and Harsha, 2016). In the case of an externally applied force, forced vibration of the structure may be assumed and the same procedure for solving Equation 1.2 applies (Inman, 2014).

If a differential equation of motion is transformed using the Laplace transform, the link between the excitation and response reduces to a simple algebraic expression. This is a very powerful approach and may be used for a variety of excitation conditions. By transforming Equation 1.2 to the Laplace domain and assuming zero initial conditions, it yields (Heyns, 2008):

$$[D(s)]\{X(s)\} = [M]s^2 + [C]s + [K]\{X(s)\} = \{F(s)\}, \quad (1.4)$$

with $[D(s)]$ as the dynamic stiffness matrix. By defining the transfer function matrix $[H(s)] = [D(s)]^{-1}$, Equation 1.4 becomes

$$\{X(s)\} = [H(s)]\{F(s)\} \rightarrow [H(s)] = \frac{\{X(s)\}}{\{F(s)\}}, \quad (1.5)$$

which relates the Laplace transform of the system forcing functions $\{F(s)\}$ to the system response $\{X(s)\}$ through the matrix $\{H(s)\}$. The Fourier transform relates the transfer function matrix and the complex FRF by substituting $s = i\omega$ into the Laplace transform given in Equation 1.5, yielding (Heyns, 2008):

$$[H(i\omega)] = \frac{\{X(i\omega)\}}{\{F(i\omega)\}} = [D(i\omega)]^{-1} = [K] - \omega^2[M] + i\omega[C]^{-1}, \quad (1.6)$$

which provides a measure of the steady state response of a system to a unit harmonic excitation force.

Experimental results may be utilised to improve numerical models such as finite element models through model updating, which allows detailed and accurate mathematical models of structures to be built from the measured test data. This technique is an extension of FRF measurements (Heyns, 2008; Avitabile, 2014; Inman, 2014).

1.2.3.1 Frequency Response Function

An FRF expresses the frequency domain relationship between an input force and output response of a linear, time-invariant system at specified input- and response points. Thus, the FRF relates the system forcing function (input) to the system response (output) (Mix, 2005; Heyns, 2008; Siemens, 2016a). Three

common interrelated formulations of the FRF are available. The form of the FRF depends on the response parameter used and is subjected to the analysis objective, i.e. displacement, velocity or acceleration is used to generate receptance, mobility or accelerance, respectively. These ranked parameters are derivatives of each other with respect to time, whereas the ranked FRF forms are derivatives of each other with respect to frequency (Heyns, 2008).

Three important parameters with any FRF are the magnitude, the phase, and the coherence. FRFs are very useful for the rapid identification of natural frequencies of structures from either the magnitude or the phase (Heyns, 2008; Avitabile, 2014; Siemens, 2016a). With modal analysis, the measured time data is transformed to the frequency domain through a Fast Fourier transform (FFT) algorithm. This transformation leads to functions with complex valued numbers that can be geometrically represented on the complex plane. The complex plane is a modified Cartesian plane with a real axis (*x*-axis) and a perpendicular imaginary axis (*y*-axis). Hence, the functions can be described by real (*Real*) and imaginary (*Imag*) components or by magnitude and phase components (Heyns, 2008; Avitabile, 2014; Siemens, 2016a):

$$Magnitude = \sqrt{Imag^2 + Real^2}, \quad (1.7)$$

$$Phase = \tan^{-1}(Imag/Real). \quad (1.8)$$

Figure 1.8, showing a typical FRF of a structure, demonstrates the rapid identification of natural frequencies of structures from either the magnitude or the phase. It can be seen that magnitude (Amplitude) has peaks corresponding to natural frequencies of the test object as the FRF is 'normalized' to the input, and that Phase has an abrupt shift at natural frequency as the main component of the motion stimulation has changed. The width of the peaks about their maximum is proportional to the damping of the structure and can be estimated by using the half-power method at the *3dB* down point. It is important, however, to note that good coherence is essential for the identification of natural frequencies (Heyns, 2008; Avitabile, 2014; Inman, 2014).

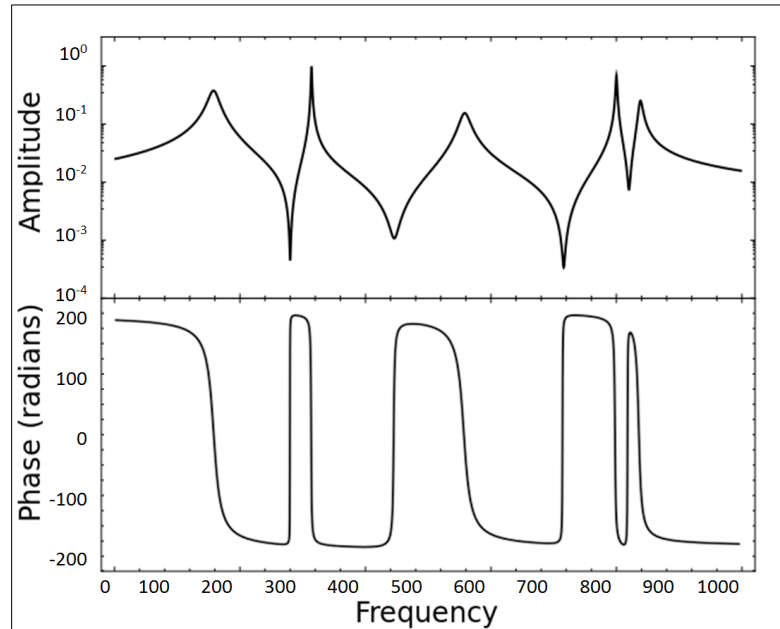


Figure 1.8: A typical frequency response function (FRF) and phase plot, Top – Amplitude (magnitude) has peaks corresponding to natural frequencies of test object; Bottom – Phase has an abrupt shift at natural frequency

The coherence function is a measure of linearity and noise, which identifies how much of the output signal is related to the measured input signal. This characterises the relationship between the measured system input and output signals at each frequency. Thus, the coherence function quantifies the quality of the FRF measurement at each frequency and therefore evaluates the consistency or repeatability of an FRF measurement (Smith, 2005; Heyns, 2008; Avitabile, 2014; Siemens, 2016a). Figure 1.9 demonstrates the coherence function of which the value ranges from 0–1. The higher the values at a particular frequency, the

more repeatable the measurement to measurement. For instance, when the amplitude of the FRF is very high, e.g. at a natural frequency, this value will be close to 1. However, the opposite is true for a very low amplitude at a natural frequency or across the entire frequency range, this indicates a possible error with the measurement. Note that this applies for the reverse case as well. For instance, when the amplitude of the FRF is very low, e.g. at an anti-resonance, this value will be close to 0. The coherence is expected to drop here as there is no response to measure since the structure is non-resonant. Thus, the repeatability is made inconsistent by the instrumentation noise floor due to too low measurement values. This, however, is normal and thus acceptable (Smith, 2005; Heyns, 2008; Avitabile, 2014; Inman, 2014; Siemens, 2016a).

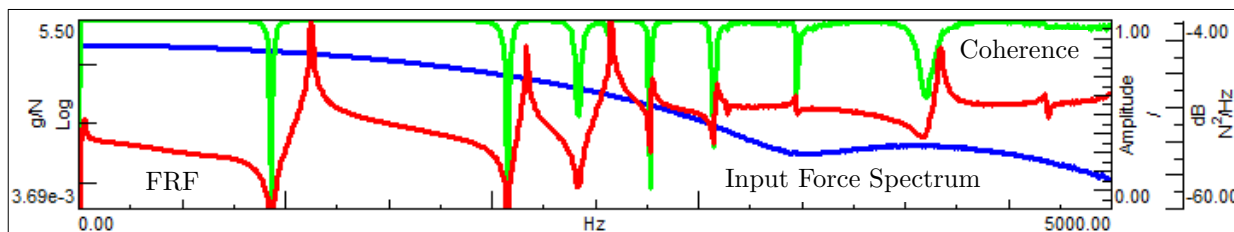


Figure 1.9: Optimal coherence from good impact for a high quality frequency response function (FRF) measurement, Blue - Input force spectrum; Green - Coherence; Red - FRF (Siemens, 2016b)

Hence, assuming that the output signal is without error and thus controlled, good or sufficient impact will ensure good coherence and thus a good FRF measurement. To excite all the modes of interest, an adequate input excitation frequency range must be selected. This is shown by the desired input excitation forcing function in Figure 1.9, which has an evenly distributed amplitude and reasonable roll-off over the frequency range of interest. This renders the optimal coherence function. Depending on the objective of the tests and application of the results, the quality of the coherence function, and thus the FRF quality, may differ (Smith, 2005; Heyns, 2008; Avitabile, 2014; Siemens, 2016a).

1.2.3.2 Non-contact Measurement Methods

In practice, the structure's natural modal shapes are used to visualize its movement at its respective natural frequencies. These mode shapes are collectively formed through curve-fitting from FRF measurements acquired through a series of sensors (e.g. force transducers and accelerometers) applied or mounted at different geometrical locations (Mix, 2005; Heyns, 2008). Mounting several sensors requires only one measurement when using a shaker. However, a single sensor (measurement point) is sufficient for many practical applications but requires the use of an impact hammer and several input excitation points to successfully capture the respective mode shapes at these frequencies (Gillich and Praisach, 2015). Both these approaches are labour-intensive and the structural and vibrational properties are affected. Using contact measurement techniques have three common shortcomings (Heyns, 2008; Song et al., 2014):

- Attaching sensors can add to the mass of the structure, altering its modal properties.
- The size of the accelerometer limits the number of sensors deployable, which can reduce the accuracy of the damage localisation by spatial resolution impediment of the acquired modal shapes.
- Cabling throughout the structure is necessary if the accelerometers are not wireless.

These difficulties can be overcome through non-contact structural motion measurement methods to accurately identify the modal parameters of a structure (Song et al., 2014), such as laser Doppler vibrometry (LDV) (Castellini et al., 2004; Chen et al., 2015). This is the application of the Doppler Effect to measure vibrations on an object. A laser beam is directed onto a target, where the reflected light is then shifted in frequency in accordance with the target's vibration velocity. The target's vibration velocity is then obtained by combining the reflected light with a reference beam, allowing the extraction of the object's modal information (Oberholster, 2010; Chen et al., 2016). Oberholster (2010) investigated the application of Eulerian laser Doppler vibrometry to the on-line condition monitoring of axial-flow turbomachinery blades, in which he covers laser vibrometry extensively.

1.2.3.3 Impact Vibration Testing

With an impact vibration test, a loaded or automated impact hammer is used to hit (impact) the test object and thus excite a broad range of frequencies. By studying the measured response from the structural excitation, the modal and dynamic stiffness characteristics can be determined (Mix, 2005; Inman, 2014). Impact excitation is intended to be impulsive to contain a broad range of frequencies and desirably coincident with the system's natural frequencies of interest. The response to this sudden application of a large non-periodic force over a short duration can be physically understood as the response to an initial velocity with no initial displacement. The system response to an impact is equivalent to the free response of the system to certain initial conditions (Inman, 2014). Built into the head of this hammer, is a force transducer (load cell) that measures the force of the impact. The peak impact force is closely related to the mass of the head and the impact velocity. Different hammer tips are available, which primarily controls the input excitation frequency range, depending on the tip hardness. Selecting the correct hammer tip ensures that adequate input energy is applied, with nearly constant amplitude over the desired frequency range, to the structure to excite the full frequency range of interest (Lackner, 2005; Avitabile, 2014; Siemens, 2016b).

Impact hammer excitation avoids the mass loading problem and is much faster than using a shaker. It is also more appropriate and accurate for stationary modal testing than other non-contact excitation methods due to the ability of direct applied force measurement (Oberholster, 2010; Inman, 2014). Impact testing is recommended for quality assurance and control processes of testing of individual blades in the Electric Power Research Institute (EPRI) standards (Dewey and Lam, 2008). These blades can be mounted in a fixture to represent a cantilever beam or suspended to represent a free-free state. The vibration frequencies for several modes are obtained from the processed measured signal and are then tabulated to form a distribution about a mean value for each mode. Outliers or blades, whose dynamic response indicates that it might not behave as predicted, are identified from a fixed allowable frequency range. This method can also be performed on blades installed on the disk, either as groups or as individual structures (Dewey and Lam, 2008).

1.2.3.4 Model Validation by Frequency and Vibration Testing of Turbine Blades

Frequency data for turbine blades can be acquired in several forms by different methods for different goals; however, the key purpose here is to verify the correlation with the FEM. Dewey and Lam (2008) identify five ways of validating FEM models against experimental data. These are in order of increasing complexity:

1. Impact testing of individual blades.
2. Shaker testing of assembled rows.
3. Spin pit testing of rotating blades.
4. Blade vibration measurement of rotating rows.
5. In-situ testing of rotating blades.

It is implied that as the level of difficulty and expense increase, the cost and accuracy of the method also increase. However, this depends on the area of interest. For example, if the end goal is to develop an on-line condition monitoring method, the last three levels are of concern and must be included in the process. However, if the end goal is an in-situ off-line (stationary) monitoring method, only the first two levels need to be considered with some flexibility on the procedure (i.e. practicality, financial implications, etc.). FEA is performed on a constructed model corresponding to the selected level with appropriate boundary conditions. The numerical frequencies are then calculated for correlation with experimental data during model validation. A reasonably well-modelled simulation will have a general uncertainty of $\pm 2-3\%$ associated with any calculated natural frequency. It should be kept in mind that the individual blades do not represent the row in a fully assembled condition or with any at-speed operating and environmental conditions imposed on the blades (Dewey and Lam, 2008). These levels are not limited to only FE model validation, but if applied appropriately it holds the potential to be utilised in a damage detection or identification approach.

1.2.4 Structural Damage Identification Strategy

The extended structural damage identification problem can be considered as a hierarchical strategy of five levels (Worden and Dulieu-Barton, 2004; Barthorpe, 2011):

1. **Detection** – Determining qualitative presence of damage in a structure without prior knowledge of system behaviour from this damage.
2. **Localization** – Probable location of the structural damage.
3. **Classification** – Description of the structural damage through machine learning (Newly added and is referred to as Level 2.5 in Section 1.1).
4. **Assessment** – Quantifying the extent of the structural damage, requires structural model.
5. **Prediction** – Estimating remaining useful life of the structure.

To solve each level, it is required that details on all preceding levels are available. Hence, success of any level is largely dependent on the success of its lower level.

Structural damage identification approaches are either response- or physics-based. The response-based or data-based approach is dependent only on experimentally measured response data from structures, without the support of physics-based numerical models, and typically work on statistical pattern recognition principles. Note that experiments on undamaged structures are not necessarily possible, especially for in-situ cases. The physics-based or model-based approach is dependent on an accurate detailed numerical model of the structure, and thus the initial FE model requires continuous updating from newly-presented structural data to identify damage. However, numerical analyses can be computationally expensive, and its reliability can be questionable in the case of limited availability of experimental data from intact or undamaged structures. For this reason, the physics-based approach is unfit for real-time structure damage detection. Hybrid approaches, which are combinations of the response- and physics-based approaches, are also available but are not often used (Barthorpe, 2011; Fan and Qiao, 2011).

Response-based methods are simple, easy to apply, and not computationally intensive to implement and can recognize the first two levels of structural damage identification, i.e. qualitative damage detection (Level 1) and probable damage location (Level 2). However, this cannot provide enough detail for quantifying the extent of the structural damage (Level 4). It is a valuable tool for damage identification in the preliminary stage (Yan et al., 2007; Fan and Qiao, 2011; Kong et al., 2017). Therefore, an additional level that provides information about the type of damage is required that not only uses the characteristics of the measured responses to differentiate the structure state of health as well as enhance the accuracy of vibration-based damage detection, but also enables effective identification at higher levels where understanding the physics of damage (i.e. characterisation) is a prerequisite. This level is capable of overcoming the above-mentioned drawback, or at the least, it clarifies the path toward the answer, and involves classification or description of the structural damage (Level 3) and employs machine learning. Class labels are assigned to a sample of features of the measured data from a finite set and each class' specific damage properties are then encoded to a model through training, which categorizes new data accordingly (Worden and Dulieu-Barton, 2004).

Changes in modal properties or derived properties can be used as damage indicators, thus the problem of modal-based damage detection can be solved with pattern recognition (Farrar and Doebling, 1997; Martinez-Luengo et al., 2016). Kong et al. (2017) address the most recent on the background of vibration-based damage identification as guide to researchers and engineers to implement step-by-step the structure damage identification using vibration measurements. This includes the detection of damage occurrence using response-based methods, building reasonable structural models, selecting damage parameters, damage characterization, and objective feature selection.

1.2.5 Vibration-based Structural Damage Identification

When using vibration for damage identification, the complexity required to analyse the problem determines the type of signal analysis technique used. On-line application includes condition monitoring of rotating machinery, and off-line application includes characterising structural components with noise and vibration signals (Heyns, 2008). It can thus be argued that off-line condition monitoring of stationary machines or components proves less difficult due to results being independent of the time history and thus only leaves instantaneous measurement techniques to apply.

Vibration analysis applied to structures is classified as a global non-destructive damage identification method that can be used to find problems relating to unknown, inaccessible damaged areas in engineering structures. The fundamental concept behind these methods is that changes in a structure's modal properties (natural frequencies, modal damping, and mode shapes) are functions of changes in the structure's physical properties (mass, damping, and stiffness) induced by damage (i.e. stiffness reductions due to cracks or weakening of a connection) (Farrar and Doebling, 1997; Fan and Qiao, 2011; Song et al., 2014). The modal parameters are extracted through modal analysis of the stationary structure (Bray and Stanley, 1997), compressing the data for easier interpretation (Farrar and Doebling, 1997). This procedure is simplified through transforming the time domain data into the frequency domain through a Fast-Fourier transform (FFT). This allows analysis of the modal domain data by modal analysis techniques (Heyns, 2008). Vibration-based inspection is one of the most promising techniques for health monitoring, as modal parameter measurements are sensitive to the initiation and progression of damage in the structure (Kannappan et al., 2007; Lorenzino and Navarro, 2015).

Yan et al. (2007) present a general summary and review of most recent and development of vibration-based structural damage identification in which various methods, based on structural dynamic characteristic parameters, are summarised and evaluated. Fan and Qiao (2011) conducted a comprehensive review on modal parameter-based damage identification methods for beam- or plate-type structures in which they discuss the merits and drawbacks of these methods. This includes an FEA study evaluating various damage detection algorithms for beam-type structures, such as single damage detection, multiple damage detection, and large-area damage detection. Both authors classified the traditional-based damage detection methods into four major categories, based on the vibration features:

- Natural frequency-based methods
- Mode shape-based methods
- Curvature/strain mode shape-based methods
- Methods using both mode shapes and frequencies

Farrar and Doebling (1997) and Yan et al. (2007) provide an overview of modal-based damage identification methods, including critical issues for future research in the field of structural damage identification and health monitoring. These issues include the following. First, the impracticality of application-specific methods, which is dependent on prior numerical models and test data for the detection and location of damage. Second, many methods are fundamentally dependent on linear structural models, and is inadequate in describing the non-linear effects of a damage scenario. Third, the number and location of measurement sensors. Methods should not be limited to a few measurement locations and these locations must be deducible in advance. Fourth, the general sensitivity level of modal parameters to small defects in a structure. This will ensure that damage will be detected to allow remedial action. However, thus far, this has only been established for specific structures or systems and not proven in a fundamentally. Finally, the discernment of changes in the modal properties from damage or statistical variations in the measurements. Additionally, a suitably objective direct comparison of the relative merits of these methods, applied to a common dataset, has not been conducted. These issues must be addressed to ensure that the identification of damage using vibration measurements becomes a feasible and practical option that can be generally implemented.

Yan et al. (2007) discuss modern vibration-based structural damage detection methods based on wavelet transforms, neural networks, and genetic algorithms. These methods essentially combine the use of modern signal-processing techniques and artificial intelligence. This includes other methods such as static load redistribution, static noisy data, support vector machines, fuzzy optimum system hierarchy analysis selection, combined parameters, iterative general-order perturbation, probability density, virtual passive controllers, etc. They found that all methods were feasible in structural damage detection, each with their own special advantages, and that vibration-based structural damage detection will be an active future long-term research topic in structural dynamics. They also suggest the development of new multidisciplinary structural damage detection technologies as future research topic. Kong et al. (2017) address the most recent on the background of vibration-based damage identification as guide to researchers and engineers to implement step-by-step the structure damage identification using vibration measurements. This includes the detection of damage occurrence using response-based methods, building reasonable structural models, selecting damage parameters, damage characterization, and objective feature selection.

Vibration-based inspection holds much potential as a method for crack detection due to local flexibility imparted to the component when a crack is present, which reduces the natural frequency of the free vibration of the component (Barad et al., 2013). The mode shapes of the component are also affected by the local damage. Thus, it is possible to detect damage through analysing the changes in vibration properties of the structure (Farrar and Doebling, 1997; Yan et al., 2007; Kong et al., 2017). Many authors pursued this assumption in an attempt to develop analytical or numerical structural damage identification models for different scenarios regarding the crack location and severity. This includes varying crack orientation, the presence of single or multiple cracks (i.e. single-location and multi-location), and homogeneous or composite materials. Most methods reported showed promise in their application on simple structures.

1.2.5.1 Natural Frequency-based Methods

Natural frequencies are the frequencies a structure will likely respond to on free vibration or vibrate at when subjected to certain external forces. These frequencies depend on the mass- and stiffness distribution within the structure (Heyns, 2008; Inman, 2014). These distributions can change due to introduced damage, causing change in natural frequencies. To explain this concept, Dimarogonas (1996), Lackner (2005) and Barad et al. (2013) considered a slender cantilever beam with a local flexibility at the crack and found that the beam's structural mode frequencies are related to the square root of the structural stiffness of the beam due to mass remaining constant. This is shown in Equation 1.9. They also assume that a blade can be modelled as a slender cantilever beam. Shukla and Harsha (2016) also use this approach to find the natural frequencies and mode shapes of a lightly damped or undamped last stage steam turbine blade.

$$f_{n_i} = \frac{\omega_{n_i}}{2\pi} = \frac{1}{2\pi} \sqrt{\frac{k_i}{m}}, \quad \begin{array}{l} k : E, \text{ geometry} \\ m : \rho, \text{ geometry} \end{array} \quad (1.9)$$

With:

E = Elastic modulus [GPa]

f_{n_i} = Natural frequency at mode i [Hz]

k_i = Material stiffness at mode i [$N \cdot m/rad$]

m = Material mass [kg]

ρ = Material density [kg/m^3]

ω_{n_i} = Eigenvalue or natural frequency at mode i [rad/s]

Salawu (1997) conducted a broad review on natural frequency-based damage detection methods and found the approach potentially useful for routine integrity assessment of structures. Through recurrent vibration testing, the measured frequencies can be used to observe the structural behaviour and assess structural condition. This is the basic attribute for damage identification. The location of the measurements can also be customised as the identified frequencies have a global nature. This is an attractive method due to the ease of measuring the natural frequencies from just a few accessible points on the structure, and its low

experimental noise contamination levels (Fan and Qiao, 2011). It is also easier to extract information from natural frequencies on possible damage events, especially for concentrated damages like cracks or notches in beams, in ideal undamped systems than other dynamical parameters (Fernández-Sáez et al., 2016). Another advantage of this approach is that the natural frequency modal parameter has the least statistical variation from random error sources and that the measurement is much easier with higher accuracy than that of mode shapes or modal damping (Yan et al., 2007; Fernández-Sáez et al., 2016). It can also be deduced that complex geometry of a structure will complicate its mode shapes, which is already the case with higher modes, leading to rejection of the mode shape-dependent methods for damage identification. This amplifies the application of natural frequency-based methods.

With the forward problem of natural frequency-based methods, the known damage location and severity is used to determine the change in natural frequency of a given structure. With the inverse problem of natural frequency-based methods, the known natural frequency measurement is used to determine the damage location and its sizing of a given structure (Ngwangwa et al., 2006; Fan and Qiao, 2011). According to Yan et al. (2007), the natural frequency is often not sensitive enough to initial structural damage and can normally only determine if large damage is present and not the location. This is because structural damage in different locations may cause the same shift in frequency; however, this may not be the case with all structures as natural frequencies are a function of geometry (Inman, 2014).

Salawu (1997) notes that a variation of 5–10% in in-situ measured frequency due to ambient vibration and environmental effects can generally be expected, and that confident damage detection requires a $\pm 5\%$ change in natural frequency. A pattern recognition-based statistical damage detection model is required to resolve this effect by separating damage-induced changes from environment-induced changes. However, Lorenzino and Navarro (2015) were able to detect crack initiation and propagation stages of a crack growing from a circular notch with change in natural frequency smaller than 1%. They conducted fatigue tests on aluminium specimens with a centre hole in under load-controlled conditions. Shukla and Harsha (2015) compared the results from their finite element (FE) model and experimental modal analysis (EMA) of an uncracked and cracked fir-tree turbine blade root and found less than 5% variation in natural frequencies.

Research on using changes in natural frequency for crack detection revealed promising results and several limitations. Fan and Qiao (2011) considered these limitations and found that the frequency change-based damage identification method can be successfully applied to simple slender beam-type structures, with small artificially induced cracks, in a controlled laboratory condition. This, however, has limited applications for real complex structures or multiple or severe damage detection because of its underlying disadvantages. These include that the basic assumptions of these methods limit the suitable range of vibration modes for damage detection to the first few modes, change in environmental and operational conditions can suppress small changes in frequency caused by damage, and that damage at different locations with different severity can cause the same change or shift in natural frequencies. Hence, in developing any method to quantify and extend the life of structures, all possible damage events at various locations on the structure must be considered. The method will be restricted in application to specific structural geometries and the assumed type of damage model (Farrar and Doebling, 1997; Kong et al., 2017).

A more general term for the natural frequency-based technique, which is a developing NDT procedure, is known as acoustic resonance testing (ART). Inconsistent parts are identified during its manufacturing stage by change in natural frequencies of a part. This is achieved through sophisticated sorting algorithms that rapidly and reliably inspect and sort these parts accordingly. The sorting accuracy of the ART process for a complex, production level part can potentially be improved by applying FEM-based modal analysis to reduce the algorithm teaching process (Stultz et al., 2003; Lai et al., 2011). ART has been widely used in the automotive industry for quality inspection due to its many advantages, such as low inspection cost, high testing speed, and broad applicability to complex structures (Xu et al., 2015). The authors also stress that, compared to other current direct visualization-based NDT methods, a more extensive application of ART faces an ultimate challenge since such technology is unable to quantify the flaw details (location, dimensions,

and types). They systematically investigated the efficiency of a maximum correlation-based inverse ART algorithm on a range of common structural flaws (stiffness degradation, voids, and cracks). They found that the predicted results were able to accurately locate the damages and quantitatively measure the physical characteristics of the defects. Thus, this approach can effectively help retrieve the actual state of health of the engineering structures in a computationally efficient way. According to the EPRI standards (Dewey and Lam, 2008), the natural frequency-based method is applied during quality assurance and control of individual turbine blades.

1.2.5.2 Effect of Damage on Dynamic Behaviour of Structure

Research based on structural health monitoring for crack detection deals with changes in natural frequencies and mode shapes of a structure (Ngwangwa et al., 2006; Agarwalla and Parhi, 2013). Lackner (2005) notes that the natural frequencies of a cracked structure should be lower than an uncracked structure since a crack reduces structural stiffness, which leads to a decrease in natural frequencies as illustrated in Figure 1.10. The basic assumption is that damage can be directly related to a decrease of stiffness in the structure. Thus, stiff structures have higher frequency modes than compliant structures.

Pandey and Biswas (1994) and Ngwangwa et al. (2006) presume that structural damage changes the mass, stiffness and damping matrices of the system. However, for a structure with surface cracking, where mass loss due to disintegration is unlikely and changes in the system damping are not considered, damage may be assumed to affect only the stiffness matrix of the system. The authors also note that the influence of the crack on the system's stiffness matrix is localized in the elements where the cracks are located. This is supported by Garcia-Palencia et al. (2015). The stiffness matrix of the cracked beam is derived from a flexibility matrix calculated from fracture mechanics (Nguyen, 2014). Pandey and Biswas (1994) use the change in the flexibility (inverse of stiffness) matrix to accurately detect and locate damage in a structure. This is a very popular research topic.

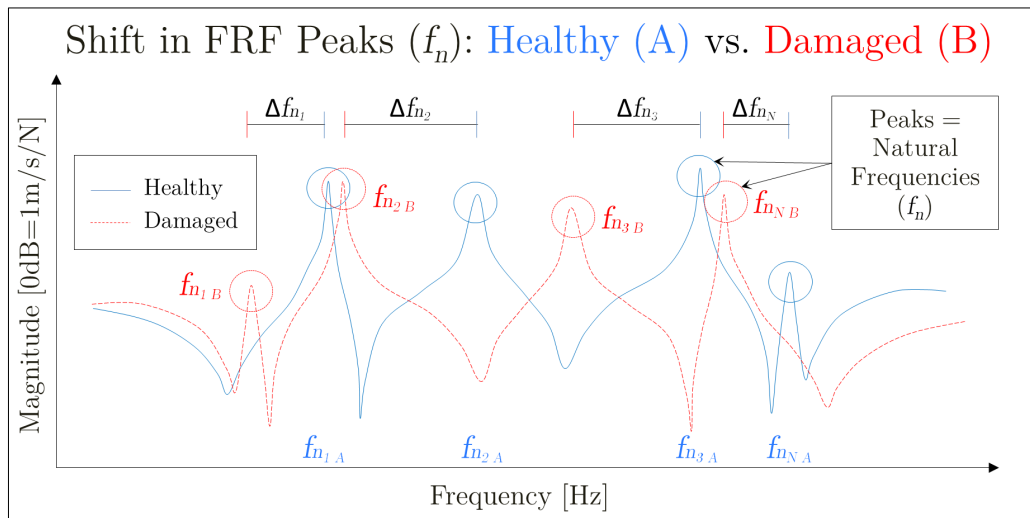


Figure 1.10: An example of shift in FRF peaks, i.e. natural frequencies, due to damage in a structure

A crack can be represented as a fracture-hinge with a rotational spring with stiffness k . In the absence of a static force, which keeps the crack open, the crack will close during the part of the cycle when the stresses are compressive, behaving as a bilinear spring (Dimarogonas, 1996). This is based on flexural vibration for uniform beams, for an edge cracked cantilever beam having a rectangular cross-section (Rizos et al., 1990; Lee and Chung, 2000; Kannappan et al., 2007; Fan and Qiao, 2011; Barad et al., 2013; Agarwalla and Parhi, 2013). This model relates natural frequencies, crack locations, and crack depths through the effect of damage on the dynamic behaviour, particularly the stiffness, of a structure (Jassim et al., 2013). Knowing the effect of crack on stiffness of a structure, Euler-Bernoulli or Timoshenko beam theory can be applied to model the structure. The beam boundary conditions are used along with the crack compatibility relations to derive the characteristic equation. This relates the natural frequency, the crack depth and location to the other

beam properties (Fan and Qiao, 2011; Jassim et al., 2013). Many parts and structures cannot be modelled by axial vibration only; hence, a finite element is required to describe transverse vibration (Inman, 2014).

When the crack is located at the peak or trough positions of the strain mode shapes, the percentage change in frequency values are higher for corresponding modes, whereas if the crack is located at the nodal points of the strain mode shapes, the percentage change in frequency values are lower for corresponding modes (Ngwangwa, 2004). Agarwalla and Parhi (2013) observed a drop in natural frequency of a cantilever beam when a crack is present. For the same cantilever beam, they observe a rise in natural frequency with increasing distance of the crack position from the fixed end. They compared the results of experimental modal analysis (EMA) to FEA and found a discrepancy of 3–5%. This is supported by Gillich and Praisach (2015). They found that the shift in natural frequency for a certain vibration mode of a beam-like structure is dependent on the damage location, while the damage depth only amplifies this event. This is due to the effect of the mode shape vector for a given location.

1.2.5.3 Change in Natural Frequency from Fatigue effecting Stiffness of Structure

McGuire et al. (1995) explores the feasibility of using the change of an effective elastic modulus (equivalent to the change of natural frequency) to study the crack propagation of a fatigue-loaded tension bar specimen with a 1.6mm centre-drilled hole. They measured crack length and natural frequency as functions of the number of fatigue cycles and were able to establish a link between these properties. This is shown in Figure 1.11 in which the natural frequency, effective elastic modulus, and average crack length are plotted over the number of cycles of the fatigue test. Calculating the effective elastic modulus of the sample required its fundamental natural frequency. A clear steadily increase throughout the early fatigue life of the specimens can be seen. This is due to plastic deformation of the fatigue specimens. A prominent dependence between the elastic modulus and the crack length, and thus natural frequency, was detected since the elastic modulus reached a maximum and then started to decline as cracks initiated and propagation occurred. It can also be seen that the maximum elastic modulus corresponds with the onset of a crack at the specimen surface, thus the consequent decrease in elastic modulus seems to be dependent on the crack length. Hence, a drop in natural frequency and elastic modulus occurs as the crack starts to propagate.

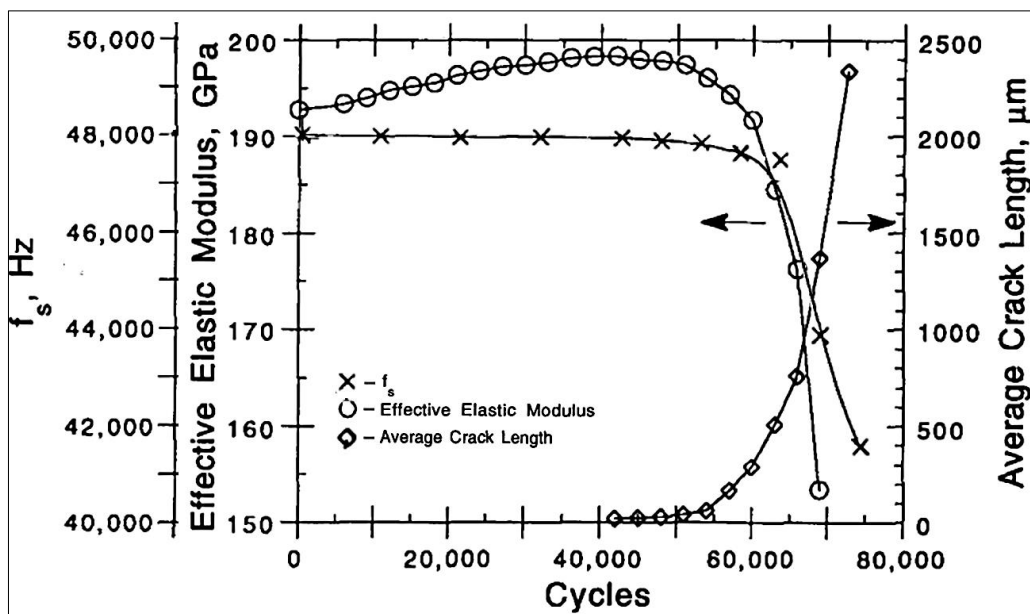


Figure 1.11: Natural frequency f_s , Effective elastic modulus E_{ef} and Average crack length vs. number of cycles N for a stainless steel bar specimen (McGuire et al., 1995)

Giannoccaro et al. (2006) used the shift in resonance and anti-resonance modal data to evaluate fatigue damage in notched specimens. They developed a solution to overcome the uncertainty of accurately predicting the number of cycles to failure for identical specimens subjected to identical fatigue loading, by considering the systematic decrease of resonances and anti-resonances at about 90% of fatigue life. Their results are

shown in Figure 1.12 in which the FRFs and their peaks are plotted regarding fatigue life percentage. This is evident in the fatigue life final stage ($\geq 90\%$ of the specimen life) in Figure 1.12b. The authors note that the variation induced in the first frequency has greater significance since the damage process has a greater effect on this frequency, which is also easier to detect. This agrees with the experimental failure process, which begins with the crack initiating at the notch and then propagates in the plane normal to the axial load.

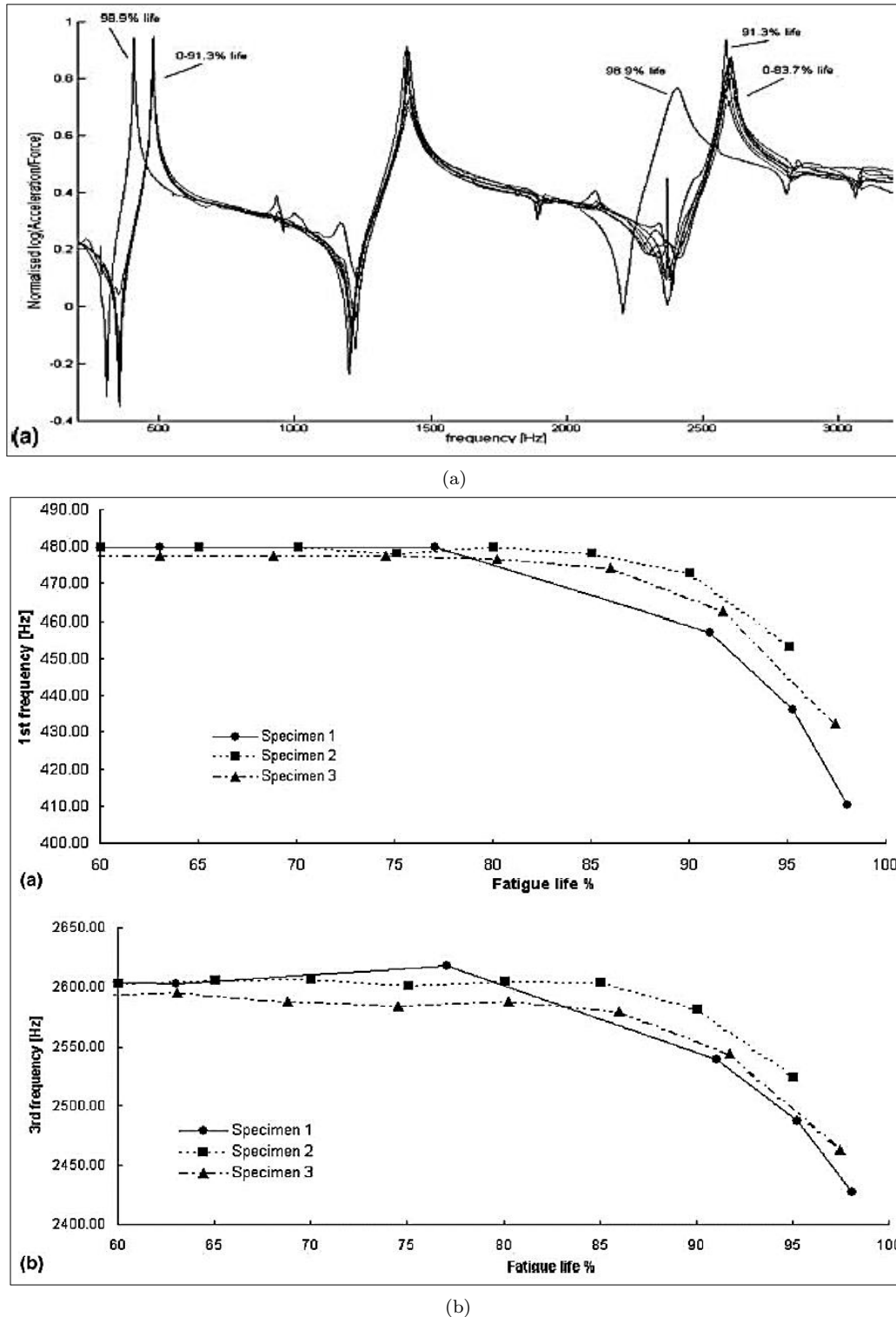
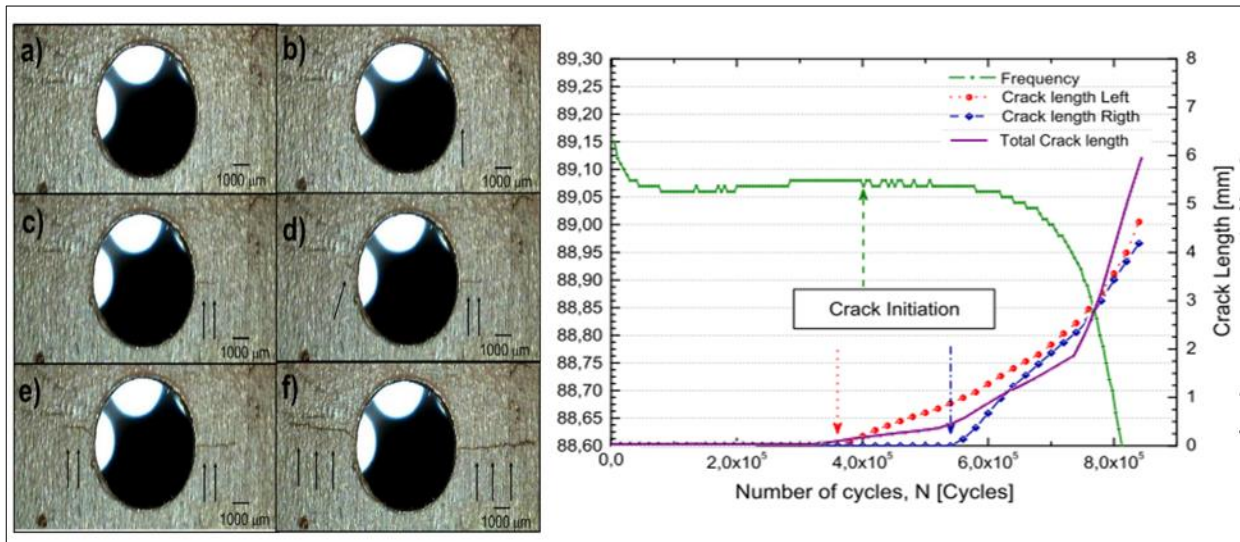


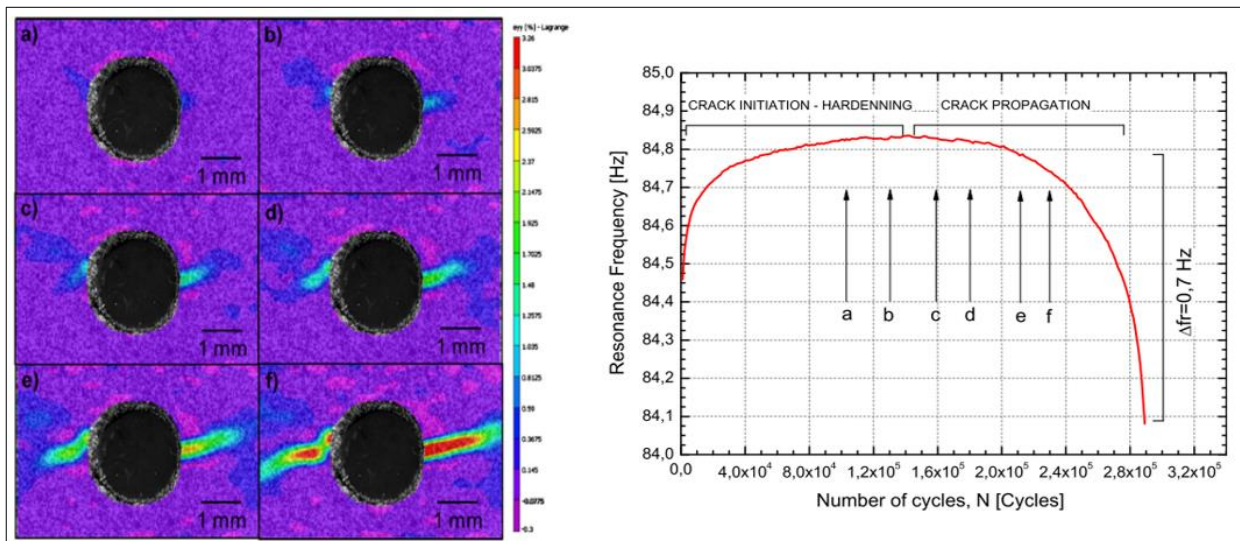
Figure 1.12: Modal data regarding fatigue life percentage (Giannoccaro et al., 2006), a) FRFs throughout fatigue test; b) Trend in 1st and 3rd natural frequency over fatigue life percentage

Lorenzino and Navarro (2015) were successful in using the variation of natural frequency in fatigue tests as a tool for in-situ identification of crack initiation and propagation stages, which allow confirmation of

crack progression from natural frequency variation. This is clearly shown in Figure 1.13 in which it is observed that crack initiation occurs at the radial hole and then propagates in the plane normal to the axial load. The natural frequency rises during the initiation stage; however, drops considerably as the crack starts to propagate. Additionally, by using the variation of natural frequency in fatigue tests, they were able to determine the total cracked areas during fatigue crack growth in a wide plate with a radial hole. The experimental results in Figure 1.13a and Figure 1.13b correspond to that of McGuire et al. (1995) and Giannoccaro et al. (2006), respectively. This confirms the relationship between natural frequency, crack length, and number of fatigue cycles. This suggests that as the crack starts to propagate, a decrease in the elastic modulus or stiffness causes a decrease in the natural frequency of the specimen.



(a)



(b)

Figure 1.13: Variation of the resonance frequency as a function of crack progress and number of cycles (Lorenzino and Navarro, 2015), Test results for the a) 6mm specimen and correlation with the video results; b) 2mm specimen and correlation with the digital image correlation results

1.2.6 Machine Learning-based Damage Detection

The goal of machine learning, which originated from the scientific discipline of pattern recognition, is the classification of data into different categories or classes according to the fundamental patterns recognised within the data. These fundamental patterns hold features or quantities that make the rule to be learned by the models explicit. The curse of dimensionality, which causes problems in the implementation of these models due to the large dimensional feature spaces, can be bypassed through feature extraction, -selection,

and dimensionality reduction techniques. The models are then trained on the low-dimensional discriminant feature vectors of interest, extracted from the high-dimensional collected data, to allow class predictions of new data (Worden and Manson, 2007; Theodoridis and Koutroumbas, 2009; Schmidt, 2017).

1.2.6.1 Feature Extraction and -Selection

In real-world structural health monitoring (SHM) applications, the damage-related changes in the features can be obscured by operational and environmental effects, which can also influence the total features to the damage-level. Usually, the sensitivity of a feature to damage and the sensitivity to it changing in the operational and environmental conditions (e.g., temperature and wind speed) are proportional. This can be overcome through robust feature extraction procedures (Santos et al., 2016).

With feature extraction, dominant (damage-sensitive) characteristics or features of the noisy collected data are extracted from the original space, and then enhanced by removing redundant noise and information or estimating missing values and are subsequently transformed and mapped into a new feature space. To ensure minimizing false judgements in the classification phase, it is essential that these damage-sensitive features correspond with the damage severity present in monitored structures. With feature selection, the dimensionality of the feature space is reduced by selecting a subset of features without any transformations that enhance the separation between the classes. In this process, redundancy is minimized and the relevance to the target is maximized, resulting in a low-dimensional feature vector. Implementing proper feature extraction and -selection methods improve the learning performance by lowering computational complexity, building better generalizable models, and decreasing required storage (Worden and Dulieu-Barton, 2004; Tang et al., 2014; Santos et al., 2016; Schmidt, 2017). This process is based on confidence in feature performance when presented with new data. It is preferred that the feature vector consists of several well-performing neighbouring features rather than features that perform prominently better than their neighbours (Barthorpe et al., 2017). If selected features are not suitable, the performance of even the most sophisticated classification algorithm will be poor (Long and Buyukozturk, 2014).

Dimensional reduction techniques can be used to reduce the dimensions further, if necessary; however, it is essential to first ensure that the discarded information is not strongly related to the damage diagnostics. Low-dimensionality is essential in pattern recognition problems as the training set size increases dramatically with the dimension of the problem. The generated feature vector is then used in the pattern recognition algorithm to assign a class. Feature selection and feature extraction are carried out based on engineering judgement (Worden and Dulieu-Barton, 2004; Theodoridis and Koutroumbas, 2009; Tang et al., 2014). For damage detection, the most suitable features are particular to the application and are sourced from the time, frequency, or modal domains depending on the employed level of data consideration. Damage-sensitive features in the modal domain have physical significance and are therefore simplest to interpret of these domains. This includes natural frequencies, assurance criteria of modal shapes and derivatives, modal strain energy, modal strain, damping, dynamic flexibility matrix, residual force vector, and a combination of some features (Kong et al., 2017). Application of machine learning for damage classification can be addressed once features, that allow one to differentiate between damage states with confidence, are identified (Barthorpe et al., 2017).

1.2.6.2 Machine Learning Methods

Application of machine learning methods in diagnostics generates a model that operates on the extracted damage-sensitive features. This model is capable of identifying and quantifying the damage state of the structure based on the given feature vector. The relation between the extracted features and the structure's state of health are described by categorizing the data into different groups consistent with the underlying patterns within the data. This data is divided into separate sets for training and validation. The model parameters are optimized in the training phase with the labelled training set, while the accuracy of the set parameters is determined in the validation phase with the labelled testing set. These phases work together

since the accuracy is dependent on the parameters. In the testing phase, new independent data is used to verify the generalization of the developed model, i.e. the capacity of correct classification (Theodoridis and Koutroumbas, 2009; Martinez-Luengo et al., 2016; Barthorpe et al., 2017).

Two broad categories of statistical pattern recognition algorithms or machine learning are available, based on the desired function and information available to the learning system (Theodoridis and Koutroumbas, 2009; Martinez-Luengo et al., 2016): supervised and unsupervised. With supervised learning of which either discrete classification or regression analysis (continuous classification) can be used, the available data from both the healthy (undamaged) and damaged state(s) can be statistically sorted, providing an inherent confidence component in the damage diagnostics. This is recommended for damage diagnostics from a discrete set. This is an expensive method since data from all damage states must be obtained and damage is irreversible. However, it can be employed as an exploratory method for developing a structural damage identification technique as this is not limited to only damage detection (Level 1) but can diagnose probable damage location (Level 2) as well as damage type (Level 2.5), and possibly damage severity (Level 3). Hence, supervised machine learning methods are favoured in damage classification problems (Yin and Hou, 2016). In combination with Kernel-based machine learning methods primarily based on support vector machines (SVMs), high sensitivity and accuracy in structural damage detection and identification can be achieved (Santos et al., 2016). SVMs also exhibit good generalization for a limited number of samples (Gryllias and Antoniadis, 2012; Martinez-Luengo et al., 2016). With unsupervised learning, clusters of data with similar behaviour are identified from unlabelled data of all states in which membership of new data to labelled healthy data is tested with novelty detection. However, this is only applicable to damage detection (Level 1). The labelling, in both cases, is done by an expert if needed (Worden and Dulieu-Barton, 2004; Theodoridis and Koutroumbas, 2009).

1.2.6.3 Support Vector Machines

A problem with data-driven approaches is that the acquired datasets are likely to be sparse as the data collection or generation for training the model is likely to be expensive. This strains the feature selection activities due to sparse data usually requiring low-dimensional features to ensure that the model generalizes away from the training set. Thus, regularization of the training data is required in the training stage. However, support vector machines (SVMs) are implicitly regularized and thus, can better generalize based on sparse data. Noise can also be added to the training data (Worden and Manson, 2007). This is a popular classification approach for damage detection and identification. It first finds the class boundary, an optimal separating hyperplane that maximizes the margin between the nearest points (i.e. support vectors, SVs) of different classes, as shown in Figure 1.14, and then it classifies new data within the respective regions. The classifier only requires the essential information held in the SVs and the rest of the feature set can be discarded, making the classifier computationally efficient (Samanta et al., 2003; Yin and Hou, 2016).

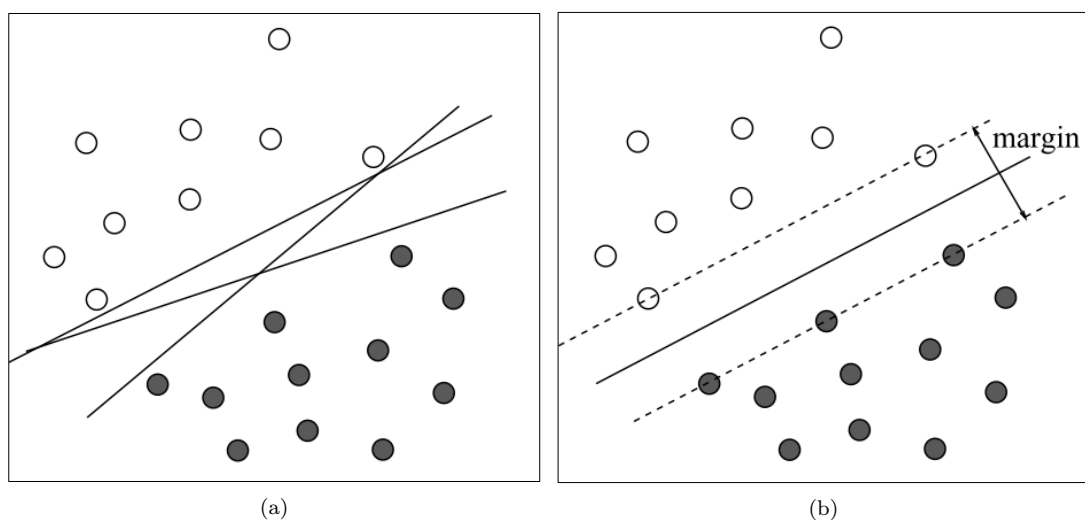


Figure 1.14: Separating hyperplanes (Worden et al., 2007), a) Arbitrary; b) Optimal (with SVs on margins)

The kernel method or 'kernel trick' is utilized to transform non-linearly separable classes in the original feature space to a higher-dimensional space where the classes can be linearly separated, which is then projected back with a non-linear boundary of given complexity more suitable to the distribution in the original space. Non-linearity in the low-dimensional space is therefore represented by the linearity in the high-dimensional space (Yang and Widodo, 2008; Brereton and Lloyd, 2010; Hasni et al., 2017; Schmidt, 2017). This is illustrated in Figure 1.15. The preferred kernel function or regulator is the non-linear radial basis function (RBF) kernel since it prevents over-fitting of training data, due to its low parametrization and its consequent smooth classification bound preference. Its parameters can be determined iteratively and optimal values derived from the full feature set are selected (Samanta et al., 2003; Barthorpe et al., 2017). Brereton and Lloyd (2010) presented detailed examples for two-class SVMs and multi-class SVMs, in which they discuss and illustrate the fundamentals with extensive visualisation. This includes learning machines, kernels, and penalty functions as well as the consequence of different parameters for the different learning machines.

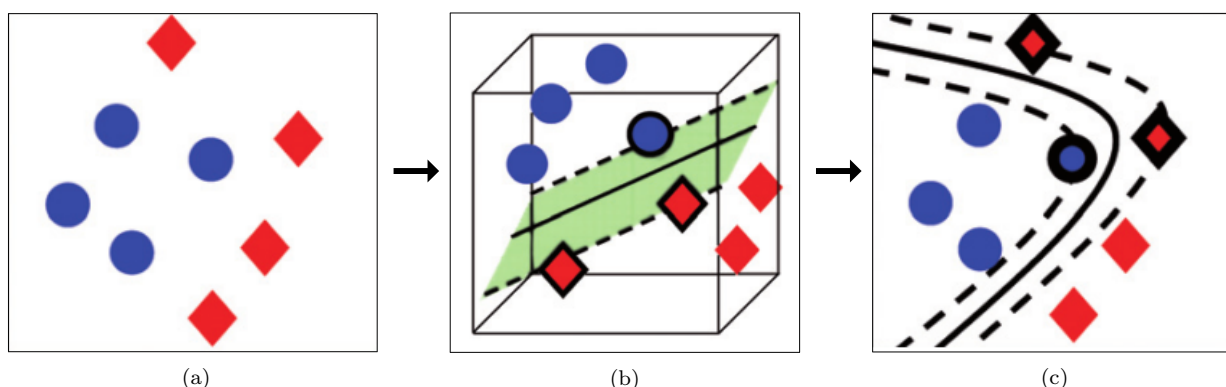


Figure 1.15: Creation of the boundary for a non-separable case (Brereton and Lloyd, 2010), a) Linearly non-separable training samples in the original space; b) Non-linearly separable training samples in the higher-dimensional space (with 3 support vectors indicated); c) Projection back into original space with non-linear boundary

Several advantages of the SVM method exist. This includes high generalization capabilities due to non-linear mapping from the original data space into high-dimensional feature space (Pawar and Jung, 2008; Yin and Hou, 2016; Barthorpe et al., 2017), and over-fitting avoidance due to regularization parameters (Hasni et al., 2017). It is suitable for a small training set (Gryllias and Antoniadis, 2012), which is sufficient for maximal recognition of underlying patterns or classification knowledge in the data (Yin and Hou, 2016). It is capable of direct classification of extracted features, i.e. when data from all conditions exist, and can remove cumulative operational and environmental effects in extracted features (Fan and Qiao, 2011; Santos et al., 2016). It is versatile and has a powerful framework for general classification (Martinez-Luengo et al., 2016) since it supports different types of discriminant functions (i.e. linear, non-linear, polynomial or radial basis functions) without requiring substantial modification (Barthorpe et al., 2017). It is a unique and global solution and is less prone to over-fitting (Hasni et al., 2017).

Two-class (binary) SVMs can be extended to a multi-class model that chooses to which group or class a sample from a multi-class dataset belongs to, and then superimpose the multiple decision functions. The multi-class problem can be solved by the following most popular and task-specific approaches (Theodoridis and Koutroumbas, 2009; Brereton and Lloyd, 2010):

- One-versus-All (OvA), which selects the best class from individually modelling a sample as each class using multiple binary SVM models, where respective samples are considered as part of a class or not. The number of binary classifiers to be trained are equal to the number of classes. This is illustrated in Figure 1.16a.
- One-versus-One (OvO), which models a sample pair for all comparisons using a binary SVM model for each case, where respective sample pairs are assigned the probable class. The number of binary classifiers to be trained are equal to the number of class pairs. This is illustrated in Figure 1.16b.

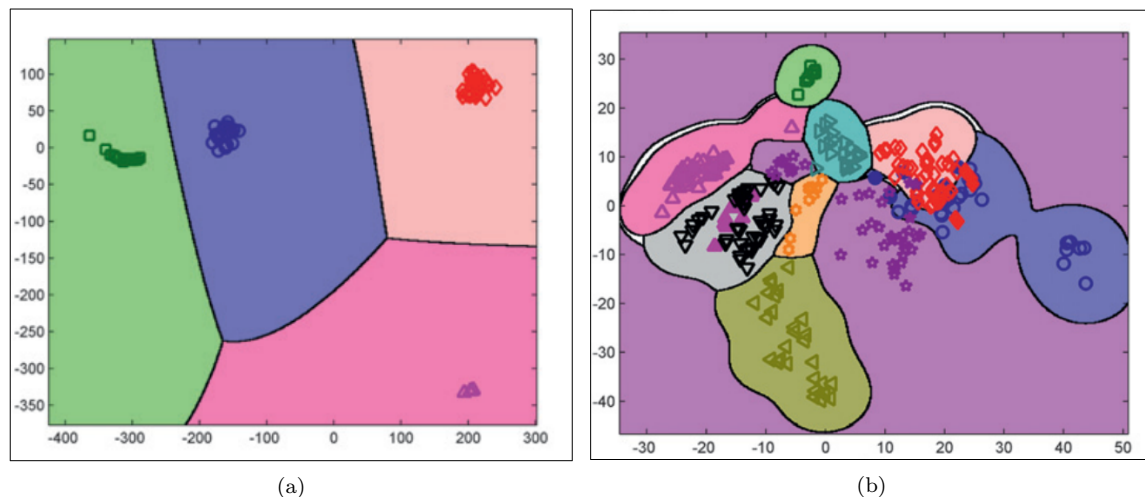


Figure 1.16: Extension of binary SVMs to a multi-class model (Brereton and Lloyd, 2010), a) One-versus-All (OvA); b) One-versus-One (OvO)

Different authors present reviews and examples of SVM damage detection in multiple structural health monitoring applications. Yan et al. (2007) discussed modern-type vibration-based structural damage detection methods, stating the feasibility of these methods, having some special advantages in structural dynamics-based structural damage detection. Fault diagnosis and process monitoring in various components and equipment used in complicated industrial processes are discussed by Yang and Widodo (2008) and Yin and Hou (2016). The former summarized earlier research and development of pure SVM in machine fault diagnosis, whereas the latter summarised more recent papers from 2007 to 2015 on techniques, in which SVM is combined with other pattern recognition algorithms (SVM-based). The advancement in this field is encouraged by the numerous proposed SVM-based concepts. They also recommend the necessity of developing new methods to deal with very complicated industrial systems.

1.3 Scope of Research

The early detection of damage in structures, which may eventually lead to failure of the individual component or system, is possible through damage diagnosis. Damage diagnosis can also indicate early deterioration in performance levels. These observations may possibly be used to update remedial decisions. Two damage identification strategies in structures are available, i.e. structural health monitoring (SHM) and non-destructive testing (NDT). SHM is a global method and entails the indirect observation of a structure in real-time (on-line) using various permanently installed sensors. The damage-sensitive features are extracted from the measured time-history data, and interpretation of these features is accomplished through e.g. statistical analysis, to determine and objectively quantify the current state of health of the structure. NDT entails off-line inspection of the structure during scheduled maintenance using portable instruments, and the measured data usually depends on human expert interpretation. NDT is mostly local methods, which employ direct measurements to assess the structural health (e.g. ultrasonic testing and eddy current inspection) but global methods, which employ indirect measurements to assess the structural health (e.g. vibration analysis), are also available. Issues of inaccessibility can limit inspection using local methods and can possibly be overcome by using global methods. With NDT, the damage can be characterized, or its extent can be monitored when its location is available, which allows a time-history of the progressing damage to be recorded (Worden and Duijvelde, 2004; Mix, 2005; Barthorpe, 2011; Scheepers and Booyens, 2012; Kong et al., 2017). When applying NDT as a monitoring tool, the time-history data can be treated similarly to that obtained with SHM and can thus be interpreted through e.g. statistical analysis.

There is a need for a structural damage identification method to be used in support of conventional NDT techniques for inspection of stationary blades to detect cracks, specifically in the vicinity of the root. This requires some background on the common blade failure locations. It was shown that the most probable

damage locations are found at the upper pinhole of the leading edge and on both the leading and trailing edges at the aerofoil base just above the root. These areas experience the highest stress from massive centrifugal forces causing fatigue cracking. The basics of fracture mechanics are important since cracks initiate and propagate due to damage accumulation during turbine operation. Since local NDT methods are insufficient in detecting cracks in geometrically complex and installed blade roots, development of global methods is encouraged. The change in stiffness of the blade due to the presence of a crack is expected to result in a change in natural frequencies. This implies that natural frequency has a damage-sensitive nature. Therefore, vibration-based damage detection methods applying natural frequencies show promise. Modal analysis will be performed to extract the modal properties from the structure. These can be used to indicate if a structure is damaged by comparing it pre- and post-event. Thus, modal-based health monitoring qualifies as a pattern recognition problem (Farrar and Doebling, 1997; Martinez-Luengo et al., 2016).

A feasibility study is defined as an assessment of the practicality of a proposed plan or method. This study, is an introduction to using vibration-based structural damage identification to detect and classify the most probable worst-case damage near or on the root of installed turbine blades. A simplified problem is presented as illustrated in Figure 1.17, in which only uninstalled individual turbine blades are considered to solve a part of the real-world problem, and is broken down into the following questions:

- Is it possible to identify defects, i.e. geometrical variability, in an unconstrained and isolated blade using vibration response?
- Is it possible to detect damage in an unconstrained and isolated blade using vibration response?
- If so, can different damage scenarios be identified?

The answers to these questions will enable further development of the proposed method into a real-world application to use in support of conventional NDT for in-situ inspection of installed stationary blades. The approach to assess the feasibility study is illustrated in Figure 1.18 and outlined in the following paragraphs.

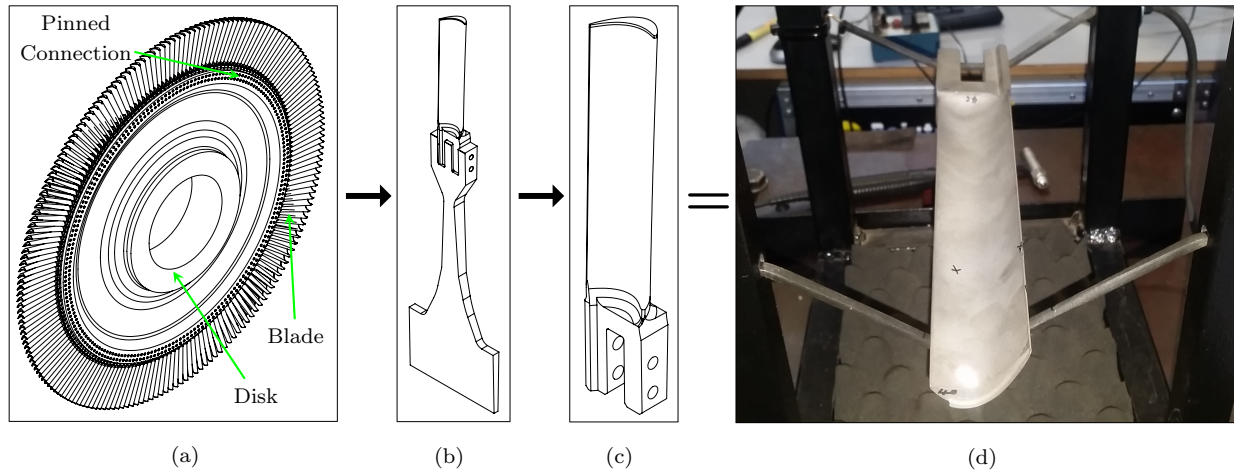


Figure 1.17: Simplified problem extracted from real-world problem, a) Full assembly = Turbine disk; b) Sub-assembly = Cyclic symmetry section of bladed disk; c) Component = Individual blade; d) Freely supported individual test blade

In this feasibility study, a response-based structural damage identification approach using supervised machine learning, with support of numerical models is applied. In Step 1, experimentally measured response data is acquired through modal analysis of a freely supported individual pinned turbine blade. In Step 2, numerical response data is obtained and used to establish expected behaviour of a specific scenario. This behaviour relates to the sensitivity of natural frequencies to geometrical variability as well as damage. The experimental set-up involved an accurate and reliable impact vibration test conducted on a set of discarded healthy blades and their damaged counterparts. The system was suspended (i.e. freely supported), lightly damped (elastic bands), with non-contact measurement (laser vibrometer). Modal analysis was performed in the frequency domain to allow accurate extraction of the modal frequencies from FRF peaks (Step 3). The single excitation- and measurement location for the system were selected for maximum mode participation and observation, and operator-convenience. The numerical model was also used to determine the most probable damage

location in the root during turbine operation (at the maximum stress) and explore the responses of the damage scenarios through modal- and harmonic response analysis, before implementing into experiments (Step 1 \longleftrightarrow Step 2). Thus, the FEM serves only a supportive role since model updating was not part of the scope, and direct association with the experiment is not possible. It is only possible to compare and conclude on the blade's output behaviour due to input parameters, and not the exact values. In this study, only the healthy and worst-case scenarios were considered. This is mainly due to the limited number of blades available for proper representative results. Time constraints, the complex geometry of the root, and the damage initiation location on the root also contributed to this decision. These factors limited the damage induction procedure, as the root geometry was difficult to access and reliably alter in a controlled fashion at the specified location in the root.

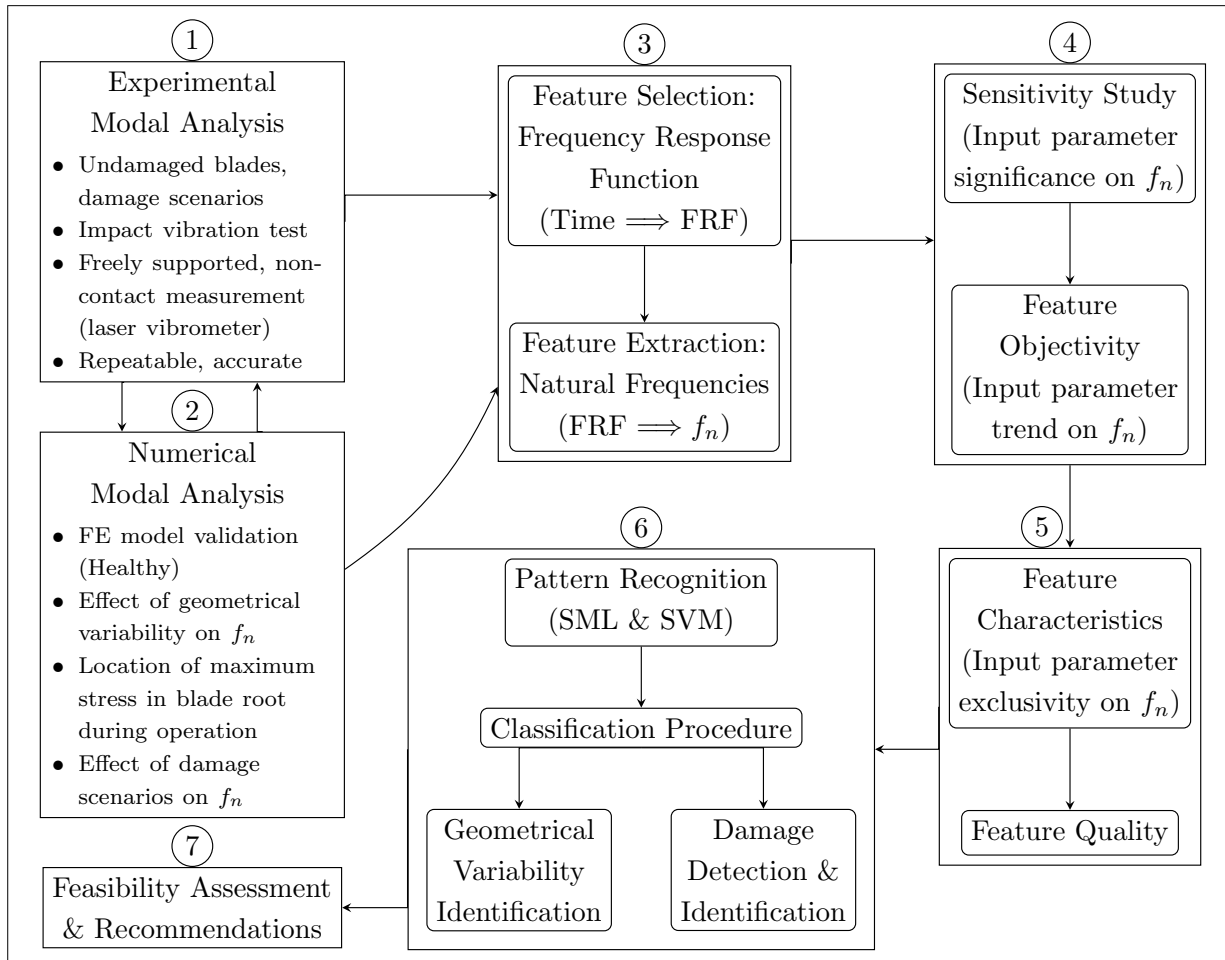


Figure 1.18: Approach to test feasibility of damage detection and identification method

Response-based methods are simple, easy to apply, and not computationally intensive to implement and can recognize the first two levels of structural damage identification, i.e. qualitative damage detection (Level 1) and probable damage location (Level 2). However, this cannot provide enough detail for quantifying the extent of the structural damage (Level 4). It is a valuable tool for damage identification in the preliminary stage (Yan et al., 2007; Fan and Qiao, 2011; Kong et al., 2017). Therefore, an additional level that provides information about the type of damage is required that not only uses the characteristics of the measured responses to differentiate the structure state of health as well as enhance the accuracy of vibration-based damage detection, but also enables effective identification at higher levels where understanding the physics of damage (i.e. characterisation) is a prerequisite. This level is capable of overcoming the above-mentioned drawback, or at the least, it clarifies the path toward the answer, and involves classification or description of the structural damage (Level 3), and employs machine learning (Worden and Dulieu-Barton, 2004).

During the feature selection stage (Step 3a), in which the measured noisy raw data is compressed through some transformation, the size of the original dimension is substantially reduced and only a feature space

sensitive to change in a specific parameter remains. Features are application specific and can differ depending on the type of data measured and its inherent properties. During the feature extraction stage (Step 3b), the quality of the feature space is refined by removing redundant information without transforming the feature space, resulting in highly sensitive feature space containing a suitable objective feature. In this study, the frequency domain was selected as the feature space, which was obtained by time to frequency conversion of the measured response within the signal processing software, and the natural frequencies were extracted from this feature space as the discriminant feature. This reduced the size of the feature space from 25 600 spectral lines to 14 natural frequencies for each blade.

To investigate the discriminant feature's objectivity or independence of the output response on input parameters, the degree of sensitivity and consistency with the expected structural response must be determined (Step 4). A sensitivity study is recommended to establish the significance of input parameters to a specific output feature (Kong et al., 2017). Thus, when considering the geometrical variability at the blade roots, which were introduced during their installation (tuning or individually reamed holes for pin insertion), or damage scenarios near or on the root as the input parameters, their effect on the natural frequencies, the specific output feature, must be determined. This is achieved through using a reasonably well-modelled numerical blade to replicate simplified versions of the existing geometrical variability and produce simplified versions of the damage to be introduced in the experimental blades to predict the expected behaviour. This will allow confirmation of the objectivity of the feature from the specified geometrical modification as well as evaluation of the consistency of the feature through exploring the experimental damage trends (Step 4b).

To ensure that the discriminant feature is of quality, the exclusivity of the output response due to input parameters must be determined. This is done in Step 5. The distribution of each class is explored in one-dimensional and two-dimensional space to determine its separability from the rest. The further apart the classes, the more exclusive the damage-sensitive feature. Hence, the separability is regarded as a characteristic of the feature. By projecting the results to a higher dimensional space, the size of the feature vectors is reduced further, and clusters are formed, allowing better judgement on the class separability. Thus, changes in natural frequencies for the different classes represent the distance between these classes, and therefore the separability of each class distribution from the rest.

The proposed method incorporates natural frequency as the discriminant feature, a quantity contained in the underlying patterns of the data, and supervised machine learning to detect if damage is present as well as identify different damage scenarios (Step 6). Thus, this method has a foundation of inverse formulation of traditional vibration-based damage identification methods, which determines damage properties of a given structure based on natural frequency measurements, and a supervised machine learning core. Changes in modal properties or derived properties can be used as damage indicators, thus the problem of vibration-based damage detection can be solved with pattern recognition (Farrar and Doebling, 1997; Martinez-Luengo et al., 2016). A class is assigned to the measured modal data by a pattern recognition algorithm, i.e. classification using support vector machines (SVMs), which relates the change in the measured data through an explicitly learned rule as classification boundaries. These boundaries are used to decide on the state of health of the system (Worden and Duijue-Barton, 2004; Yin and Hou, 2016). Classification can be done in any higher dimensional space in which sufficient clusters are formed as this is required to create the decision boundaries that differentiate between different classes. In this study, SVMs are practically applied without modification for optimization purposes.

This approach is first applied on the healthy data to establish if geometrical variability can be identified and then on the damage scenario data to establish its detection and identification, allowing a final verdict on the feasibility of this damage classification approach (Step 7). The sensitivity of the features to geometrical modifications (i.e. geometrical variability and damage scenarios) will greatly contribute to these outcomes. The proposed global method can then be verified by conventional NDT to ascertain the obscured damage, if any.

1.4 Document Overview

In Chapter 2, the numerical model design and experimental procedure are discussed. The baseline or benchmark for the investigation is established in which experimental modal analysis is utilised to extract the natural frequencies from the undamaged or healthy test blades. The experimental set-up, protocol, and its repeatability are presented, as well as the validation of the numerical model, allowing a supportive behaviour predictor to be established.

Chapter 3 presents a sensitivity study on the natural frequencies. The variance in the healthy blade vibration responses due to slight geometrical modifications (or defects) is explored. Additionally, the effect of the most likely damage locations near the root for stage 2 pinned turbine blades on the healthy response is examined. The investigation was designed through utilising FEA models, literature, and experiments, and considered the geometrical variability observed in the root of healthy blades as well as the most likely damage scenarios near the root. The raw experimental results are also given here, as well as the extracted FRF peaks and their variance, which are explored to establish natural frequency f_n as the candidate feature for discrimination by studying its sensitivity to change in input parameters. The damage trend from the change in natural frequency for each damage class is further studied to ensure that the manually selected feature is suitable to distinguish healthy and damaged data. Numerical crack propagation is also briefly explored in which discrete crack lengths are manually modelled to describe the damage trend more effectively.

Chapter 4 focuses on damage detection and identification by relating the natural frequencies f_n of healthy cases and different damaged cases (i.e. damage classes). This discriminant feature is characterized for each mode by establishing the level of separability between different classes. This is achieved through exploring the data distributions in a one-dimensional space. This is further enhanced by exploring the tendency of classes to form distinct clusters in a two-dimensional space, reinforcing the damage-specific behaviour. This allows quantification of the confidence in the suitability (i.e. quality) of the modal property, natural frequency, to be used as discriminant feature. The feasibility of the proposed method is determined through a series of hypothesis tests, which are formulated from the research questions that considers the detection and identification of geometrical variability in the healthy blades and damage scenarios. The validity of each hypothesis is tested using a classification procedure applied on the experimental data in a two-dimensional space. Lastly, a low-cost classification model is briefly investigated in which FEM is used as training data to establish its possibility as a supplementary or substitution dataset. This allows for a final verdict on the feasibility of this damage classification approach. The conclusion and recommendations are presented in Chapter 5.

Chapter 2: Design of Experimental Procedure and Finite Element Model

In this chapter, the experimental procedure is designed along with building the healthy numerical model to establish a baseline or benchmark for this investigation. A brief summary of the layout and the required equipment for this procedure, as well as the FEA model validation are provided. Throughout this chapter, ANSYS Workbench R19.0 was employed to perform all the simulations, and MATLAB R2015b was used to process the data. The CAD model was generated using SolidWorks 2015.

2.1 Basic Information on Test Blades

The experiments made use of a set of 36 (discarded) stage 2 LP pinned turbine blades. These blades have different service lives and are not necessarily from the same installation. MAN Diesel & Turbo (MDT-ZA) declared the blades healthy after magnetic-particle inspection (MPI). Various surface indications were detected; however, none were identified as critical surface defects, particularly in the root and on the aerofoil. While the blades do show slight deterioration due to operational usage, they are not damaged and are referred to as healthy in this study. The blades contain visible geometrical differences from manufacturing, detuning or individually reamed holes for pin insertion during installation (Dewey and Lam, 2008; Rama Rao and Dutta, 2012). These include variability in the root pinhole diameters, correctional grinding on the root, varying aerofoil-edge thickness, and combinations. Since the varying aerofoil-edge thickness is difficult to quantify, it was not considered in this study. The location of the stage 2 blade in a LP turbine section is shown in Figure 2.1. The typical blade material properties are provided in Table 2.1, and a typical geometry of a stage 2 pinned turbine blade, which was procured along with the discarded blades, is shown in Figure 2.2. For additional information, the reader may wish to consult (Booyesen et al., 2015; Plesiutchnig et al., 2016).

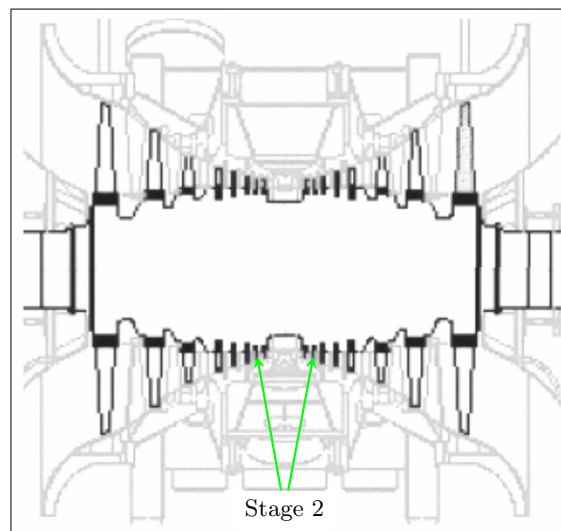


Figure 2.1: Typical construction of dual-flow LP steam turbine rotor and location of stage 2 blade (Shukla and Harsha, 2015)

Table 2.1: Material properties of X20Cr13 (AISI 420 – Martensitic Stainless Steel)

Property	Symbol	Value	Unit
Temperature*	T	20	$^{\circ}C$
Elastic Modulus*+	E	190 – 215	GPa
Density*	ρ	7700	kg/m^3
Poisson's Ratio*+	ν	0.27 – 0.3	–
Yield Strength*	σ_y	760	MPa
Tensile Strength*+	σ_{ts}	770 – 930	MPa
* (Vaishaly and Ramarao, 2013)			
+ (Search Steel, 2013; Plesiutchnig et al., 2016; SIJ Metal Ravne d.o.o, 2016)			

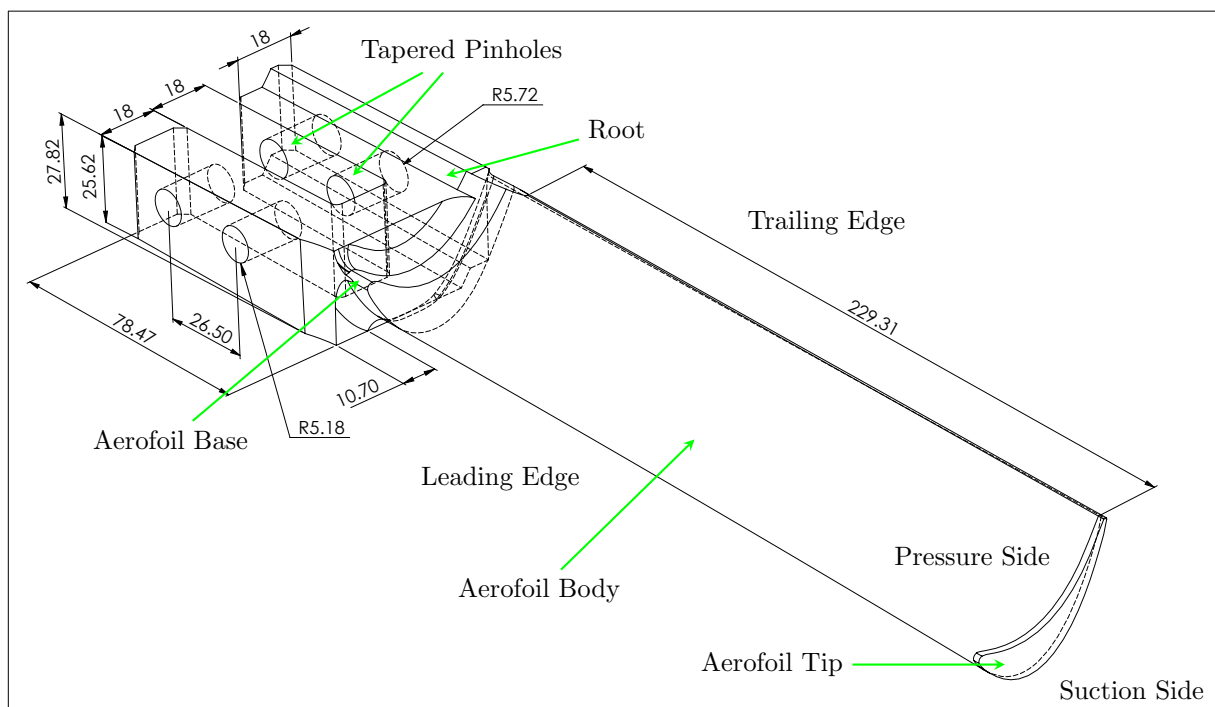


Figure 2.2: Labelled CAD geometry of a typical stage 2 pinned turbine blade

2.2 Experimental Modal Analysis - Design and Set-up

The accurate acquisition of frequency response functions (FRFs) for these individual blades is essential for obtaining reliable modal information. This was ensured by a repeatable and reliable experimental design and set-up for free vibration analysis. The blade was isolated from the environment by using a non-contact and free-free configuration set-up with implied light or negligible damping from suspension by elastic bands. The elastic bands have implied minimal stiffness and little damping. To ensure a controlled and more stable set-up, the blades were rested on top of the elastic bands. Since this is a feasibility study, the decision on the experimental design is based on the first level for model validation by frequency and vibration testing of turbine blades found in the EPRI standards (Dewey and Lam, 2008). This entails impact testing of individual blades with appropriate boundary conditions (i.e. in a free-free state of suspension), removed from the bladed disk. According to Zhou et al. (2016), in using a free-free configuration during testing above other boundary conditions (e.g. cantilever or simply supported), the influence induced by boundary conditions and environmental uncertainties can be negated, making it the preferred option. This configuration is also utilised during the quality assurance and control operation of individual blades through impact vibration tests (Dewey and Lam, 2008).

The literature survey revealed that the natural frequencies are superior to the other modal parameters and will thus be considered in this study. Since natural frequencies have a global nature, their acquisition is not dependent on multiple points and thus a single-input-single-output (SISO) system was used. This utilised a laser Doppler vibrometer (Polytec PSV400) for measuring the vibration velocity at a specific point, and a modally tuned steel-tip impact hammer (PCB Piezoelectric, 086 C 03, SN 8131) for mode excitation at a specific point. These points were established by a trial-and-error approach to guarantee sufficient energy transfer for maximum mode participation and observation. This maximum number of modes was determined from numerical modal analysis on a preliminary basic FE model of the blade. A reasonable large bandwidth was considered as the frequency range was not predefined. During the trial-and-error approach, the number of modes identified within the selected bandwidth was desired in the experimental results. The configuration settings of the experimental set-up are provided in Appendix A. The schematic of the experimental design is provided in Figure 2.3, and the experimental set-up is shown in Figure 2.4.

2.2.1 Experimental Protocol

Modal analysis is a function of input excitation and output response measurement of the impact test object. Thus, it is essential that the input and output variables as well as the object set-up variables are properly described in terms of setting up the non-contact impact test. The output measurement variables depend on the laser vibrometer. The laser head was adjusted in parallel with the XY-plane to a meaningful stand-off distance of 915mm from the measurement plane. Within the software, a scanning grid was added over the blade surface to ensure a consistent scanning region, with only the single measurement point enabled. The laser was then centred to ensure that its beam is perpendicular to the measurement plane. The optimal signal was ensured by autofocusing the camera on the scanning region as well as the laser on the reflective dot. This dot was placed on the slight curvature of the blade, i.e. at a slight angle from the measurement plane, to capture in-plane and out-of-plane motion. This ensured maximal observation of modes.

After the laser vibrometer preparation is completed, the blade set-up variables must first be attended to before the input excitation variables. This entails the alignment procedure of the blade within the testing frame. In the set-up, elastic bands suspend the blade at the bottom pinholes of the root and the aerofoil tip. At the first location, an elastic band was inserted through the bottom pinholes to ensure that the orientation of the bottom flat surface of the root (suction side) can be aligned with the XY-plane (the floor). This alignment was done through using a level tool and adjusting the length of the elastic band accordingly. The level tool was placed so that its mass distribution has minimal effect on the orientation. At the second location, the length and curvature of the band was designated by first resting the aerofoil tip on top of it. The predefined measurement location (reflective dot) was used as a pivot point during the alignment procedure through ensuring that the laser point stays pointed in the centre of the reflective dot. Then this band was fixed to the testing frame by a wire in that set position. This ensured that when the blade was added to the set-up, the interference from the tension in the band was minimal. The elastic bands were configured so that the blade is only kept in place, thus it is assumed that the blade has free but controlled movement. Hence, the boundary conditions complied with the freely suspended state. The predefined excitation point was also marked on the blade (black spot).

After the blade set-up preparation is completed, the testing can commence. The input excitation variables depend on the impact from the modal hammer, which is dependent on the operator. Consistent excitation required meticulous care by the operator to ensure nearly identical and controlled impact attempts. This includes consistent body position (standing), hammer orientation (tip parallel to XY-plane), hand support (hand/middle fingernail sliding against frame support) and launching and landing distances from the excitation point (before and after impact). The combined success of all these factors was evident in the input excitation spectra (force diagrams), i.e. the time pulse and the forcing function. From this observation, these two variables were selected to be used as the indicator for successive impacts by attempting to replicate them during each test. Since the input excitation is operator dependent, it is assumed that this is the only fluctuating variable for this experiment. This successive impact indicator along with a similar output response (i.e. magnitude, peak locations, and noise) was used to evaluate the success of each test for an individual blade. This is explained in the repeatability of the experiment, discussed in the following section.

An overview of the experimental set-up in a controlled environment is given in Figure 2.4a, showing the test blades, the testing frame, and the laser vibrometer with the data acquisition equipment. A more detailed view of the testing frame is given in Figure 2.4b and Figure 2.4c, showing the freely supported set-up, the excitation- and measurement point, modal hammer, the level tool, and the isolated test blade.

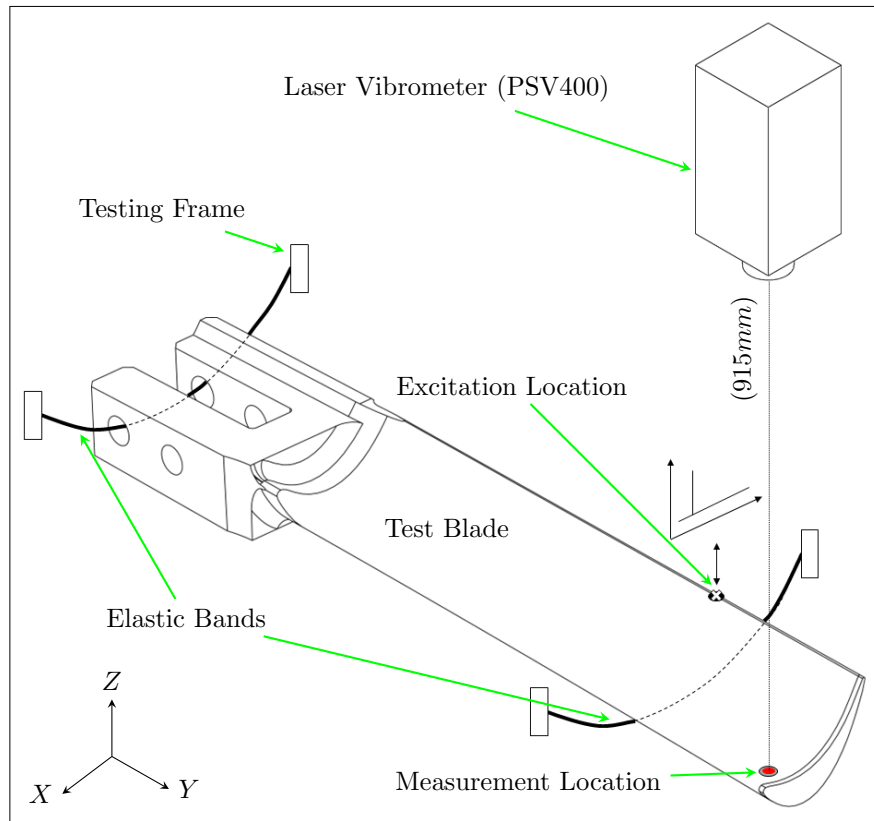
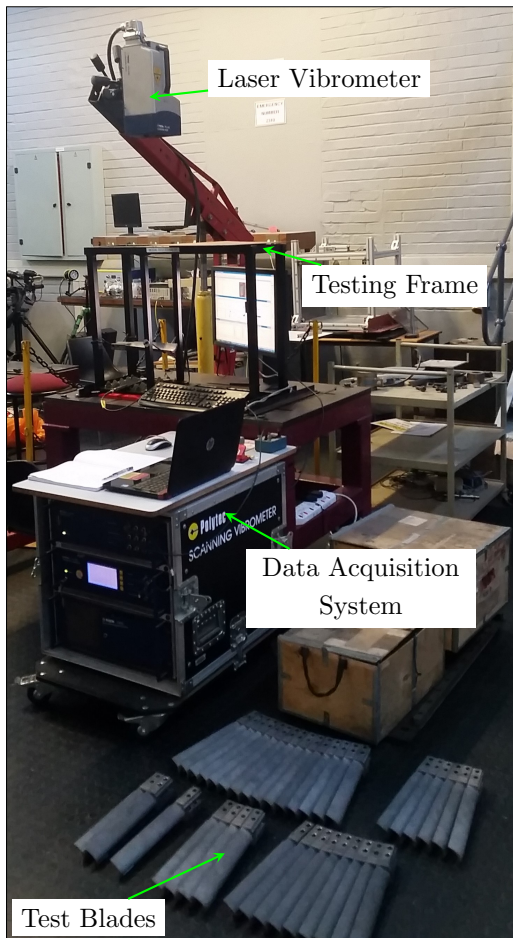
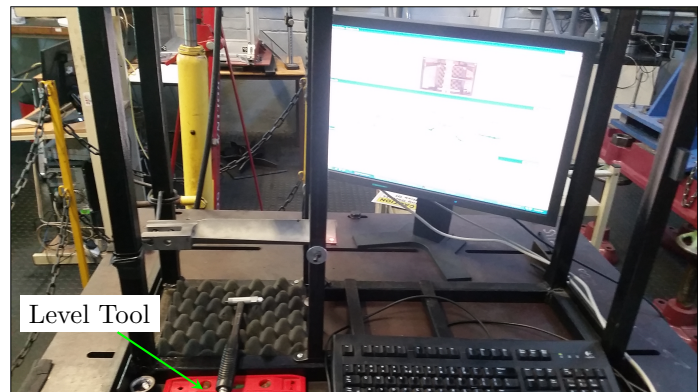


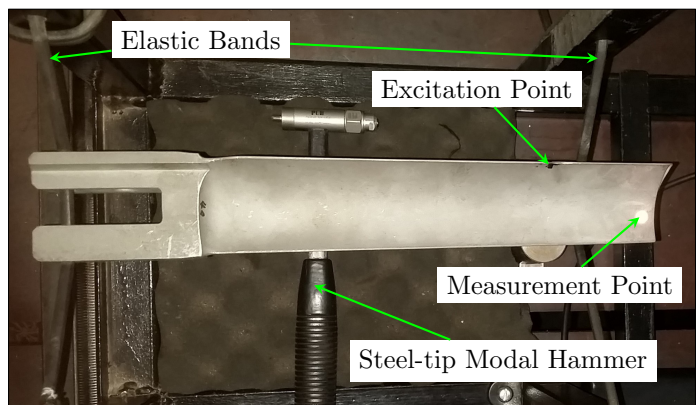
Figure 2.3: Schematic of experimental design for freely supported modal analysis with coordinate system



(a)



(b)



(c)

Figure 2.4: Experimental set-up in controlled environment , a) Overview; b) Detailed view of testing frame with suspension set-up; c) Isolated test blade with excitation- and measurement-point and steel-tip modal hammer

When performing impact vibration tests, there are many main aspects to consider, however, three of these are most critical. First, the selection of the hammer tip, which controls the input excitation frequency range. The hardness of the tip determines the modes to be excited by the impact force over the considered frequency range. Second, the use of an exponential weighting function or window for the response transducer. This window forces the measured data to better satisfy the periodicity requirements of the Fourier transform process and thus minimizes the distortion effects of leakage. Third, the selection of a narrower frequency bandwidth of interest, depending on the number of modes of concern, and an increase in the number of spectral lines of resolution. Both these signal-processing parameters have the effect to increase the required amount of time to acquire a measurement as well as reduce the effects of leakage, and possibly the use of an exponential window (Heyns, 2008; Avitabile, 2014; Inman, 2014).

The raw data, obtained from sensors (i.e. laser vibrometer and modal hammer), is signal processed to extract features. This entails data cleansing and de-noising through filtering and preliminary dimensional reduction of data vectors by domain conversion. With domain conversion, the domain of the measured data is transformed from time to frequency using Fourier transform and/or from frequency to modal using modal property extraction methods. The modal domain is independent of time (Worden and Dulieu-Barton, 2004). With time- to frequency domain conversion, the loss of information is negated through averaging of the effects of random noise (Kong et al., 2017). This conversion is applied within the analyser software (i.e. Polytec PSV400) along with further signal processing for both the input and output signal. This includes anti-aliasing filters, exponential windowing, computation of FFT, averaging of samples, and computation of averaged power spectra. The product is a low-noise FRF as the direct output.

A detailed FRF with a large bandwidth is central to this investigation and was achieved by using a steel-tip modal hammer, ensuring adequate levels of energy and excitation, and a fine frequency resolution of $390.625mHz$ over a bandwidth of $0 - 10kHz$ (25 600 spectral lines of resolution) to accurately capture the peak locations of the measured FRFs, i.e. natural frequencies. From the preliminary basic modal analysis of the FEM blade, which considered the same bandwidth, 14 non-zero modes or natural frequencies were calculated, and thus the experimental set-up was configured to effectively capture the same number of modes. Hence, 14 modes will be considered in this study, and will ensure that a comprehensive number of modes are available for analysis.

2.2.2 Repeatability of Test

An experimental protocol or methodology was developed to evaluate the repeatability of the test, following the guidelines set out by Avitabile (2014) for conducting proper impact testing. The test was repeated on a single test blade until the best-suited procedure was established for repeatable results. This was then implemented on the complete test set. The methodology ensured that if there were uncertainties or systematic errors, they were present for every test. This enhanced the consistency regarding the procedure and measured responses.

During the development of the methodology, it was necessary to determine how to control the variables present in the experimental procedure. The output response measurement variables were identified from the laser vibrometer and were controlled by its arrangement. The orientation of the blade during the set-up was identified as an important set-up parameter and was controlled by an alignment procedure. The input variables were identified from the input excitation (i.e. time pulse and forcing function). These were controlled by a meticulous operator-dependent approach in which it was attempted to replicate the impact signal. To evaluate the success or repeatability of a test, the impact signal was used as the successive impact indicator along with a similar output response for each test (i.e. magnitude, peak locations, and noise). The configuration of the instrumentation was also fine-tuned during this process. It was observed that the repeatability of the results, and the test itself, are dependent on the following:

- The output response measurement (laser vibrometer), which includes the measurement location.

- The set-up itself, which includes the test object orientation that has an effect on impact and measurement angles.
- The input excitation (modal hammer), which includes the force velocity, location and angle as well as the tip contact stiffness.

These observations concur with observations by Avitabile (2014). Now, considering the experimental variables, it is assumed that only the impact excitation fluctuates as it relies on the operator. This is because the orientation of the blade and laser vibrometer can be controlled by an alignment procedure. The measurement angle is also dependent on the laser vibrometer. Even though the input excitation location is also specified, consistent excitation here is still dependent on the operator. This was identified as the main influence on the output response shape and noise level. This is because the energy distribution determines the level of excitation and coherence. The coherence function is a measure of the linearity and noise – characterising the relationship between the measured system input and output signals at each frequency, thus quantifying the quality of the FRF measurement at each frequency. In assuming that the output variables are controlled and thus constants, good or sufficient impact will ensure good coherence and thus a good FRF measurement. The desired input excitation forcing function for a ‘good’ impact is provided in Figure 2.5. This has an evenly distributed amplitude and reasonable roll-off over the frequency range of interest. This renders the optimal coherence function. The correct hammer tip ensures that adequate input force is applied to the structure to excite the full frequency range of interest. Preferred impact excitation practice and the operator influence on the impact are discussed in more detail by Avitabile (2014); Siemens (2016b) and were considered in the design of the experiment.

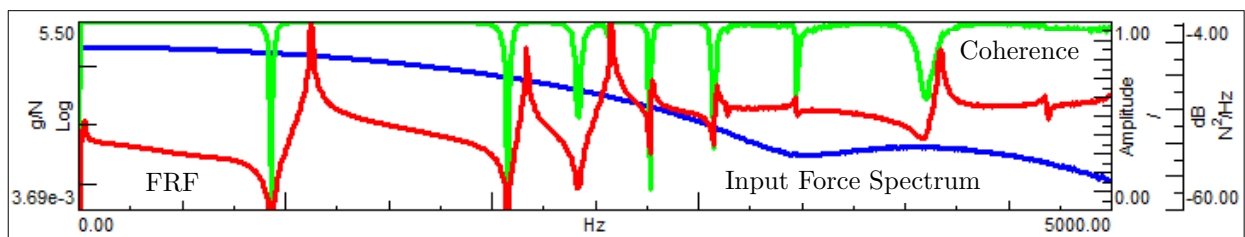


Figure 2.5: Preferred input spectra for a high quality frequency response function (FRF) measurement, Blue: Input force spectrum; Green: Coherence; Red: FRF (Siemens, 2016b)

Tests were conducted on a single blade to develop and evaluate the testing procedure regarding its repeatability, considering the factors mentioned above, as well as reliability. To obtain an accurate FRF and an acceptable test result, the test was repeated for each blade until at least three similar outputs were obtained, after which their average was taken. This demanded many tests as unsatisfactory results were discarded. The approach in establishing the protocol is based on best practices (Avitabile, 2014; Siemens, 2016b) and was developed by comparing the following:

1. Repetitive testing (test repeat)
 - A single blade is set up on which tests are conducted.
 - Impact is the only variable (single set-up).
 - The aim is to define behaviour of impact variable.
2. Subsequent testing (test reset)
 - A set-up-restart per blade on which tests are conducted.
 - Impact and orientation are the variables (set-up restart).
 - The aim is to define behaviour of orientation variable.

This comparison was required to prove that the result of resetting the test correlates with the result of repeating the test. This would then allow different blades to be compared by using the same experimental set-up and testing procedure. The same blade was used in both methods, so that the only variability present would be from the set-up and the input. It is important to note that no reference signal was available to which the results could be compared. Therefore, by using similar results per blade per test, a reference or

confidence rate was established. The repeatability results for a single healthy blade are provided Figure 2.6 below for a single healthy blade in which four sets comprising three tests each are shown. The measured FRFs are plotted with the measured input forcing functions for each set. The dark lines show the average of each set, whereas the faint lines show the individual tests per set. Note that inter-test variability is present within the results due to geometrical variability in the blades. Additionally, not all the tests were conducted on the same day and the test temperatures (room temperature) were not controlled.

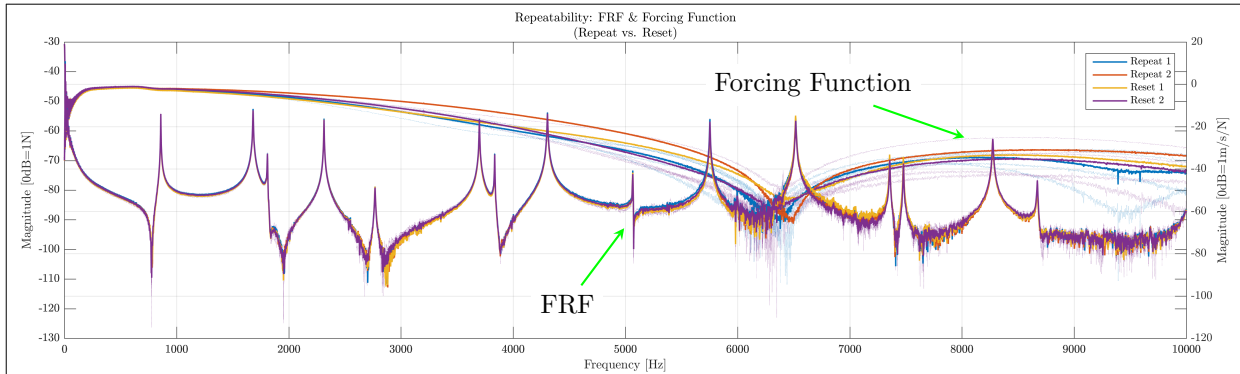


Figure 2.6: Repeatability results from developed methodology showing FRFs with input excitation forcing function for a single healthy blade

It is evident in Figure 2.6 that the blade substitution (test reset) correlates well with the test repeat and stable results for both cases were obtained. It is also very effective to conduct tests until at least three similar results are obtained, especially since no reference is available. It confirms that the orientation variable can be controlled and considered as a constant, leaving only the input variable to which attention must be directed. It is observed that the input excitation forcing function compares well to the preferred shape of a 'good' impact in Figure 2.5, which delivers good coherence and thus good FRF measurements. Thus, this demonstrates that by attempting to replicate the input excitation per test, the success rate of each test can be evaluated when comparing between tests per blade for each set. The selected steel-tip is also adequate in exciting all the modes in the considered frequency range of interest and delivers a good measurement that shows 14 easily identifiable peaks. It is also clear that at the higher frequencies, some variance in the measurements exist when compared to the lower frequencies. The FRFs are noisier beyond 6000Hz due to the plunging energy input amplitude. This is because the stiffness of the hammer tip is incapable in providing constant amplitude beyond this point. However, this does not significantly influence the peak positions and thus all 14 peaks can be regarded.

After concluding that the test is repeatable, all the blades were tested consecutively using the developed methodology. The superimposed FRFs along with the input excitation forcing function for all healthy cases are shown in Figure 2.7. A large frequency spectrum with a fine frequency resolution is shown with 14 easily identifiable frequency modes. Note that even with a fine frequency resolution to ensure definitive peaks, noise is introduced and slight inconsistencies are present in the results regarding the shape, magnitude, and possibly the peak-positions. This is due to operator-dependent input excitation. To compensate for this, the average for all the tests for each blade is considered, and the troughs are smoothed. This reduces the noise present in the signal and amplifies the participating modes, which simplifies the peak extraction procedure.

From Figure 2.7, it is evident that the experimental protocol delivers repeatable and reliable results for the complete set of test blades. The input excitation forcing function is well represented by its mean, which demonstrates the reliability of the testing procedure. This curve shows consistency in the required energy distribution for maximal mode participation and observation throughout the tests. It is also worth mentioning that the energy level decreases beyond 6000Hz , causing noisier results above 6000Hz . However, the peaks are prominent and thus this influence is deemed minimal. Important to note is that inter-test variability is present within all the results for the different blades. This is due to operator-dependency and that the tests were conducted over a span of a few days, which resulted in slightly differing magnitudes from minor inconsistent impact applied during the experiment. This, however, does not affect the peak-positions.

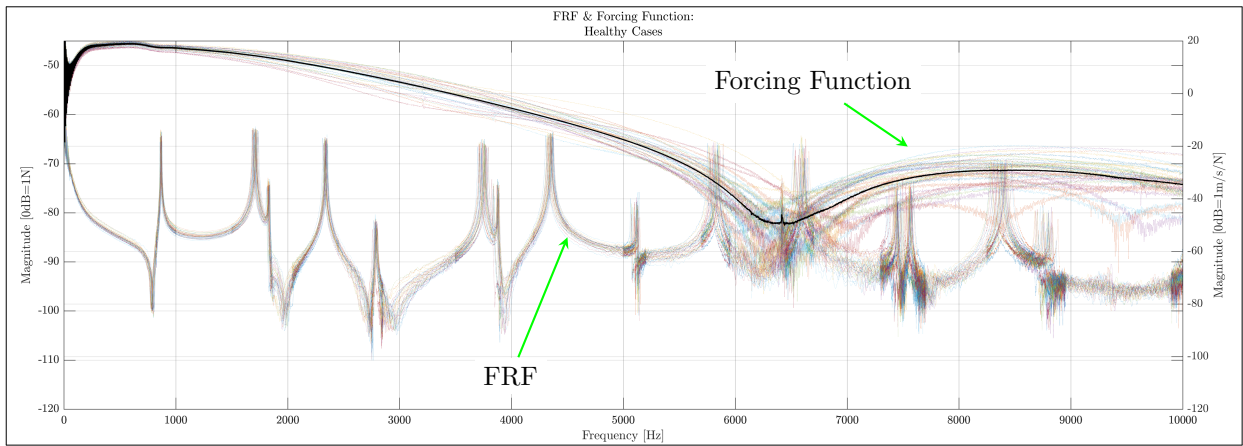


Figure 2.7: Repeatability results showing FRFs with input excitation forcing function for the complete test set

2.2.3 Definition of Benchmark Result

Three of the healthy blades were selected - blades #16, #22, and #31 - to establish a benchmark result to use in the FE model validation. During visual inspection, it was observed that these blades have undergone the least geometric modification and are thus considered the 'healthiest' or the benchmark cases. The experimental benchmark is the average of the results of these cases. Figure 2.8 shows the experimental benchmark FRF along with the benchmark cases. From Figure 2.8, it is clear that the FRFs of the selected three blades are very similar in shape, magnitude, and have comparable peak positions. Hence, these cases are well represented by the experimental benchmark. The benchmark frequencies, calculated from the mean of the extracted peaks (f_n), are listed in Table 2.2.

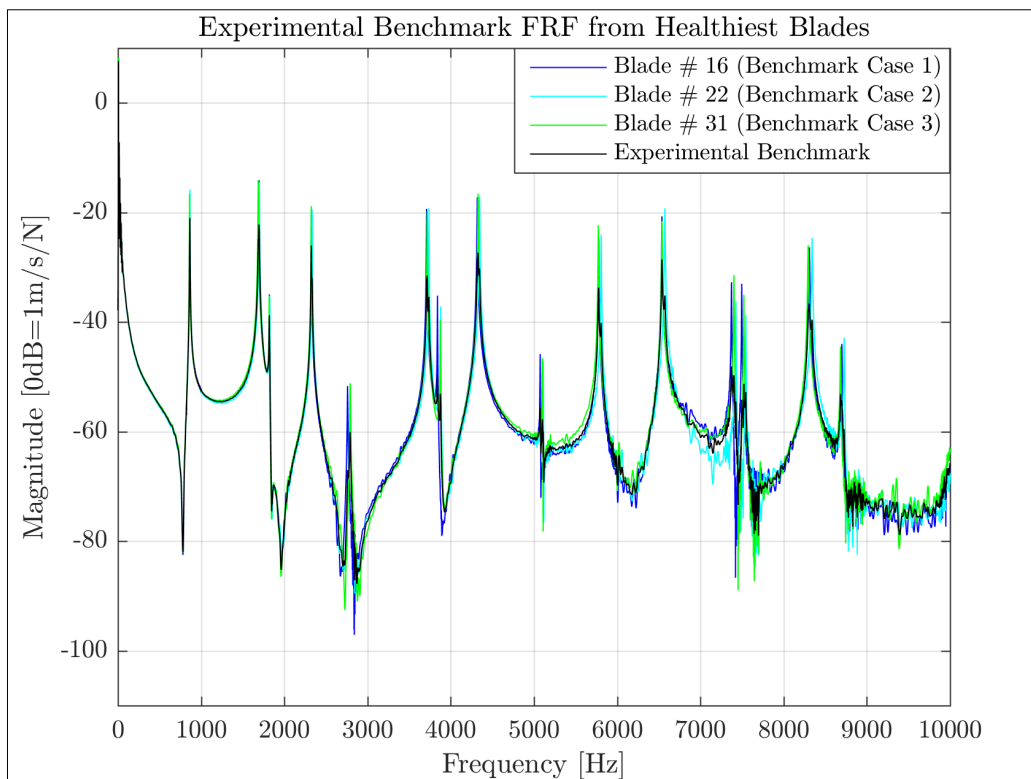


Figure 2.8: FRFs from the 3 healthiest blades used to calculate the experimental benchmark FRF

Table 2.2: Natural frequencies of the 3 healthiest blades used to calculate the experimental benchmark frequencies

Mode #	Natural Frequencies [Hz]			
	Blade #16	Blade #22	Blade #31	Benchmark
1	864.8	865.6	860.9	863.8
2	1694.5	1699.2	1685.9	1693.2
3	1819.1	1825.4	1818.4	1821.0
4	2322.3	2334.8	2323.0	2326.7
5	2759.8	2788.7	2792.6	2780.3
6	3709.0	3736.7	3716.0	3720.6
7	3840.2	3878.9	3873.8	3864.3
8	4318.0	4346.5	4327.7	4330.7
9	5074.2	5110.9	5101.2	5095.4
10	5777.0	5807.4	5772.7	5785.7
11	6537.1	6573.0	6537.9	6549.3
12	7371.9	7425.0	7401.2	7399.3
13	7497.3	7545.3	7522.3	7521.6
14	8309.4	8341.8	8294.5	8315.2

2.3 Numerical Modal Analysis - Development and Validation

In this section, a finite element model of the blade is described that is based on the chosen experimental set-up. The blade model is validated by comparing the predicted modal response with experimental results. This model will be used in Chapter 3 to study the sensitivity of the blade modal response to geometric variability and damage. The procedure and modal analysis results of the FEA are discussed and compared to the benchmark (most geometrical unaltered) experimental result. Note that the FEA model represents a healthy new blade in perfect condition without any defects.

2.3.1 FE Model Set-up

The experimental set-up of a freely supported (suspended) blade was modelled in finite element software, ANSYS R19.0, as shown in Figure 2.9. The CAD geometry (Figure 2.2) was acquired along with the procurement of the test blades. To obtain reliable results from the 3D FEA model, which will be compared with the experimental case, the simulation model and its parameters must represent the experimental set-up. The boundary conditions are essential. Since the blade is freely suspended, the blade is considered unconstrained (i.e. free boundary conditions). The model will thus experience rigid-body-motion (RBM) for the first six modes. Their natural frequencies approximate zero and will be ignored after confirmation. In the numerical modal- and harmonic response analysis of the healthy cases, the system is assumed to be linear. No contact definition is required other than the contact-based connection (bonded) between the root and aerofoil; however, this is linear.

After performing a parametric study on the material properties with a preliminary adequate mesh using modal analysis, Table 2.3 was compiled. The material properties of X20Cr13 (Table 2.1) were adjusted until agreeable values were obtained that delivers an accurate model validation. These properties are assumed to have linear elastic behaviour. It was observed that the natural frequencies are very sensitive to the change in geometry and material properties since stiffness k is a function of both these properties of the model, considering that $f_n = \sqrt{k(E, geom)/m(\rho, geom)}$, with E (elastic modulus) having the greatest effect.

Table 2.3: Selected material properties used in FEA modelling

Property	Symbol	Value	Unit
Elastic Modulus	E	210	GPa
Density	ρ	7700	kg/m ³
Poisson's Ratio	ν	0.29	—

Take note that a minor difference in geometry at the aerofoil tip of the test blade and the FEA model exists. A thin lip protrudes from the blade profile edge in the length of the blade on the suction side. However, only the aerodynamics of the blade is affected, which is not relevant to this study. This difference in mass, if any, can be disregarded as it will have minimal effect on the natural frequencies.

The meshing is essential for producing accurate results and must be optimized. The blade was decomposed into a root-section and an aerofoil-section, which were then meshed separately according to priority of the geometric profile to reduce the number of nodes for a reduced solving time. Since the blade was decomposed, bonded contact was applied between the two sections. To account for the complex geometry, such as variation of twist, taper, width and thickness along its length, and ensure adequate quality and appropriate piece-wise linear or quadratic meshing for each section, the smoothness of the mesh regarding shape and geometry was considered (Bhat et al., 1996). Using the built-in tools in ANSYS, the meshing was done as follows: Quadratic tetrahedral elements (TET10) with kept mid-side nodes were used on both sections. The patch independent method with coarse proximity and curvature sizing functions and high smoothing with slow transitions were also applied on both sections. To further enhance the mesh quality, sizing functions and virtual topology were applied to the different sections where necessary. Mesh convergence was achieved, which ensured equilibrium between solving time and accuracy. The root section consisted of 23 879 nodes and 15 210 elements, and the aerofoil section of 69 800 nodes and 42 836 elements.

2.3.2 Modal Analysis and Harmonic Response Analysis

Modal- and harmonic response analysis were performed on an ideal FEM blade to obtain the natural frequencies and its FRF, respectively. The modal analysis result was used as input for the harmonic response analysis. The numerical natural frequencies and the corresponding mode shapes of an undamped system are computed through applying the theory of elastic dynamics and solving the eigenvalue problem (Equation 1.2 and Equation 1.3).

The suspended blade in the FEM environment is shown in Figure 2.9 along with the excitation- and measurement point. The locations of these points were replicated from the test blades used in the experimental set-up and are shown in detail in Figure 2.9b. In the FEM, a remote (unit) force of $-1N$ was applied in the $+x$ -direction at the excitation point, allocated by a global coordinate system. The frequency response of the directional velocity in the x -direction was measured at the measurement point, represented by a mesh node found at the midpoint of the reflective dot used in the experiment. A broad frequency range of $0 - 8750Hz$ was used, in which 14 modes were considered for the validation. The PCB Lanczos modal solution method was applied for both modal- and harmonic response analysis. Global damping was not considered in the model since it is implied that the experimental set-up is very lightly damped.

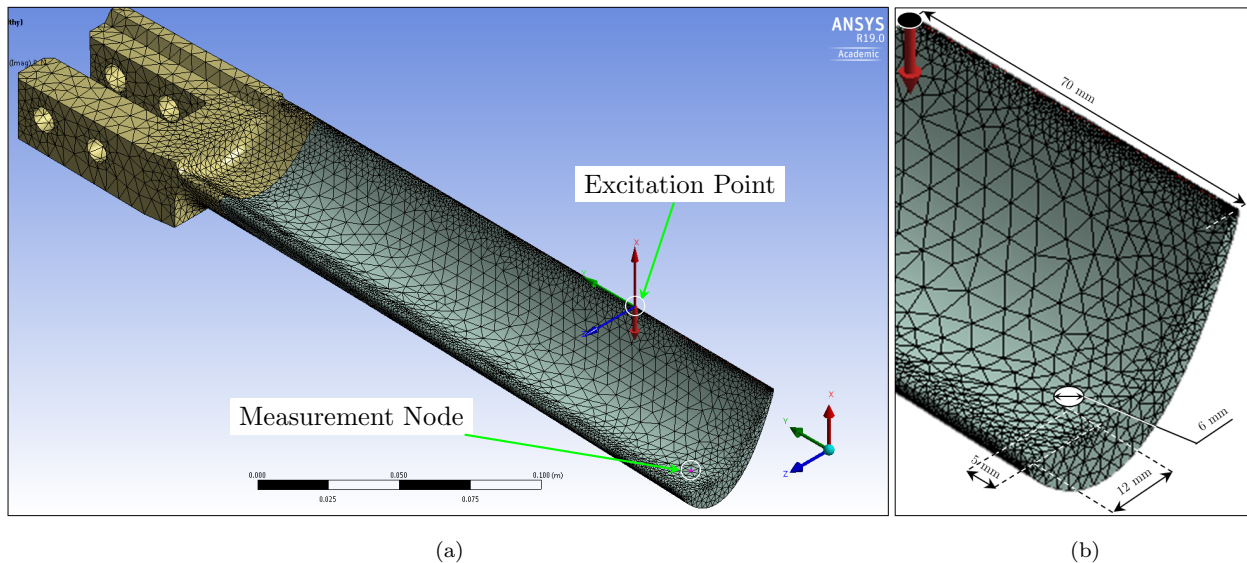


Figure 2.9: Meshed geometry and set-up in FEM environment prepared for harmonic analysis, a) Overview; b) Detailed excitation- and measurement location obtained from experiment (black and white dots, respectively)

2.3.3 FE Model Validation

For validation of the numerical blades, the FEM results were compared to the benchmark experimental result as defined in Section 2.2.3. The FEM and the benchmark FRFs are plotted in Figure 2.10. Note that the FEM FRF only consists of 500 points compared to the experimental FRF of 25 600 points or spectral lines over the full frequency bandwidth. Additionally, only the first 14 natural frequencies were considered within the large bandwidth. Thus, the FEM FRF is interrupted at 8750Hz . The FEM FRF is measured in velocity (m/s); however, decibel (dB) is generally used in the measurement of vibration and was originally defined in terms of the base 10 logarithm of the power ratio of two electrical signals. This corresponds to the ratio of the square of the amplitudes of the measured signal (A) and the reference signal (A_0) (Heyns, 2008; Inman, 2014). In this case, $A_0 = 1$ and $A = A_{measured}$ in m/s :

$$dB = 10 \log_{10} \left(\frac{A}{A_0} \right)^2 = 20 \log_{10} \left(\frac{A}{A_0} \right) = 20 \log_{10} \left(\frac{A_{measured}}{1} \right). \quad (2.1)$$

In Figure 2.10, each magnitude has peaks corresponding to the natural frequencies of the respective cases. This is because the response is 'normalized' to the input and the peaks are not a consequence of this but is a physical property. Since the benchmark FRF was computed from the benchmark cases, multiple peaks are observed. However, the benchmark frequencies are the mean of these values, and thus these peaks should not be explicitly considered. When comparing the shapes of the FRFs, it is evident that the FEM shape captures the general shape of the benchmark and is thus equivalent. Within the FEM model, damping was not considered. Thus, when comparing the FRF peak widths, the claim of very light or negligible damping in the experimental system is supported. This is because the damping can be estimated by considering the width of the peaks about their maximum value at the $3dB$ down point (Heyns, 2008; Inman, 2014). Since interest lies only at the peak values and not at the FRF shape, the differences in amplitude, which is relative to the system, as well as the shape can be ignored.

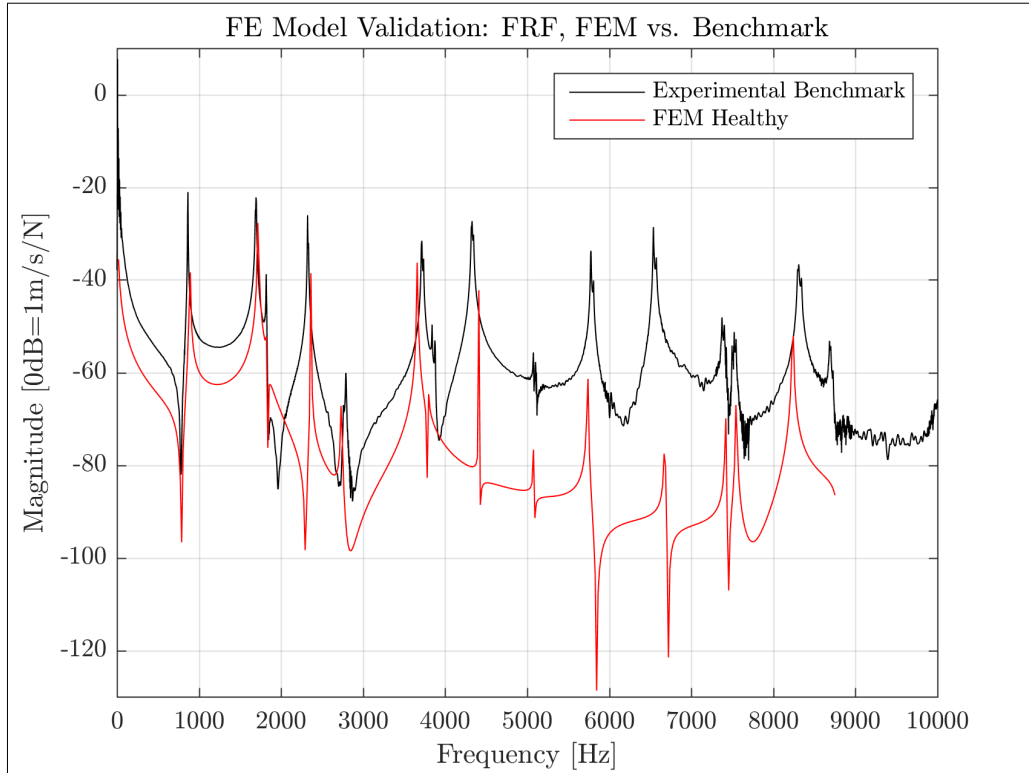


Figure 2.10: Superimposed FRFs for FEA model validation: FEM vs. Experimental benchmark

The benchmark frequencies f_n are compared with the numerically obtained natural frequencies, with the error e_i defined as:

$$e_i = \frac{(FEM_i - Benchmark_i)}{(Benchmark_i)} \times 100. \quad (2.2)$$

And the total error $e_{\mu(abs)}$ is defined as:

$$e_{\mu(abs)} = \sum_{i=1}^n \frac{|e_i|}{n}, \quad (2.3)$$

The frequencies and associated errors are shown in Table 2.4 and plotted in Figure 2.11.

Table 2.4: FE model validation - Comparison of computed natural frequencies with experimental benchmark

Mode #	Natural Frequency [Hz]		Error, e_i [%]
	EXP	FEM	
1	863.8	888.3	2.8
2	1693.2	1719.6	1.5
3	1821.0	1830.7	0.5
4	2326.7	2366.2	1.7
5	2780.3	2747.3	-1.2
6	3720.6	3664.4	-1.5
7	3864.3	3796.1	-1.8
8	4330.7	4414.2	1.9
9	5095.4	5089.5	-0.1
10	5785.7	5741.8	-0.8
11	6549.3	6680.4	2.0
12	7399.3	7415.9	0.2
13	7521.6	7559.8	0.5
14	8315.2	8238.2	-0.9
		$e_{\mu(abs)}$	1.2

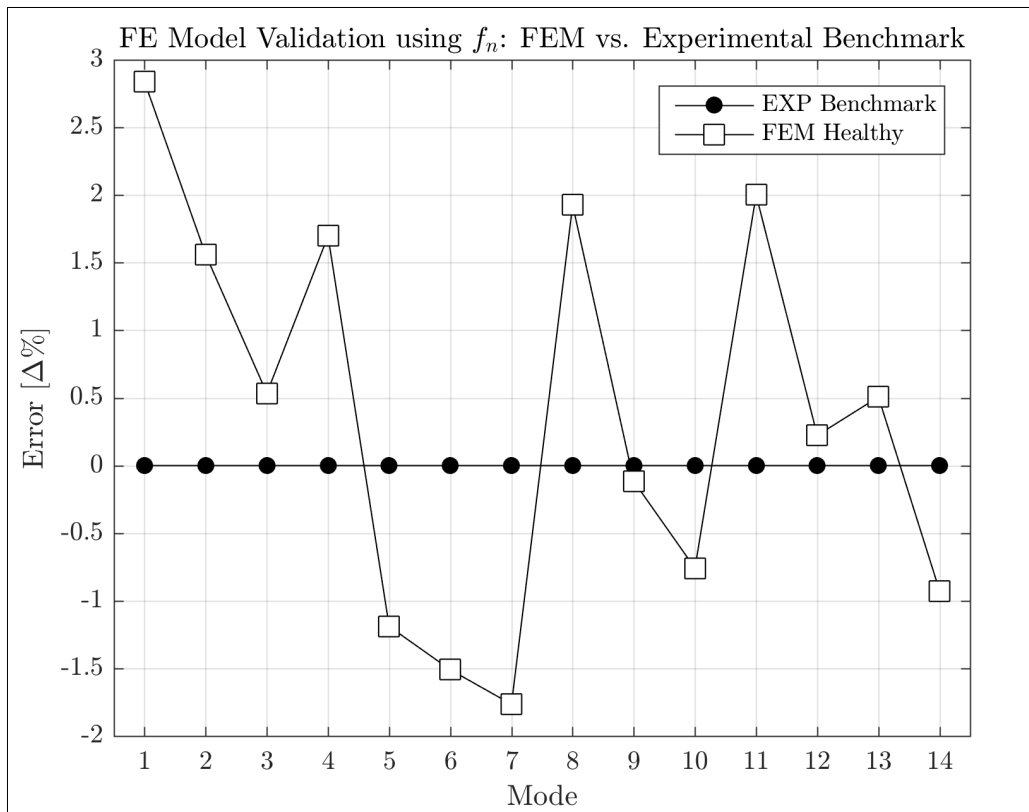


Figure 2.11: Validation error between the computed natural frequencies and experimental benchmark

From Table 2.4 and Figure 2.11, it is evident that good correlation in the model exists as the FEM natural frequencies fall within the frequency range of the experimental results. This is supported by $-2.0\% < e_i < 3.0\%$ and $e_{\mu(abs)} = 1.2\%$. Thus, the system was modelled reasonably well with good representation of all modes from acceptable assumptions made for the numerical model. The highest error of 2.8% was found for Mode 1, while six frequency values are smaller than 1%. These results correlate well with the required frequency ratio of $\pm 3 - 5\%$ in the installed (healthy) blades, deemed acceptable within EPRI standards. This translates to a small margin, generally considered to imply a well-tuned mode of vibration, where the

statistical chance of resonance is likely to be remote (Dewey and Lam, 2008). This standard also references the general uncertainty with any computed natural frequency to be $\pm 2-3\%$ (Dewey and Lam, 2008). Shukla and Harsha (2015) conducted modal analysis on a fir-tree root with unknown health and their FEM, which was compared to the experimental case, contained errors of 1.77%, 2.34%, and -4.15% for the first three fundamental frequencies.

Elastic bands that impose minimal damping in the system supported the blade. However, the elastic band configuration could have possibly introduced slight movement restrictions for the blade during excitation, especially in the first bending mode (normal to the XY-plane). From the results above, this effect can be assumed negligible on all modes. The larger influence on the overall error value can be ascribed to possible reasons such as material properties varying throughout the blade (Scheepers and Booyesen, 2012), and that the FEA model does not consider any indications, flaws or material loss due to altered geometry of the blade.

The numerical model serves only a supportive role since model updating was not part of the scope, and direct association is thus not possible. Hence, only the output behaviour due to the input parameters of the experiment and FEM are compared. Therefore, the errors found in comparing the FEM and the experiment are acceptable as evidence of a reasonably well-modelled numerical blade. This reinforces the idea that the FEM can be compared to the real case to establish expected behaviour from geometrical variability and damage scenarios. This will be discussed in Chapter 3.

2.3.4 Conclusion

The modal analysis results from the 3D FEA ideal blade and the experimental benchmark showed good agreement for Modes 1 – 14. The error between the peaks of the experimental and FEM results is small and a tendency of correlation is observed. It can thus be concluded that the FEA model is valid and can be used forward in the study. These errors may be ascribed to reasons such as light damping from the elastic bands used in the experimental set-up, which was assumed negligible; the material properties that vary throughout the specimens; and ignoring indications, flaws or material loss (altered geometry) in the model. Therefore, the experimental and the numerical cases can be indirectly compared, i.e. only the output behaviour due to the input parameters can be compared, and direct association is not possible since model updating was not part of the scope. Hence, numerical model serves only a supportive role. The peaks of the FRFs are essential to this study. However, to realise the complete effect of the input parameters on the output to establish unique behaviour, the FRFs are used as preliminary visual representation and judgement. The sensitivity of using natural frequencies as a damage indicator, especially on the severity and location in a structure, requires further investigation since the structural damage in different locations may cause the same shift in frequency. The error equation in Equation 2.2 will be modified to calculate the variance in natural frequencies in the work to follow.

Chapter 3: Feature Sensitivity Study

To investigate the feasibility of vibration-based damage detection for pinned turbine blades, an approach to establish the input parameter significance and its trend on the natural frequencies (f_n) was implemented. This approach is demonstrated in Figure 3.1 below. A sensitivity study was conducted (Step 1) using both numerical and experimental results. The sensitivity of FRFs, including their natural frequencies, to slight changes in the blade geometry (i.e. geometrical variabilities) as well as damage (i.e. different damage scenarios) was investigated. The study specifically assessed the potential of using only natural frequencies as a distinctive health status indicator by exploring the damage trend in the blades. In the first part of the Step 1, the geometrical differences present in the healthy test blades were explored so that a reference or benchmark could be established. The second part of Step 1 explored how three single-location damage scenarios compare to the healthy experimental benchmark. These damage cases are at the most likely locations near the root that will lead to failure at some stage in the near future. The study of damage-specific responses enables better description of response behaviour regarding the effect of defects or damage present in a blade. By comparing the experiment and FEM to correlate the significance of the input parameters on the output vibration response, motivation for further investigation can be provided. The mode shapes were also briefly visually explored to attempt to understand their damage-induced behaviour. The objectivity or independence of the natural frequencies was examined (Step 2) by considering the distinctiveness of each damage scenario result. The f_n -trend produced by the geometrical variability in the blades as well as the introduced damage was assessed to ensure that an explicit shift in natural frequencies occurs for each damage scenario. This allowed assessing the potential of using the natural frequencies as a distinctive health status indicator.

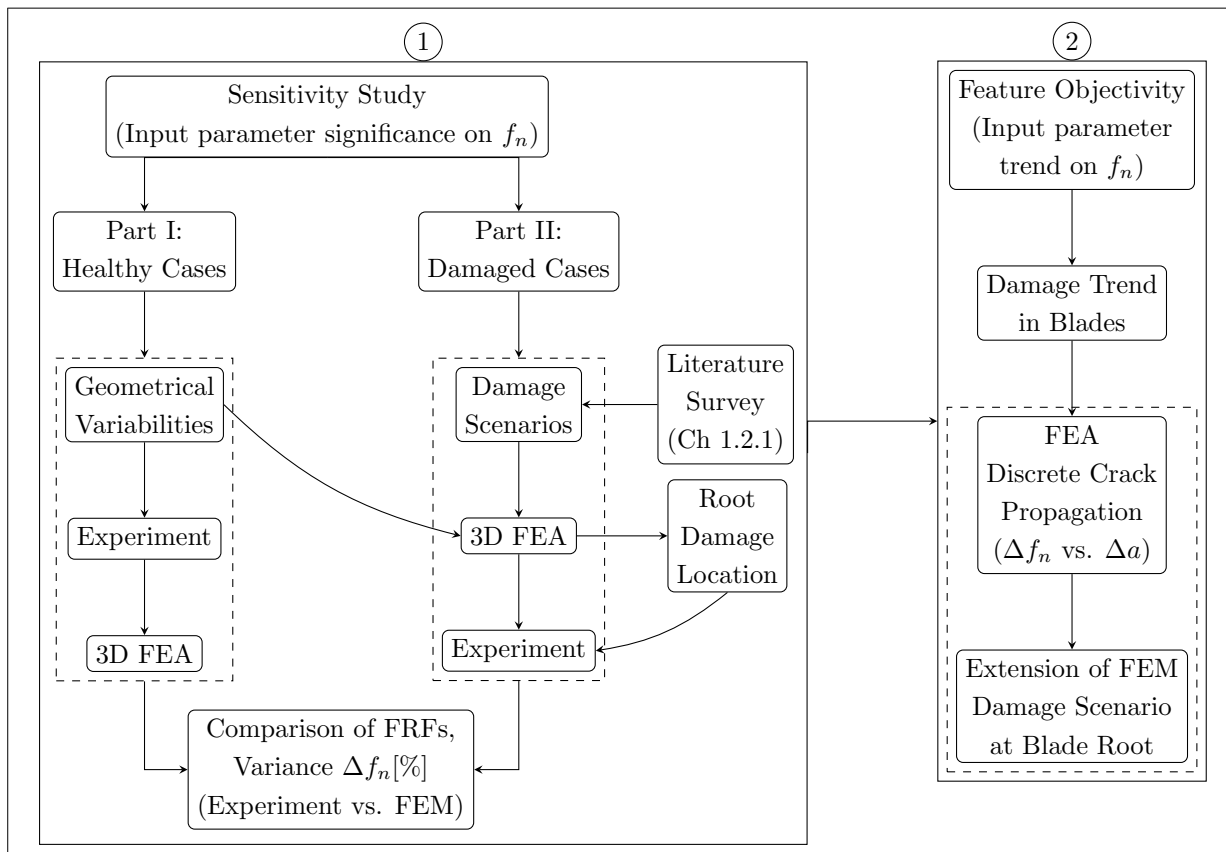
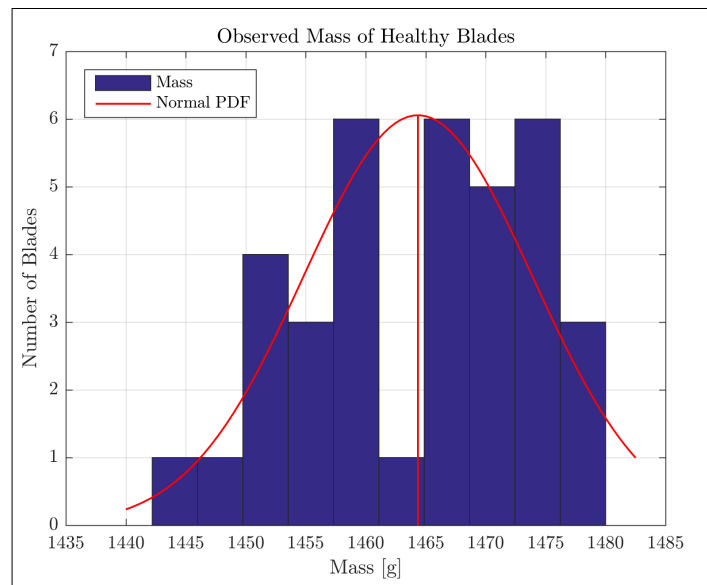


Figure 3.1: Approach to establish input parameter, 1) Significance on f_n ; 2) Trend on f_n

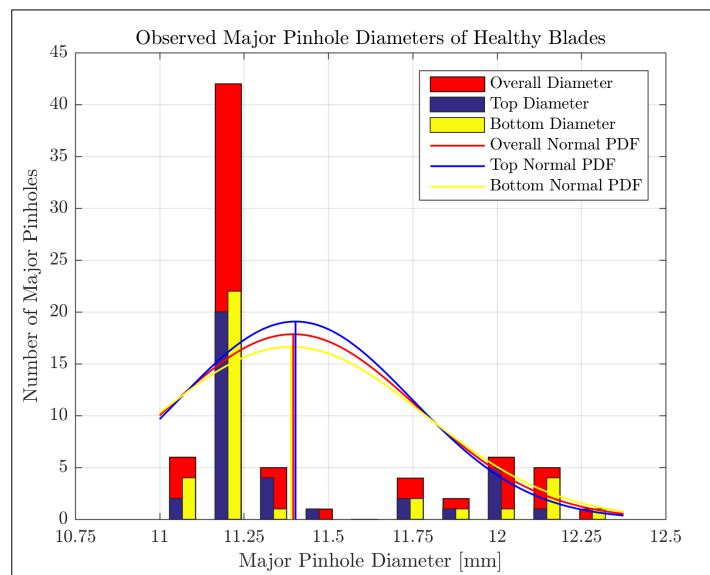
The natural frequencies were extracted from the total amount of FRFs using an automated version of the peak-amplitude or peak-picking method using the MATLAB *findpeaks.m* function. Slight errors were introduced by this since the accuracy of peaks is a function of frequency resolution; however, this was minimized through using a fine frequency resolution.

3.1 Sensitivity to Small Geometrical Variability in Healthy Blades

From the literature (Bhat et al., 1996; Rauschenbach et al., 2008; Drozdowski et al., 2015), discussions with experts in the industry, and observations of the procured blades, it was noted that defects (slight geometric differences) arise in the blades due to the manufacturing process. This variability includes individually reamed holes for pin insertion during the installation stage, and manual tuning through correctional grinding. Quantifications of this variability is provided in Figure 3.2. The variation in the overall blade mass is shown, which is caused by the variation in the pinhole diameters as well as the presence of grinding at the blade root. These quantifications are simplified in Figure 3.3, which gives a summary of the number of blades having minimum and maximum major pinhole diameters as well as those that have undergone manual tuning. More detail on the allocation of specific blades for these categories is provided in Appendix B. Even though the geometrical variability is not considered as damage, its effect on the state of health of the blades must be explored. This is achieved through a FEM-based study on the sensitivity of these small geometric differences on the vibration response. The different visible defects, observed in the test blades, to be modelled are varying correctional grinding depth on the blade root and varying diameters of pinholes. This is shown in Figure 3.4. The properties of the small geometrical variability in the healthy blades are provided in Table 3.1.



(a)



(b)

Figure 3.2: Variation in observed, a) Overall mass of the blades; b) Major tapered pinhole diameters

Table 3.1: Properties of Small Geometrical Variability in Healthy Blades

Statistical Property	Mass, m [g]	Major Pinhole Diameter [mm]		
		Top	Bottom	Overall
Minimum	1442.2	11.0	11.0	11.0
Maximum	1480.0	12.2	12.35	12.35
Median	1466.0	11.2	11.2	11.2
Mean, μ	1464.36	11.4	11.39	11.4
Standard Deviation, σ	9.55	0.35	0.4	0.37

From Figure 3.2a, it is evident that a variation in the mass of the blades exists with a minimum of 1442.2g, a maximum of 1480.0g, and a mean of 1464.36g. As only 36 data points are available, it is difficult to capture the actual distribution of the mass; however, a normal probability distribution ranging from minimum to maximum was assumed. These inconsistencies in the mass may be due to the manufacturing process, the installation procedure or caused during operation of the turbine blades. Considering the manufacturing process, the blades are machined from an extruded piece of material and then polished by hand. These manufacturing tolerances already introduce discrepancies in the mass. Additionally, the material properties may vary throughout the piece of material and the surface finish may be more meticulous in some cases. Considering the installation procedure, the tapered pinholes are individually reamed, and specific blades are manually tuned by correctional grinding at the root. An individual blade may contain a combination of these geometric differences. The variation in mass due to different pinhole diameters is further explored in Figure 3.2b, which shows the variation in the major tapered pinhole diameters. For the top diameters, a minimum of 11.0mm, a maximum of 12.2mm, and a mean of 11.4mm are observed. For the bottom diameters, a minimum of 11.0mm, a maximum of 12.35mm, and a mean of 11.39mm are observed. Thus, the overall mean major pinhole diameter is 11.4mm. It is also clear that more than 50% of the blades have overall pinhole diameters (top and bottom) close to the median of 11.2mm, and that an increase of 10–12% in diameter occurs.

Figure 3.3a shows the number of blades having minimum and maximum major pinhole diameters. The largest major diameter for each blade was assigned into a minimum and maximum group, according to the value falling below or above the median value of 11.2mm, and then totalled. The outcome was 21 blades in the minimum group and 15 blades in the maximum group. This is fairly distributed. Figure 3.3b shows the blades that have undergone manual tuning. The blades were assigned according to the presence of correctional grinding at the root and then totalled. Because the correctional grinding was difficult to quantify as it involves material removal according to a vibration range of the blade, only its occurrence in the blade root was noted. The observed outcome was that 20 blades did not undergo manual tuning at the root whereas 16 blades did. This is also fairly distributed.

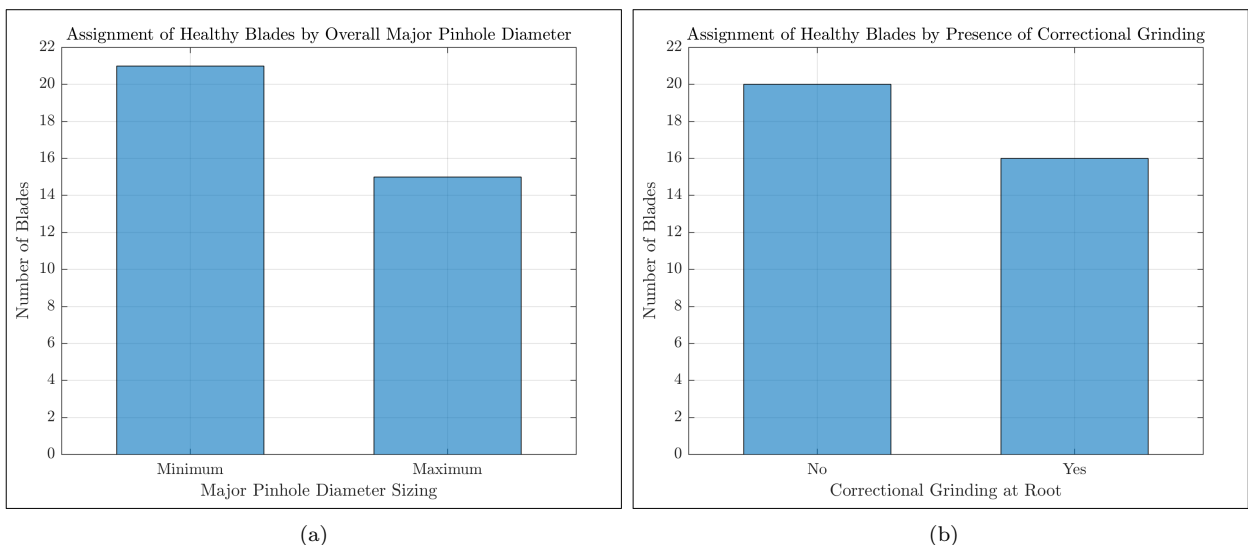


Figure 3.3: Assignment of healthy blades into condition groups from observed, a) Major pinhole diameter according to the largest on blade root; b) Grinding at the blade root according to presence of feature

3.1.1 3D FEA Modelling of Small Geometrical Variability

A FEM parametric study regarding these defects was done in which the effect of geometrical modifications on natural frequencies was explored. A reference for realistic variations in the defects was established from the test blades, considering the least altered to the most altered. The modelled defects range from 0 – 3mm for the varying grinding depth and $11.2mm \pm 12\%$ for the varying pinhole diameters. The original mesh settings are sufficient for a quality mesh. However, a sizing function was applied at the defect areas to ensure that the slight geometric changes are captured. The aerofoil section consisted of 69 800 nodes and 42 836 elements for both cases. For the varying correctional grinding depth, the root section consisted of ca. 163 000 nodes and ca. 111 000 elements. An edge sizing function was added to this feature to ensure proper capture of the geometric changes. For the varying pinhole diameters, the root section consisted of ca. 40 000 nodes and ca. 26 000 elements. Mesh convergence for all FEA models was achieved. The mesh at the pinhole diameters was sufficient and a sizing function was not required.

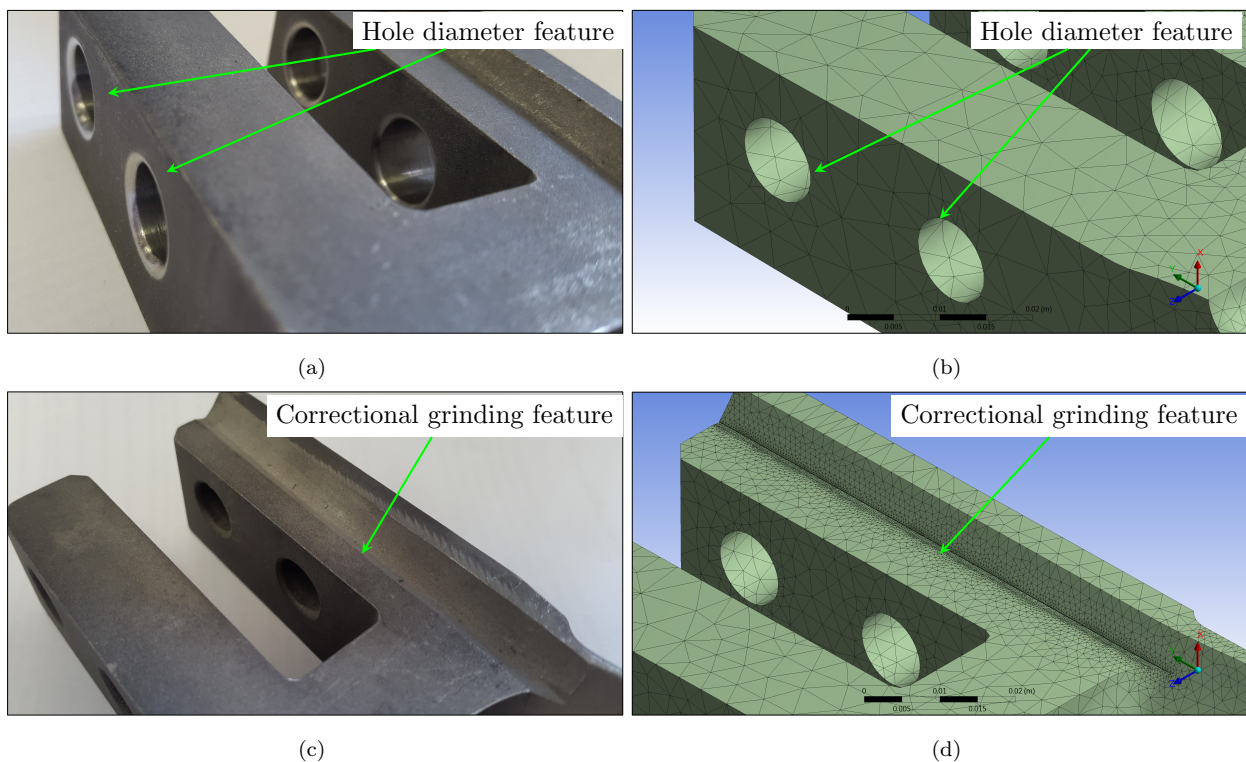
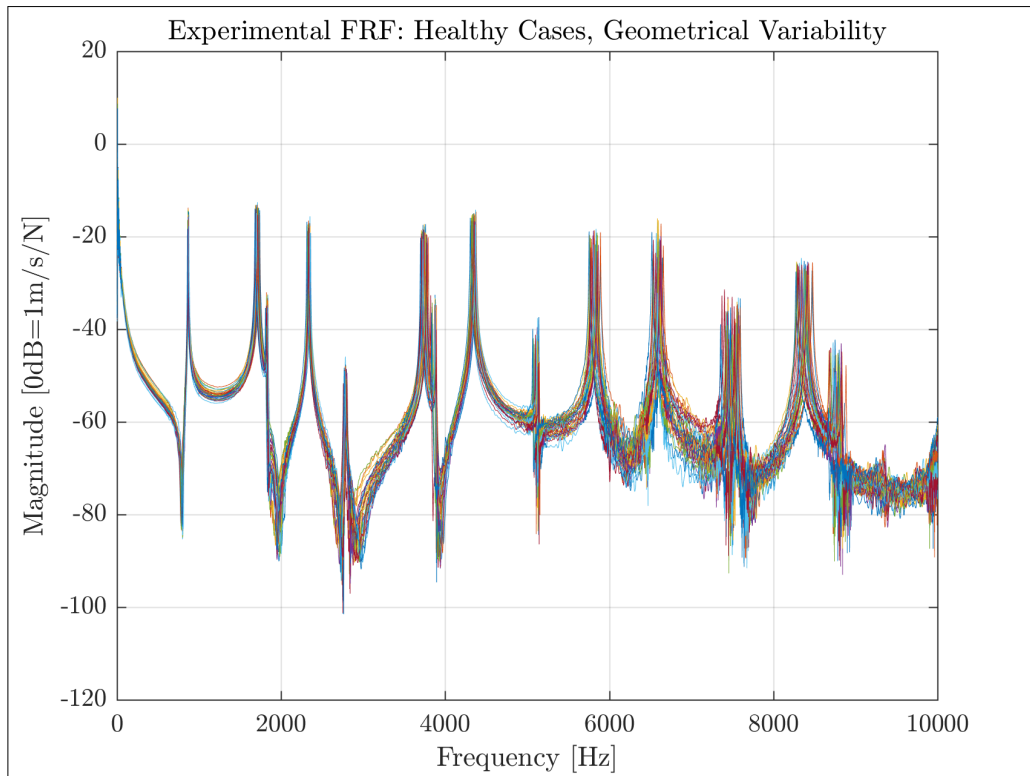


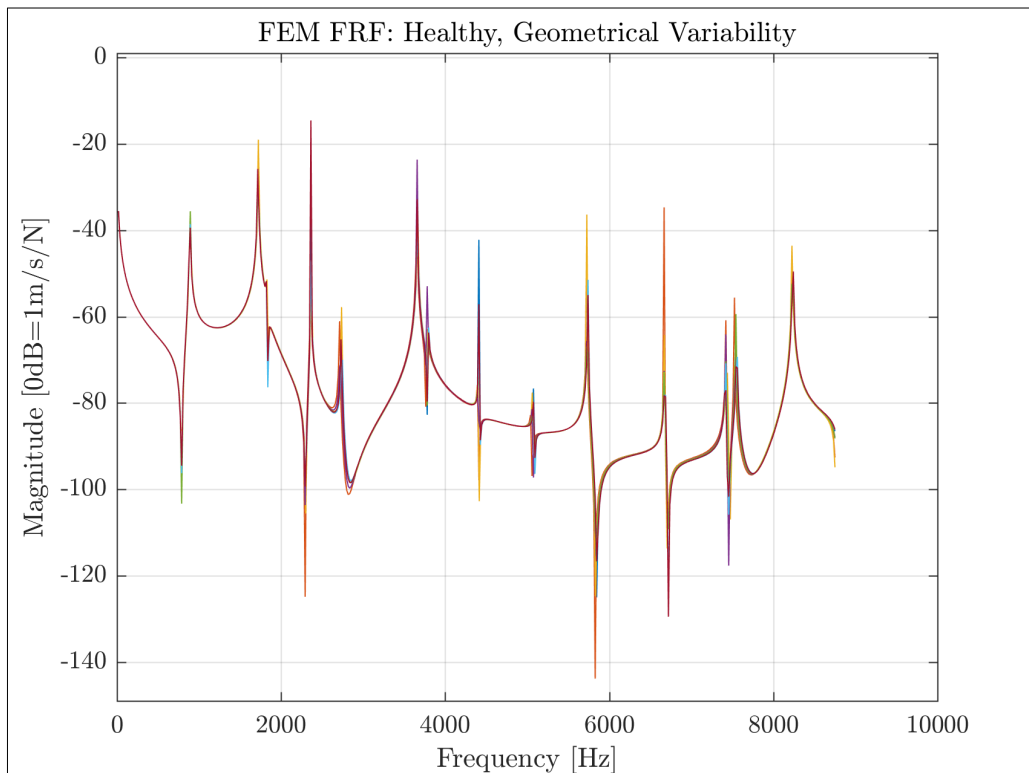
Figure 3.4: Modelled geometrical differences present in test blades, a)-b) Varying pinhole diameters; c)-d) Varying correctional grinding depth

3.1.2 Comparison of Results: Experiment vs. FEM

Figure 3.5a shows the good quality experimental FRFs obtained for the 36 healthy test blades, and Figure 3.5b shows the numerical FRFs obtained from FEM for 10 discrete cases. In the experimental FRFs, peaks are not obscured and are easily identifiable. It is also observed that the peak variation at higher modes increases. With the FEM FRFs, the magnitude at some peaks is lower; however, the peaks can still be easily identified. Little variation in the peak locations are observed, even at higher modes. Thus, the geometrical variability is not fully accountable for the variation. This is further explored in the section to follow.



(a)



(b)

Figure 3.5: Frequency response functions for healthy blades obtained from, a) Experiments of 36 test blades; b) FEM of 10 discrete cases

The experimental FRFs and FEM FRFs agree in both shape and having a small variance in peak locations (i.e. natural frequencies, f_n). This small variance increases slightly with higher modes; however, no prominent outliers are present. It is evident that the experimental protocol was successful in delivering high quality comparable results. This was ensured by a consistent (attempted replication) input excitation for each test. It is also clear that a narrow magnitude band displaying the inter-test variability is present. This also supports the protocol outcome.

To better understand the healthy response behaviour, the variations in the peak locations is now considered. This variance is quantified by the natural frequency f_n and change or variance in natural frequencies Δf_n [%]. This is shown in Figure 3.6 in which the healthy blades are compared to the experimental benchmark. The blades are sorted according to their geometric variability, i.e. a combination of sizing of the major pinhole diameter and presence of correctional grinding. From Section 3.1 and Appendix B, the blades are allocated a No Grind or Grind condition and a Min D or Max D condition, resulting in groups of 11, 10, 9, and 6.

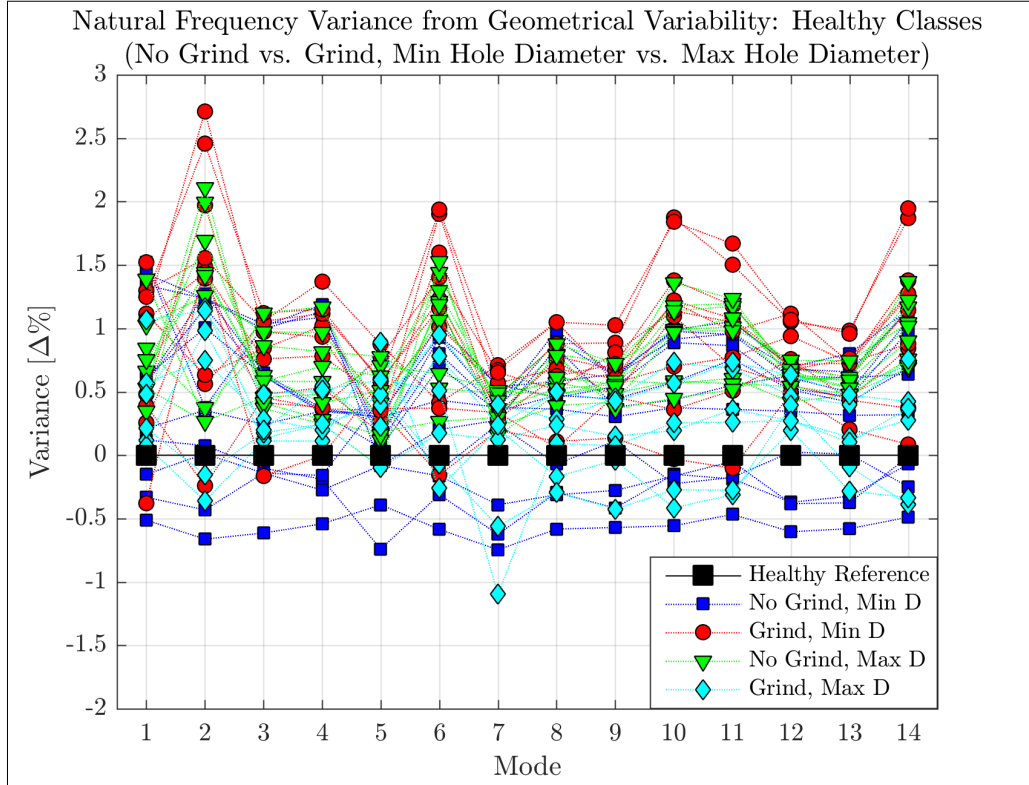


Figure 3.6: Variance in natural frequencies from geometrical variability in healthy test blades (relative to benchmark)

The geometric variability in the blades results in a maximum 3% variation in the peak frequencies. It is expected that the largest variation occurs within the group where most material is removed (Grind/Max D); however, it occurs for the Grind/Min D case. This supports the claim that the explored geometrical variability is not the only contributor to the variation. Since the healthy test blades contain manufacturing and operational defects, it makes sense that a small statistical distribution or variability is present within the natural frequencies of the healthy blades. This is better described in the variance of $-1\% \leq \Delta f_n < 3\%$ with the benchmark as reference. From Section 2.3.3, a maximum FE model validation error of 3% was found. This discrepancy demonstrates that the FEM blade will suitably represent the behaviour of the test blades due to the input parameters.

In Figure 3.7, the variances present in the experimental results as well as the FEM results are compared, relative to their healthy reference. The modelled geometrical features range from 0 – 3mm for the varying grinding depth and $11.2\text{mm} \pm 12\%$ for the varying pinhole diameters. It is apparent that the FEM cases fall within the same variance than the test blades, however, its variance-band is much tighter with $-1\% < \Delta f_n < 0.5\%$. This confirms the low sensitivity to slight geometrical differences in the healthy response. Hence, the geometrical variability in the root only partially accounts for the variance in the healthy blades. When considering the maximum experimental variance of 3% as the entire section that needs to be described, the maximum FEM variance of 1% only accounts for a small portion. Thus, other sources of variance must be responsible for the remaining 2%. This includes varying material properties, mainly because these were kept constant during the FEM study. This also clarifies on the magnitude of the FEM validation errors.

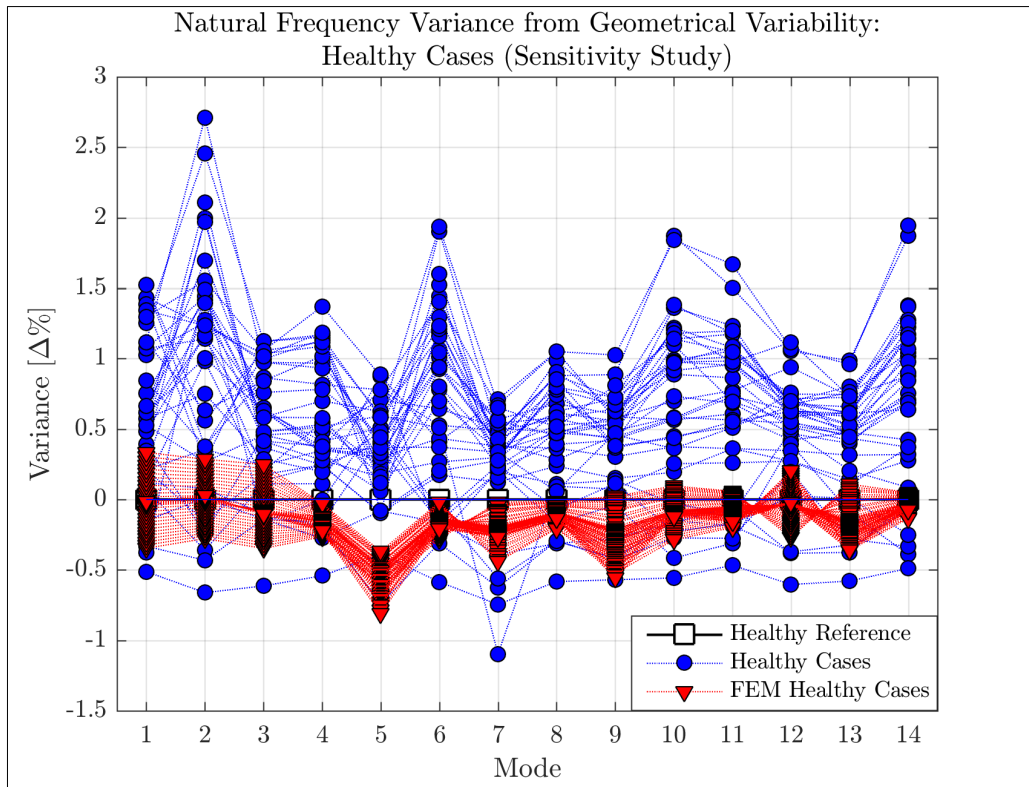


Figure 3.7: Variance in natural frequencies from geometrical variability in healthy blades (Experiment vs. FEM)

Since the material properties in the FEM cases are constant but the geometrical variability varies, it can be assumed that the material properties play a significant role in the larger variance band of the experimental cases. By considering that $f_n = \sqrt{k/m}$ with stiffness k , the geometric differences cause slight reduction in mass m with no structural compromise that can significantly affect k . Thus, it can be assumed that $k \cong 1$. Hence, the geometrical variability does not lead to noticeable Δf_n and are inconsequential. During the selection of material properties for the FE model, it was determined that Δk is more significant from varying material properties. The primary influence on this change was identified as Young's modulus of elasticity E , which may vary throughout the material. This introduces a slight variance in the experimental results. Thus, the relationship of $\Delta k \propto \Delta f_n^2$ is established since Δm from geometrical variability has minimal effect on Δf_n . This observation is also supported in literature (McGuire et al., 1995; Giannoccaro et al., 2006; Lorenzino and Navarro, 2015). Hence, it can be assumed that Δf_n is more sensitive to change in material properties or other unknowns than the geometrical variability as defined in this study. Since the blades are made from the same material, which has minor variability in its properties, it is implicitly consistent. Since no historical data of the test blades are available, especially of its material properties, it is difficult to capture this fully. Thus, it can be concluded that the healthy test blades are similar. The narrow variance band in Figure 3.7 supports this assumption.

3.1.3 Conclusions

From the 3% variance in natural frequencies caused by geometrical variability in the healthy test blades, it can be concluded that the effect of this input parameter on the vibration response is insignificant. This was explored by considering only the experimental case and attempting to visually recognize a pattern in the variance. This was done according to the assigned groups comprising a No Grind or Grind condition and a Min D or Max D condition. No clear pattern was observed, and it was established that the geometrical variability was not the only participating factor causing the variation in the natural frequencies. This was confirmed in the FEM in which the only variable was the geometrical variability. It was found that this factor only partially accounts for the variance as it had a maximum variance of 1% inside the range of the experimental results. The FEM was thus unable to capture this variance completely. Hence, other factors

such as material properties must play a role. The pattern recognition problem is addressed thoroughly in Chapter 4.

3.2 Sensitivity to Damage in Blades

In this section, large damage was introduced into the blades to quantify the sensitivity of the frequency response. If the frequency response is sensitive to damage, this damage can possibly be detected. The most probable failure locations in or near the blade root were obtained from literature, summarised in Table 1.1 in Section 1.2.1. A static structural analysis of a cyclic symmetry section of the bladed disk was performed to identify critical stress locations in the blade root during operation. The designated damage scenarios are discussed in Section 3.2.2 and were all corroborated through knowledge and insight acquired from industry, based on observations during routine off-site inspections. While these damages may only lead to failure at some stage in the future, and immediate failure or rupture of these cracks may not be expected for some time, they must be corrected as soon as possible.

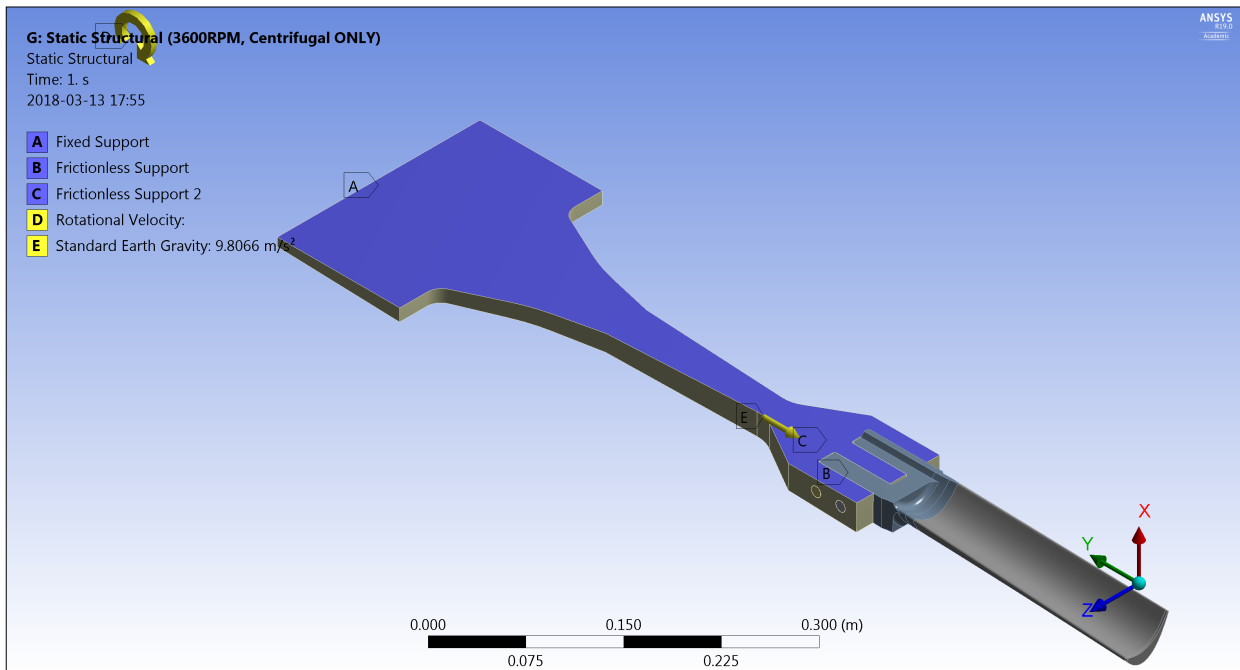
Difficulties in modelling the damage may arise, and the damage itself may make the structure dynamically non-linear, i.e. a breathing fatigue crack, which also presents a challenging problem (Worden and Dulieu-Barton, 2004). This includes contact in the model between the crack faces, which is non-linear. Therefore, simplified versions of the hypothetical worst-case scenarios at the most probable damage locations were modelled to explore the effect of damage on the healthy response. In the numerical modal- and harmonic response analysis of the damaged cases, the system is assumed to be linear. This reasons that the distance between the crack faces is large enough that no contact occurs between these faces. However, the bonded contact-based connection between the root and the aerofoil is linear. For the static structural analysis of the healthy installed blade, the system was assumed as non-linear and required definition of suitable contact between components.

3.2.1 3D FEA Modelling to Identify Most Probable Damage Location in the Blade Root during Turbine Operation

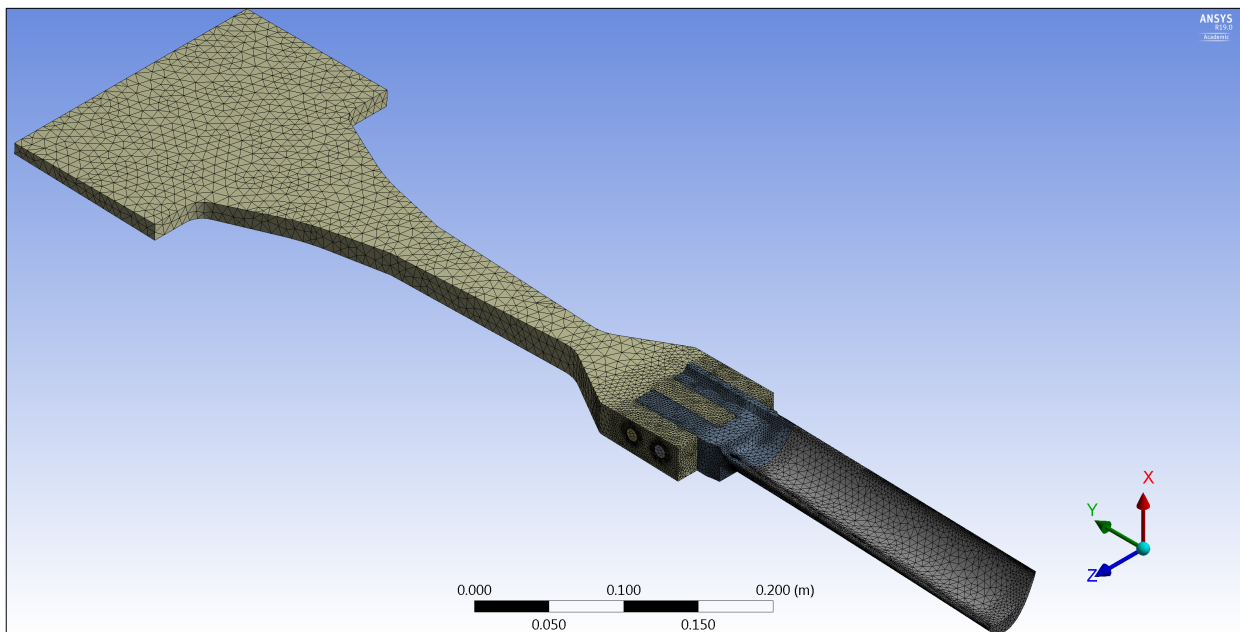
Static structural analysis was conducted on a cyclic symmetry section of a stage 2 LP pinned turbine disk to establish the most probable failure location on the root of the blade during operation. The operating and boundary conditions, including the contact, were adjusted from Hattingh et al. (2016) and is shown in Figure 3.8a. They conducted a case study on a stage 1 LP turbine disk in a 200MW unit to determine the acceptability of stress-corrosion cracks detected in-situ in the central prong of three. A hypothetical worst-case scenario was assumed in which the rotating velocity for an over-speed incident of 3600RPM at room temperature was applied. Standard gravity was also applied since the mass of these blades result in large centrifugal forces during operation, which are primarily responsible for failure of these blades. Vaishaly and Ramarao (2013) conducted a finite element stress analysis on a typical LP steam turbine, with similar operating conditions, to understand the dynamic behaviour of a last stage T-root blade. Their generalised FEA strategy was considered in this study.

For cyclic symmetry, frictionless supports were applied to the sides of the disk (in the circumferential direction) and a fixed support was applied at the disk inner diameter (disk-to-shaft connection). The installation of pinned turbine blades is critical. During this process, tapered pins are inserted securely through the rim and the individually reamed holes in the root, which were made during the alignment of the individual blades with the pre-reamed disk. The assembly is then permanently fixed, and the process is completed by sinking the pins and finishing the surface on the protruding sides. The parts are tight-fitting; however, no penetration occurs. Therefore, the presumed contact between all parts are frictional with a static friction coefficient $\mu_s = 0.3$, except for the pin and the disk on the outlet (trailing edge) side, which is bonded contact. The model was assembled from the different components, each meshed separately. The previous mesh settings used for the blade, were adapted for the disk section and pins and is shown in Figure 3.8b. An adaptive sizing function was used with the patch independent method applied on the disk section and

sizing functions applied on the edge holes and faces. Mesh convergence was achieved. The cyclic symmetry section consisted of 120 4247 nodes and 852 684 elements.



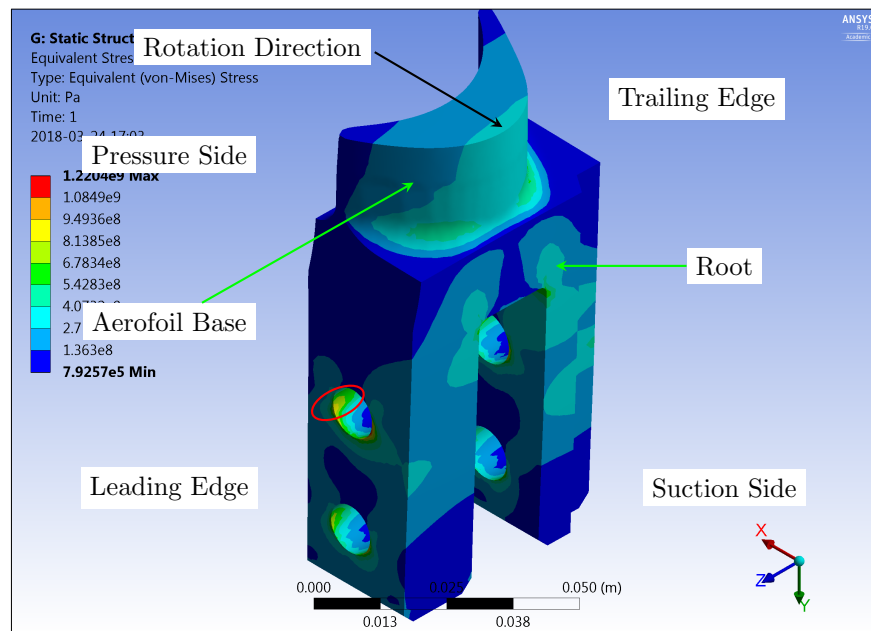
(a)



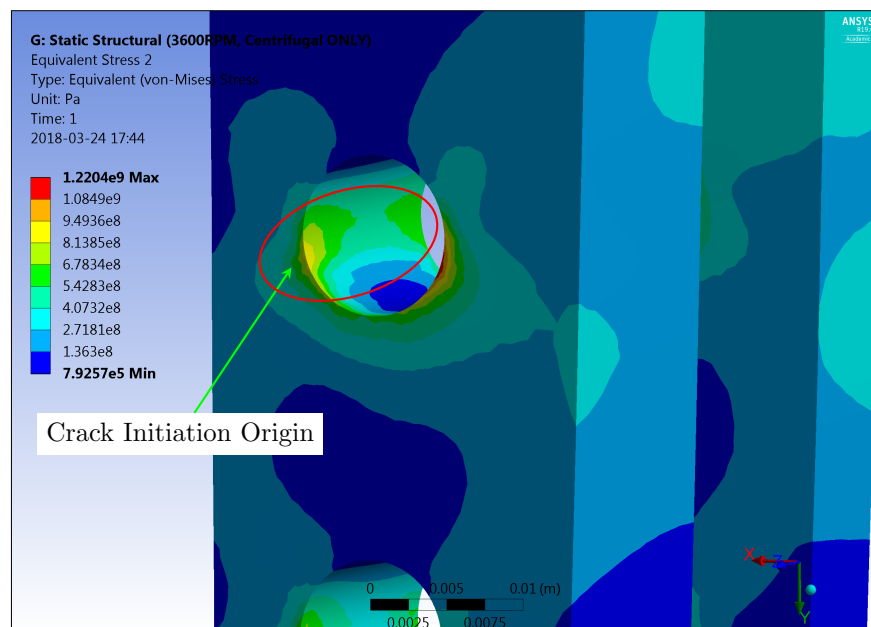
(b)

Figure 3.8: Static structural analysis of turbine disk section, a) Boundary conditions; b) Meshed 3D FEA model of cyclic section

In Figure 3.9, maximum equivalent stresses are observed in the areas of the pinholes. The initiation location of the most probable fatigue damage is found at the high stress region at the upper pinhole on the leading edge pressure side of the blade during an operating speed of 3600RPM. Fatigue will occur at this region as it experiences the highest stress in tension. This leads to crack initiation from cumulative surface dislocations during cyclic loading, causing the blade to oscillate, leading to crack propagation that originates at the edge at a similar rate in both the radial and circumferential direction during breathing of the crack. The crack trajectory will follow the path of the highest stress intensity, considering the material thickness and geometry, in the direction normal to the applied stress. An unsymmetrical stress field results due to the twisted geometry of the aerofoil. Since this is a linear problem, similar results will be obtained in analyses considering different operating speeds.



(a)



(b)

Figure 3.9: Crack initiation site on root for turbine disk section due to centrifugal force only - FEM static structural analysis results showing Von-Mises stress at 3600RPM, a) Overview; b) Detailed view of the hotspot at the upper pinhole on leading edge pressure side

At some stage after the crack has propagated through on the pressure side (9 o'clock position), the crack will continue to propagate on the other side. This second stage propagation starts at the opposite initiation location in the direction toward the suction side (3 o'clock position). At this area, the stress is first in compression; however, it changes into tension during the second stage as the crack hinge changes direction, and the crack starts to breathe. This will eventually lead to a complete separation of the blade finger from the blade root. Hence, this crack will have a propagation stage on the pressure side as well as the suction side. In this study, the first stage is considered as the worst-case scenario as anything past this point will be closer to failure than progressing damage. This will be discussed further in Section 3.3.3.

Note that the analysis only served as a critical location or hotspot indicator, thus the Von-Mises stress magnitudes can be ignored. This is the first worst-case damage scenario. More detail on the loads experienced by a LP steam turbine blade are presented by Plesiutchnig et al. (2016). The author identifies that the blade natural frequencies cause crack initiation at the root and the unsteady centrifugal and steam forces

(during starts and stops) cause crack propagation. This observation is supported by Booyesen et al. (2015). Two other most likely damage scenarios or types, occurring near the root, were obtained from literature (Table 1.1) and confidential industry reports. They are edge cracks on the trailing- and leading edge at the aerofoil base, just above the root.

3.2.2 Introduction of Damage

The designated three worst-case damage scenarios are given in Figure 3.10, showing the experimental and FEM cases. The dimensions of the simplified induced damage were determined from the worst-case scenarios to ensure that a unique damage-specific response can be achieved. Damage was induced in the blade by machining a through-thickness uniform notch at the upper pinhole on the leading edge pressure side of the blade ($1\text{mm} \times 6.7\text{mm}$), the base on the trailing edge of the blade ($1\text{mm} \times 20\text{mm}$), and the base on the leading edge of the blade ($1\text{mm} \times 20\text{mm}$). These damage scenarios will be referred to as Damage Classes 1-3. The original mesh settings are sufficient for a quality mesh; however, an edge sizing function was added at the damage locations. The mesh of the aerofoil section for all cases consisted of 69 800 nodes and 42 836 elements, whereas the root sections differed slightly. The total mesh of the blade for the damaged cases consisted of 10 2713 nodes and 63 782 elements for the root radial notch, 122 681 nodes and 77 400 elements for the base trailing edge notch, and 121 293 nodes and 76 486 elements for the base leading edge notch. Mesh convergence was achieved for all cases. The damage classes consist of blades with similar geometrical variability per group (see Appendix B) to ensure that a similar healthy variance is transferred to each class.

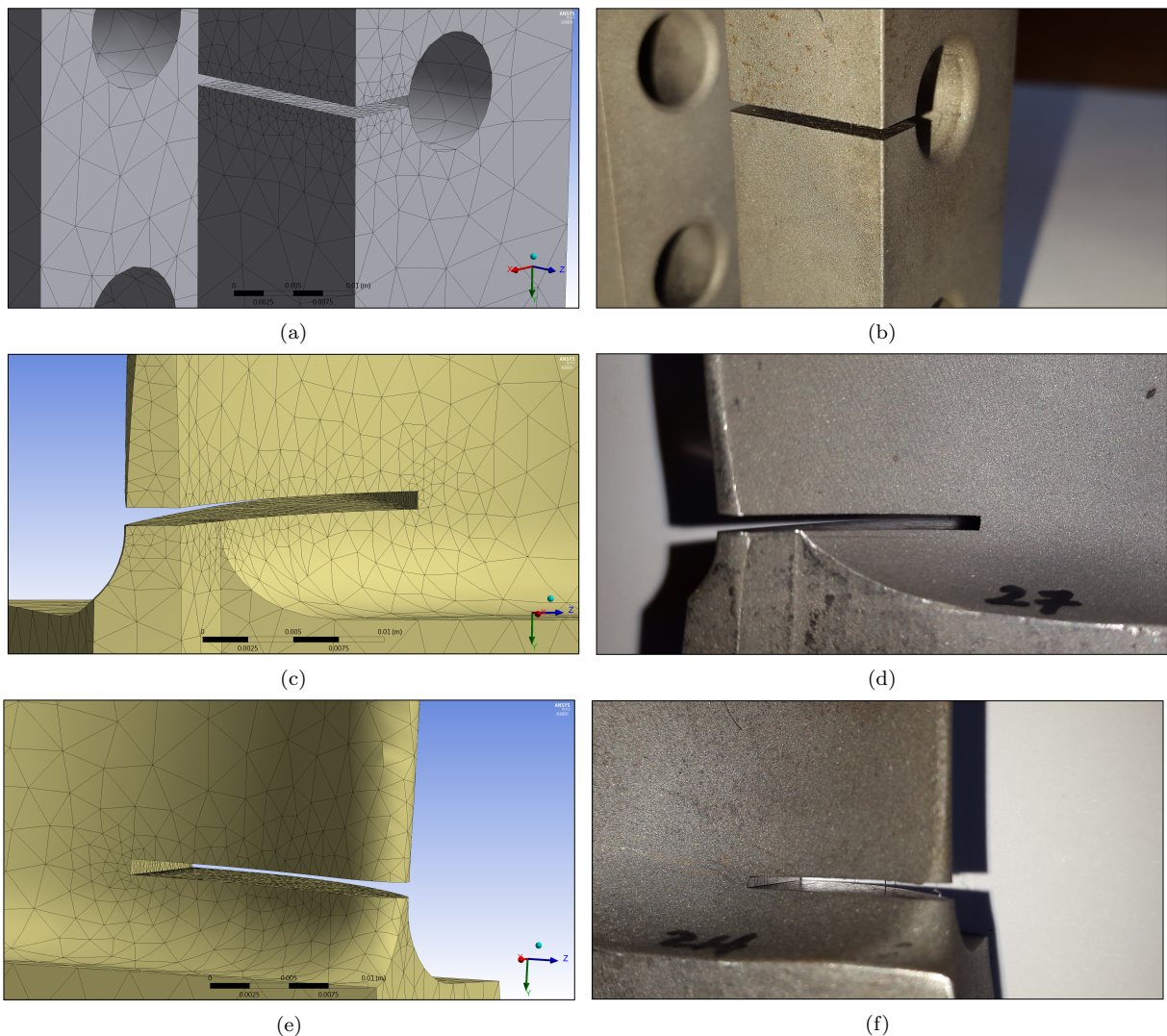


Figure 3.10: Test- and FEM blades with through-thickness uniform notch at most likely locations near the root, a)-b) Damage Class 1 = Root radial ($1\text{mm} \times 6.7\text{mm} \times 18\text{mm}$); c)-d) Damage Class 2 = Base trailing edge ($1\text{mm} \times 20\text{mm}$); e)-f) Damage Class 3 = Base leading edge ($1\text{mm} \times 20\text{mm}$)

The crack orientation for all cases was set normal to the length of the aerofoil. A natural crack will be non-uniform with a sharp crack tip (Dowling, 2012) and its orientation will be much more complex (Rau et al., 2016). The thickness of a natural crack would obviously be much smaller than 1mm ; however, a parametric study on all three cases revealed that 1mm is sufficient since negligible maximum errors (smaller than 0.25%, 0.5%, and 0.45%) exist when compared to a 0.3mm notch thickness. This is the minimum thickness available for the fine-tooth slitting saw disc that was utilised for cutting the notches. To ensure accurate and uniform damage, a reliable milling machine spindle was used as well as a suitable disc thickness. This was advised and executed by the workshop. The results of the parametric study are shown in Figure 3.11 in which the crack thickness was varied from 1.0mm down to at least 0.2mm in increments of 0.1mm . This was the minimum allowable thickness the configured mesh settings allowed.

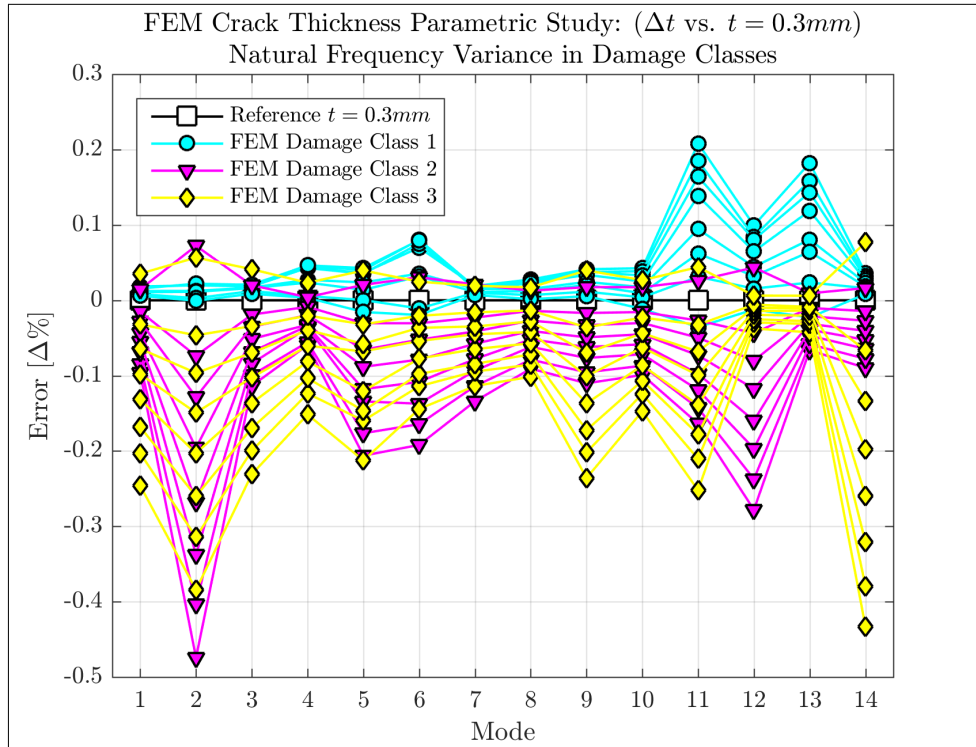
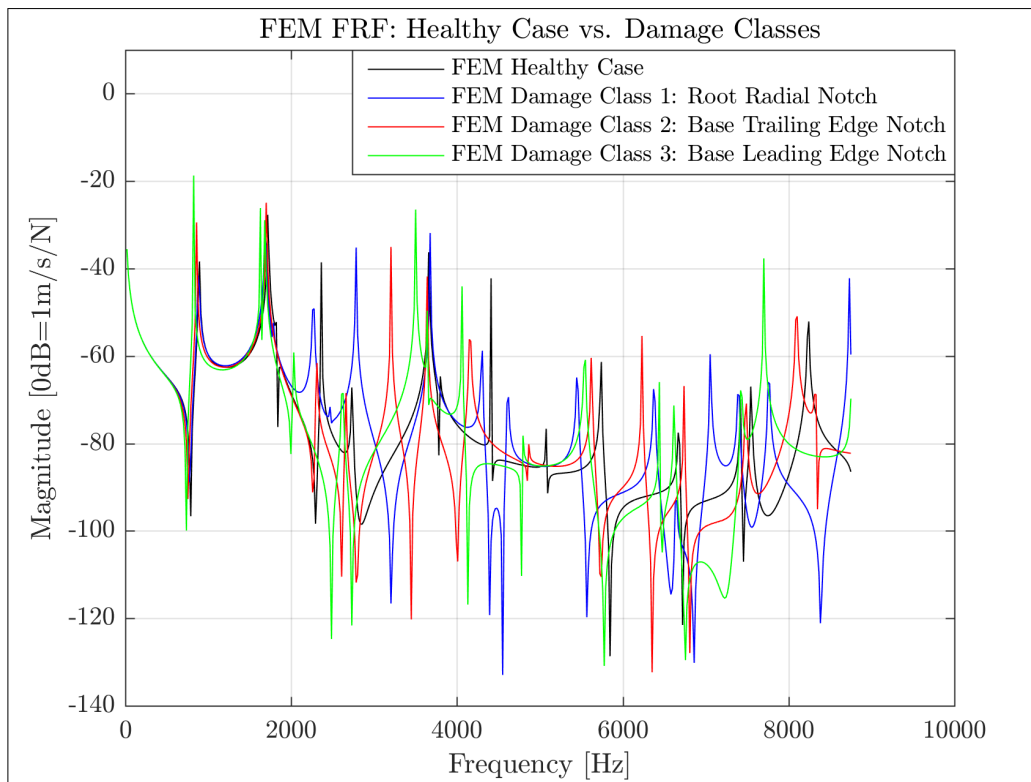


Figure 3.11: Results from FEM parametric study of crack/notch thickness for damaged blades: Δf_n vs. Δt

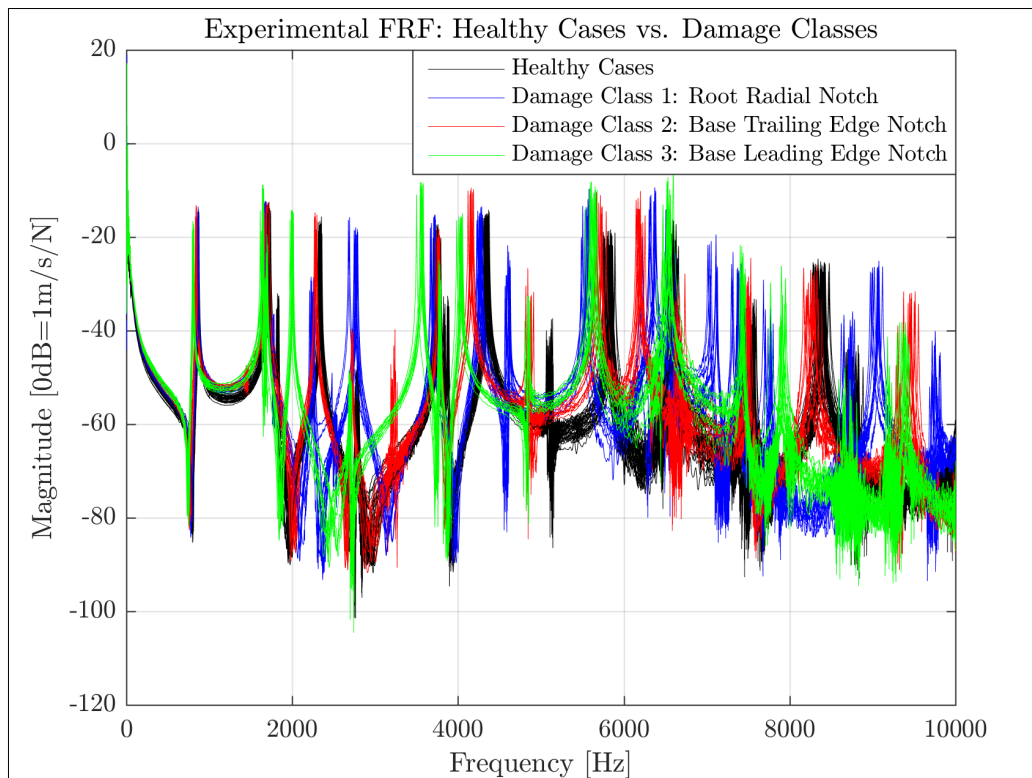
Figure 3.11 confirms that the effect of material removal from varying crack thickness on the natural frequencies is insignificant. This is because the errors observed are even smaller than the variances observed in the FEM healthy cases as shown in Figure 3.7 with values $\Delta f_n < 1.0\%$. This means that the stiffness k is the only remaining variable that plays a role in the change in natural frequency. Considering the location of the notch on the different damage classes, the stiffness of the blade is differently affected and thus the mode shapes for each case will also vary. This is explored in more detail in Section 3.2.3. Additionally, it is observed that the crack thickness contributes to the stiffness of the blade.

3.2.3 Results

The FRFs for the different damage classes obtained from the FEM simulations are given in Figure 3.12a. It is evident that four distinct damage-specific responses with clearly different shapes and varying peak locations (f_n) are observed. This means that the expected behaviour, established in the previous section, of the experimental case should show similar results. A decrease in natural frequencies is also expected as can be seen by the negative shift in FRF peaks. These findings are confirmed by the good quality FRFs of the different damage classes shown in Figure 3.12b that were obtained in the experiments. A small variance, increasing as the modes do, is observed at the peaks. Besides the healthy FRFs, three additional prominent FRF groups are identified, each with different damage-sensitivity at the different peaks.



(a)



(b)

Figure 3.12: FRFs for damaged blades obtained from, a) FEM; b) Experiments of 12 test blades per damage scenario

The resultant variances from all peaks for all damage classes are shown in Figure 3.13. The FEM damage classes are compared to the healthy FEM case, and the experimental damage classes are compared to the experimental benchmark. Figure 3.13 clearly shows the prominent and significant effect of damage on the healthy response with $-30\% < \Delta f_n < 0\%$, using their respective individual healthy cases as references. This is a significant difference. This is clearly more significant than the effect of geometrical variability on the responses. A reduction in natural frequency f_n occurred because of the introduced damage, implying a reduction in the stiffness k of the blade since a crack can be modelled as a fracture-hinge with a rotational

spring with varying k as the crack breathes (Rizos et al., 1990; Barad et al., 2013). The FEM cases are also shown to fall within the experimental result range, confirming that distinctive behaviour is present per case as well as verifying reasonably well-modelled damage classes. Since damage was introduced into the healthy test blades, similar f_n -variability is present within the blades in each damage class. This is explored in Section 3.3.4.

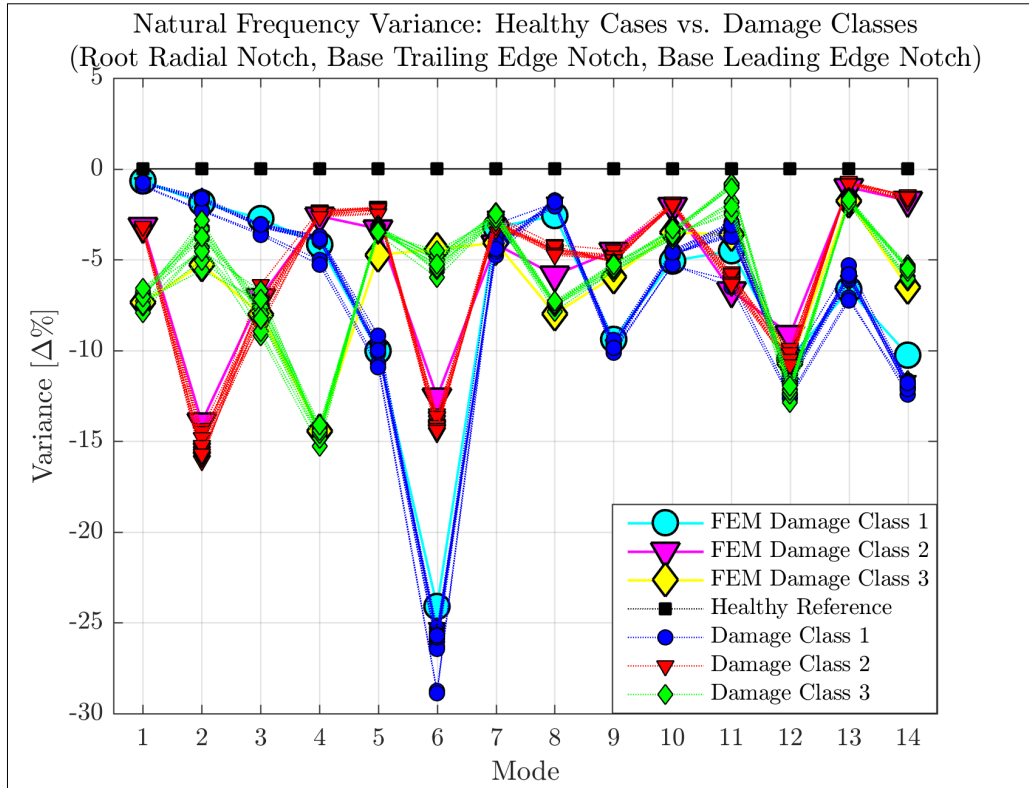


Figure 3.13: Variance in natural frequencies of damaged blades (Experiment vs. FEM)

It is evident that distinctive damage classes can be identified from the exclusive shift in f_n as well as from the large variances present per mode between different damage scenarios. It is clear that the variance in natural frequency at Mode 6 is the best distributed for the damage scenarios with values of 30%, 12.5%, and 5%, respectively. It can be seen that the variance at Mode 12 is nearly equal for the damage scenarios or classes with values around 11%. Consequently, it is obvious that the sensitivity to damage is significant at all modes where the variance is greater than 3%. This is the maximum variance found in the healthy blades, so any value around this is difficult to assess. Mode 12 displays a high sensitivity to damage, but the damage classes are challenging or not possible to distinguish. However, Mode 6 delivers the best representation of how distinct the sensitivity to damage can be.

The notch thickness parametric study confirmed that mass loss, in this case, can be disregarded in its effect on Δf_n , and the assumption that $m = 1$ is accepted. This correlates with the statement above of $k \propto f_n^2$, substantiating the sensitivity of f_n to k and thus, to the worst-case damage scenarios near the root. In the previous argument k was considered a function of material properties, however, in this case it can be concluded that k is also a function of a simplified crack with negligible loss in mass. It was also determined that the effect of geometrical variability was insignificant, thus the material properties are no longer a factor and only the effect of damage must be considered in Δk for Δf_n .

It is observed that the variation differs per mode, implying dependence on the vibration pattern and crack orientation since different crack behaviour is expected from different mode shapes. This is explored in Figure 3.14 and Figure 3.15. The behaviour of each feature differs to a degree, which can be attributed to natural frequencies f_n being affected differently regarding the mode shape, considering the different damage cases. Note that the mode shapes are relative values associated with free vibration. This is due to the

damage location that influences the stiffness k of the blade through allowing or restraining the crack to open or close in a specific direction, and thus changing the mode shape for a specific mode. Agarwalla and Parhi (2013) and Gillich and Praisach (2015), who found that the shift in natural frequency for a certain vibration mode of a beam-like structure is dependent on the damage location, while the damage depth only amplifies this event, supports this statement. This is due to the effect of the mode shape vector for a given location. Research on damage detection by mode shape-based vibration analysis is available (Fan and Qiao, 2011), confirming this argument. Based on these observations, it is possible to identify sets of values that uniquely characterize the behaviour of the blade with a given damage. The following FEM mode shapes illustrate this in which an arbitrary scale factor was applied for visualisation purposes:

- Mode 6, shown in Figure 3.14. This is the best example for **damage distinction** (implying damage detection and identification). This is supported by the fully distinguishable variance of each class. This suggests that the mode shapes are exclusive to each damage class. This mode will be used as the representing example in Chapter 4 regarding the classification for healthy cases and its distinction from damage classes. This will allow better understanding of the results.

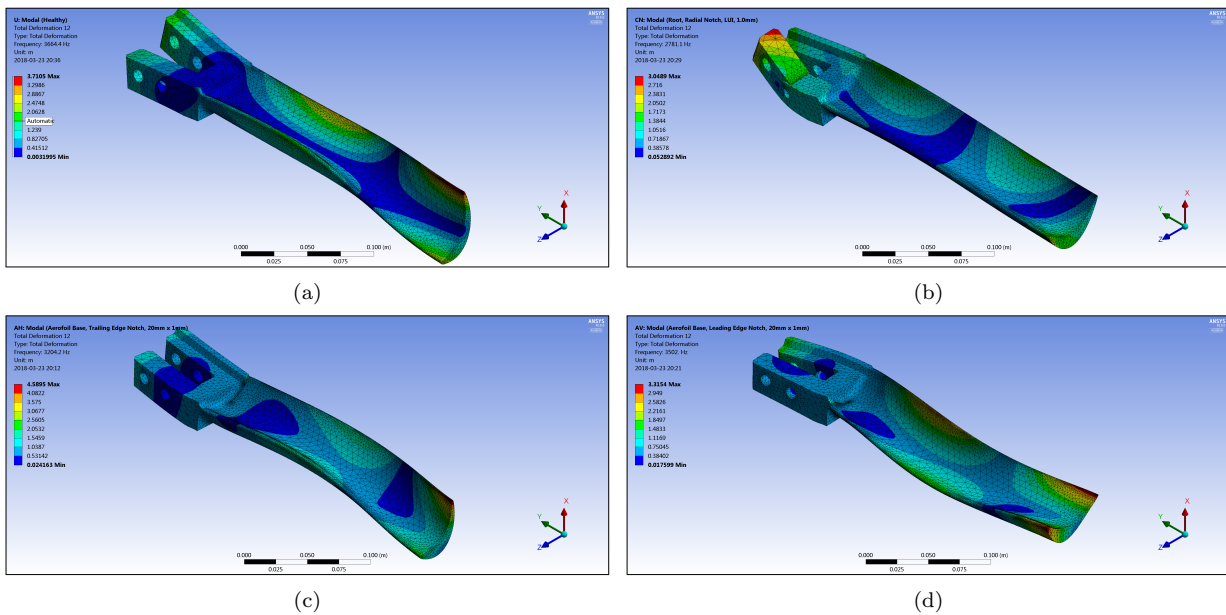


Figure 3.14: FEM mode shape study to understand variances - Mode 6, a) Healthy; b) Damage Class 1 (root, upper pinhole at leading pressure side); c) Damage Class 2 (base, trailing edge); d) Damage Class 3 (base, leading edge)

It is observed that the overall mode shape for each class is different with some similarities. The deformation for Damage Class 1 varies the most from the healthy case, and is significant around the location of damage, compared to the other classes. It is clear that this mode is more complex and more dynamic, which clarifies why the variance is so high for this mode. The deformation for Damage Class 2 is also complex, but much closer to that of the healthy blade. Large deformation is also present at the aerofoil tips. This explains why the variance is second highest for this mode. When comparing the deformation of Damage Class 3 to the healthy case, it can be seen that the shapes of these two classes are more similar when compared to the rest, especially at the aerofoil tips and body. Thus, this variance is the lowest of the damage classes. The basic pattern of deformation, observed in Figure 3.14, is described in Table 3.2.

Table 3.2: Basic pattern of deformation for Mode shape 6

		Damage Scenario							
		Healthy Case		Damage Class 1		Damage Class 2		Damage Class 3	
		Edge (Side of Occurrence)							
Part	Location	Trailing	Leading	Trailing	Leading	Trailing	Leading	Trailing	Leading
Blade Root	Bottom Section		x		x		x		x
	Body (Finger)	x		x		x		x	
	Upper Section				x		x		x
Aerofoil	Bottom Section			x			x		
	Body	x	x				x		x
	Upper Section Tip	x	x	x		x	x	x	x

- Mode 12, shown in Figure 3.15. This is the best example for **damage detection**. This is supported by the large variance of all damage, compared to the healthy case. This suggests that the damaged mode shapes are exclusive from the healthy case. This mode will be used as the representing example in Chapter 4 regarding the differentiation of healthy and damaged cases. This will allow better understanding of the results.

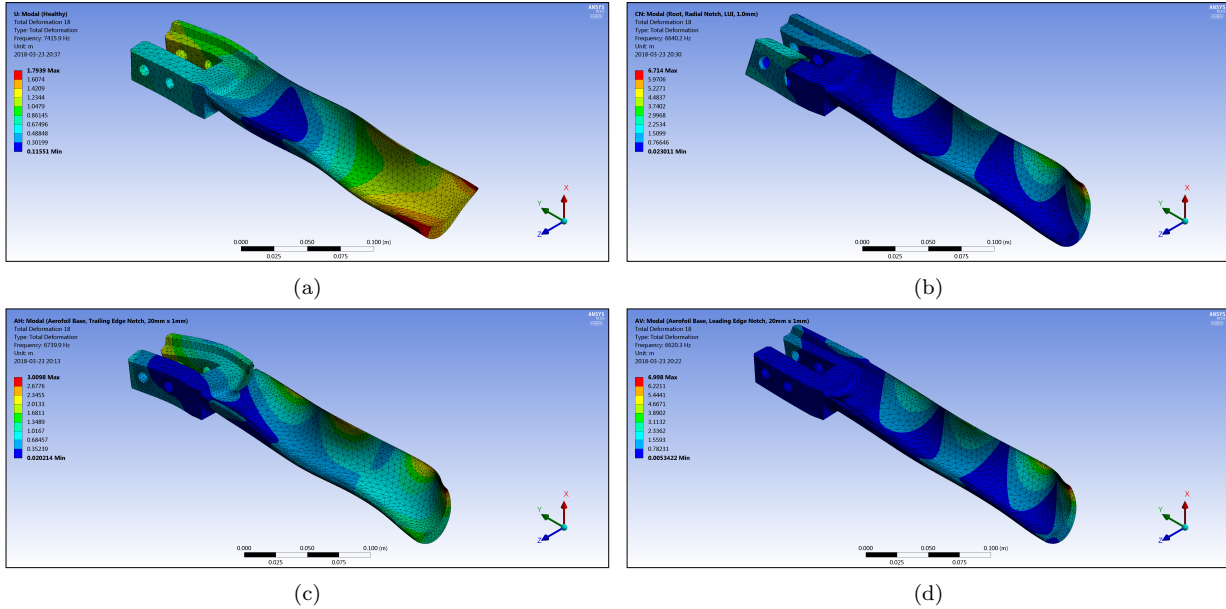


Figure 3.15: FEM mode shape study to understand variances - Mode 12, a) Healthy; b) Damage Class 1 (root, upper pinhole at leading pressure side); c) Damage Class 2 (base, trailing edge); d) Damage Class 3 (base, leading edge)

It is observed that the overall mode shapes of the damage cases are very similar, but that they all differ from the healthy case. This is especially so with Damage Classes 1 and 3, where Damage Class 2 is to some extent more dynamic. When considering the aerofoil tips and the aerofoil, this likeness is apparent. This explains why the variance for the damaged cases is so similar. However, it is clear that the mode shape for Damage Class 2 is the intermediate between the damaged cases and the healthy case. The deformation is largest in the healthy case, and is more dynamic than the damaged cases, sharing little resemblance. The basic pattern of deformation, observed in Figure 3.15, is described in Table 3.3.

Table 3.3: Basic pattern of deformation for Mode shape 12

		Damage Scenario							
		Healthy Case		Damage Class 1		Damage Class 2		Damage Class 3	
		Edge (Side of Occurrence)							
Part	Location	Trailing	Leading	Trailing	Leading	Trailing	Leading	Trailing	Leading
Blade Root	Bottom Section	x		x		x	x	x	
	Body (Finger)	x		x	x				
	Upper Section	x	x			x			x
Aerofoil	Bottom Section			x			x	x	
	Body	x	x	x	x	x	x	x	x
	Upper Section	x	x	x		x	x	x	
	Tip	x	x	x		x	x	x	

It can be concluded from the argument above that, the damage-sensitivity per mode differs, and that all f_n are prominent concerning damage-sensitivity. This is due to the location of the damage that plays a key role as the extent of change in stiffness or crack breathing depends on the vibration pattern. The degree of prominence for each mode can probably be determined to see which has the highest quality. This was not explored in the study. The FEM mode shapes are merely representations of the expected experimental mode shapes of which the acquisition was not included in the scope of work, owing to the reasonably well-modelled scenarios. Formal methods of matching mode shapes are available (e.g. Modal Assurance Criteria) but this is out of scope. The mode shapes were visually explored only to attempt to understand the observed variances in the blades.

From this, the different damage classes, compared to their healthy references, are assumed distinct. However, a constant effect of geometrical variability and material properties per class is also assumed since this was transferred to the damage classes. Hence, it can be anticipated that f_n are more sensitive to damage than geometrical variability or other sources responsible for the variation in the healthy blade response, and thus its sensitivity to f_n is high enough that the distinction of the damage classes can be established. This shows promise for the success in detection and identification of damage in using the natural frequencies as a distinctive health status indicator. This, however, requires further investigation for a clear verdict.

3.3 Damage Trend in Blades

In this section, the trend in the change in natural frequency f_n in the blade as a result of a specific damage class or scenario is explored. This enables the evaluation of the validity and quality of the selected natural frequencies and its sensitivity to damage.

3.3.1 Effect of Geometrical Variability on Damage Classes

The effect of geometrical variability on the damage classes is investigated in Figure 3.16 to prove the appropriate representation of the variance found in the healthy blades (Figure 3.16a).

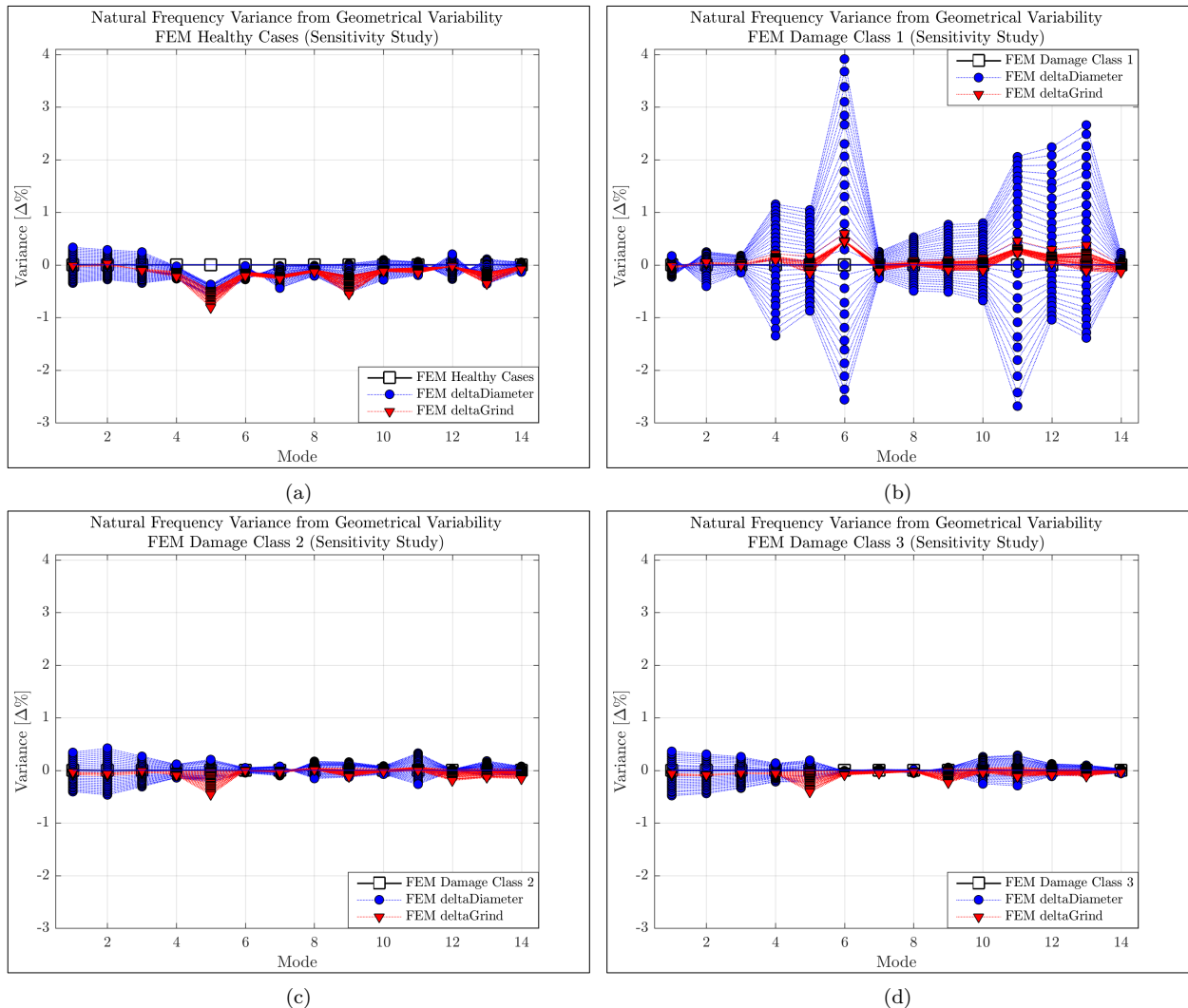


Figure 3.16: Variance in FEM natural frequencies from geometrical variability found in healthy blades from, a) Healthy Cases; b) Damage Class 1; c) Damage Class 2; d) Damage Class 3

It can be seen that the effect of the correctional grinding on the natural frequencies is minimal and very similar, considering the absolute values. This is quantified for the damage classes on the trailing- and leading edge just above the root (Damage Class 2 and 3) with $-0.5\% < \Delta f_n < 0.1\%$, and for the upper pinhole

damage in the root (Damage Class 1) with $-0.1\% < \Delta f_n < 1\%$, compared to the healthy variance of $-1\% < \Delta f_n < 0\%$. This is because this variability is not located at a critical area and does not noticeably influence the mode.

The effect of the varying pinhole diameters on the natural frequencies is greater since it is located at a more critical area. In Figure 3.16b, variances from the varying pinhole diameters are much larger with $-3\% < \Delta f_n < 4\%$ compared to the other damage classes with $-0.5\% < \Delta f_n < 0.5\%$. The latter is equivalent to the healthy case with $-1\% < \Delta f_n < 0.5\%$. The former is due to the presence of the introduced damage (in the upper pinhole of the root) and this variability is located in a critical area. This amplifies the effect on the natural frequencies with more prominent influence on specific modes. Hence, the effect of geometrical variability is reasonably constant and minimal with varying pinhole diameter having a larger influence on the change in natural frequencies due to its location.

The total and steady effect of the geometrical variability as well as the damage scenarios on the healthy case is shown in Figure 3.17, in which the experimental and FEM variances are compared. It can be seen that the geometrical variability forms a narrow band around the damage variance as expected since it was transferred from the healthy blades to the damage classes and is thus appropriately represented. Noticeable variances, dependent on the vibration pattern and crack orientation, are evident for Damage Class 2 and 3 with $-15\% < \Delta f_n < 0\%$ and Damage Class 1 with $-30\% < \Delta f_n < 0\%$. The amplification effect of the varying diameter is clearly visible in the variance in Damage Class 1, which is best represented by the FEM.

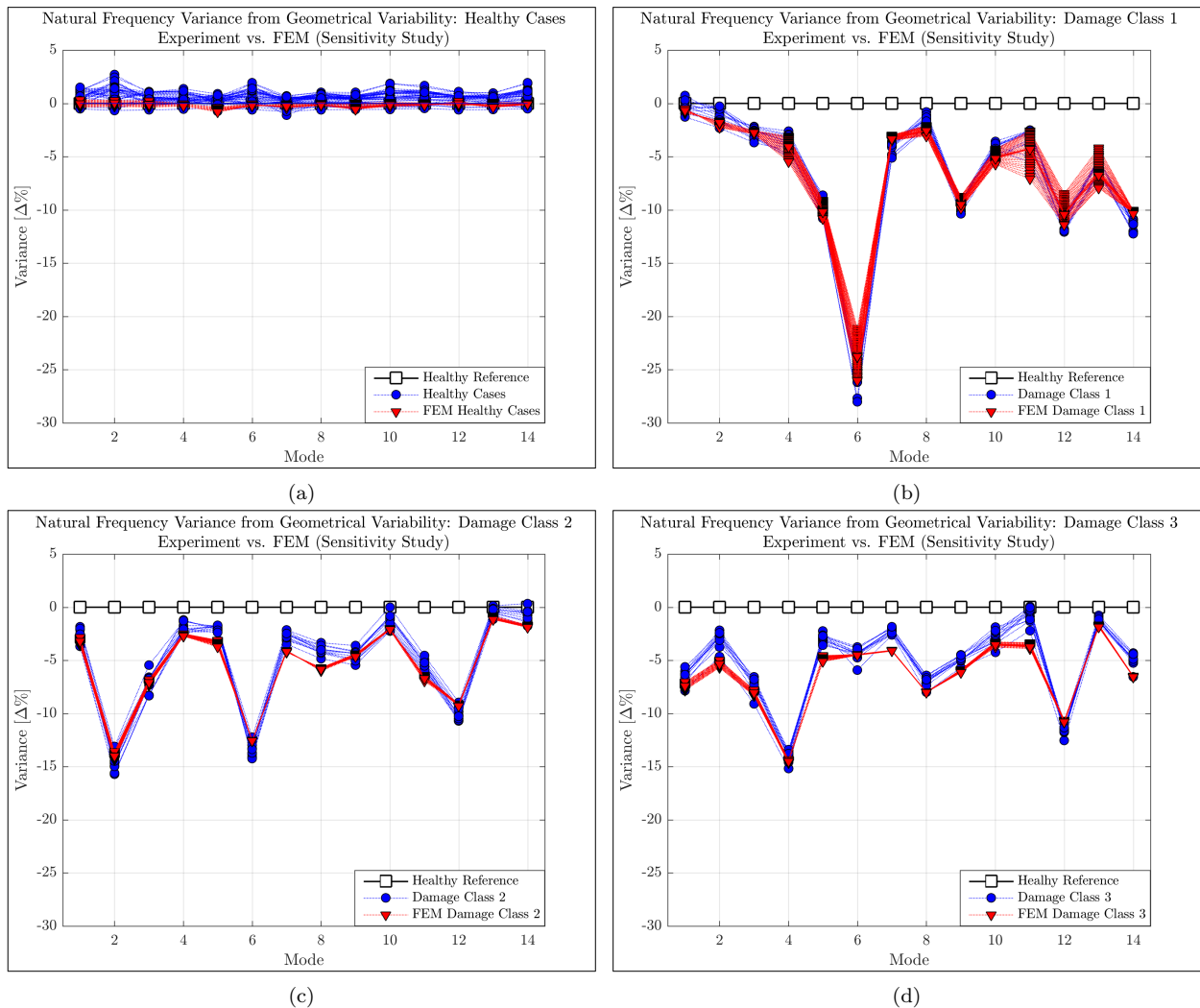


Figure 3.17: Variance in natural frequencies from geometrical variability in healthy blades (Experiment vs. FEM), a) Healthy Cases; b) Damage Class 1; c) Damage Class 2; d) Damage Class 3

3.3.2 Shift in Frequency due to Damage

The shift or change in the 14 natural frequencies for each damage scenario is shown in Figure 3.18, starting at the first mode in a rising order. The magnitudes may not be constant for each type due to the geometrical and inter-test variability; however, it is evident that a negative shift is observed for all modes in the damage scenarios. Considering the superimposed shifts, it can be seen that a particular arrangement per natural frequency is present within the damage classes. In this study, only the healthy and worst-case scenarios were considered. This is mainly due to the limited number of blades available for proper representative results. However, the following factors also contributed to this decision: Time constraints, the complex geometry of the root, and the damage initiation location. These factors limited the damage induction procedure, as the root geometry was difficult to access as well as reliably alter in a controlled fashion at the specified location in the root. As crack propagation was not part of the scope of this research, the area between the points in Figure 3.18 is unknown and a linear relationship cannot be assumed. This requires further investigation. Unfortunately, no experimental results could be obtained for this unknown area. However, this can be numerically explored with the reasonably well-modelled cases with some margin of error. This is discussed in the next section.

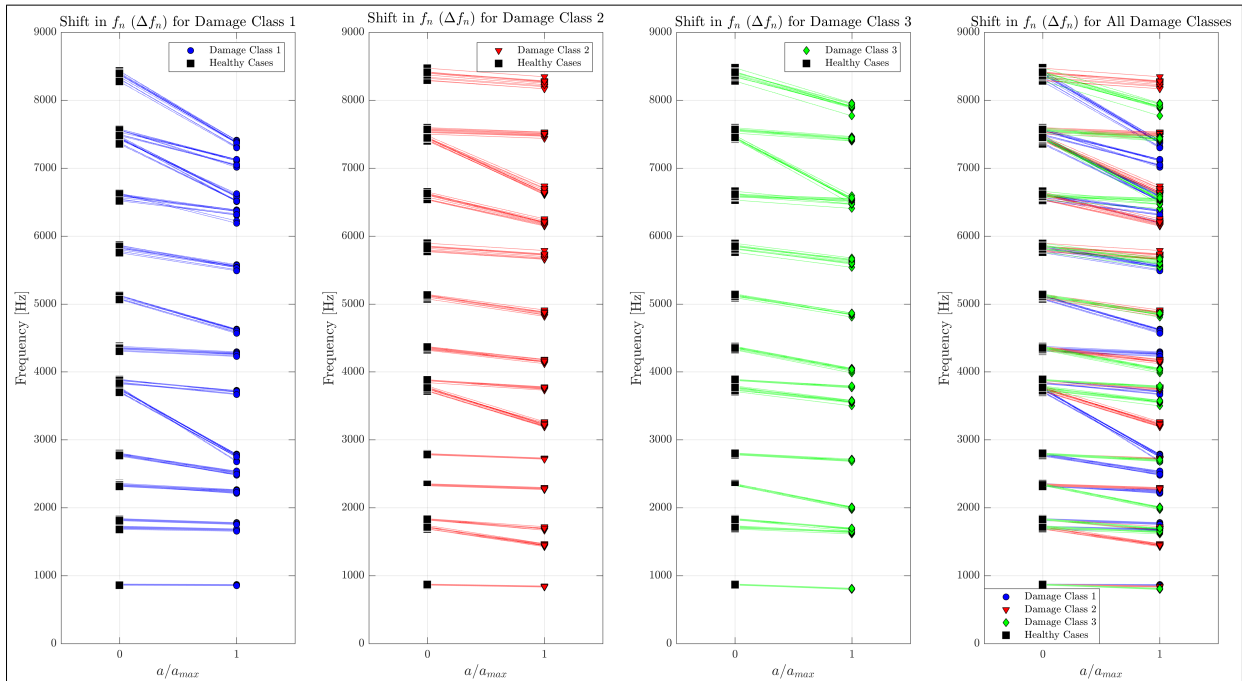


Figure 3.18: Shift in f_n (Δf_n) for damage classes starting at the first mode in rising order

3.3.3 Numerical Damage Propagation

In this section, interest lies in what happens between the crack initiation stage and the worst-case scenarios, i.e. the trend between $a = 0$ and a_{max} . This was explored numerically through a parametric study in which the notch length for each damage case was discretely varied. Only pure damage without geometrical variabilities was considered. Due to the damage propagation and the complex geometry of the blade, the parametric study could not consider all increments between $a = 0$ and a_{max} . For Damage Class 1, the crack was propagated from $0.2mm$ to $6.6mm$ in increments of $0.4mm$. For Damage Class 2, the crack was propagated from $3.1mm$ to $20.0mm$ in increments of $1.0mm$. For Damage Class 3, the crack was propagated from $1.6mm$ to $20.0mm$ in increments of $1.0mm$. The original mesh settings were used for Damage Classes 2 and 3 but were adapted for Damage Class 1. An edge sizing function was added to the crack point to properly capture the notch geometry. The initial crack length used in the FEM discrete crack propagation parametric study for all damage cases are shown in Figure 3.19. The results for the worst-case scenarios were discussed in Section 3.2.3 and were added to the damage propagation results as a_{max} .

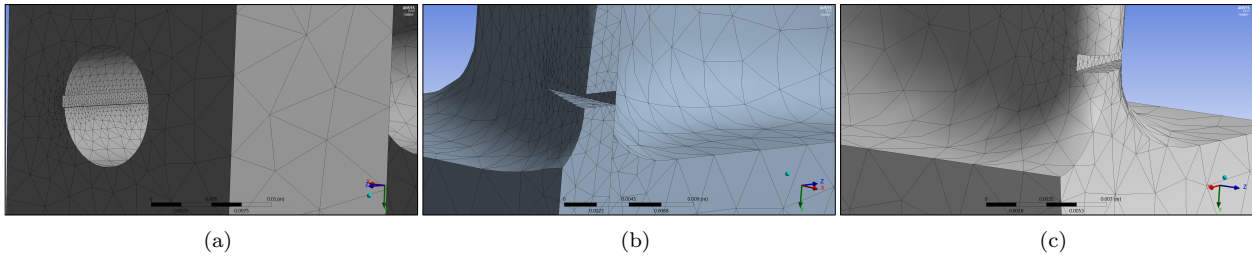


Figure 3.19: The initial crack length used in FEM discrete crack propagation parametric study for, a) Damage Class 1 ($a = 0.2\text{mm}$); b) Damage Class 2 ($a = 3.1\text{mm}$); c) Damage Class 3 ($a = 1.6\text{mm}$)

Figure 3.20 shows the variance in natural frequencies from FEM crack propagation for discrete cases up to the critical crack length a_{max} of the worst-case scenarios. The FEM damage classes are compared to the healthy FEM case. It is observed that the effect of damage on the healthy response intensifies as the crack propagates. The larger the crack length, the more prominent and significant its effect on the variance. For Damage Classes 2 and 3, it is evident that the variance in natural frequencies increases steadily as the crack grows. However, this is not the case for Damage Class 1 as its variance-band is much narrower up until the crack length approaches a_{max} , where a sudden increase or spike is then observed for some of the modes. For example, the maximum variance jumps from -11% to -30% for Mode 6. This is because of the location of the damage, and as the crack has not fully propagated, the structural integrity of the blade finger has not been fully compromised. However, when the full-crack stage is reached, a significant reduction in the stiffness k of the blade finger occurs, and the crack can fully open and close. A gradual decrease in the blade aerofoil stiffness k occurs with the crack growth for Damage Classes 2 and 3.

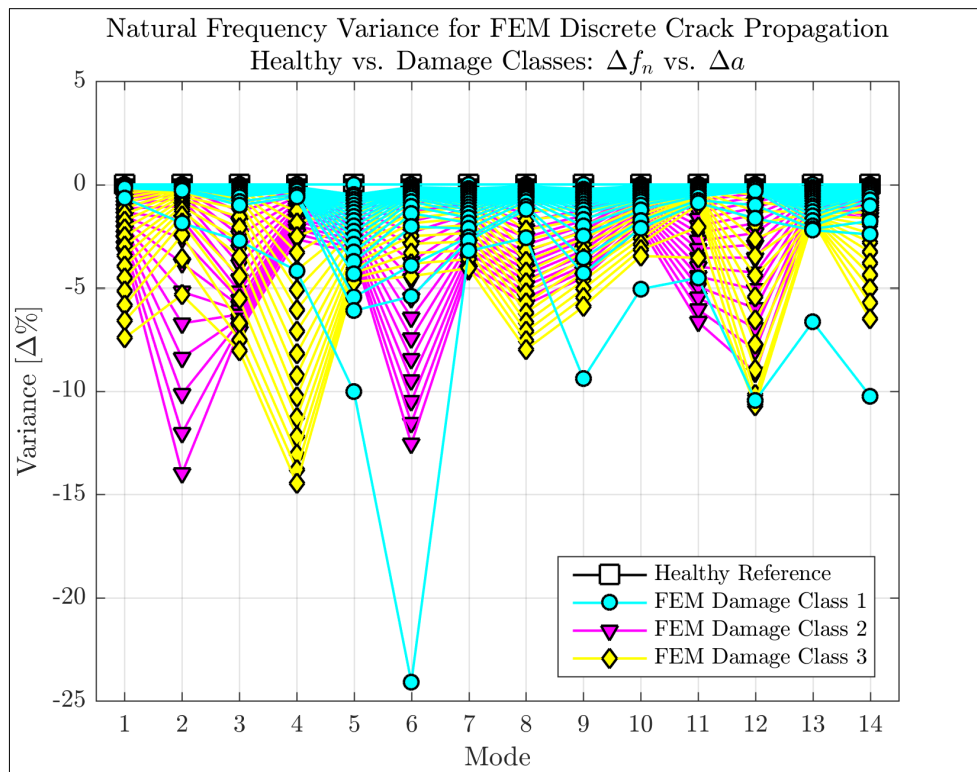


Figure 3.20: Variance in natural frequencies from FEM discrete crack propagation: Δf_n vs. Δa for damaged blades

In Figure 3.20, it can be seen that the effect of Damage Class 1 on the variance is much smaller until the crack is fully propagated, when compared to the Damage Classes 2 and 3. So in view of damage detection, Damage Class 1 is more difficult to detect since the critical crack length a_{max} is a $1/3$ of a_{max} of the other two classes, i.e. 6.7mm compared to 20.0mm . This means that the size of the propagation increments is also much smaller and thus, the detection is much more sensitive. Moreover, since a_{max} is not considered as failure but as the worst-case scenario preceding the failure, this sudden increase in the variance can possibly be used as an alarm threshold. With critical crack length reached for Damage Class 1, the crack can fully

open and close. This will result in the initiation and propagation of an additional crack on the opposite side. Now the question is: What happens after this spike in variance as the crack continues to grow but on the opposite side? This is explored below and demonstrated in Figure 3.21 and Figure 3.22.

From the statement above, it is argued that Damage Class 1 involves two stages, i.e. the initial cracking case and the additional cracking case. In the first stage, the crack initiates and propagates at the 9 o'clock position on the upper pinhole. In the second stage, the crack initiates and propagates at the 3 o'clock position shortly after the first stage. Note that the first stage is considered as the worst-case scenario as anything past this point will be closer to failure than progressing damage. Thus, the second stage is regarded as failure since it will eventually lead to a complete separation of the blade finger from the blade root. This is discussed in Section 3.2.1 in which static structural analysis was conducted on a cyclic symmetry section of a stage 2 LP pinned turbine disk. This FEA was done to establish the most probable failure initiation location on the blade root during operation. To avoid confusion, the first stage of Damage Class 1 will be referred to as Damage Class 1, and the second stage will be referred to as Damage Class 1(2).

Figure 3.21 shows examples of additional FEM cases for discrete crack propagation of the root radial notch at the upper pinhole. When only considering Damage Class 1 in Figure 3.21a, the critical crack length is $a_{max} = a_1 = 6.7mm$. When considering Damage Class 1(2) in Figure 3.21b to Figure 3.21d, the critical crack length is $a_{max} = a_1 + a_2 = 16.7mm$, where $a_2 = 10.0mm$. For Damage Class 2 and 3, the critical crack length is $a_{max} = 20.0mm$. The original mesh settings are sufficient for a quality mesh for these two cases. Damage Class 1(2) was numerically explored through a parametric study in which the notch length at the 3 o'clock position was varied. Due to the damage propagation and the complex geometry of the blade, the parametric study could not consider all increments between $a = 0$ and a_{max} . For Damage Class 1(2), the crack was propagated from $0.3mm$ ($6.73mm$) to $10.0mm$ ($16.73mm$) in increments of $0.4mm$. The mesh settings from the propagation of Damage Class 1 were used, but the edge sizing function was now added to the crack point at the 3 o'clock position to properly capture the notch geometry. In some places, the mesh may not properly capture the geometry. However, since only the FEM trend will be explored and the results will not be compared to their experimental counterparts, this error due to an insufficient mesh can be disregarded.

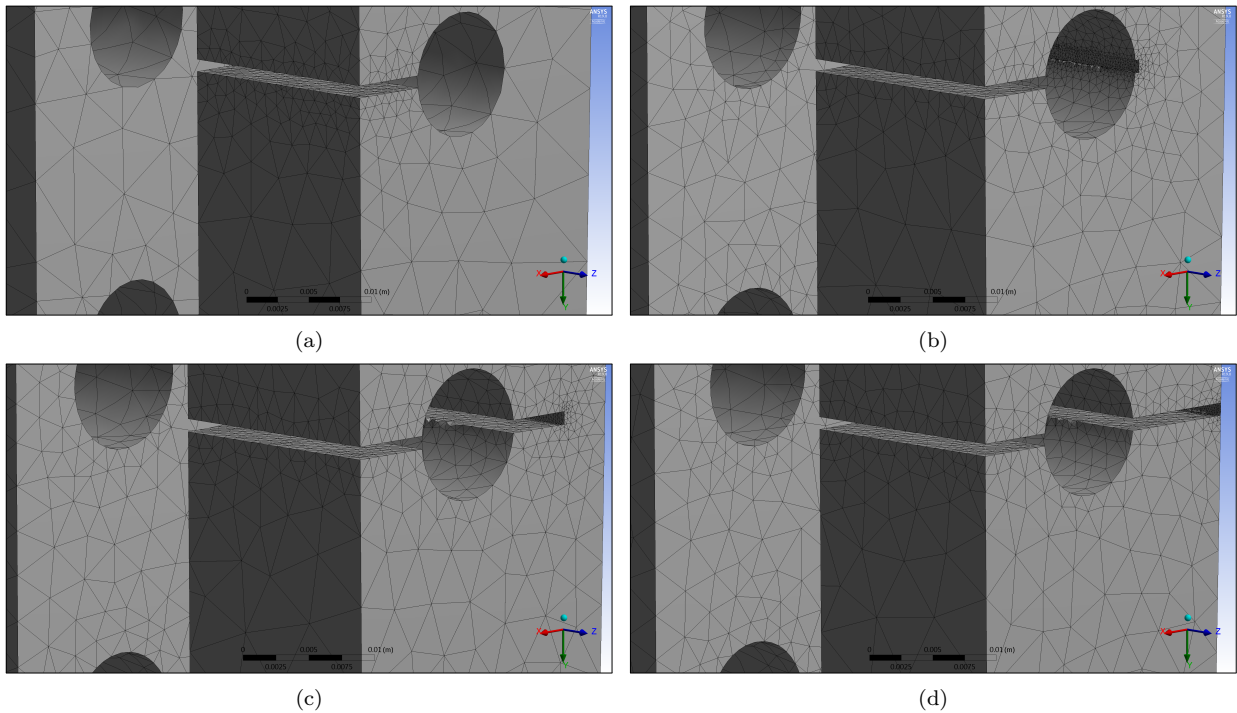


Figure 3.21: Examples of discrete FEM crack propagation cases of the second stage of Damage Class 1 or Damage Class 1(2), which includes full crack at 9 o'clock on upper pinhole ($a_1 = 6.7mm$), a) $a_2 = 0.0mm$ ($a/a_{max} = 0.4$); b) $a_2 = 0.3mm$ (initiated, $a/a_{max} = 0.42$); c) $a_2 = 5.5mm$ (propagated post midway, $a/a_{max} = 0.73$); d) $a_2 = 9.9mm$ (propagated almost fully, $a/a_{max} = 0.99$)

Figure 3.22 demonstrates the variance in FEM f_n caused by discrete crack propagation. This is the same results plotted in Figure 3.20, but for each mode and with different axes. The variance (y-axis) was transformed into a log-scale (semi-log plot) and is plotted over the ratio of crack length and critical crack length, a/a_{max} (x-axis). The ratio a/a_{max} normalises the crack length to allow comparison of all damage classes, which have different critical crack lengths and propagation increments. The additional damage case, Damage Class 1(2), is also shown.

From Figure 3.22, it is observed that the variance in natural frequencies increases as the discrete crack length increases. This implies the stiffness k of the blade decreases as the crack propagates, and thus the natural frequencies decrease as well. This decrease in k is a complex function and occurs differently for each damage scenario. This means that the natural frequencies are also affected differently for each mode. For example, in some instances, an exponential growth tendency is observed as in Mode 1 for Damage Class 1. In other instances, a logarithmic growth tendency is observed as in Mode 1 for Damage Classes 2 and 3. Near-linear behaviour is also observed as in Mode 3 for Damage Class 3, as well as a near constant gradient as in Mode 14 for Damage Class 1(2). Combinations of these behaviours are also apparent as in Mode 4 for Damage Class 1(2), where exponential growth precedes logarithmic growth. Thus, it was correct to not make any assumptions regarding the behaviour of the gradient between $a = 0$ and a_{max} . Concerning the relationship between Damage Class 1 and Damage Class 1(2), it is evident that the first growth stage of Damage Class 1(2) is equivalent to Damage Class 1 but on an altered x-scale as its a_{max} differs. Thus, the earlier statement made that Damage Class 1(2) comprises two stages, i.e. the initial cracking case and the additional cracking case, is demonstrated by the observed trend. These two stages are easily identified for each mode where the behaviour of the trend suddenly changes. This sudden change occurs where the crack from Damage Class 1 is fully propagated. This instant could only be detected in Figure 3.20; however, considering the trends in Figure 3.22, it is confirmed that this spike can be used as a failure warning. At the failure point, where $a_{max} = 1$, complete separation of the blade finger occurs and a sudden drop in variance is observed. This is due to a rise in natural frequencies because the system's physical properties changed and thus its dynamic behaviour will be different.

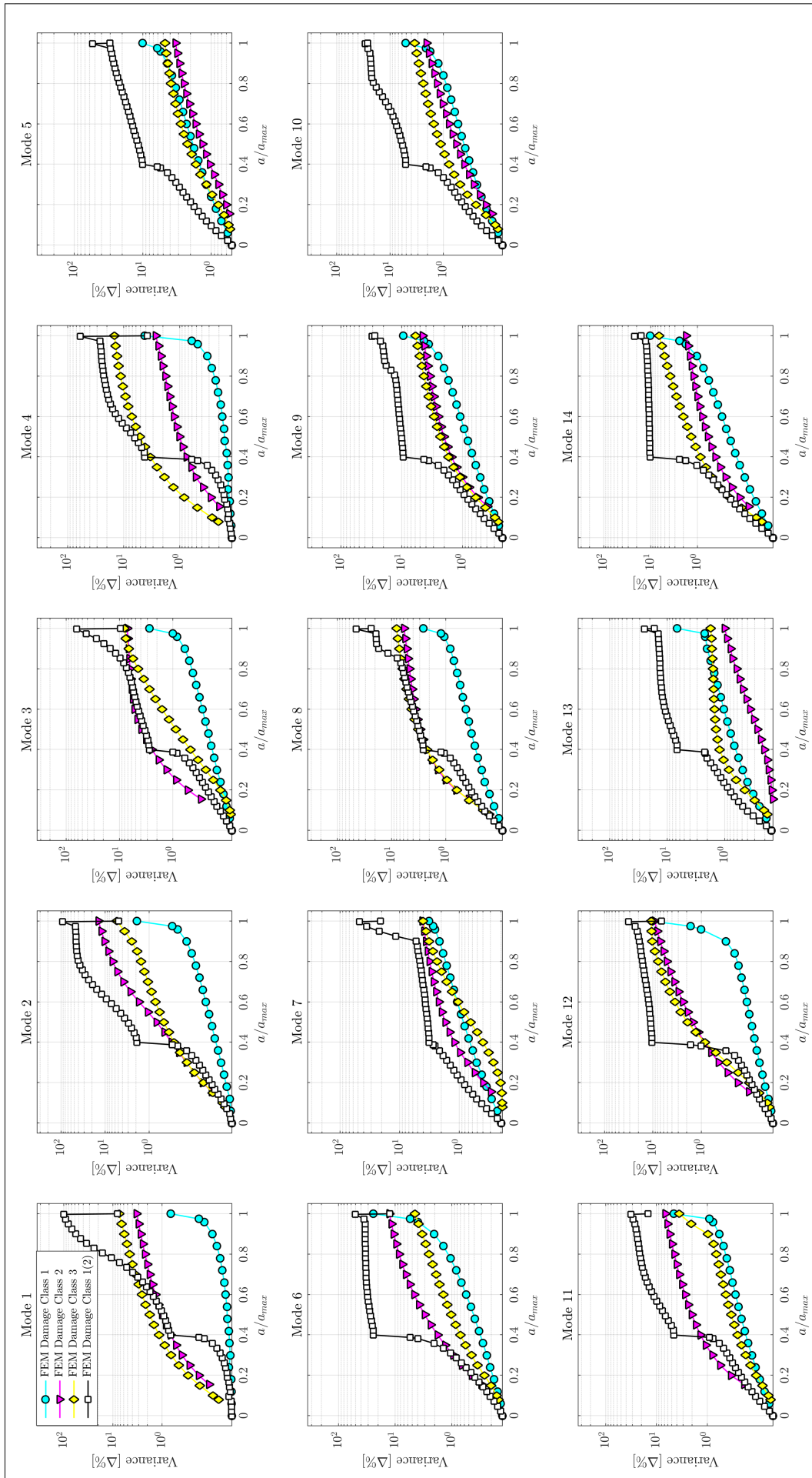


Figure 3.22: Variance in natural frequencies from FEM discrete crack propagation for damage classes: Δf_n vs. Δa

3.3.4 Spatial Relation of Natural Frequencies for Damage Classes

The shift in f_n per damage class for all modes is further examined in Figure 3.23. The distinct damaged data is superimposed on the healthy data, allowing the change in natural frequency to be observed for a particular blade as a consequence of damage. It is apparent that since the healthy data is consistent, a straight-line can be fitted through the data points per mode. This would not be the case when considering all the damage data, implying that the three separate Δf_n -cases should be considered. This is confirmed when individually observing the different damage classes, finding that a straight-line can be fitted to each class per mode. From this, it may be concluded that the consistency from the healthy data was transferred successfully to the damage classes, suggesting that a difference between classes exists. Hence, the sensitivity of the geometrical variability, considering the minimal mass loss, is very low in comparison with the sensitivity of the unknown and possibly varying material properties, considering the stiffness, on the variance of the healthy response. Therefore, very small differences in the healthy blades exist. The generated data for the geometrical variability from the parametric study in Section 3.1.2 corresponds with this. Henceforth, the experimental data and the unmodified explicit numerical cases with constant material properties are considered in this study, as the variability of the experimental data, and thus its behaviour, could not be properly captured with FEM.

Directing attention to the uniformity of the change in natural frequencies, i.e. fixed spatial relation of test blades regarding frequency magnitudes, Figure 3.24 is considered. Herein, the shift in f_n (Δf_n) is viewed from the zero-line, allowing a more detailed view and additional analysis of the magnitudes. Considering the different modes, tracing the Δf_n -size and -location for a specific test blade, it is found that the spatial relation is constant. For example, the minimum and maximum will remain as such after damage is introduced (see Mode 11) and/or outliers will remain outliers. The normal distribution and mean values (μ , dashed lines) for each class are also shown. An approximate straight-line fit is observed for each class, whereas this is not the case when considering the full dataset. This implies that differentiation is possible between the damage classes but not between the data points within each class. The distributions might be misrepresented due to the limited size of the data set; however, the assumption is made that the normal distribution is regarded above the data points to solve for this. The distance between the mean values allows separability of the data to be established. This will be discussed in the next section.

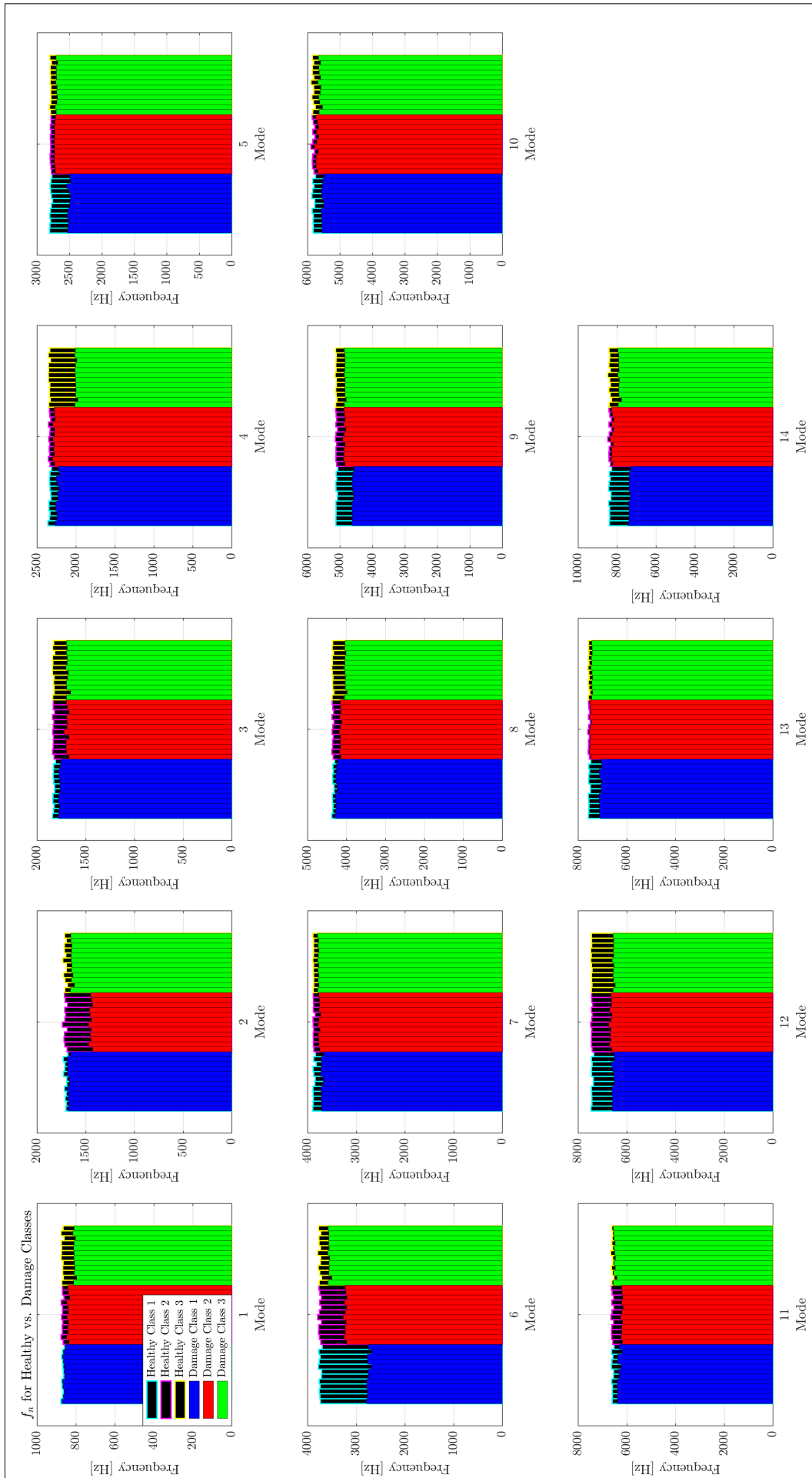


Figure 3.23: Natural frequencies f_n for damage classes, establishing their uniformity and spatial relation per blade for each class

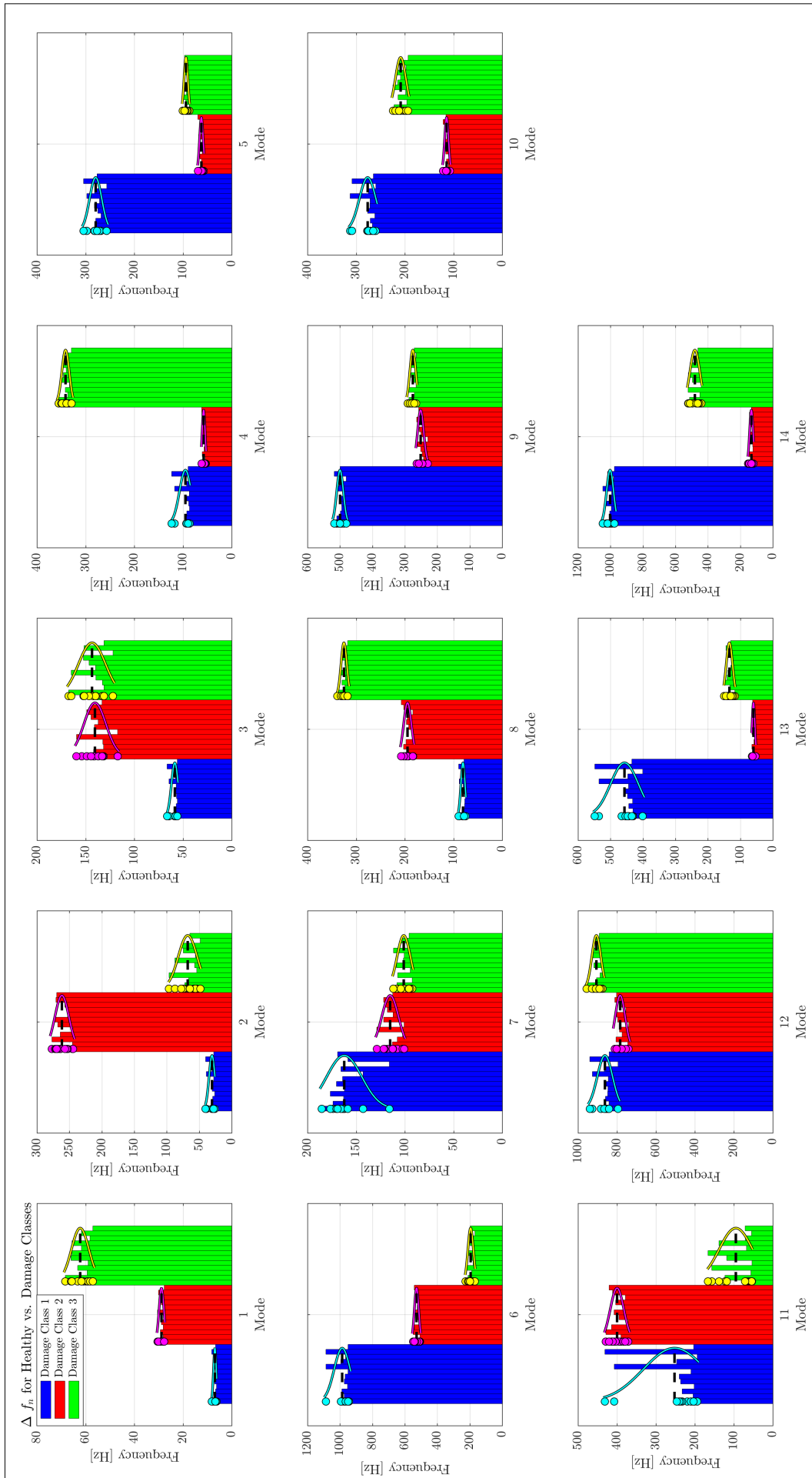


Figure 3.24: Absolute values of Δf_n for damage classes confirming the spatial relation per blade for each class, and showing the normal distribution and mean μ per class

3.4 Conclusion

A feasibility study for vibration-based damage detection was conducted through a FEM study and was subsequently investigated through experiments. First, the sensitivity of small geometrical variability present in the healthy blades was experimentally explored to establish the variability in the healthy response so that it can be used as a reference. Very similar results with a small variance were found. Then this was investigated through FEM, confirming low sensitivity of change in natural frequencies to geometrical differences. Additionally, the geometrical variability was identified as the secondary source of variability, whereas material properties were identified as the primary source of variability since it leads to higher sensitivity in the change in natural frequencies. According to Barthorpe et al. (2017), identifying and allowing for sources of variability at an early stage will result in good generalisation of the classification mode at a later stage. Next, the sensitivities of different damage scenarios at the most likely locations in the blade were explored to establish the damage-specific response and prove that structural damage in different locations does not cause the same shift in frequency. It was found that each scenario had a distinctive response in which the variability from the healthy blades are appropriately represented in the damage datasets with the varying pinhole diameter having a larger influence on the change in natural frequencies than the varying correctional grinding depth. Since the generated data for the geometrical variability from the parametric study was unable to properly represent the experimental trend, the experimental data and only the unmodified explicit numerical cases are considered from this point forward. Lastly, the spatial relation of shift in natural frequencies Δf_n and the test blades was explored to confirm the stability of the feature sensitivity to individual damage scenarios. This result identified and confirmed the natural frequencies as a suitable candidate discriminant feature for damage classification in the next chapter.

Chapter 4: Damage Detection and Identification

In this section, the means of damage detection and identification is explored according to Figure 4.1. Based on the observations in Chapter 3, the set of natural frequencies (f_n) was selected as the discrimination feature, with the potential to distinguish between healthy and damaged blades. This feature is sensitive to damage and is a low-dimensional noiseless feature. This feature was characterized (Step 1) by establishing the distinctiveness of the effect of the input parameter on the natural frequencies to determine the feature quality. This was done through defining the separability of data groups or classes. The data was visualised in a one-dimensional space wherein the class distributions were studied. Hereafter, the data was visualised in a two-dimensional space wherein the variation and clustering of the classes were investigated. In assessing the feature quality, the decision of employing the natural frequencies as the discrimination feature for feature classification can be made. In Step 2 of this approach, pattern recognition using supervised machine learning with support vector machines (SVMs) is applied to recognize different class behaviour in a dataset. This includes geometrical variability identification in healthy data, and damage detection and identification in healthy and damaged data. In using this manually selected feature instead of the FRFs, the curse of dimensionality is mitigated as the size of feature space was significantly reduced through transformation from frequency domain to modal domain (FRF to f_n), in which 14 peaks were extracted from 25 600 spectral lines per blade. This also reduced the noise in the signal. Thus, the effectiveness of the pattern recognition method is increased.

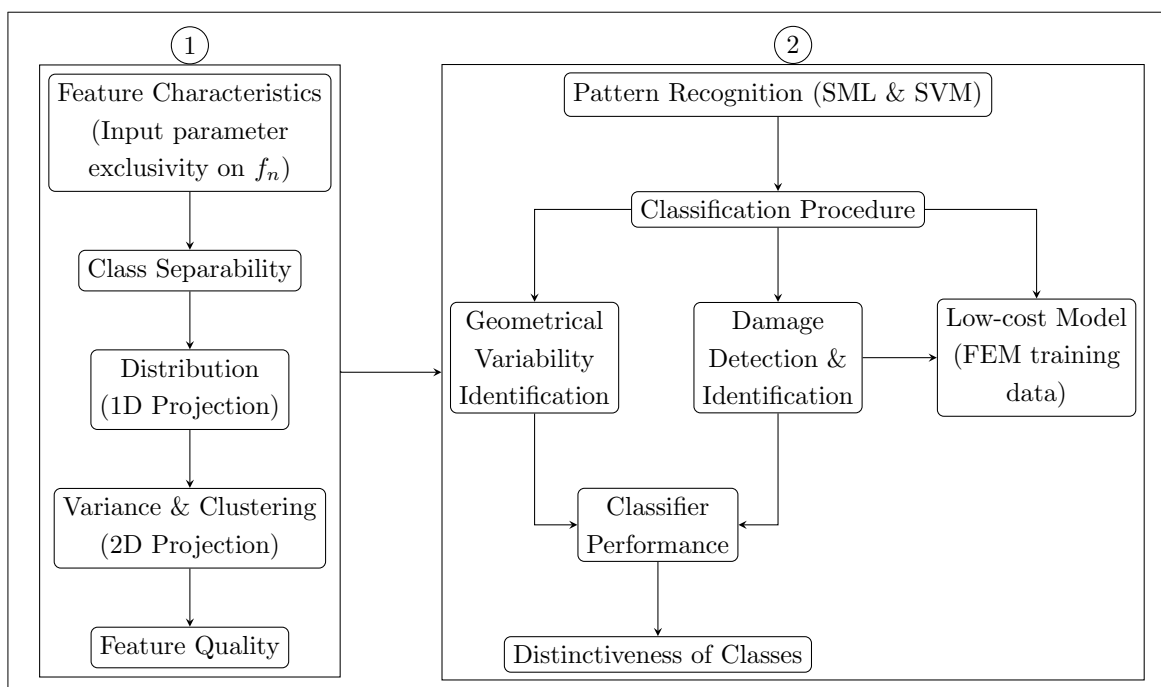


Figure 4.1: Approach to recognizing different class behaviour in datasets through classification using SML and SVMs

To assist in determining the outcome of the feasibility study, hypothesis tests are conducted. This approach is borrowed from (Barthorpe et al., 2017). The following hypotheses were formulated by considering the research questions in Section 1.3, the conclusions of Chapter 3, and integrating the approach in Figure 4.1. This scheme was followed to establish an approach in separating damage from healthy data and identifying different damage scenarios. In testing each hypothesis, a binary support vector machine (SVM) or its extension for multiple classes was utilised for classification of the relevant data, where observations of each class are available for training:

1. **Geometrical variability** can be effectively *identified* in **normal healthy data**, i.e. separate all distinct healthy data groups from each other.

2. **Damage** can be effectively *detected* in **healthy- and damaged data**, i.e. separate all data groups different from the normal healthy data group.
3. **Damage** can be effectively *identified* in **healthy- and damaged data**, i.e. separate all distinct data groups from each other.

The quality of the feature is explored in the first part of this chapter, which focuses on characterizing the feature vectors to ensure that it meets the classification prerequisites (Step 1). The complete classification procedure and results are discussed in the second part of this chapter (Step 2), where the hypotheses are tested to deliver a verdict on the feasibility of vibration-based damage detection and identification for freely supported pinned turbine blades.

Recall that inter-test variability is present within the results since all the tests were not conducted on the same day and the healthy cases and that the damage classes were tested months apart, not to forget the geometrical variability discussed in the previous section. This adds to the generalisation capacity of the classifiers. Note that features of each class are available for training, damage refers to all damage classes, and damage classes refer to single-location damage at different locations.

4.1 Data Characterization of Healthy and Damaged Cases

The experimental datasets or feature matrices ($[f_n]$), used to develop the classifiers and test the hypotheses, are sampled from 36 test blades or observations. Within each observation, 14 natural frequencies ($\{f_n\}$) are available, either in a healthy or damaged state, depending on the hypothesis. Natural frequency qualifies as a discrimination feature because its sensitivity to damage is apparent. However, by comparing the feature vectors or modes, a prominent damage-sensitive f_n may be identified. In this section, the compatibility and quality of these selected features, pertaining to each hypothesis, are evaluated through describing the datasets.

The discriminant feature vectors are presented in a one-dimensional space to further explore the variability in their spread and the separability between classes. Considering each feature vector $\{f_n\}$, a generalised description of the variance or behaviour of each class is provided. A normal probability distribution ranging from minimum to maximum was assumed for each dataset due to the limited sample size that made it difficult to capture the actual distribution. It was also assumed that no outliers are present. The data is characterized to effectively describe the behaviour of the specific datasets by exploring the distributions and separability between classes through data visualization methods. By doing this, the sensitivity study results from Chapter 3 will be enhanced. This will also ensure appropriate conditions of the sets for the hypothesis tests and classification regarding the separability of classes. To reduce the dimensions of the feature vectors for a clearer verdict on separability between classes, the natural frequencies are projected to a two-dimensional space to form distinct clusters, if obtainable. This means that the entries of the feature vector will be plotted against each other as illustrated in Figure 4.2, which shows the new perspective of the plotted feature vectors at a given entry.

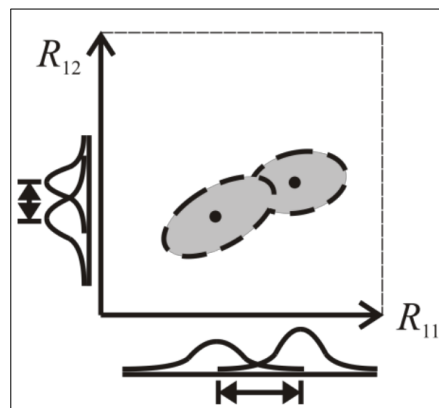


Figure 4.2: Projection of feature dataset distributions into two-dimensional space at a given entry (Barthorpe, 2011)

From Section 3.2.3 and Figure 3.13, it was apparent that the variance in natural frequency at Mode 6 was the best distributed for the three damage scenarios with values of 30%, 12.5%, and 5%, respectively. It was also evident that the variance was nearly equal at Mode 12 for the three damage scenarios with values around 11%. From this, it is obvious that Mode 6 will deliver the best clustering results and Mode 12 the worst. These two modes are used throughout this chapter, where relevant, to illustrate the discussions to follow. Therefore, for all two-dimensional visualisation plots to follow, Mode 6 will be fixed and thus be the independent variable, and the other modes will vary and thus be the dependent variables.

4.1.1 Healthy Blades

The first dataset consists of only healthy data distributed into four groups of 11, 10, 9, and 6 blades that contain combinations of the geometrical variability, i.e. the presence of grinding and size of the tapered major pinhole diameter (minimum or maximum). These groups are assigned a No Grind or Grind condition and a Min D or Max D condition (see Section 3.1 and Appendix B). The first hypothesis, i.e. identification of geometrical variabilities in healthy blades, will be tested with this dataset. From the observations in Chapter 3, a small variance in the natural frequencies is present within the healthy blades due to geometrical variability. This would suggest similarity of these results. To verify this assumption, the distribution of the natural frequencies for each class is explored as well as the possible separability of these distributions in Figure 4.3 in which the possible separation of these distributions is considered.

It is evident in Figure 4.3 that the data points are spread at random and that distances between the mean μ (dotted line) of each class are small, resulting in almost total overlap of the distributions for all features. This makes it extremely difficult to visually separate the classes, and it is anticipated that this would be the case even when projecting to a higher dimension to allow a different perspective of the datasets. This uncertainty or ambiguity is due to the limited size of the datasets and the feature's low sensitivity to geometrical variability in the blades. This confirms the similarity of healthy blades, as the results are closely matching. This is corroborated by the healthy FEM falling either within or on the tail of the distribution, depending on the model validation error, relating the experiments and the FEM. The mean of the healthiest cases also falls around the centre of the total distribution, confirming that the selected cases are adequate in representing the healthy reference or benchmark.

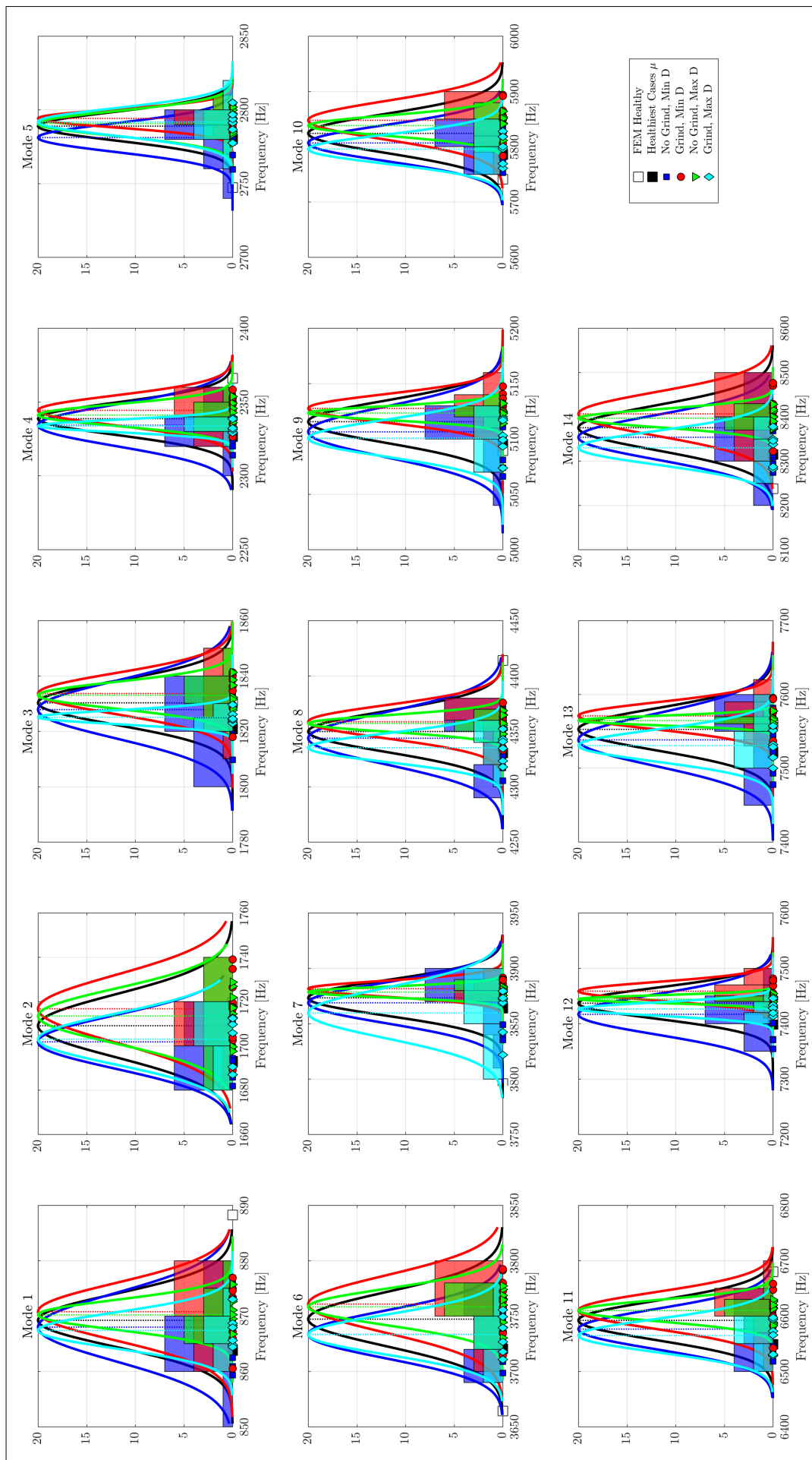


Figure 4.3: Distribution of natural frequencies from geometrical variability of healthy blades

To reduce the dimensions of the feature vectors for a clearer verdict on class discrimination, the natural frequencies are projected to a higher-dimensional space to form distinct clusters, if obtainable. With a numerical model, a single blade can be modelled and replicated, resulting in multiple blades identical in geometry, material composition, and all points of contact. However, in reality this is not the case as each of these three parameters are inherently affected by a small variation, resulting in the experimental natural frequencies to fall within a range about a mean value in an ambiguous cluster (Dewey and Lam, 2008). This is illustrated in Figure 4.4.

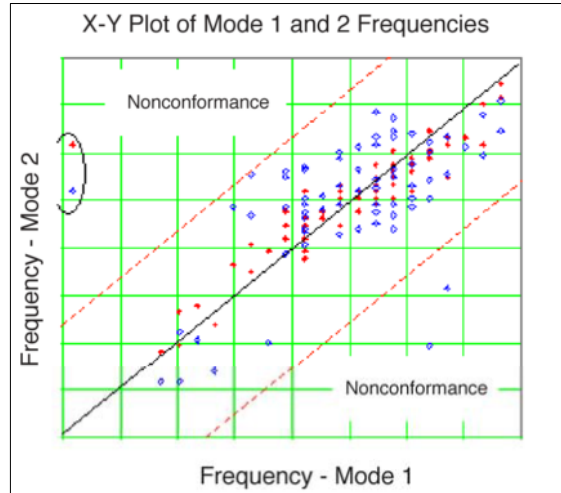


Figure 4.4: An example of the expected variance in the first and second natural frequencies of healthy blades (Dewey and Lam, 2008)

It is expected that similar state of health cases will closely follow the example above, in which it is evident that where the distribution of the two classes overlap, it will be very difficult to separate the scattered data. Moreover, that distinct state of health cases will render separable clusters of the former, each with natural frequencies falling in their respective ranges about its mean. Hence, the clusters from the healthy cases as well as the damage classes should behave as described above when considered individually.

The argument based on Figure 4.4, is indeed the case for the healthy data, as illustrated in Figure 4.5. The expected variance in natural frequencies for healthy blades, obtained from experiments and FEM, are shown in a two-dimensional space. Two separate clusters are observed, the FEM and the experimental frequencies. The distance between the experimental and FEM clusters are equivalent to the model validation error. This agrees with the two neighbouring clusters observed in Figure 4.4. Thus, when considering the scale of the feature space and this distance, the FEM is insufficient in describing the experimental geometrical variability and supports that the primary source of variability requires further investigation (see Section 3.1). However, it is sufficient in describing the general behaviour of the experimental datasets from the same state of health. This presents further evidence of the selected feature's low sensitivity to geometrical variability and increases the chance of its higher sensitivity to damage, and thus enhancing its discriminative capability.

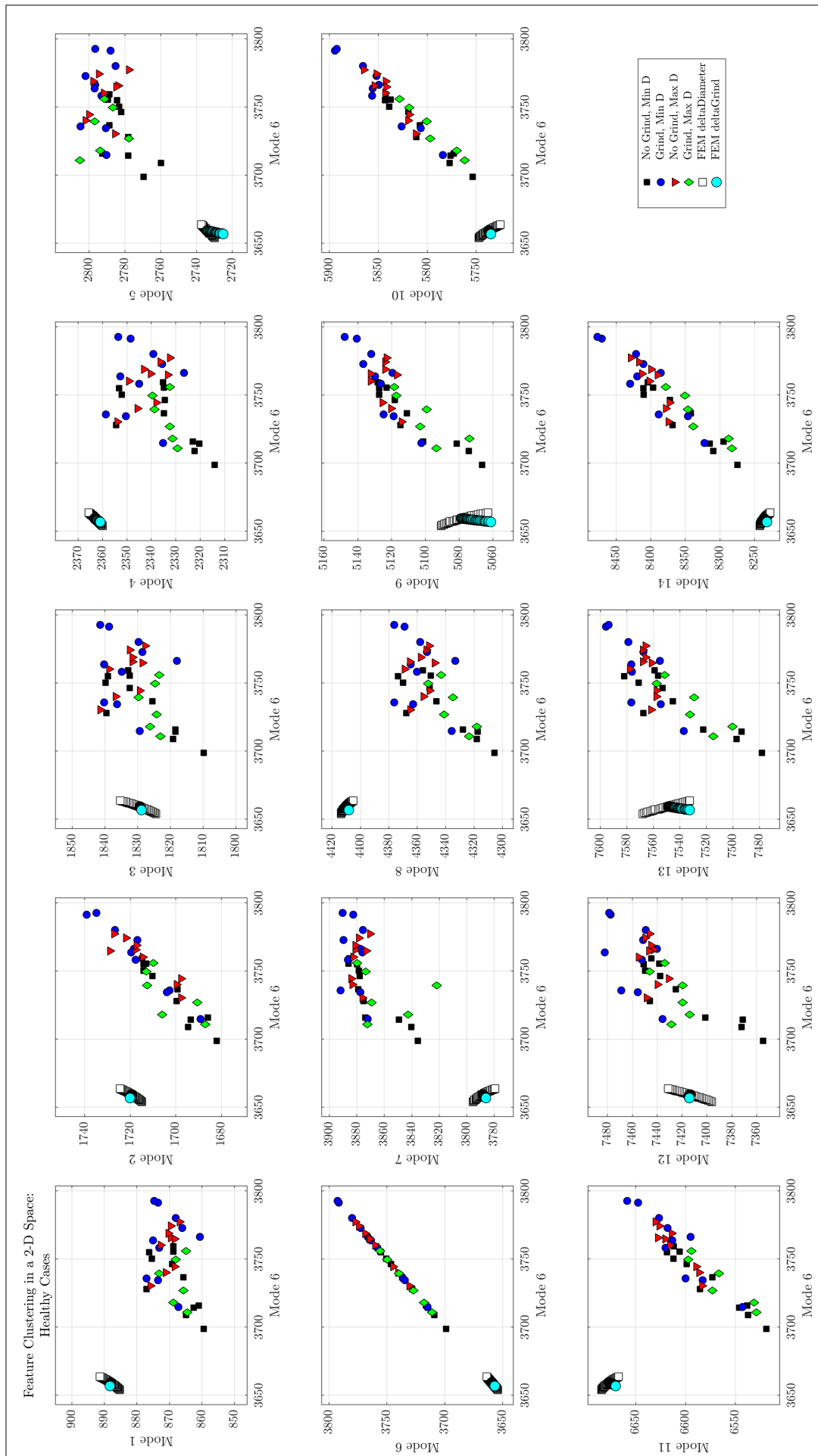


Figure 4.5: Clustering of natural frequencies (feature vectors) from geometrical variability of undamaged blades in two-dimensional space, Mode 6 vs. all modes

4.1.2 Damaged Blades

The second dataset consists of healthy and damaged data and comprises three equally sized groups that represent the designated damaged scenarios so that the particular blades can be compared, i.e. the damaged blade to its healthy counterpart. To ensure that these groups have a similar healthy variance in natural frequencies, the healthy blades were divided according to consistency of geometrical variability (see Section 3.2 and Appendix B). The three damage scenarios are assigned labels Damage Classes 1–3 and are a $1mm$ uniform notch on the root at 1) the upper pinhole on the leading pressure side, and just above the root on 2) the trailing- and 3) the leading edge. The second and third hypotheses, i.e. detection and identification of damage blades, will be tested with this dataset. From the observations in Chapter 3, distinct variances in the natural frequencies of the damaged blades exist regarding the introduced damage scenarios. This would suggest distinction of these results. To verify this assumption, the distribution of the natural frequencies for each class is explored in Figure 4.6 in which the possible separability of these distributions is considered.

It is evident in Figure 4.6 that the data points are grouped in an arbitrary pattern and that distances between the mean μ (dotted line) of each class, in most cases, are large. This results in slight or larger overlapping of the distributions for some features. This makes it very possible to visually separate the classes, and it is anticipated that this would be the case especially when projecting the vectors to a higher dimension to allow a different perspective of the datasets. Even though the datasets have a limited size, it can be concluded that a difference or distinction between healthy and damaged blades exist, as well as between the damage classes. The FEM damage classes fall either within, on the tail of, or close to the distribution, depending on the model validation error. This supports the indirect comparison between experiments and FEM for the damage classes. Note that even though some FEM results are outliers since they do not fall close to their respective classes (e.g. Mode 7) and cannot be successfully separated, the possibility of separation and thus definitive clustering with its experimental counterpart in a higher dimension still exists.

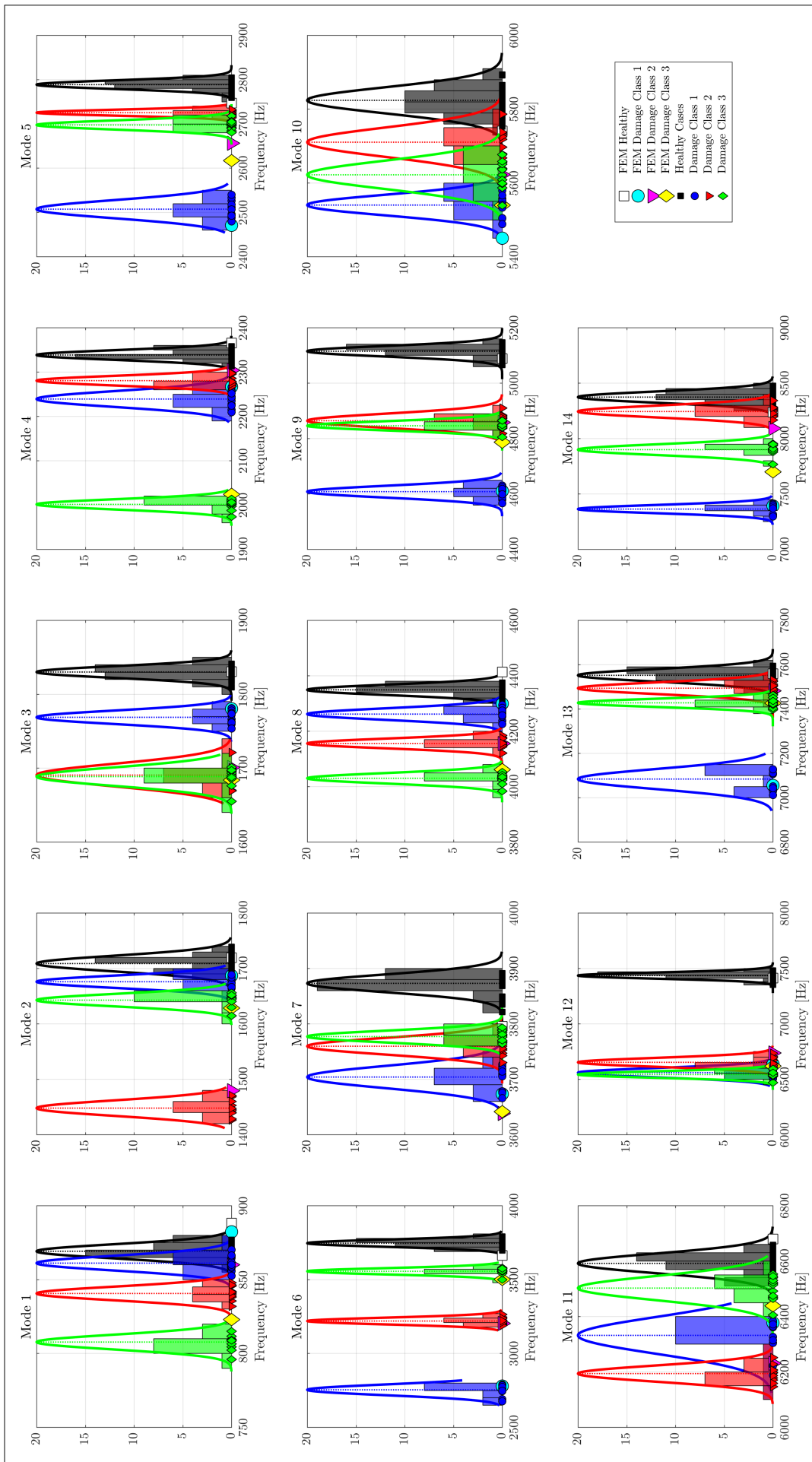


Figure 4.6: Distribution of natural frequencies from damaged blades (Experiment vs. FEM)

Figure 4.7 illustrates an example of projecting vectors to higher-dimensional space in which it is observed that the scattered data form three clusters. The dataset contains three classes. In some case, the three clusters are well separated, while in other cases, overlapping of some clusters occurs (Pawar and Jung, 2008). It is also seen that a small variation is present in each cluster, and that the data points fall within a range about a mean value.

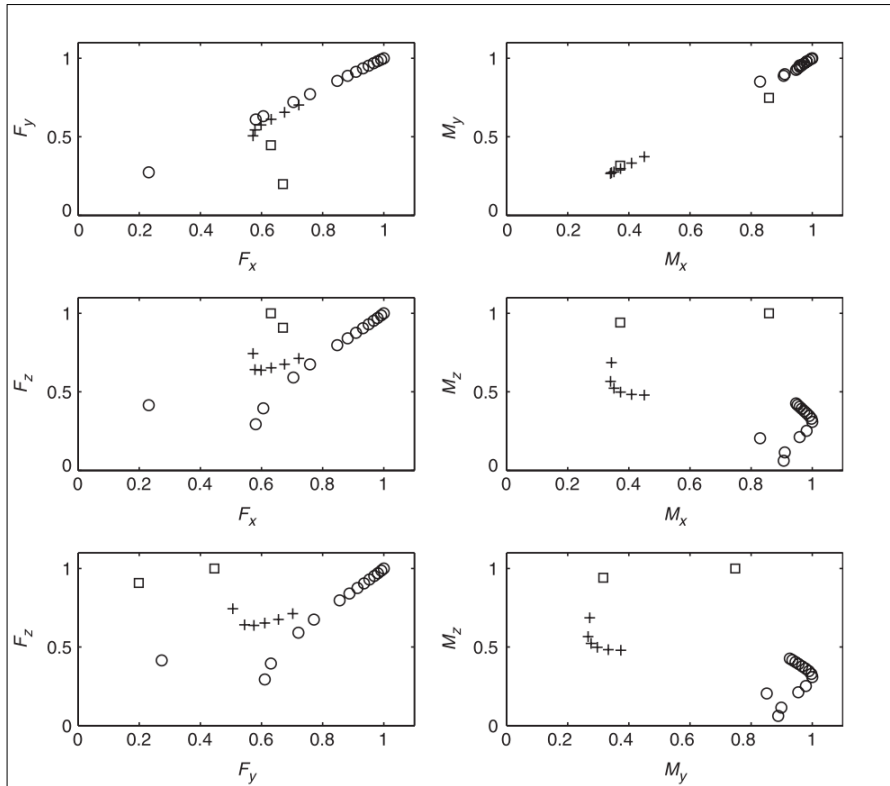


Figure 4.7: An example of clustering of three damage classes in two-dimensional space (Pawar and Jung, 2008)

It is expected that if different state of health cases is separable, the behaviour of the data will follow the clustering as in the example above. It is clear in Figure 4.7 that, where the distribution of two classes overlap, it will be very difficult to separate the scattered data. However, separation of distinct clusters will be less problematic.

The explicit clustering of the natural frequencies in a two-dimensional space is shown in Figure 4.8 in which four separate clusters are observed. This confirms the suitability of the feature and presents further evidence of the selected feature's high sensitivity to damage, thus enhancing its discriminative capability. Considering the scale of the feature space and the excellent separability of classes, direct comparison of the experiment also seems likely as the FEM falls close to the experimental clusters (the distance is equivalent to the model validation error). It is observed that the FEM falls within or close to the cluster bounds for all classes at most modes except for Mode 7, where Damage Classes 2 and 3 is out of bounds. Considering Damage Class 1, it is evident that the behaviour of the test data is properly represented by the FEM, particularly at Modes 4, 6, 9, and 11–14. This is best demonstrated at Mode 11. The scatter of the remaining FEM classes is insufficient in capturing the behaviour of their test counterparts. This suggests that numerical data could be used to supplement the experimental data or even substitute it for training data to predict the expected behaviour and classification of a damage scenario, which is reliant on the scatter of the datasets. However, this requires further investigation through an extensive numerical study. This includes parametric studies for geometrical variability and material properties to properly capture the spread and behaviour of the data. This is required since discrepancies in the model can hinder the outcome of the proposed method if not thoroughly understood, making this a risky suggestion. If this is pursued, it will allow fewer experiments for fewer damage scenarios to be required and thus possibly overcome a drawback of supervised machine learning. This will be discussed in Section 4.3.3. This extensive investigation is not part of the present scope of work. Hence, only experimental data will be used in the classification procedure to follow.

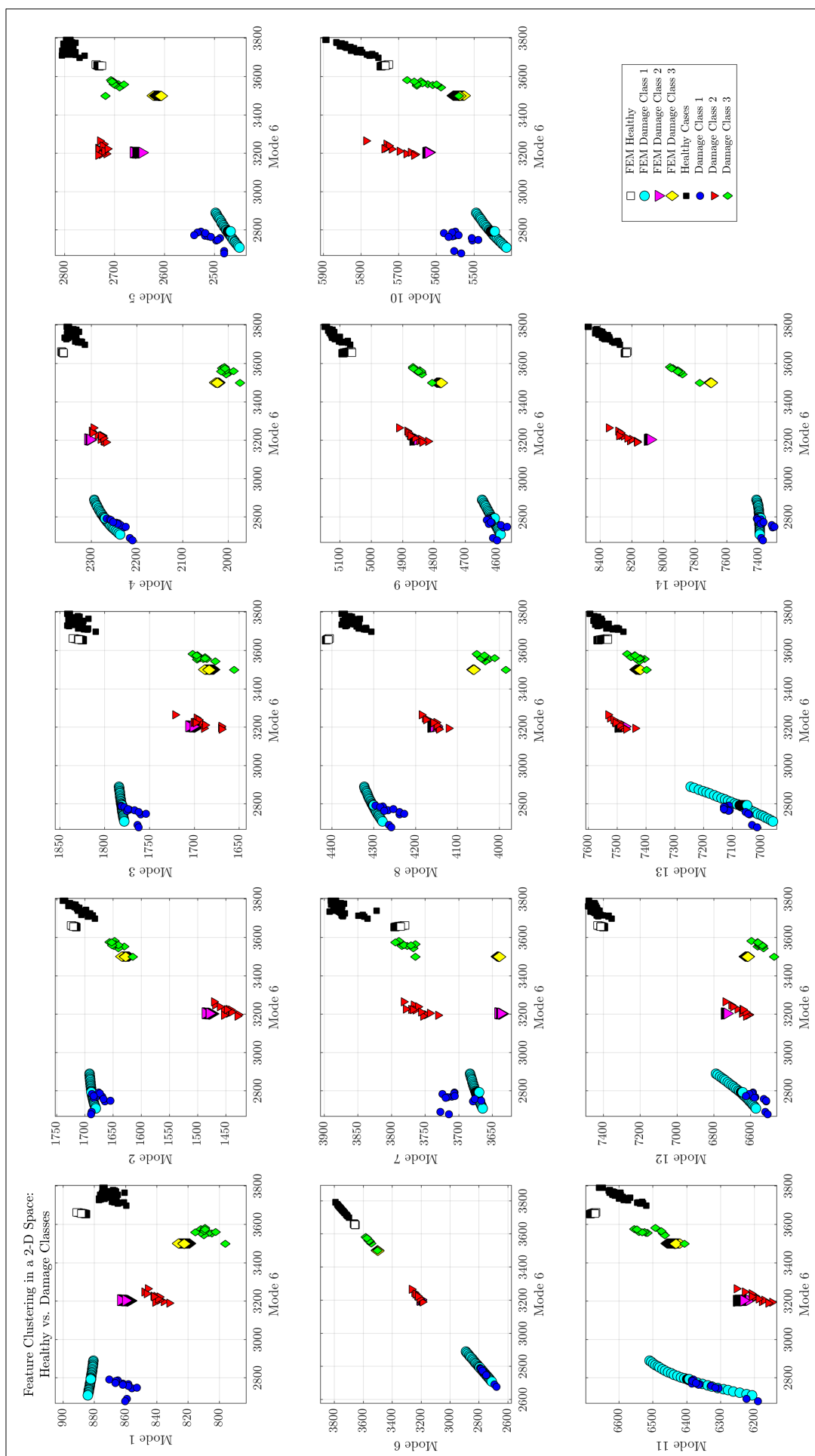


Figure 4.8: Clustering of natural frequencies (feature vectors) of damaged blades in two-dimensional space, Mode 6 vs. all modes

According to (Barthorpe, 2011), the discriminative ability between healthy and damaged cases, as well as between damage classes, of the selected feature influences the success of the classifier. He assessed the strength of his selected feature by considering four criteria specific to his work. Thus, they are not worth mentioning. However, by considering these criteria, and the observed behaviour of the datasets in Figure 4.6 and Figure 4.8, the following remarks were noted in reference to this study. These remarks justify and increase the suitability of natural frequency as the discrimination feature:

1. The feature is sensitive to the introduced damage. From the separability of the datasets, it is clear that distinctive clusters for each damage class exist.
2. The feature vectors for a specific class contain consistent values between tests per blade, i.e. inter-test variability, where the feature vectors between classes or blade sets contain opposing values. The consistent feature vectors in each class increase the robustness of the feature. Both these observations increase the distinct clustering of classes.
3. The visual separation of classes is increased by projecting the feature vectors into a higher dimension to explore their distributions. This also decreases the possibility of outliers. Note that this should be analysed thoroughly by considering all feature vectors, i.e. the different modes. This is demonstrated by examining the increase in separability of classes in Mode 7 from Figure 4.6 to Figure 4.8.

Now that confidence in the suitability of natural frequency as selected discriminant feature has been established, damage classification (i.e. detection and identification) through employing this feature in statistical pattern recognition can be pursued. It is observed that the natural frequencies qualify as a quality selected feature as they have the capacity to adequately discriminate between damage states. Features with these attributes are central to statistical classification using SVMs (Barthorpe et al., 2017). Note that the highest quality feature vector can probably be determined by considering the degree of prominence for each feature vector. However, this was not explored in the study.

4.2 Classification Procedure

A multi-class support vector machine (SVM) is considered for the feasibility study and discussed in this section. A similar approach and method was employed by other authors such as Yang and Widodo (2008) as well as Yin and Hou (2016), who discussed recent advances on SVM-based fault diagnosis and process monitoring in components and equipment used in complex industrial processes. These authors describe the general application of the approach. Barthorpe et al. (2017) focused on detecting multi-location damage with an effective and well-developed classifier, requiring only single-location damage training data to classify multi-location damage. In this study, only the application of a default SVM classifier without modification is of concern, and not its detailed development for optimization. Thus, neither classifier optimization nor a hyperparameter study was conducted. The regularization values were obtained by trial-and-error and are kept constant during the validation phase, leaving the training set as the only variable in the accuracy of the classifier. Values that rendered an acceptable probability of correct classification were selected. The classification procedure is illustrated in Figure 4.9.

To investigate the hypotheses introduced at the start of this chapter, two identical classifiers, discussed in the following section, are built and tested for each hypothesis. The first is trained on the healthy dataset, which consists of different observations of defect combinations or geometrical variability. The second is trained on the healthy dataset in comparison with the different damage class datasets, consisting of healthy and different damage class observations. The classifier parameter values are prescribed by the training set, whereas the success of the developed classifier is verified, for an independent set of observations, by the validation set. All feature vectors $\{f_n\}$ comprising 14 entries each, are used during the training and validation phases. Thus, for adequate classification results, the limited size of the dataset will not be a problem if each class holds strong support vectors that are capable of describing the respective class behaviour.

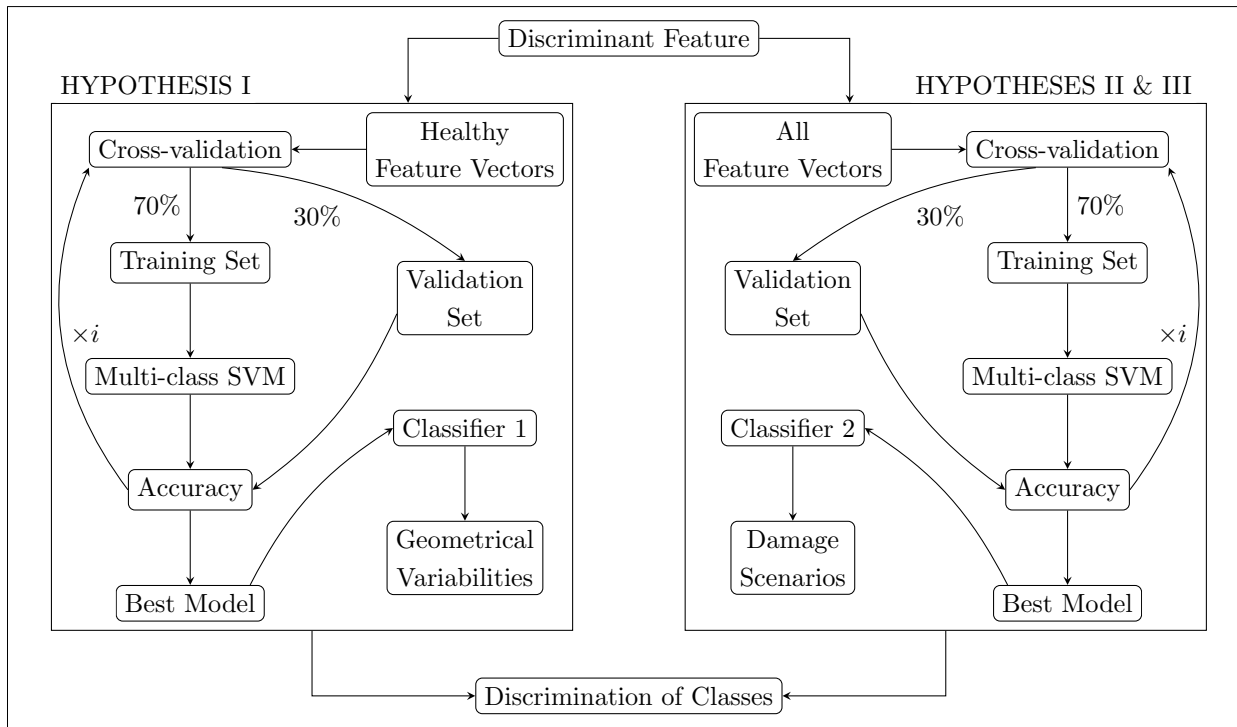


Figure 4.9: Classification Procedure

The cross-validation method was applied to examine the accuracy of the resulting fitted model. It was selected to ensure minimal loss in modelling or testing capability since insufficient data is available for partitioning into separate training, validation, and testing sets. This is also the most popular method to ensure optimal regularization parameters (Santos et al., 2016). The procedure entails a random holdout sample proportion specified as the validation set (comprising 30% of the original set), whereas the rest is the training set (comprising the remaining 70% of the original set). During the validation phase, the classifier performance is calculated as the correct prediction rate of the classifier for a sequence of iterations, each with a new independent training set of previously unseen observations (Santos et al., 2016; Barthorpe et al., 2017). Depending on the size of the dataset, repeating sets may occur.

Since the original datasets are small and the mapped classification plot serves only as a visual representation of the classifier performance, the best model obtained in cross-validation per class for each classification were selected to obtain the highest quality depiction. This has no influence on the classifier performance. The mapped classifier plot is also easier to interpret than the performance plot. In the case of a larger dataset, a non-overlapping testing set can also be allocated. Note that the classification was executed for all 14 feature vectors except for where the projected feature vectors are equal (i.e. where Mode $n = \text{Mode } n$). For the classification results to follow, the first feature vector is constant (Mode 6, on x-axes) and the second varies (Modes 1 – 14, on y-axes). This is because of the perfect separability of the class clusters in Mode 6 (see Figure 4.8) that ensures a strong foundation for excellent classification results. The computed classifier accuracy for each mode will also be in reference to this combination.

4.2.1 Classifier Structure

This study employs non-linear multi-class support vector machines (SVMs), comprising a combination of One-versus-All (OvA) binary SVMs, for damage detection and identification. The classifiers were built using the MATLAB Statistics and Machine Learning Toolbox and Bioinformatics Toolbox pertaining to SVM classification. The classifier structure is based on the binary SVM extended to the multi-class problem. In the classifier, the predictor data is standardized and the radial basis function (RBF) kernel is used. The regularization or hyperparameters, used to help prevent over-fitting to the training data, for the employed RBF kernel are: radial basis kernel width ('KernelScale'), $\alpha = \text{auto}$; and the misclassification tolerance parameter ('BoxConstraint'), $C = 15$. These values were obtained by a trial-and-error approach for best performance

to ensure an appropriate balance between the calculation complexity and the separation error (Gryllias and Antoniadis, 2012). This application of the SVM supports low-dimensional or moderate-dimensional datasets.

Both classifiers consist of four binary SVM classifiers and have the objective of detecting and identifying discriminant classes from their input feature vectors. The classification occurs in two-dimensional space, in which the optimal separating hyperplanes or decision boundaries between classes are displayed. The correct classification rate, a property of the classifier performance object, of each classifier per iteration is plotted to obtain the feature set's discriminatory performance.

4.2.2 Approach to Address Degree of Over-fitting and Uncertain Regions

The background of classified regions was shaded through classifying a fine grid's coordinates, which were used as new observations from the training data's distribution. Note that the more dispersed the class from its training samples, the broader the surface, and thus certain background regions are assigned a class. To obtain an unambiguous answer, every region of the plot must be assigned to a specific class, even if no training samples are present at a specific location. Hence, the employed multi-class SVMs attempt to assign samples into one of the respective designated classes with some degree of over-fitting. This is illustrated in Figure 4.10a. This degree of over-fitting is dependent on the distances between the number of discrete populated areas or clusters on the classification map. The optimal separating hyperplane or decision boundary, which maximises the margin between the nearest points (i.e. support vectors, SVs) of different classes, between classes is determined from these distances.

To compensate for the degree of over-fitting, a perimeter that is based on an elliptical distribution, which generalizes the multivariate or joint normal distribution, was constructed around each class to place emphasis on these specific regions. This is illustrated in Figure 4.10b, in which the transitions between classes, which are uncertain classification regions, are also indicated. The centre of the perimeter is calculated as the means of the training data (μ_A, μ_B), and the radii of the perimeter is calculated as 3 standard deviations of the training data ($R_{A,B} = 3\sigma_{A,B}$). This ensures that 99.73%, i.e. $\mu \pm 3\sigma$, of the data is represented by the perimeter. This adds a confidence level to the captured concentrated area, solving the problem of the uncertain classification regions, limited data, and limited classes. This implies that all data points inside these perimeters should be considered as true observations above the outside areas without any observations that are bound by the borderlines. This simplifies the interpretation of results when adhering to these perimeters. This implemented idea is derived from one-class support vector domain description (SVDD), which attempts to find an enclosing circle in the original space (or hypersphere in kernel space) of a class rather than finding class separation lines in the original space (or hyperplanes in kernel space) (Breton and Lloyd, 2010). This method is illustrated in Figure 4.10c, using $\sigma = 2$ of each class SVs.

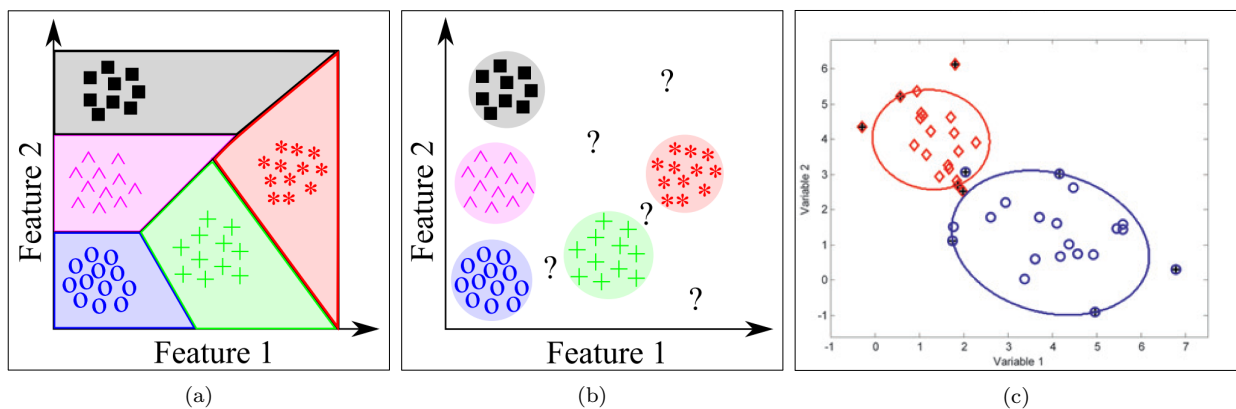


Figure 4.10: Example of decision boundaries for, a) Multi-class SVM showing some degree of over-fitting (Schmidt and Heyns, 2019); b) Regions of concern based on true observations, showing uncertain classification regions indicated by question marks (?) (Schmidt and Heyns, 2019); c) One-class support vector domain description (SVDD) with $\sigma = 2$ of each class SVs indicated by symbols with crosses (+) (Breton and Lloyd, 2010)

Both classifiers were presented with a hypothesis-specific dataset, i.e. a dataset relevant to the scope of the hypothesis test, comprising a validation and training set, with both containing the same class labels. Each classifier was validated using the same procedure to establish its generalization or accuracy, which is used to support the outcome of each hypothesis test along with its actual classification.

4.3 Classification Results

4.3.1 Hypothesis Test I - Geometrical Variability Identification

The first hypothesis stated that geometrical variability could be effectively identified in normal healthy data, i.e. separate all distinct healthy data groups from each other. This hypothesis is tested using Classifier 1, and the healthy geometrical variability dataset. The healthy observations with geometrical variability comprise four classes of 11, 10, 9, and 6 observations labelled as 1) No Grind, Min D; 2) Grind, Min D; 3) No Grind, Max D; and 4) Grind, Max D. These labels come from combinations of the presence of correctional grinding on the root, and the sizing of the major pinhole diameter (minimum or maximum). Classifier 1 is trained using $(\text{Dataset } 1)_{train}$, i.e. respective class observations of 8, 7, 6, and 4; and tested using $(\text{Dataset } 1)_{test}$, i.e. respective class observations of 3, 3, 3, and 2. Note that the combination of the number of classes and the limited number of observations already restricts the classifier even before its execution, imposing a questionable performance that will result in an ambiguous mapping of the predictor data and low and inconsistent classification accuracy. The classification is mapped in a two-dimensional space in Figure 4.11, and its accuracy for all iterations is shown in Figure 4.12.

From Figure 4.11, it is evident that the classification of the geometrical variability in healthy blades failed. In all modes, the disorder and worthless decision boundaries, which have no predictive power, indicate this failed attempt in identifying defects in healthy blades. This is caused by the bad separability of the different classes (see Section 4.1.1) and the inadequate support vectors available for each class. This is due to the limited number of observations for each class that are incapable of describing the behaviour of the respective class. It is observed that many ambiguous islands (kernel decision boundaries), without a recognisable pattern, exist. This is due to excessive over-fitting of the classes, which delivers an inconclusive answer. Regarding the perimeters, which were constructed to address the over-fitting issue, it is clear that they were unsuccessful in concentrating the classification regions to consider. In most cases, these perimeters capture a large portion of the whole classification map. The wide scatter of each class causes this.

In Figure 4.12, it is observed that the overall discriminatory performance of Classifier 1, in most cases, for all classes is between 50% and 80% with an all-class average of about 70%. The explicit class accuracy can be derived from the classification mapping in Figure 4.11, in which inconclusive identification is observed. From both these outcomes, it can be understood that the accuracy in differentiating between explicit classes are very low. With the One-versus-All (OvA) approach, the overall accuracy of the classifier is calculated and not the classification accuracy of explicit classes. The overall classifier accuracy depends on the quality of the training dataset. This is because the classifier predicts the class of all test data and then compares it to an explicit class. This high misclassification rate for all feature vectors can be ascribed to their low sensitivity to geometrical variability, and the damage-sensitive nature of natural frequencies, noted in Chapter 3.

The performance of the constructed SVM, used to evaluate the first hypothesis, demonstrates that it cannot detect and identify defects, i.e. geometrical variability. Thus, the first hypothesis is rejected. This implies that the healthy classes are very similar and cannot be distinguished. This agrees with the ambiguous classification results. Considering this conclusion, it is anticipated that similar classes will behave correspondingly.

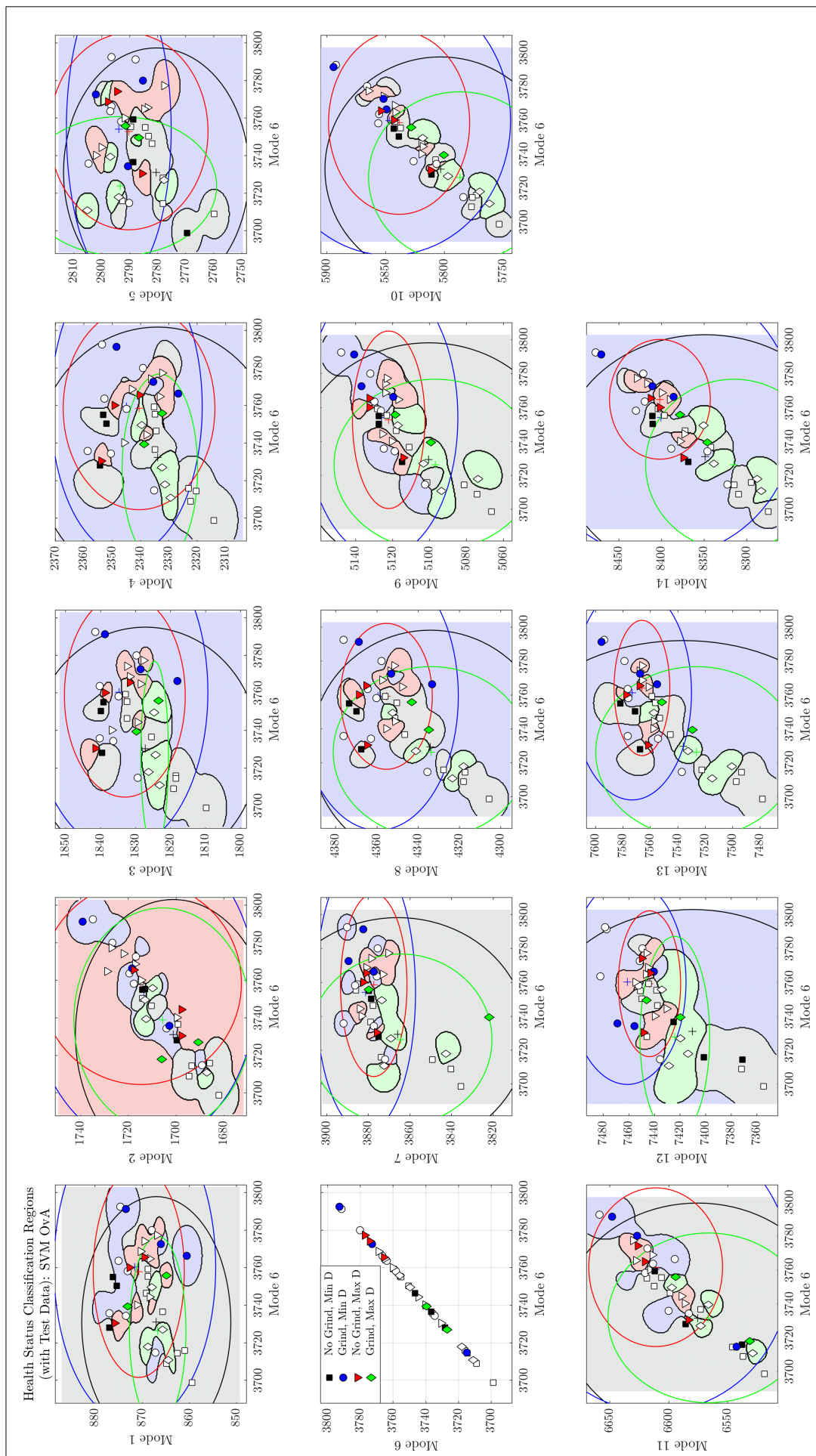


Figure 4.11: Results for Hypothesis Test I - Geometrical variability identification through classification of healthy cases, Mode 6 vs. all modes

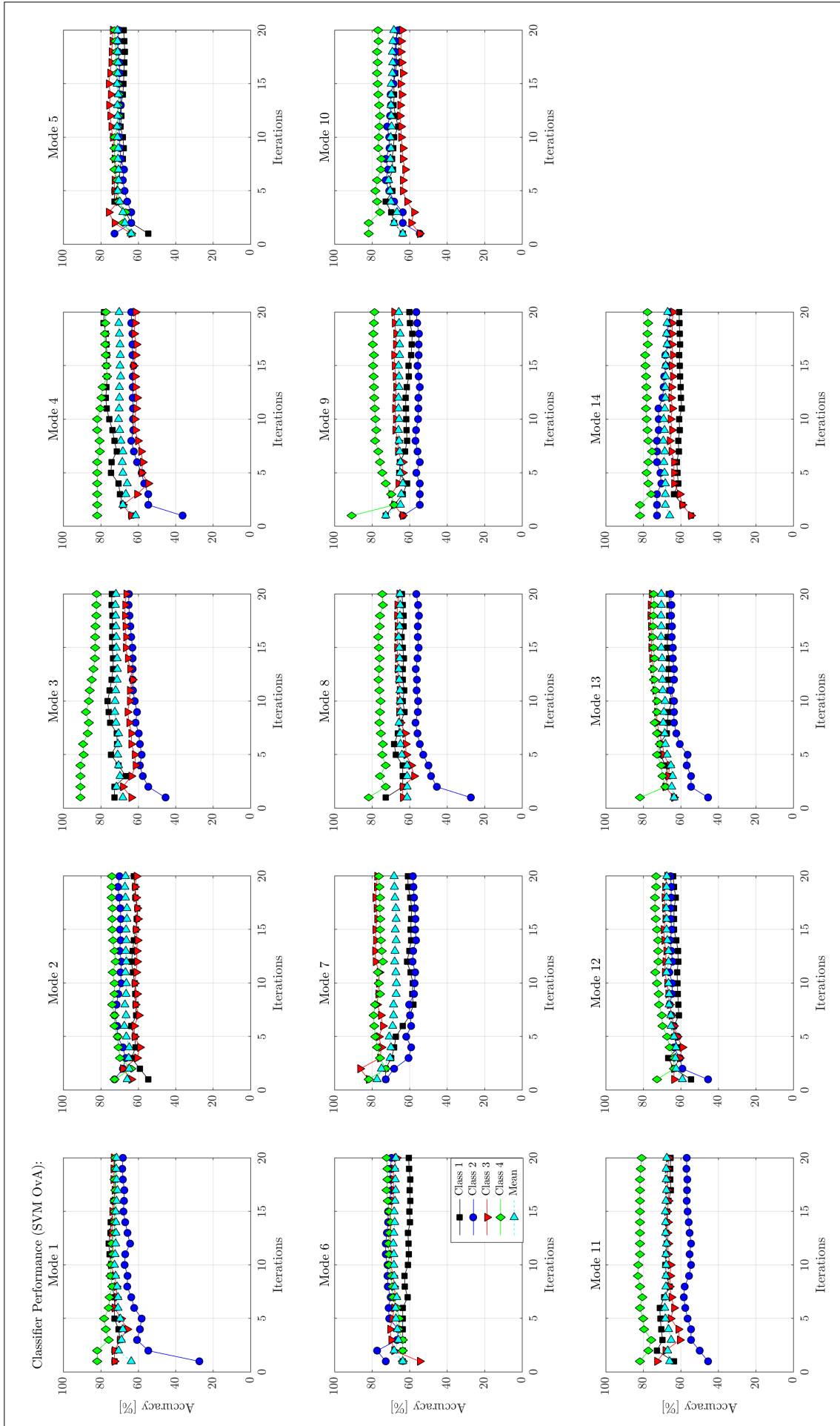


Figure 4.12: Results for Hypothesis Test I - Overall classifier performance from healthy cases, Mode 6 vs. all modes

4.3.2 Hypothesis Tests II and III - Damage Detection and Identification

The second and third hypotheses are evaluated simultaneously using Classifier 2, and the healthy and damaged dataset. The second hypothesis stated that damage could be effectively detected in healthy- and damaged data, i.e. separate all data groups different from the normal healthy data group (essentially a two-class SVM). The third hypothesis stated that damage could be effectively identified in healthy- and damaged data, i.e. separate all distinct data groups from each other. These hypotheses can be assessed in conjunction because the second hypothesis will automatically be accepted if the third hypothesis is accepted. This is because success in damage identification implies success in damage detection, which is a prerequisite to damage identification. However, this is not the case vice versa because if damage can be detected, it does not necessarily mean that the damage can be identified. Thus, the outcome of testing the third hypothesis will deliver the verdict on the acceptance of both hypotheses.

The healthy observations, which are now the overall geometrical variability data, comprise one class of 36 observations, and are labelled as Healthy Cases. The damaged observations comprise three equal-sized classes of 12 observations each and are labelled as Damage Classes 1-3. Classifier 2 is trained using $(\text{Dataset } 2)_{train}$, i.e. 24 healthy observations with 8 damaged observations damage per class, and tested using $(\text{Dataset } 2)_{test}$, i.e. 12 healthy observations with 4 damaged observations per damage class. The classifier is substantially less restricted compared to Classifier 1. This is due to Dataset 2 being double the size than the dataset on which Classifier 1 was trained, and that the separability of its classes is much more significant (see Section 4.1.2). This imposes a noteworthy performance that will result in a highly encouraging mapping of the predictor data and classification accuracy. In addition, due to the relative high degree of separability of the data, the quality of the classification will not be affected by the kernel options and regularization parameters (Barthorpe et al., 2017). The classification is mapped in a two-dimensional space in Figure 4.13, and its accuracy for all iterations is shown in Figure 4.14.

From Figure 4.13, it is apparent that the classification of damage was very successful. The well-separated clusters and decision boundaries, with adequate predictive power, indicate the successful attempt in damage detection as well as damage identification. Even though $(\text{Dataset } 2)_{train}$ is only slightly larger than the training set used for Classifier 1, four distinct islands (kernel decision boundaries) are observed. This is due to the excellent separability of different classes as strong support vectors for each class are available, which can successfully describe the behaviour of the respective class. A conclusive answer is found even though some degree of over-fitting is present. It is observed that the perimeters, which were constructed to address the over-fitting issue, effectively capture the population of each class, and thus the uncertain regions can be disregarded, and emphasis can be placed on these concentrated regions. Considering the scale of the mapping, it is clear that the narrow scatter of each class and the distances between the classes, contribute to the classifier performance.

In Figure 4.14, it is observed that the overall discriminatory performance of the classifier, in most cases, for all classes was 100% with an all-class average of almost 100%. A slight discrepancy is present in Mode 11, with values between 95% and 100%. This agrees with the slight overlapping of all classes seen in Figure 4.6. The explicit class accuracy can be derived from the classification mapping in Figure 4.13, in which definitive identification is observed. Hence, the classifier performed exceptionally well in differentiating between explicit classes, with zero misclassification for all feature vectors. This can be ascribed to the damage-sensitive nature of the natural frequencies, noted in Chapter 3.

The performance of the constructed SVM, used to evaluate the third hypothesis, demonstrates that it can most certainly identify different damage classes. Thus, the third hypothesis is accepted. The classifier performance also implicitly shows that damaged data can be distinguished from healthy data. Thus, it was correct to assume that if the third hypothesis is accepted, the second hypothesis must also be accepted. This implies that if damage can be identified, it must first be detected. This validates the feasibility of damage detection and identification using natural frequency as the discriminant feature in SVMs.

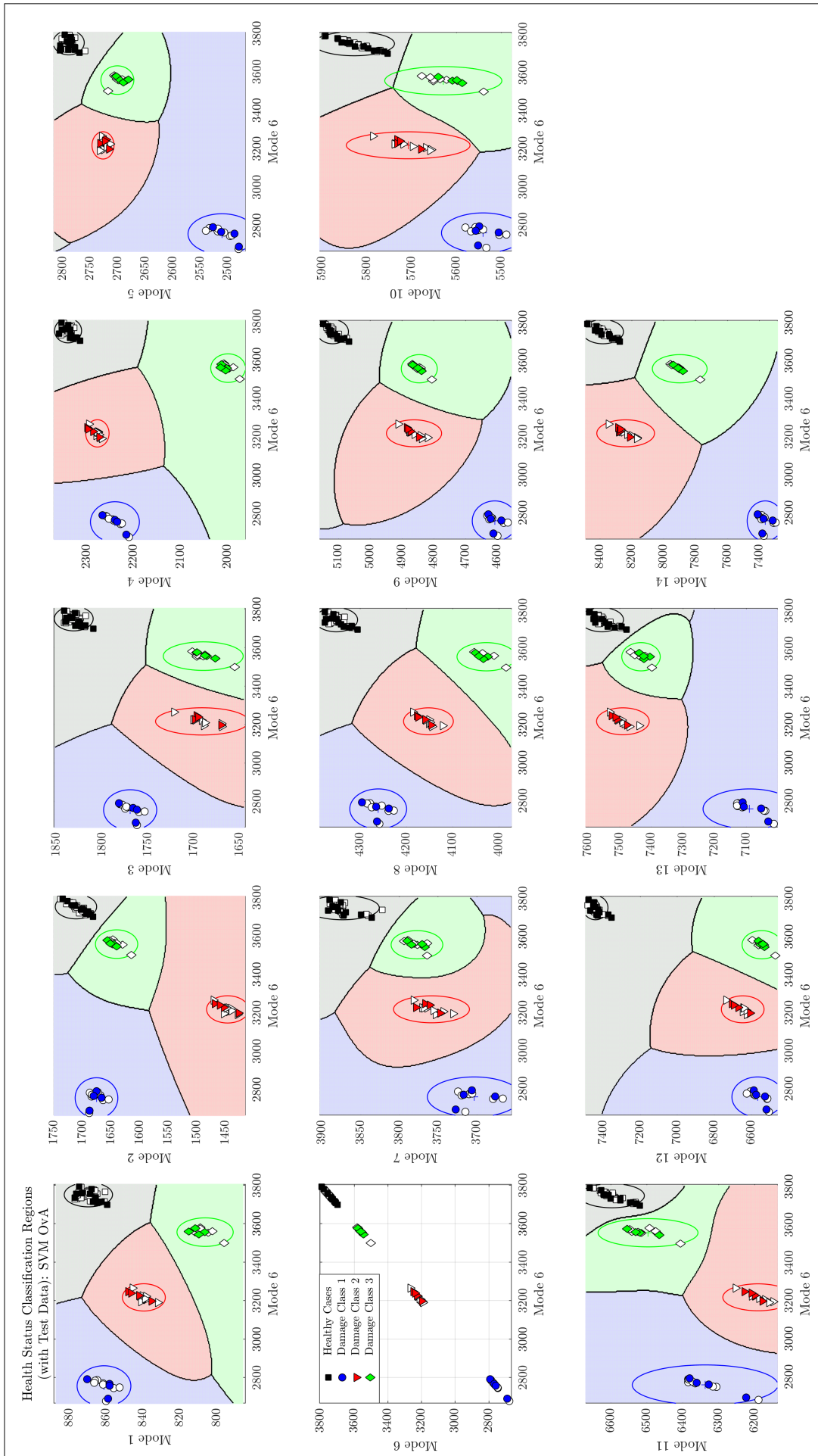


Figure 4.13: Results for Hypothesis Test II & III - Damage detection and identification through classification of different damage classes, Mode 6 vs. all modes

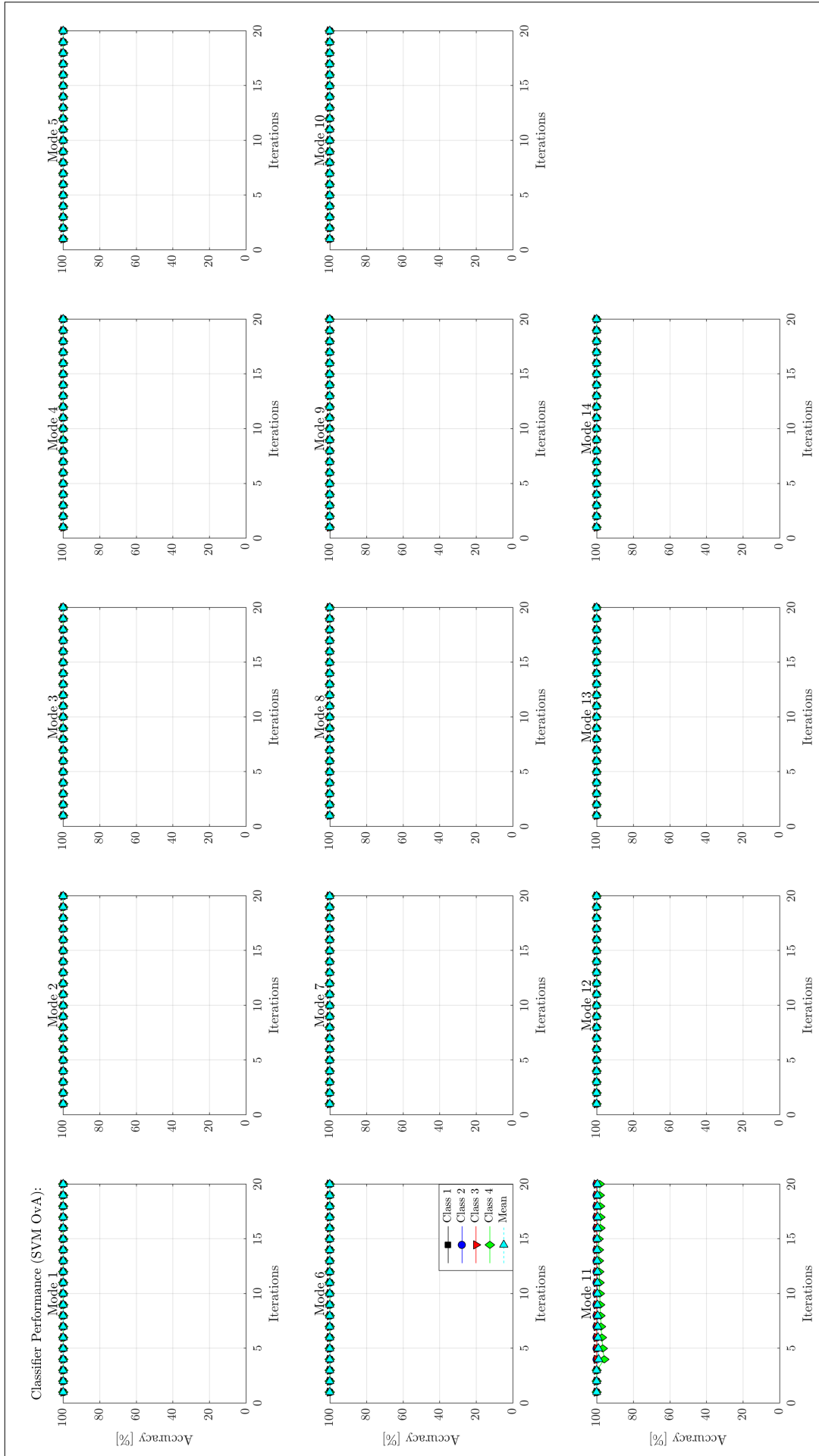


Figure 4.14: Results for Hypothesis Test II & III - Overall classifier performance from damage detection and identification of different damage classes, Mode 6 vs. all modes

4.3.3 Damage Classification using FEM as Training Data (Low-cost Model)

The structure and objective of this classifier is identical to that of Classifier 2. The training data in this case consist of only FEM data (i.e. 260 observations), while the test data is all experimental data or Dataset 2 (i.e. 72 observations). This is an important test of the potential to use lower-cost training data. Both datasets contain a healthy class and three damage classes, which are labelled accordingly. The FEM data comprises four equal-sized classes of 65 observations with one class healthy and three classes damaged, whereas the experimental data comprises one class of 36 healthy observations and three equal-sized classes of 12 damaged observations.

Considering the scale of the mapping and the separability of classes, an encouraging classifier performance is expected that will result in successful mapping of the predictor data. This, however, depends on the distance between the experimental and FEM clusters (FEM validation error) for if the unseen test data and FEM support vectors are too far apart, the decision boundaries will be insufficient. This is because the FEM support vectors are inadequate in describing the behaviour of the experimental classes. Thus, the more accurate the representation of the experimental results by the FEM, the more likely the success of damage detection and identification using FEM as training data, especially at the damage classes. The classification is mapped in a two-dimensional space in Figure 4.15. It is expected that where the FEM validation error is the smallest per mode, the classification will be very successful, indicated by the well-separated clusters and decision boundaries with adequate predictive power. Note that a FEM model validation was only conducted on the healthy blade, and that the resultant validation errors were assumed to be transferred to the FEM damaged blades without any change.

The discriminatory performance of the classifier, in most cases, for all classes was very high (e.g. Modes 8 and 12). However, in some cases the discrimination was very poor with respect to an absolute failure (e.g. Modes 5 and 7). The misclassification of feature vectors is due to FEM results that are unable to describe the experimental data. This restricts the classifier. It is also observed that the constructed perimeters are dependent on the distribution of each FEM class. This is evident in Figure 4.15 when considering Damage Class 1 for Modes 4-5 and Modes 8-13, where Modes 11 and 13 deliver the best result. With all the other modes and FEM classes, the insufficient representation of the real data limits the distributions. Thus, as mentioned previously, this is a risky suggestion since not all modes deliver the desired results. However, when considering the overall modes and not only explicit modes, the classification is effective, and thus FEM data can be used for training. Problems may arise if the classification mapping is further populated with other damage scenarios as overlapping of classes may occur and classification regions become smaller.

It is recommended that FE model updating, using experimental values as parameters, be incorporated to better the current outcome so that a closer representation of the real-world can be achieved. However, since only the healthy results will be easily available, it is proposed to first update the healthy blade and then transfer the properties to the damage models before updating all models. A level of uncertainty will remain since only the healthy blade will be a close representation of the real-world. If the accuracy is adequate, experiments on only the healthy case will be required. Obtaining training data that contains information higher than Level 1 (qualitative damage detection) of the structural damage identification hierarchy is perhaps the biggest obstacle in applying pattern recognition for damage identification (Worden and Manson, 2007). This can overcome a drawback of supervised machine learning and can possibly save on time and costs on acquiring the experimental data.

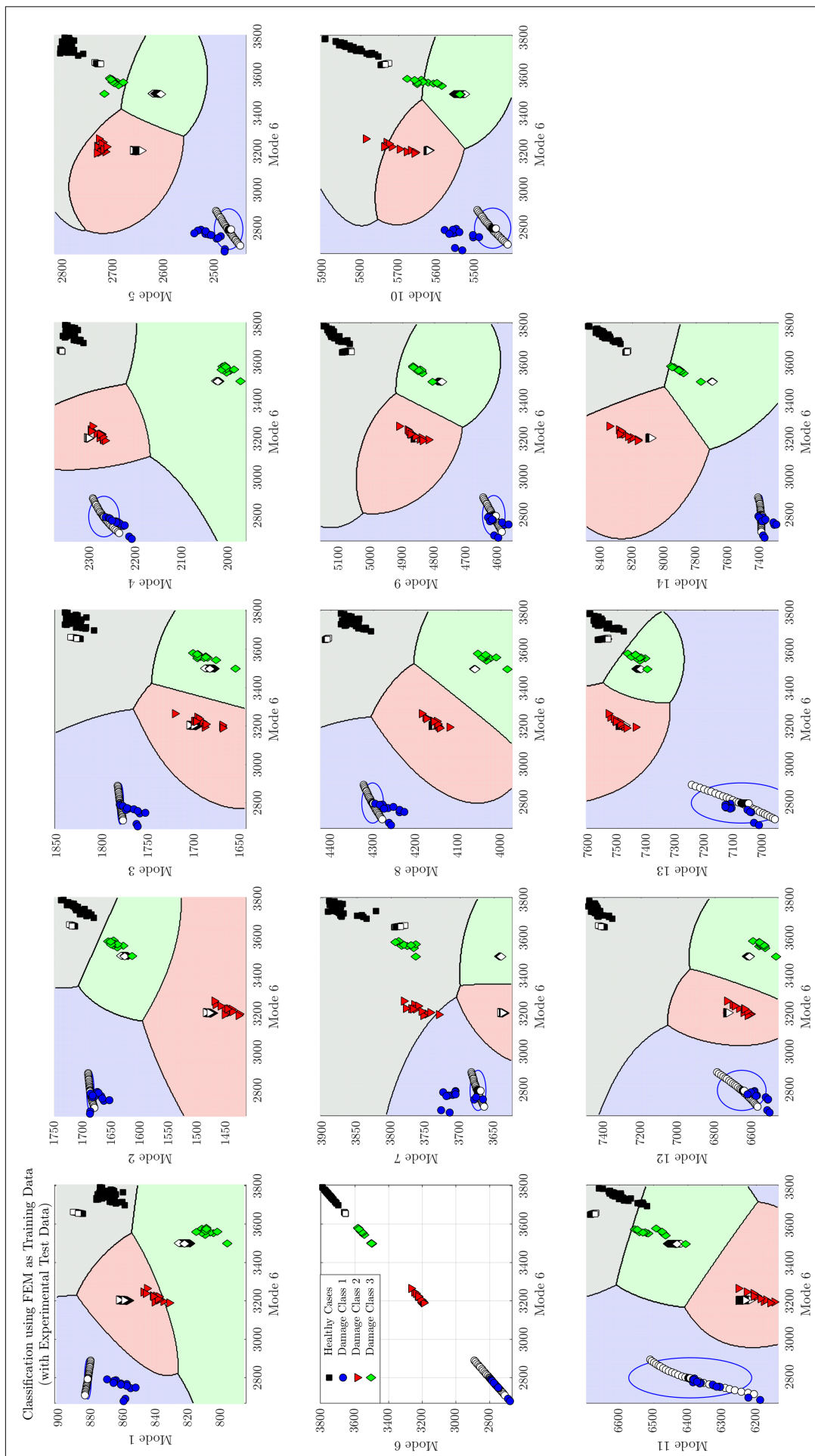


Figure 4.15: Damage detection and identification through classification of different damage classes using FEM for training data, and experimental data for unseen test data (Mode 6 vs. all modes)

4.4 Conclusion

A multi-class SVM was proposed to assess the feasibility of damage classification using natural frequency as the discriminant feature. To confirm the validity of this proposal, it was first necessary to confirm the low sensitivity of the feature to geometrical variability to justify the consistency of the healthy blades. This was followed by confirming the high sensitivity of the feature to specific single-location damage to establish the signature behaviours. However, the location of the damage plays an important role since the extent of the change in stiffness (crack breathing) is dependent on the vibrational pattern (illustrated by the mode shapes). This was done by characterizing the datasets by exploring the distributions of the healthy classes as well as the damage classes. Additionally, the clustering of the feature vectors in two-dimensional space for the healthy cases and damage classes was also done to further explore the separation between classes so that a clearer verdict on the suitability of natural frequency as discrimination feature could be delivered. Confidence in the suitability of natural frequency as discrimination feature was found from the class separability and the small variation in each case. It was observed that the experimental frequencies fall within a range about a mean value in an ambiguous cluster for a specific class, and that distinctive cluster(s) form when the healthy- and damaged data were compared. However, a more powerful differentiation in a higher dimension was required to reinforce the outcome of the evaluation and quality of the selected feature. This was necessary to verify the resultant damage-specific behaviour and separability of dataset distributions.

The investigation was coupled to testing of hypotheses that were evaluated through classification given an appropriate discriminatory feature set to enable a clear approach in obtaining an answer. The first hypothesis stated that geometrical variability could be effectively identified in normal healthy data, i.e. separate all distinct healthy data groups from each other. This was rejected as the healthy blades were found to be similar due to the low sensitivity to geometrical variability of natural frequencies. The first classification failed with only 50–80% of the healthy classes being correctly classified. From the mapping, it was also clear that the answer was ambiguous. The second hypothesis stated that damage could be effectively detected in healthy- and damaged data, i.e. separate all data groups different from the normal healthy data group (essentially a two-class SVM). The third hypothesis stated that damage could be effectively identified in healthy- and damaged data, i.e. separate all distinct data groups from each other. The third hypothesis was accepted as the damaged blades were found to be distinct from the healthy blades, implying that the second hypothesis must also be accepted since detection of damage is a prerequisite to damage identification. The second classification was very successful as 100% of all three damage classes, including the healthy cases, were correctly classified. This was confirmed through the unambiguous mapping. The results are very similar for all feature vectors even though Mode 6 was used to illustrate the outcomes (see Appendix D).

The SVM approach has the capacity to attain explicit classification results by directly recognizing underlying patterns within a small training set. This is because the support vectors hold the essential information, which describes the behaviour of a respective class, required by the classifier. Thus, it is computationally efficient as the rest of the dataset can be discarded. From this, the outcome of the hypothesis tests was only positive in the cases where the discriminant feature was strong enough, i.e. sensitive to damage. Thus, the low-sensitivity of natural frequency to geometrical variability resulted in a rejected hypothesis; whereas exceptionally high classification correction rates were obtained for the high-sensitivity of natural frequency to different types of single-location damage, resulting in the acceptance of the other two hypotheses. It was also observed that the geometrical variability in the blades enhanced the generalization capability of the second classifier to emphasise its discriminative ability to classify distinct damage scenarios according to their damage-specific behaviour. This is because the damage population comes out of the healthy population.

The problems regarding the limited sizes of the datasets, the limited number of classes, and over-fitting were addressed by adding perimeters around the mean of each of the training sets to include 99.73%, i.e. $\mu \pm 3\sigma$, of the data points. A concentrated region or cluster was created per class to regard above the limited data points for an unambiguous answer and to better interpret the classification results. Additionally, a

low-cost model that uses only FEM data as training data and test data as unseen observations was explored in an effort to prove that numerical modelling and model updating can contribute to the proposed approach by overcoming the drawback of limited datasets and expensive testing. This concludes the success of the feasibility study on vibration-based damage detection for removed freely supported individual turbine blades and establishes proof of concept.

Chapter 5: Conclusion and Recommendations

5.1 Conclusion

In this dissertation, the feasibility of a vibration-based structural damage identification method for unmounted individual pinned turbine blades was assessed, utilising natural frequencies f_n as a damage indicator and incorporating into multi-class support vector machine classification as discriminant feature. This was done to investigate the potential of using such an approach in support of conventional NDT for off-site inspection of installed turbine blades. It is necessary to be able to perform damage detection on installed blades as removal and reinstallation of blades is too expensive. However, this real practical problem is too complex at this stage, holding too many unanswered questions, and thus a simplified problem is presented to establish basic principles. In the simplified problem, only uninstalled individual turbine blades are considered to solve a part of the real-world problem. Experimental data and numerical modelling were adopted as confirmatory and predictive means to enable statistical modelling for damage classification using damage-sensitive features. This serves as a prologue to the development of the methodology for application to the real-world problem.

The necessity of increasing the capability of decision-making of current NDT regarding structural integrity of blades, specifically the roots, was outlined in the literature review. The fundamentals behind global vibration-based methods were explored including their application value from employing damage-sensitive properties, which is ascribed to changes in stiffness from a breathing crack. The means of extracting the modal properties was also discussed of which natural frequencies are easiest and more accurate to acquire from the measured signal. In addition, since variation in the modal properties is brought on by changes in the physical properties, it can be used as a damage indicator by comparing the frequencies before and after damage, concluding that pattern recognition can be employed as a means for damage detection.

In the experiment, a highly reliable freely supported free vibration modal analysis procedure was devised to ensure accurate, repeatable, and comparable results. This was first implemented on individual healthy discarded blades to obtain experimental data and establish a reasonably well-modelled blade. Since only FE model validation was done and not FE model updating, direct association between the experimental and numerical cases is not possible, but the relation of behavioural tendencies of the vibration responses can be established. Finally, the experimental set-up was implemented on the different damage scenarios, near or on the root, introduced in these blades to obtain experimental data for a pattern recognition problem.

A sensitivity study was conducted to establish the input parameter significance on the natural frequencies (f_n). The study concluded that geometrical variability in the root retains low sensitivity and material properties retain a higher sensitivity. It was found that the introduced artificial damage, near or on the root, retain the greatest sensitivity with a distinctive nature. This also established the natural frequencies f_n as discriminant feature in the pattern recognition problem. These damage scenarios were modelled separately to confirm and predict the expected behaviour of the vibration response, including the variance in f_n concluded by geometrical variability. The three worst-case single-location damage scenarios at the most probable locations were obtained from literature and discussions with industry experts, and were a machined through-thickness $1mm$ uniform notch on the root at 1) the upper pinhole on the leading pressure side (verified by static structural analysis), and just above the root on 2) the trailing- and 3) the leading edge. The feature objectivity or independence was confirmed from the damage trend on the natural frequencies caused by the input parameters, in which only the test blades were considered to examine the consistency in the shift in natural frequency (Δf_n) for each damage scenario. Due to time constraints, the limited number of blades, the complex geometry of the root, and the damage initiation location on the root, discrete crack propagation could only be explored using FEM. It was found that the variance in f_n grows exponentially or logarithmically as the crack propagates, depending on the mode and damage scenario considered.

To ensure that the selected discriminant feature, i.e. natural frequencies f_n , is of quality, its exclusivity due to the input parameters must be determined. The results were visualised for easier and convenient interpretation for more efficient decision-making. This involved characterizing the diverse datasets by first exploring the distribution of the features in a one-dimensional space for the healthy case as well as the damage classes. By visualising the natural frequencies in a two-dimensional space, in which it is observed that ambiguous or distinct clusters form, a conclusion on their separability was possible. For the healthy classes, an ambiguous cluster with values ranging about a mean was found, implying that their results are very similar. For the damage classes, distinct clusters were found, each behaving like the healthy case. This implies that a similar statistical distribution is present within each class, and the distance between clusters determines the degree of their dissimilarity.

To detect and identify single-location damage, a non-linear multi-class SVM, in which an array of One-versus-All (OvA) binary SVMs were coupled, was proposed. Three hypotheses were introduced to test the feasibility of the proposed method, and thus answer the research questions in Section 1.3, namely: Is it possible to identify geometrical variability in healthy blades; is it possible to detect damage in blades, and if so; can damage be identified. The first hypothesis was rejected as inconclusive results with ambiguous classification regions were found. This means that the proposed method cannot distinguish between geometrical variability in healthy blades, implying that healthy blades are statistically similar due to low sensitivity of natural frequencies to geometrical variability. The second and third hypotheses were jointly accepted, as the test for damage identification was very successful, and thus damage detection must also be possible. The definite mapping and classification of damage classes implies that natural frequencies are highly sensitive to damage. However, it was observed that the location of the damage plays an important role in the change in natural frequencies since the extent of the change in stiffness (crack breathing) is dependent on the vibrational pattern. With SVM classification, decision boundaries are produced based on the optimal separating distance between the cluster bounds, which hold the description of each cluster and depend on the quality of the feature training set. Thus, the less overlap between clusters, the better the chance on effective classification. This is because the SVM approach has the capacity to attain explicit classification results by directly recognizing underlying patterns within a small training set. As the OvA multi-class extension on the binary SVM classifier is applied, over-fitting of the decision boundaries for each class occurs, resulting in uncertain classification regions where no observations are found. A limited number of classes also add to this issue. In this study, this was addressed by adding elliptical perimeters around the mean of each training set to include 99.73%, i.e. $\mu \pm 3\sigma$, of the data points, resulting in a concentrated region or cluster per class to consider instead. This allows an unambiguous answer to be obtained and better interpretation of the classification results.

Additionally, the potential to use lower-cost training data obtained from FEM and experimental test data as unseen observations was assessed. It was found that numerical modelling could contribute to the proposed approach by overcoming the drawback of limited datasets and expensive testing. This outcome can be enhanced by applying model updating to this low-cost model.

To summarize on introducing the use of vibration-based structural damage identification to solving a part of the real-world problem:

- Is it possible to identify defects, i.e. geometrical variability, in an unconstrained and isolated blade using vibration response?

No, this is not possible as natural frequencies are not sensitive enough to geometrical variability, and even a pattern recognition algorithm struggles to detect the difference in the varying healthy data. This is because healthy blades are statistically too similar to differentiate.

- Is it possible to detect damage in an unconstrained and isolated blade using vibration response?

Yes, this is possible as natural frequencies are sensitive enough to damage, and a pattern recognition algorithm can detect the difference between healthy and damaged data. This is because changes in a structure's

natural frequencies are functions of changes in the structure's physical properties (mass, damping, and stiffness) induced by damage (i.e. stiffness reductions due to cracks or weakening of a connection).

- If so, can different damage scenarios be identified?

Yes, this is possible as natural frequencies are highly sensitive to different damage scenarios, and a pattern recognition algorithm can successfully distinguish between the different damaged classes, including the healthy class. This is because the location of the damage plays an important role in the change in natural frequencies since the extent of the change in stiffness is dependent on the vibrational pattern.

This concludes on the success of the feasibility of vibration-based damage detection for removed freely supported individual turbine blades and establishes proof of concept. From the outcome of this study, the potential of future development of the proposed method into a real-world application to use in support of conventional NDT for in-situ inspection of installed stationary blades is established.

5.2 Recommendations

By developing the proposed methodology toward solving more succeeding partials of the real-world problem so that it can be used in support of conventional NDT, potential increase in the capability and reliability of crack detection in stationary installed turbine blades are likely, especially in the root. The build-up of the success in solutions will provide confidence in continuing the development of the methodology for real-world application to enable possible prevention of in-service failures with consequential damage and extended outage durations. This type of analysis may also allow development of the maintenance schedule and inspection intervals with the purpose of establishing remedial action to increase turbine availability. The following recommendations are made for future work succeeding the current study. Investigate:

1. Freely supported modal analysis on a single installed blade. This will also be a simpler problem than the real-world case, but more complex than the current work. This will allow study of the effect of the influence of the installation boundary conditions on the system dynamics (i.e. contact between the blade, pins, and disk section) as well as on the damage (crack), especially in the pinhole.
2. Freely supported modal analysis on multiple installed blades.
3. Modal analysis of cantilever set-ups of the installed blade configurations, from 1 and 2, to simulate in-situ inspection. This will approach the real-world boundary conditions much closer.

The current study still has room for improvement as well as unanswered questions and this must be considered before or when moving to the next partial problem. Hence, the following recommendations are made for future work on the current study. Investigate:

- multi-location damage scenarios to establish new coordinates on the classification map to expand the current findings and examine the possibility of using single-location damage to detect multi-location damage (Barthorpe et al., 2017) on pinned turbine blades.
- the trend on the classification map of advancing single-location damage to expand and populate the current classification map.
- other more likely single-location damage scenarios to expand and populate the current classification map.
- natural cracks to approach real-world conditions.
- support vector domain description (SVDD) as alternative to current method to ensure that only the populated areas of the classification map are described to enhance the class-exclusivity.
- the robustness of this method by employing other discriminant features selected from other characteristics, which can be extracted from the highly reliable FRF measurements.
- unsupervised machine learning techniques, in which all the possible damage scenarios are not required, that can be developed for industrial application.

- the option of using an extensive numerical model, with parametric studies on geometrical variability and material properties, to generate data to supplement or substitute experimental features as training data to predict expected behaviour or mapping. This will make the proposed method more attractive since all damage scenarios can be modelled instead of acquired from expensive experiments, which requires different real damaged cases. FE model updating will also add to the accuracy of the FEM.
- the use of changes in internal data variability measured by a test statistic χ_0^2 , which values has been found to provide better sensitivity to structural damage than the shift in natural frequency method (Ngwangwa et al., 2006).

References

- Agarwalla, D. K. and Parhi, D. R. Effect of crack on modal parameters of a cantilever beam subjected to vibration. *Procedia Engineering*, 51(NUiCONE 2012), 665–669, 2013.
- Anderson, T. *Fracture Mechanics: Fundamentals and Applications*. Taylor & Francis Group, LLC, 3rd edition, 2005.
- Avitabile, P. Modal space - In our own little world. *Experimental Techniques*, 39(1), 3–10, 2014.
- Barad, K. H., Sharma, D. S., and Vyas, V. Crack detection in cantilever beam by frequency based method. *Procedia Engineering*, 51(NUiCONE 2012), 770–775, 2013.
- Barthorpe, R. J. *On Model- and Data-based Approaches to Structural Health Monitoring*. PhD: Mechanical Engineering (thesis), University of Sheffield, 2011.
- Barthorpe, R. J., Manson, G., and Worden, K. On multi-site damage identification using single-site training data. *Journal of Sound and Vibration*, 409, 43–64, 2017.
- Bhagi, K., Ratogi, V., and Gupta, P. A Brief Review on Failure of Turbine Blades. In: *Proceedings STME-2013 Smart Technologies for Mechanical Engineering*, pp. 1–8, Delhi, India, 2013.
- Bhat, M. M., Ramamurti, V., and Sujatha, C. Studies on the Determination of Natural Frequencies of Industrial Turbine Blades. *Journal of Sound and Vibration*, 196(5), 681–703, 1996.
- Booyesen, C., Heyns, P. S., Hindley, M. P., and Scheepers, R. Fatigue life assessment of a low pressure steam turbine blade during transient resonant conditions using a probabilistic approach. *International Journal of Fatigue*, 73, 17–26, 2015.
- Bray, D. E. and Stanley, R. K. *Nondestructive evaluation: A tool in design, manufacturing, and service*. CRC Press, Inc., Revised edition, 1997.
- Brereton, R. G. and Lloyd, G. R. Support Vector Machines for classification and regression. *The Analyst*, 135(2), 230–267, 2010.
- Budynas, R. and Nisbett, K. *Shigley's Mechanical Engineering Design*. McGraw-Hill, 9th edition, 2011.
- Castellini, P., Revel, G. M., and Scalise, L. Measurement of vibrational modal parameters using laser pulse excitation techniques. *Measurement: Journal of the International Measurement Confederation*, 35(2), 163–179, 2004.
- Charlesworth, C. *Ultrasonic phased array testing in the power generation industry: Novel wedge development for the inspection of steam turbine blades roots*. DEng thesis, University of Warwick, 2011.
- Chen, D.-M., Xu, Y. F., and Zhu, W. D. Damage Identification of Beams Using a Continuously Scanning Laser Doppler Vibrometer System. *Journal of Vibration and Acoustics*, 138(5), 1–16 (051011), 2016.
- Chen, J. G., Wadhwa, N., Cha, Y. J., Durand, F., Freeman, W. T., and Buyukozturk, O. Modal identification of simple structures with high-speed video using motion magnification. *Journal of Sound and Vibration*, 345, 58–71, 2015.
- Citarella, R., Lepore, M., Shlyannikov, M., and Yarulin, R. Fatigue Crack Growth by FEM-DBEM Approach in a Steam Turbine Blade. *Industrial Engineering and Management*, 4(2), 2–6, 2015.
- Clossen, M., Opheys, M., Rauschenbach, H., and Siegel, M. Lifetime extension through advanced non-destructive examination methods. In: *POWER-GEN Europe*, pp. 1–10, Cologne, Germany, 2006. Siemens AG.

- Dewey, R. P. and Lam, T. C. Steam Turbine Blade Failure Root Cause Analysis Guide. Technical report, Electric Power Research Institute, 2008.
- Dimarogonas, A. D. Vibration of cracked structures: A state of the art review. *Engineering Fracture Mechanics*, 55(5), 831–857, 1996.
- Dowling, N. E. *Mechanical Behavior of Materials: Engineering Methods for Deformation, Fracture, and Fatigue*. Pearson Education Limited, 4th edition, 2012.
- Drozdzowski, R., Völker, L., Häfele, M., and Vogt, D. M. Experimental and Numerical Investigation of the Nonlinear Vibrational Behavior of Steam Turbine Last Stage Blades With Friction Bolt Damping Elements. In: *Proceedings of ASME Turbo Expo 2015: Turbine Technical Conference and Exposition*, pp. 1–11, Montreal, Canada, 2015.
- Duong, L., Murphy, K. D., and Kazerounian, K. Guided Tuning of Turbine Blades: A Practical Method to Avoid Operating at Resonance. *Journal of Vibration and Acoustics*, 135(5), 054502–1 – 054502–5, 2013.
- Fan, W. and Qiao, P. Vibration-based Damage Identification Methods: A Review and Comparative Study. *Structural Health Monitoring: An International Journal*, 10(1), 83–111, 2011.
- Farrar, C. R. and Doebling, S. W. An overview of modal-based damage identification methods. In: *EUROMECH 365 International Workshop: DAMAS 97, Structural Damage Assessment Using Advanced Signal Processing Procedures*, Volume 111, pp. 270–78. 1997.
- Fernández-Sáez, J., Morassi, A., Pressacco, M., and Rubio, L. Unique determination of a single crack in a uniform simply supported beam in bending vibration. *Journal of Sound and Vibration*, 371, 94–109, 2016.
- Garcia-Palencia, A., Santini-Bell, E., Gul, M., and Catbas, N. A FRF-based algorithm for damage detection using experimentally collected data. *Structural Monitoring and Maintenance*, 2(4), 399–418, 2015.
- Giannoccaro, N. I., Messina, A., Nobile, R., and Panella, F. W. Fatigue damage evaluation of notched specimens through resonance and anti-resonance data. *Engineering Failure Analysis*, 13(3 SPEC. ISS.), 340–352, 2006.
- Gillich, G. R. and Praisach, Z. I. Modal identification and damage detection in beam-like structures using the power spectrum and time-frequency analysis. *Signal Processing*, 12, 2311–2329, 2015.
- Gryllias, K. C. and Antoniadis, I. A. A Support Vector Machine approach based on physical model training for rolling element bearing fault detection in industrial environments. *Engineering Applications of Artificial Intelligence*, 25(2), 326–344, 2012.
- Hasni, H., Alavi, A. H., Jiao, P., and Lajnef, N. Detection of fatigue cracking in steel bridge girders: A support vector machine approach. *Archives of Civil and Mechanical Engineering*, 17(3), 609–622, 2017.
- Hattingh, D. G., James, M. N., Newby, M., Scheepers, R., and Doubell, P. Damage assessment and refurbishment of steam turbine blade/rotor attachment holes. *Theoretical and Applied Fracture Mechanics*, 83, 125–134, 2016.
- Heyns, P. S. *Mechanical Vibration: Measurement and Analysis*. University of Pretoria, 2008.
- Inman, D. J. *Engineering Vibrations*. Pearson Education, Inc., Upper Saddle River, New Jersey, 4th edition, 2014.
- Jassim, Z. A., Ali, N. N., Mustapha, F., and Abdul Jalil, N. A. A review on the vibration analysis for a damage occurrence of a cantilever beam. *Engineering Failure Analysis*, 31, 442–461, 2013.
- Kannappan, L., Shankar, K., and Anavatti, S. G. Damage detection using frequency measurements. *48th AIAA/ASME/ASCE/AHS/ASC Structures, Structural Dynamics, and Materials Conference*, 2007.

- Kim, H. Crack evaluation of the fourth stage blade in a low-pressure steam turbine. *Engineering Failure Analysis*, 18(3), 907–913, 2011.
- Kong, X., Cai, C.-S., and Hu, J. The State-of-the-Art on Framework of Vibration-Based Structural Damage Identification for Decision Making. *Applied Sciences*, 7(5), 497, 2017.
- Kubiak Sz, J., Gonzalez, G. R., Juarez, D. R., Nebradt, J. G., and Sierra, F. E. An investigation on the failure of an L-O steam turbine blade. *Journal of Failure Analysis and Prevention*, 4(3), 47–51, 2004.
- Kubiak Sz, J., Segura, J. A., Gonzalez R, G., García, J. C., Sierra E, F., Nebradt G, J., and Rodriguez, J. A. Failure analysis of the 350 MW steam turbine blade root. *Engineering Failure Analysis*, 16(4), 1270–1281, 2009.
- Lackner, M. Vibration and Crack Detection in Gas Turbine Engine Compressor Blades using Eddy Current Sensors. MSc: Aeronautics and Astronautics (thesis), Massachusetts Institute of Technology, 2005.
- Lai, C., Sun, X., Dasch, C., Harmon, G., and Jones, M. Quantify Resonance Inspection With Finite Element-Based Modal Analyses. *Journal of Vibration and Acoustics*, 133(3), 031004, 2011.
- Lee, Y. S. and Chung, M. J. Study on crack detection using eigenfrequency test data. *Computers and Structures*, 77(3), 327–342, 2000.
- Long, J. and Buyukozturk, O. Automated Structural Damage Detection Using One-Class Machine Learning. In: Catbas, F. N. (editor), *Dynamics of Civil Structures. Conference Proceedings of the Society for Experimental Mechanics Series*, Volume 4, Chapter 14, pp. 117–128. Springer International Publishing, 2014.
- Lorenzino, P. and Navarro, A. The variation of resonance frequency in fatigue tests as a tool for in-situ identification of crack initiation and propagation, and for the determination of cracked areas. *International Journal of Fatigue*, 70, 374–382, 2015.
- Martinez-Luengo, M., Kolios, A., and Wang, L. Structural health monitoring of offshore wind turbines: A review through the Statistical Pattern Recognition Paradigm. *Renewable and Sustainable Energy Reviews*, 64, 91–105, 2016.
- Mazur, Z., García-Illescas, R., and Porcayo-Calderón, J. Last stage blades failure analysis of a 28 MW geothermal turbine. *Engineering Failure Analysis*, 16(4), 1020–1032, 2009.
- McGuire, S. M., Fine, M. E., and Achenbach, J. D. Crack detection by resonant frequency measurements. *Metallurgical and Materials Transactions A*, 26(5), 1123–1127, 1995.
- Mix, P. E. *Introduction to Nondestructive Testing*. John Wiley & Sons, Inc., Hoboken, NJ, USA, 2005.
- Nguyen, K. V. Mode shapes analysis of a cracked beam and its application for crack detection. *Journal of Sound and Vibration*, 333(3), 848–872, 2014.
- Ngwangwa, H. M. Assessment of structural damage using operational time responses. MSc: Mechanics (thesis), University of Pretoria, 2004.
- Ngwangwa, H. M., Heyns, P. S., and Van Tonder, F. Assessment of structural damage using operational time responses and finite element simulation. *Journal of Sound and Vibration*, 296(1-2), 23–45, 2006.
- Nurbanasari, M. and Abdurrachim. Crack of a first stage blade in a steam turbine. *Case Studies in Engineering Failure Analysis*, 2(2), 54–60, 2014.
- Oberholster, A. J. *The application of Eulerian Laser Doppler vibrometry to on-line damage detection of axial-flow turbomachinery blades*. PhD: Mechanical Engineering (thesis), University of Pretoria, 2010.
- Ooijevaar, T. H. *Vibration based structural health monitoring of composite skin-stiffener structures*. PhD thesis, University of Twente, Enschede, The Netherlands, 2014.

- Pandey, A. K. and Biswas, M. Damage detection in structures using changes in flexibility. *Journal of Sound and Vibration*, 169(1), 3–17, 1994.
- Pawar, P. M. and Jung, S. N. Support vector machine based online composite helicopter rotor blade damage detection system. *Journal of Intelligent Material Systems and Structures*, 19(10), 1217–1228, 2008.
- Plesiutchnig, E., Fritzl, P., Enzinger, N., and Sommitsch, C. Fracture analysis of a low pressure steam turbine blade. *Case Studies in Engineering Failure Analysis*, 5-6, 39–50, 2016.
- Poursaeidi, E. and Bakhtiari, H. Fatigue crack growth simulation in a first stage of compressor blade. *Engineering Failure Analysis*, 45, 314–325, 2014.
- Poursaeidi, E. and Salavatian, M. Fatigue crack growth simulation in a generator fan blade. *Engineering Failure Analysis*, 16(3), 888–898, 2009.
- Rama Rao, A. and Dutta, B. K. In situ detection of turbine blade vibration and prevention. *Journal of Failure Analysis and Prevention*, 12(5), 567–574, 2012.
- Rau, E., Bamberg, J., Burchards, J., Berwig, P., and Voelkl, W. High resolution crack detection on turbine blade roots by the use of eddy current and ultrasonic Rayleigh waves. In: *19th World Conference on Non-Destructive Testing*, pp. 1–8, 2016.
- Rauschenbach, H., Clossen, M., Opheys, M., and Siegel, M. Advanced NDE inspection methods for detection of SCC in blade attachments and blade roots. In: *17th World Conference on Nondestructive Testing*, pp. 25–28, Shanghai, China, 2008.
- Rauschenbach, H., Clossen-Von Lanken Schulz, M., Opheys, M., and Siegel, M. Advanced Ultrasonic application for the inspection of turbine components. In: *10th c*, Moscow, Russia, 2010.
- Rizos, P. F., Aspragathos, N., and Dimarogonas, A. D. Identification of crack location and magnitude in a cantilever beam from the vibration modes. *Journal of Sound and Vibration*, 138(3), 381–388, 1990.
- Rowbotham, S., Chung, O., Ko, M., and Wong, J. Failure Mechanisms Encountered in Geothermal Steam Service. In: *World Geothermal Congress 2015*, pp. 1–8, Melbourne, Australia, 2015.
- Salawu, O. S. Detection of structural damage through changes in frequency: A review. *Engineering Structures*, 19(9), 718–723, 1997.
- Samanta, B., Al-Balushi, K. R., and Al-Araimi, S. A. Artificial neural networks and support vector machines with genetic algorithm for bearing fault detection. *Engineering Applications of Artificial Intelligence*, 16(7-8), 657–665, 2003.
- Sangid, M. D. The physics of fatigue crack initiation. *International Journal of Fatigue*, 57, 58–72, 2013.
- Santos, A., Figueiredo, E., Silva, M. F., Sales, C. S., and Costa, J. C. Machine learning algorithms for damage detection: Kernel-based approaches. *Journal of Sound and Vibration*, 363, 584–599, 2016.
- Scheepers, R. and Booyen, C. The Specification of Target Flaws in Turbine Blades. In: *18th World Conference on Nondestructive Testing*, Durban, South Africa, 2012.
- Schmidt, S. A Cost-Effective Diagnostic Methodology Using Probabilistic Approaches for Gearboxes Operating Under Non-Stationary Conditions. MEng thesis, University of Pretoria, 2017.
- Schmidt, S. and Heyns, P. S. An open set recognition methodology utilising discrepancy analysis for gear diagnostics under varying operating conditions. *Mechanical Systems and Signal Processing*, 119, 1–22, 2019.
- Search Steel. AISI 420 - X20Cr13, 2013. URL: <http://searchsteel.blogspot.com/2010/04/aisi-420-hay-x20cr13.html>.

- Shlyannikov, V., Yarullin, R., and Zakharov, A. Fatigue of Steam Turbine Blades With Damage on the Leading Edge. *Procedia Materials Science*, 3, 1792–1797, 2014.
- Shukla, A. and Harsha, S. Vibration Response Analysis of Last Stage LP Turbine Blades for Variable Size of Crack in Root. *Procedia Technology*, 23, 232–239, 2016.
- Shukla, A. and Harsha, S. P. An Experimental and FEM Modal Analysis of Cracked and Normal Steam Turbine Blade. *Materials Today: Proceedings*, 2(4-5), 2056–2063, 2015.
- Siemens. What is a Frequency Response Function (FRF)?, 2016a. URL: <https://community.plm.automation.siemens.com/t5/Testing-Knowledge-Base/What-is-a-Frequency-Response-Function-FRF/ta-p/354778>.
- Siemens. What modal impact hammer tip should I use?, 2016b. URL: <https://community.plm.automation.siemens.com/t5/Testing-Knowledge-Base/What-modal-impact-hammer-tip-should-I-use/ta-p/355026>.
- SIJ Metal Ravne d.o.o. SINOXX 4021 Steel, 2016. URL: <https://steelselector.sij.si/steels/PK3.html>.
- Singh, M. P. and Lucas, G. M. *Turbine Blade Construction, Materials, and Manufacture*. McGraw Hill Professional, Access Engineering, 2011.
- Smith, A. *ECSS Space Engineering Modal Survey Assessment*. Imperial College Press and Distributed by World Scientific Publishing Co., 2005.
- Song, Y. Z., Bowen, C. R., Kim, H. A., Nassehi, A., Padget, J., Gathercole, N., and Dent, A. Non-invasive damage detection in beams using marker extraction and wavelets. *Mechanical Systems and Signal Processing*, 49(1-2), 13–23, 2014.
- Stultz, G. R., Bono, R. W., and Peres, M. A. S. Total Quality with Rapid Through-put of Powdered Metal and Cast Parts for Whole Part Flaw Detection via Resonant Acoustic Method of Inspection. In: *12th International Mobility Technology Congress and Exhibition*, Sao Paulo, Brazil, 2003.
- Tang, J., Alelyani, S., and Liu, H. Feature Selection for Classification: A Review. In: *Data Classification: Algorithms and Applications*, pp. 37–64. CRC Press, 2014.
- Theodoridis, S. and Koutroumbas, K. *Pattern Recognition*. Elsevier Inc., 4th edition, 2009.
- Totten, G. E. Fatigue Crack Propagation. *Advanced Materials and Processes*, 166(5), 39–41, 2008.
- Vaishaly, P. and Ramarao, B. S. V. Finite Element Stress Analysis of a Typical Steam Turbine Blade. *International Journal of Science and Research*, 4(7), 1059–1065, 2013.
- Wang, Z., Lin, R., and Lim, M. Structural damage detection using measured FRF data. *Computer Methods in Applied Mechanics and Engineering*, 147(1-2), 187–197, 1997.
- Witek, L. Experimental crack propagation and failure analysis of the first stage compressor blade subjected to vibration. *Engineering Failure Analysis*, 16(7), 2163–2170, 2009.
- Witek, L. Crack propagation analysis of mechanically damaged compressor blades subjected to high cycle fatigue. *Engineering Failure Analysis*, 18(4), 1223–1232, 2011.
- Worden, K. and Dulieu-Barton, J. M. An Overview of Intelligent Fault Detection in Systems and Structures. *Structural Health Monitoring*, 3(1), 85–98, 2004.
- Worden, K. and Manson, G. The application of machine learning to structural health monitoring. *Philosophical Transactions of the Royal Society A: Mathematical, Physical and Engineering Sciences*, 365(1851), 515–537, 2007.

- Worden, K., Farrar, C. R., Manson, G., and Park, G. The fundamental axioms of structural health monitoring. *Proceedings of the Royal Society A: Mathematical, Physical and Engineering Sciences*, 463(2082), 1639–1664, 2007.
- Xu, W., Lai, C., and Sun, X. Identify structural flaw location and type with an inverse algorithm of resonance inspection. *Journal of Vibration and Control*, 21(13), 2685–2696, 2015.
- Xu, Z. L., Park, J. P., and Ryu, S. J. Failure analysis and retrofit design of low pressure 1st stage blades for a steam turbine. *Engineering Failure Analysis*, 14(4), 694–701, 2007.
- Yan, Y. J., Cheng, L., Wu, Z. Y., and Yam, L. H. Development in vibration-based structural damage detection technique. *Mechanical Systems and Signal Processing*, 21(5), 2198–2211, 2007.
- Yang, B.-S. and Widodo, A. Support Vector Machine for Machine Fault Diagnosis and Prognosis. *Journal of System Design and Dynamics*, 2(1), 12–23, 2008.
- Yin, Z. and Hou, J. Recent advances on SVM based fault diagnosis and process monitoring in complicated industrial processes. *Neurocomputing*, 174, 643–650, 2016.
- Zhou, Y. L., Maia, N. M. M., Sampaio, R. P. C., and Wahab, M. A. Structural damage detection using transmissibility together with hierarchical clustering analysis and similarity measure. *Structural Health Monitoring: An International Journal*, 16(6), 711–731, 2016.

Appendix A: Notes on EMA Design and Set-up

A.1 Modal Analysis Equipment Configuration

PSV400AnalyzerInfo.txt

Name: C:\Documents and Settings\Administrator\My Documents\12020282 L Brits\MEng - Blades\Tests\Analyzer.pvd
User: Administrator
Created: Thursday, January 25, 2018 1:09:21 PM
File version: 8.80
Application version:8.8.0.0

Comment

Measurement Information

Assign focus values succeeded.

Hardware

Sensor head: OFV-505
Junction Box: PSV-E-401-M2-20
Acquisition Board:Spectrum MI3025

General

Acquisition Mode:FFT
Averaging: Complex
Averaging count:7
PCA MIMO: Not active

Frequency

Bandwidth: 10 kHz
Bandwidth from:390.625 mHz
Bandwidth to: 10 kHz

Sampling

FFT Lines: 25600
Sample frequency:25.6 kHz
Sample time: 2.56 s
Resolution: 390.625 mHz

Trigger

Source: Reference 1
Edge: Positive slope
Level: 0 %
Pretrigger: 5 %
Phase from reference:Off

Channel Vibrometer connected to Vibrometer 1

Direction: +Z
Range: 10 V
Coupling: DC
Impedance: 1 MOhm
Quantity: Velocity
Calibration factor:100e-3 m/s/V
Signal Delay: 12.6e-6 s
Filter Type: No Filter
Int/Diff Quantity:Velocity
Window: Exponential
Signal Enhancement:Active

Channel Reference 1 SN 8131, steel-tip

Reference point index:0
Direction: +Z
Range: 500 mV
Coupling: DC
Impedance: 50 Ohm

```

Quantity:      Force
Calibration factor:438.5 N/V
Signal Delay: 0 s
Filter Type:   No Filter
Int/Diff Quantity:Force
Window:        Force
Signal Enhancement:Not active

```

```
-----
Signal Enhancement

```

```

Speckle Tracking:Active
Mode:              Standard

```

```
-----
Vibrometer 1

```

```

Controller:   OFV-5000
Firmware version:2.11
Sensor head:  OFV-505
Firmware version:1.20
Tracking filter:Fast

```

```
Velocity output

```

```

Range:        VD-09 100 mm/s/V LP
Low pass filter:Off
High pass filter:Off

```

```
Displacement output

```

```

Range:        DD-300 Aux 50 nm/V

```

A.2 Design and Set-up

The following guidelines were implemented for setting up the non-contact impact test:

1. Blades suspended by elastic band at root and aerofoil tip:
 - Elastic band inserted through bottom holes in root to ensure constant orientation.
 - Elastic band curvature at tip kept constant by line, tensioned when blade is removed, and free when blade is added.
 - Alignment in XY-plane where level tool is placed on bottom flat surface with its mass distributed so that it has minimal effect on orientation.
 - Initial length (tension) in elastic cord, adjustable to ensure constant blade orientation.
 - Reflective dot/black mark added to specific locations on all blades to ensure constant measuring point/excitation point (allocated after trial-and-error approach to ensure optimal mode participation).
 - Set-up designed to study change in response due to geometrical differences and/or induced damage.
 - Laser point at centre of reflective dot to ensure constant pivot point during alignment.
2. Laser scanning vibrometer, measures vibrational velocity:
 - Head adjusted to meaningful stand-off distance from measuring plane, aligned with XY-plane @ 915mm.
 - Laser centred to ensure beam perpendicular to XY-plane.
 - Scanning grid added for constant scanning region with only measurement point enabled (SISO).
 - Optimal laser signal ensured by reflective dot/autofocus.
 - Reflective dot on slight curvature to capture in-plane/out-of-plane motion to ensure maximal observation of modes.
 - Averages taken per test/small frequency resolution to ensure cleaner signal.
 - With extraction of natural frequencies, a smoothing-filter (Savitsky-Golay) was applied on noisy areas (troughs).

3. Modal hammer, excites blades:

- Excitation point specified on blade (SISO); however, still a variable due to operator-dependence.
- Steel-tip, ensures maximum energy distribution allowing higher mode excitation/cleaner FRFs.
- Time pulse/forcing function (input excitation spectra) used as indicator for successive impacts.

A.3 EMA Protocol/Methodology

After configuring laser scanning head configuration, apply the following steps:

1. Insert band through root bottom hole and secure.
2. Place aerofoil onto cord with laser in centre of measuring point.
3. Align blade root to XY-plane using bottom surface (cross-alignment + level tool).
4. Focus camera and laser beam.
5. Excite blade at designated location.
 - Use same launching approach, with constant
 - body position (standing), convenient for next points.
 - hammer orientation (parallel to XY-plane).
 - impact support, hand/middle fingernail sliding against frame support.
 - equidistant from excitation point, before and during impact
 - Use force diagrams (time-pulse/forcing function) as successive impact indication.
 - Repeat after sample time passed, repeat test (x3), reset test per blade.
6. Export averaged input excitation spectra (time-pulse/forcing function).
7. Export FRF results (magnitude $[dB]$ + phase $[^\circ]$).
8. Process data.

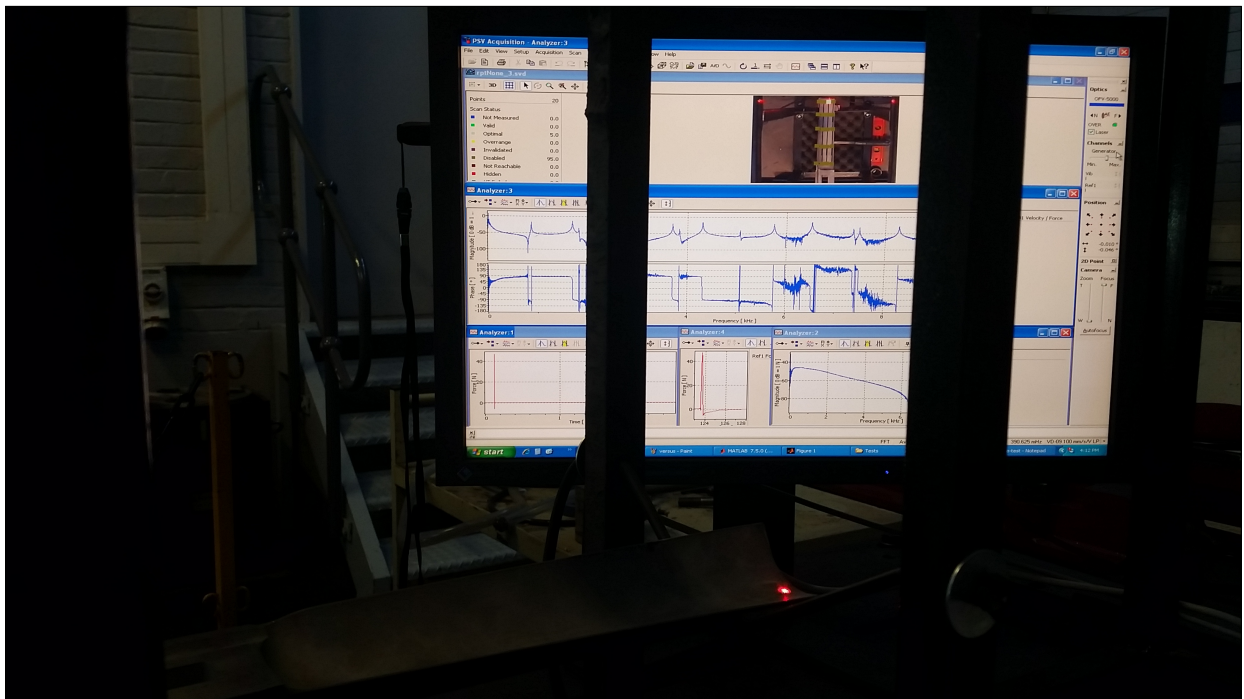


Figure A.1: Additional view of experimental set-up

Appendix B: Geometrical Variability in Test Blades and Class Allocations

The geometrical variability that was observed in the healthy blades is summarised in Table B.1. The assignment of blades into specific groups, tabulated in Table B.2 and Table B.3, are discussed in Chapter 3.

Table B.1: Geometrical variability observed in healthy blades

Blade #	Geometrical Variability	
	Grinding Depth	Hole Diameter
	Yes = 1, No = 0	Max = 1, Min = 0
1	1	0
2	1	1
3	0	1
4	0	0
5	1	1
8	0	1
9	0	1
10	0	1
11	1	0
12	1	1
13	0	1
14	1	0
15	0	0
16	0	0
17	1	0
18	0	1
19	1	1
20	1	0
21	0	0
22	0	0
23	1	1
24	0	1
25	1	0
27	0	0
28	1	0
29	1	1
30	0	0
31	0	0
32	0	1
33	0	0
35	1	0
36	1	0
37	1	0
38	0	0
39	1	0
40	0	0

Table B.2: Allocation of healthy blades for healthy classes

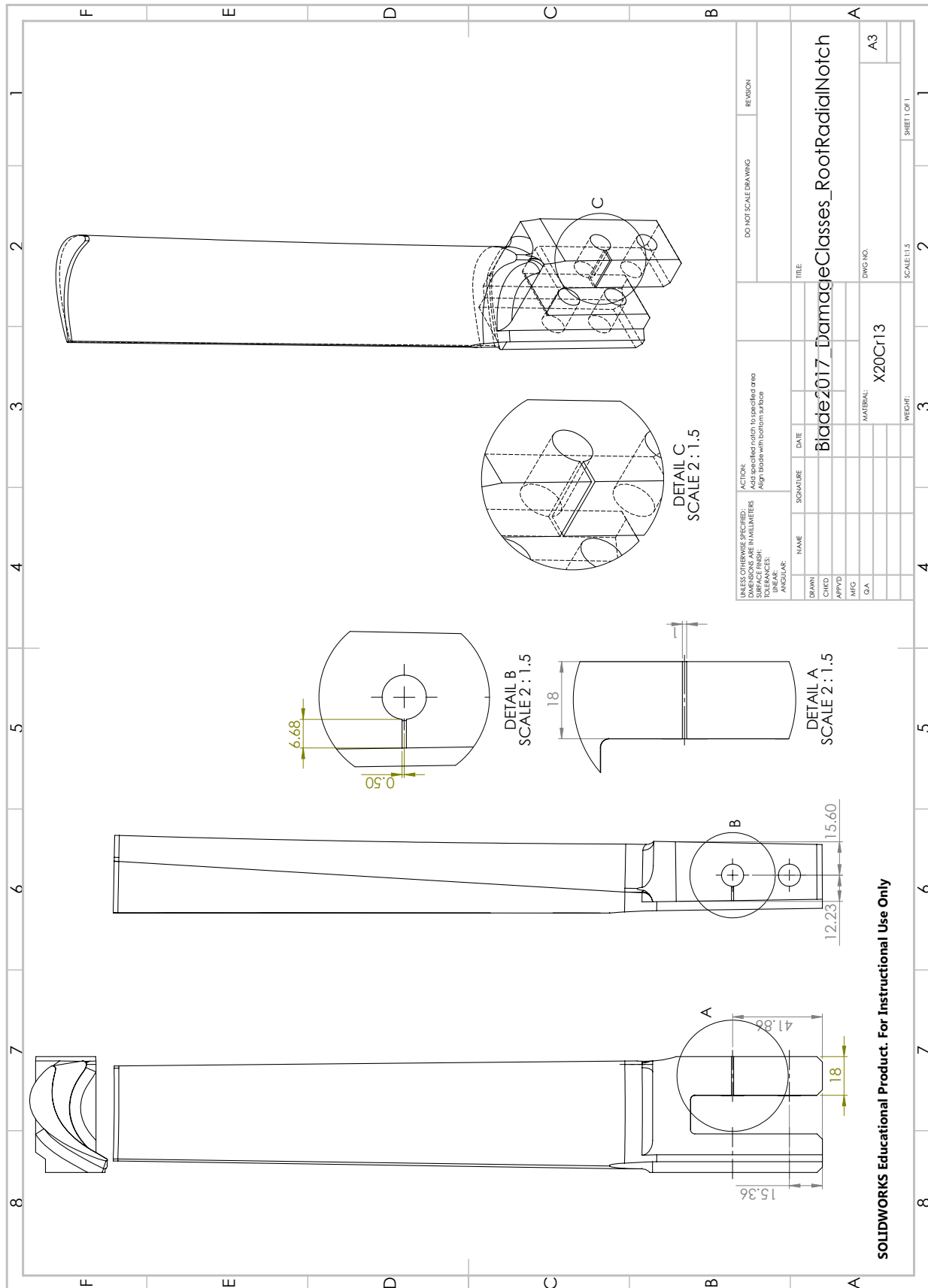
Healthy Classes	Blade #
1. No Grind, Min D	4 15 16 21 22 27 30 31 33 38 40
2. Grind, Min D	1 11 14 17 20 25 28 35 37 39
3. No Grind, Max D	3 8 9 10 13 18 24 32 36
4. Grind, Max D	2 5 12 19 23 29

Table B.3: Allocation of healthy blades for damage classes

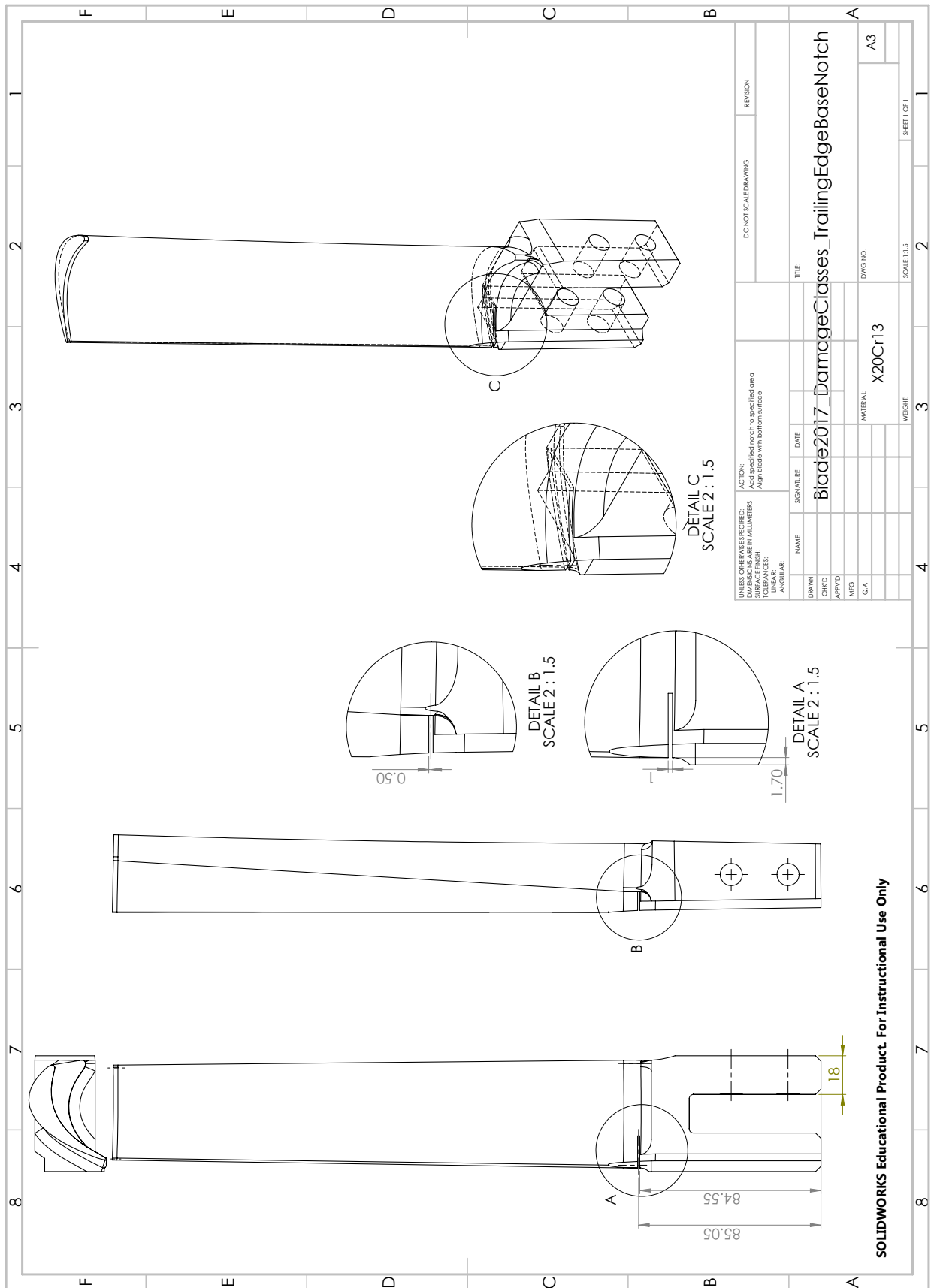
Damage Classes	Blade #
1. Root Radial Notch	1 3 5 13 14 15 16 18 21 23 32 40
2. Base Trailing Edge Notch	2 4 8 9 11 17 27 29 30 31 33 36
3. Base Leading Edge Notch	10 12 19 20 22 24 25 28 35 37 38 39

Appendix C: Drawings of Damage Scenarios

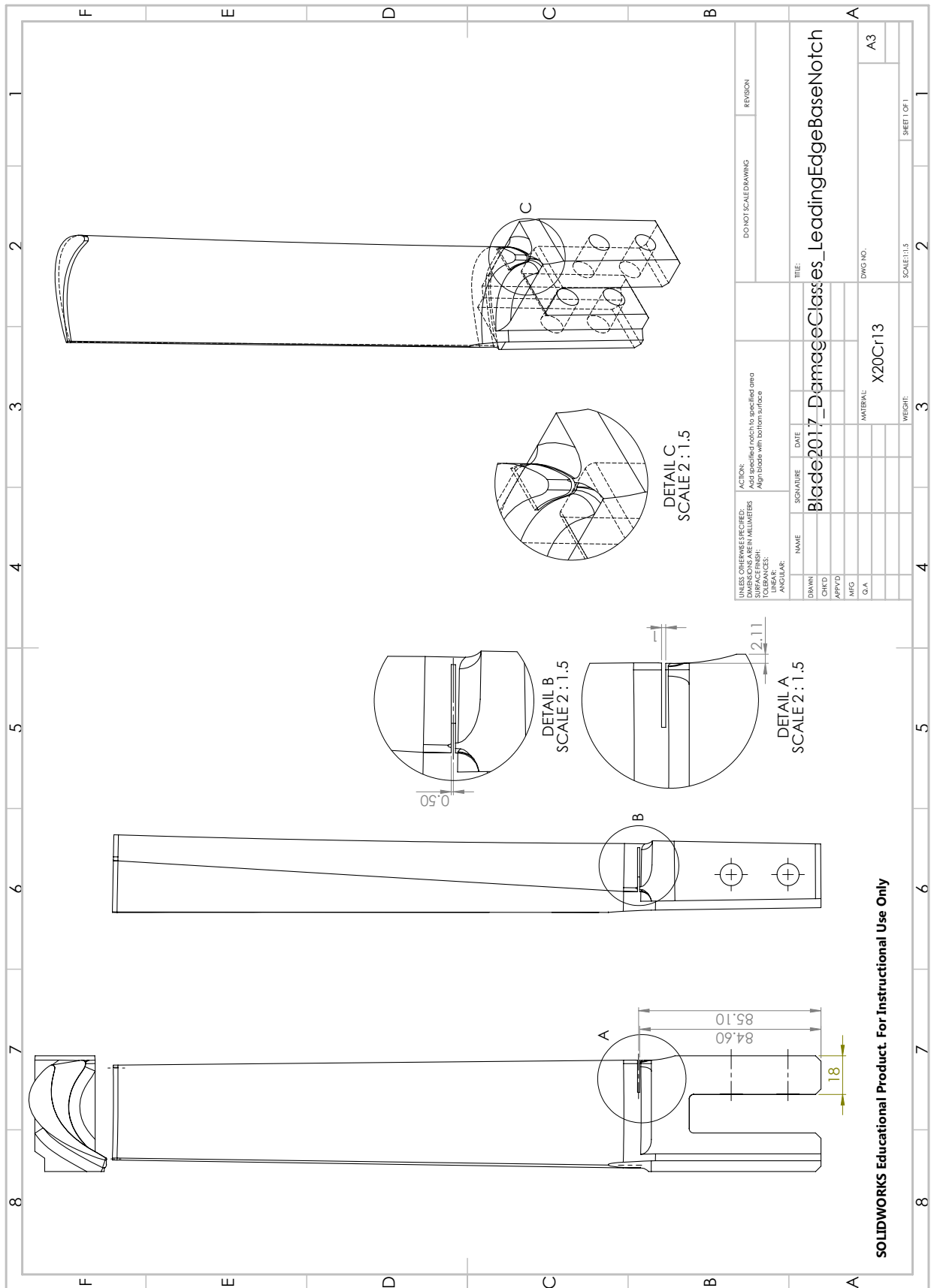
C.1 Damage Class 1: Blade Root Upper Pinhole Radial Notch



C.2 Damage Class 2: Aerofoil Base Trailing Edge Notch



C.3 Damage Class 3: Aerofoil Base Leading Edge Notch



Appendix D: Experimental Data and Additional Results and Details

The experimental data and additional results can be made available on request by contacting Prof. P.S. Heyns, the director of the Centre for Asset Integrity Management (C-AIM) research group at the University of Pretoria, at Stephan.Heyns@up.ac.za.

For more information on the group, visit <https://www.up.ac.za/centre-for-asset-integrity-management>.